AEROMECHANICS, DYNAMICS, AND CONTROL OF CYCLOIDAL ROTOR BASED MICRO AIR VEHICLES

A Dissertation

by

CARL CHRISTOPHER RUNCO

Submitted to the Graduate and Professional School of
Texas A&M University
in partial fulfillment of the requirements for the degree of

DOCTOR OF PHILOSOPHY

Chair of Committee,	Moble Benedict
Committee Members,	John E. Hurtado
	John Valasek
	Terry Creasy
Head of Department,	Ivett Leyva

May 2022

Major Subject: Aerospace Engineering

ABSTRACT

Micro air vehicles are inherently susceptible to wind because of reduced inertia and have lower aerodynamic efficiency due to the poor performance of airfoils at low Reynolds numbers. Cyclorotors can potentially overcome these challenges by using a horizontal rotation axis with blades parallel to it and cyclic pitch kinematics to produce lift. Dynamic pitching delays blade stall and altering pitch kinematics can quickly vector thrust increasing maneuverability. Design of cyclorotor-based aircraft is still in incipient stages, so this research experimentally investigated the aeromechanics, dynamics, and control of cyclocopter micro air vehicles. A cyclorotor design with cantilevered blades and elliptical, flat-plate airfoils was developed for low Reynolds number use. Parametric studies were conducted to understand the impact of pitch kinematics, blade shape, and blade size on performance. Flowfield velocity measurements were taken on the resulting optimized rotor using particle image velocimetry which revealed highly 3D flow across the entire blade span with large leading edge vortices, curved trailing wake, and highly vortical flow inside the rotor. A hover capable micro-scale aircraft (30-gram weight) was developed using two co-rotating cyclorotors and a single conventional nose rotor pointed vertically to counter pitch reaction torque. Stability and control was achieved by varying cyclorotor thrust and magnitude as well as nose rotor thrust. Flight testing showed that the aircraft was unstable and had two forms of dynamic gyroscopic coupling from the angular momentum of cyclorotors and nose rotor acting in different directions. Two additional cyclocopters were built to investigate methods of eliminating these couplings. On one, the single rotor was replaced with a coaxial rotor, balancing the vertical angular momentum. System identification was performed via flight testing to extract a linear flight dynamics model of this aircraft which showed passive stability in roll and yaw making it the first cyclocopter to exhibit these unusual characteristics. The second used four cyclorotors with front and rear rotors counter-rotating to balance torque, eliminating all gyroscopic couplings. With eight independent control parameters, this quad-cyclocopter was an over-actuated system, displayed superior performance, and was capable of performing a point hover within a range of different pitch attitudes.

DEDICATION

To all the many things left undone.

ACKNOWLEDGMENTS

Foremost, I must thank Dr. Moble Benedict for his patience, guidance, and tutelage. His influence has been instrumental in pushing me to achieve more than I otherwise would and make me better than I was, if only by a little. Graduate school was an experience for which I was not fully prepared leaving undergrad and not many people would have devoted the time, effort, or care required to make me grow.

Next I must acknowledge Dr. David Coleman whom I have learned much from. He set eminent examples of how to write scientific papers, proficiency in basic lab skills, and a Spartan work ethic. His working alongside me, his assistance, and his insight were all indispensable in the execution of this research.

Dr. John E. Hurtado first accepted me into graduate school and his class still stands out as a paradigm of the collegiate experience. I still often reference his book and use code I wrote for his projects in my work. It is unfortunate for future students that he became so successful.

Dr. John Valasek is the one that planted the seed of attending graduate school in my brain. I chose to pursue a doctorate in the course of the discussions held as part of his undergraduate airplane dynamics class. Since then he has always been ready to lend an ear or tell a story depending on what the situation called for.

Dr. Terry Creasy was kind enough to accept my invitation to sit on my committee and I thank him for his time and support. His generous flexibility with my lackluster planning skills is appreciated.

The team at the University of Maryland was also more than willing to consult with me when asked and welcomed me warmly the few times we met in person. Dr Vikram Hrishikeshavan, Dr. Elena Shrestha, and Dr. Derrick Yeo all contributed their time and knowledge that greatly aided in the success of this research.

The HRBB crew certainly deserves recognition for their roles. Brett Himmelberg contributed fundamentally to this research through his work on the 3-component force balance and cycloro-

tor testing. Hunter Denton was a figure by which I could set my watch and a sure resource for advice on a whole myriad of things. More than once he helped me solve some problem or improve some aspect of my work. Farid Saemi needs credit for having to herd us around like cats while juggling 10 other responsibilities. And also for the awesome snacks he'd bring in. James McElreath, Dr. Atanu Halder, Xuan Yang, and David made excellent partners for debate and we wasted many hours hashing out the meaning of life and other things. Carolyn Reed, Bochan Lee, and Aswathi Sudir all brightened up the lab and life in College Station with their presence and friendship throughout the years.

A special shoutout to the GoFly team: Dr. Benedict, David, Hunter, Farid, Bochan, and Atanu. This project was some of the most engaging engineering work I have ever worked on. And thanks to Scott McHarg for flying our alien prototypes around.

Finally, thanks to my now wife Alyssa as well as my family and friends for their constant encouragement and belief which was a sustaining source of motivation and esteem from beginning to end.

CONTRIBUTORS AND FUNDING SOURCES

Contributors

This work was supported by a dissertation committee consisting of Professors Moble Benedict, John E Hurtado, and John Valasek of the Department of Aerospace Engineering and Professor Terry Creasy of the Department of Materials Science & Engineering.

All other work conducted for the dissertation was completed by the student independently.

Funding Sources

This research was supported by the U.S. Army's Micro Autonomous Systems and Technology–Collaborative Technology Alliance (MAST-CTA) with Chris Kroninger (Army Research Laboratory–Vertical Technology Directorate) as Technical Monitor.

The work was also supported by Army/Navy/NASA's Vertical Lift Research Center of Excellence (VLRCOE) led by the University of Maryland with Dr. Alex Moodie and Dr. Mahendra Bhagawat as Technical Monitors.

NOMENCLATURE

Abbreviations

2D	2-Dimensional
3D	3-Dimensional
ABS	Acrylonitrile Butadiene Styrene
AR	Aspect Ratio
AVFL	Advanced Vertical Flight Lab
BEMT	Blade Element Momentum Theory
CCW	Counter-Clockwise
CFD	Computational Fluid Dynamics
CG	Center of Gravity
CW	Clockwise
COTS	Commercial-Off-The-Shelf
DARPA	Defense Advanced Research Projects Agency
DoF	Degree of Freedom
ELKA-R	Electronic Lightweight Kinematic Autopilot - Revised
ESC	Electronic Speed Controller
FoM	Figure of Merit
HARWAS	Horizontal-Axis Rotating-Wing Aeronautical Systems
IMU	Inertial Measurement Unit
LEV	Leading Edge Vortex
LiHv	Lithium-ion Polymer High-voltage
LiPo	Lithium Polymer
LTI	Linear Time-Invariant

LSB	Laminar Separation Bubble
MAV	Micro Air Vehicle
MGTW	Maximum Gross Takeoff Weight
MICOR	MIcro COaxial Rotorcraft
MITE	Micro Tactical Expendable
NACA	National Advisory Committee for Aeronautics
NASA	National Aeronautics and Space Administration
Nd:YAG	Neodymium-doped Yttrium Aluminum Garnet
PEEK	Polyether Ether Ketone
PID	Proportional-Integral-Derivative
PIV	Particle Image Velocimetry
QBiT	Quadrotor Biplane Tail-sitter
RC	Remote Controlled
RPM	Revolutions Per Minute
S/VTOL	Short/Vertical Take-Off and Landing
sCMOS	scientific Complementary Metal–Oxide–Semiconductor
SEP	Spherical Error Probable
SIDPAC	System Identification Programs for Aircraft
SLS	Selective Laser Sintering
SMA	Shape-Memory Alloy
SysID	System IDentification
TAMU	Texas A&M University
UAV	Uninhabited Aerial Vehicle
UCLA	University of California, Los Angeles
UF	University of Florida

UMD	University of Maryland

Variables

A	State matrix
A_{dia}	Projected area of cyclorotor
B	Control matrix
b	Blade span
C_D	Coefficient of drag
C_{D_o}	Profile drag coefficient
C_L	Coefficient of lift
C_L	Coefficient of thrust
c	Blade chord
D	Drag
K	Gain matrix
L	Lift; also body-axis rolling moment
L_1, L_2, L_3, L_4	4-bar pitching mechanism linkage lengths
l	Characterstic length
M	Body-axis pitching moment
N	Scale factor; also body-axis yawing moment
N_b	Number of blades
p	Roll angular velocity in the body frame
q	Pitch angular velocity in the body frame
R	Cyclorotor radius
r	Yaw angular velocity in the body frame
T	Thrust

T_X	Horizontal thrust component
T_Z	Vertical thrust component
u	Longitudinal translational velocity in the body frame
V	Relative fluid velocity
V_∞	Freestream velocity
v	Lateral translational velocity in the body frame
W	Weight
w	Vertical translational velocity in the body frame
$\mathbf{u}$	Control array
X	Body-axis longitudinal force
X_i, Y_i, Z_i	Inertial position of CG
x	Scale factor power
$\mathbf{x}$	State array
Y	Body-axis lateral force
Z	Body-axis vertical force
R^2	Coefficient of determination
Re	Reynolds number
β_1, β_2, β_3, β_4	Euler parameters (Quaternions)
γ	Phase angle between maximum pitch and thrust
δ_{lat}	Lateral control input
δ_{lon}	Longitudinal control input
$\delta_{dir_{TV}}$	Direction control input via thrust vectoring
$\delta_{dir_{\Delta T}}$	Directional control input via differential nose propeller torque
δ_{thr}	Throttle input
θ	Geometric blade pitch angle

μ	Fluid dynamic viscocity
μ_{AR}	Advance ratio
ρ	Density of air
σ	Cyclorotor solidity
Ψ	Cyclorotor azimuthal location
Φ	Phase angle of thrust from vertical
ϕ	Roll angle
ψ	Yaw angle
Ω	Cyclorotor rotation speed

TABLE OF CONTENTS

Page

LIST OF FIGURES

FIGURE Page

LIST OF TABLES

TABLE Page

1. Introduction

With the explosive rise in popularity of uninhabited aerial vehicles (UAVs) there is little worry of over-emphasizing their utility or appeal. Adoption has been swift and broad-ranging across varied sectors, from commercial to military to recreational audiences. Whether the goal is efficiency, cost savings, force multiplication, or just plain fun, UAVs have proven their worth and are becoming ever more integrated into the engine of modern life. These devices, commonly known as "drones", are aircraft that fly without a human crew onboard. The lack of a person in the air has aided adoption by reducing the size of the aircraft, the risks involved, operating costs, and barriers to entry that prevent the use of traditional aircraft in many roles. Operation, control, and guidance of UAVs fall on a spectrum anywhere from a remote pilot to fully-autonomous. Piloted remote control is typically done via line-of-sight, where the pilot can see the aircraft, or through an onboard camera that transmits real-time video to a display, which is often referred to as first person view (or FPV) control. Fully-autonomous flight is much more challenging and is achieved through combining a suite of sensors and computational algorithms that allow the UAV to chart its own course based on continuous inputs. The type and size of aircraft that can be considered as a UAV is not limited to any one particular classification or weight. From the 30 mg flapping-wing RoboBee to the 16 ton fixed-wing Global Hawk, UAVs come in all sizes. However, the vast majority of current UAVs weigh around a couple of pounds. These aircraft are predominantly hobby grade hardware in use by enthusiasts or small companies (*e.g.*, photographers and local news organizations). Larger weight classes are populated by more professional grade aircraft and military devices. It is notable that the large UAVs are almost strictly used in commercial or military applications, but with the advent of modern micro-electronics why haven't the smaller aircraft become more popular for practical applications? To understand this dilemma, and ultimately the goals of this research project, this question must first be answered.

1.1 Micro Air Vehicles

When UAVs are built below a certain size they are referred to as Micro Air Vehicles (MAVs). The Defense Advanced Research Projects Agency (DARPA) initially defined design goals for an MAV in 1997 as a UAV that possessed the following characteristics: no dimension larger than 6", approximately 100 g maximum weight with a 20 g payload, endurance of over 1 hour, range of 10 km, and a maximum speed between 10–20 m/s [37]. While no vehicle designed to date has been able to meet all of these lofty goals concurrently, this mission statement coupled with emerging technology was an impetus to start the exploration of this space. The preliminary concept envisioned these tiny aircraft as diminutive sensor platforms that could be carried by a single soldier and deployed rapidly in all manner of situations and locations. Figure 1.1 shows a realized example of this, the FLIR Black Hornet. But since DARPA's call-to-arms, the scope and number of use cases for MAVs have rapidly expanded beyond the military role as a result of the their many inherent benefits (*i.e.*, portability, compactness, low signature, reduced costs, and lowered risks) as well as the ever-growing availability of Commercial Off-The-Shelf (COTS) parts.

Figure 1.1: A soldier deploying a FLIR Black Hornet MAV. Credit: FLIR.

As a military device, the MAV can fly in any of the varied battlefields a soldier might find

himself in from dense jungles to the insides of buildings, while also being harder for an adversary to detect, enabling close range surveillance. Outside of the military scope, these same qualities are advantageous to a commercial or recreational user as well. Navigating the internals of some industrial complex to perform an inspection or maneuvering inside a venue to photograph an event are both made easier by a reduction in size. Additionally, the inherently quieter MAV is less likely to disturb its surroundings than a larger UAV, whether that be a wedding party or wildlife. They also have become common training platforms for people learning to fly UAVs because of the relatively low costs and mitigated risks. However, many of these missions often require flying conditions prohibitive to most MAVs in used today because of factors such as gusts, confined spaces, and lengthy flight times. To maximally perform these flights MAVs require specific qualities:

- Hover + vertical take-off and landing (VTOL) capability
- Maneuverability
- Gust tolerance
- High-speed forward flight
- Efficiency

Hover and VTOL capabilities are particularly important for many operations that require observation, in both constrained and open spaces. In tight spaces, hovering simplifies observation and sensing missions by giving a consistent field of view. Whereas, in open areas, the ability to hover and land is enabling to a wide array of missions including accurate delivery, retrieval, and perching. Maneuverability and gust tolerance is required for operation in tight spaces as well as flying outdoors to expand the flight envelope beyond the calmest of days. High-speed forward flight extends the range of operation and allows the pursuit of moving objects. Finally, efficiency permits a longer mission duration and range. Designing a UAV that encompasses all of these qualities is difficult enough, but there are certain factors that compound the problem at MAV scales.

1.1.1 Challenges of MAV Design

There are many challenges associated with designing aircraft at this size, however, there are two fundamental issues that are responsible for the relative performance degradation of MAVs compared to larger UAVs[38–42]. The primary limitation is the poor aerodynamic performance of airfoils at low Reynolds numbers (10,000–50,000). The second is how scaling down aircraft adversely impacts their physical properties. Regardless of design, all MAV will suffer from these two detriments. In order to maximize the aircraft performance it is paramount that designers assuage both of these issues.

1.1.1.1 Low Reynolds Number Aerodynamics

Reynolds number, Re, is a non-dimensional measure representing the ratio of inertial to viscous forces acting within a flow. It is defined as:

$$Re = \frac{\rho V l}{\mu}$$

where ρ is the density of the fluid, V is the relative velocity between the flow and the object, l is a characteristic length (commonly the chord of an airfoil), and μ is the dynamic viscosity of the fluid. The higher the Reynolds number the more prevalent the inertial forces are compared to the viscous forces. As Re decreases, the proportion of the shear layer on an airfoil that is laminar will increase. Consequently, the boundary layer will be more likely to separate reducing maximum lift and increasing profile drag. Conventional airfoils are designed to operate at or above a particular Re in order to maximize C_L/C_D. Below a critical Reynolds number, C_L/C_D will rapidly plummet because of the behavior of a Laminar Separation Bubble (LSB), explained below[43]. When generalized, this trend can be plotted for various types of airfoils, shown in Figure 1.2 by the hashed regions. Above $Re > 10^5$ smooth conventional airfoils will have the maximum C_L/C_D, but below this rough airfoils will outperform them [1, 2, 44, 45]. At extremely low Reynolds numbers ($Re < 5 \times 10^4$) where insects typically fly, flat plate airfoils will surpass both rough and smooth airfoils[3]. Even airfoils optimized to fly in these conditions have lift-to-

drag ratios well below traditional ones operating in higher Re regimes.

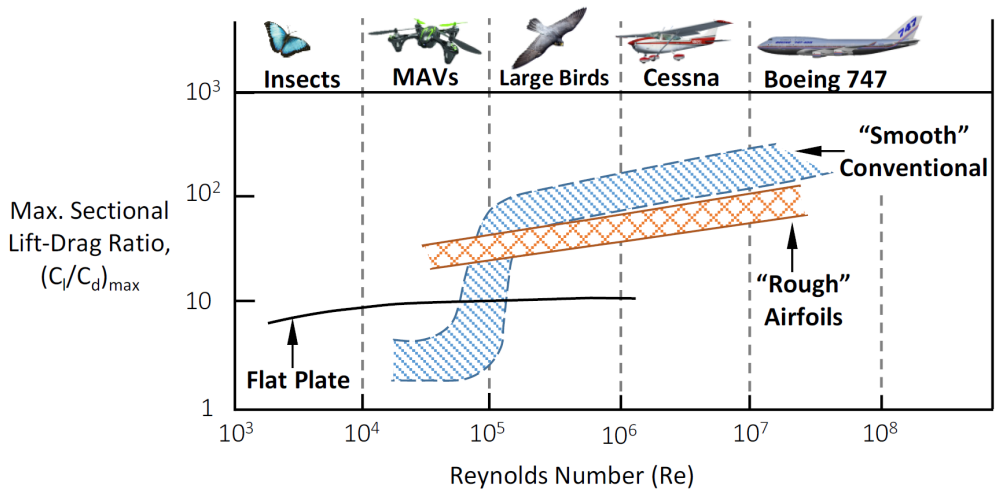

Figure 1.2: Effect of Reynolds number on airfoil maximum sectional lift-to-drag ratio[1–3].

For fixed wings, the low C_L/C_D increases the power draw for any given operating point resulting in lower ranges and decreased payloads by mass fraction[46]. Conventional rotors at MAV scales experience low maximum figures of merit (ratio of ideal to actual power) of around 0.65[41, 47, 48]. The low aerodynamic efficiency is caused by the large profile drag associated with thick boundary layer formation on the blades, large induced losses, and higher rotational and turbulent losses in the downstream wake of the rotating blades.

The laminar separation bubble (LSB) is a phenomenon that occurs on most airfoils above a Reynolds number of about 50,000. It occurs when a laminar boundary layer encounters adverse pressure gradients which cause it to go unstable and detach from the surface. Further along in the flow, the boundary layer becomes turbulent and reattaches to the airfoil surface before the trailing edge[49, 50]. The reattachment point for the LSB will occur further rearward on the airfoil as Re decreases. Below Re = 50,000 the boundary layer will not have enough time to transition to turbulent and reattach[2, 51]. Figure 1.3 illustrates the different behaviors of the LSB for varying Reynolds numbers. What this means is that a more efficient lift generation technique is needed

that can harness the inherent physics of low Reynolds number unsteady aerodynamics, something like the cyclorotor.

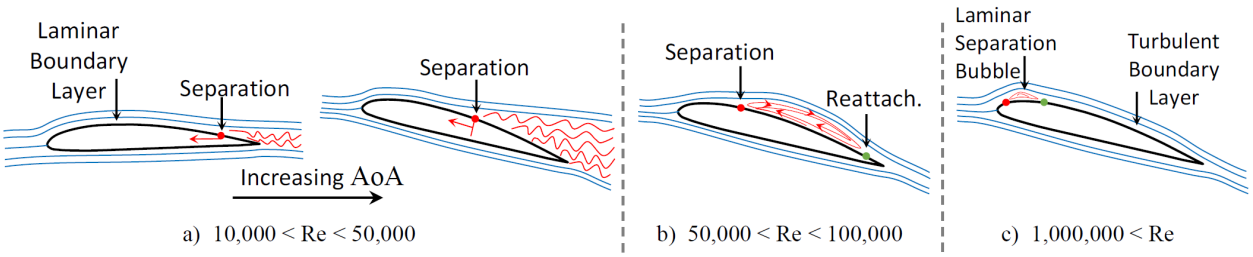

Figure 1.3: Conventional airfoil characteristics at $Re < 10^6$[3].

1.1.1.2 Scaling Properties

The second major challenge facing MAV designers is how physical properties scale with size. The effects of shrinking a design down can be represented by simple length-based relations. When reducing a UAV by a factor of N, the physical attributes of the UAV will change by a factor of $1/N^x$ where the value of x is based on the attribute being considered[52]. Table 1.1 summarizes these relationships. As an example, if a UAV is scaled down by a factor of 2 then the surface area is reduced by a factor of 4.

Table 1.1: Relationships Governing Scaling Based on Factor N

Property	Relation
Length	$1/N$
Surface Area	$1/N^2$
Mass	$1/N^3$
Moment of Area	$1/N^4$
Inertia	$1/N^5$

Because inertia and mass decrease faster than the surface area, small UAVs typically have higher thrust-to-weight ratios and more control authority than their full-scale counterparts [53–55].

On the contrary, by the same logic, small aircraft are also more susceptible to external perturbations and wind gusts because they have lower inertia to damp aerodynamic forces. As a result, most MAVs are only able to fly in quiescent atmospheric conditions. The same effect (low inertia) that allows quad-rotors to perform incredible aerobatics is responsible for their lackluster performance on windy days. The increased sensitivity to control inputs is also why most MAVs require an onboard flight controller that performs stability augmentation as the raw body dynamics are too fast for human control. Zarovy *et al*. demonstrate this downward trend in gust rejection capabilities by comparing the ability of several remote-controlled coaxial helicopters of varying size to perform a point hover in the presence of gusty wind[56]. Data from this experiment is shown in Figure 1.4. The Spherical Error Probable (SEP) metric quantifies how well each craft is able to maintain point-hover by measuring the radius of a sphere centered at the desired location that encapsulates 50% of the trajectory (lower is better). As the size of the coaxial helicopter is increased it can maintain a tighter point-hover in harsher wind conditions.

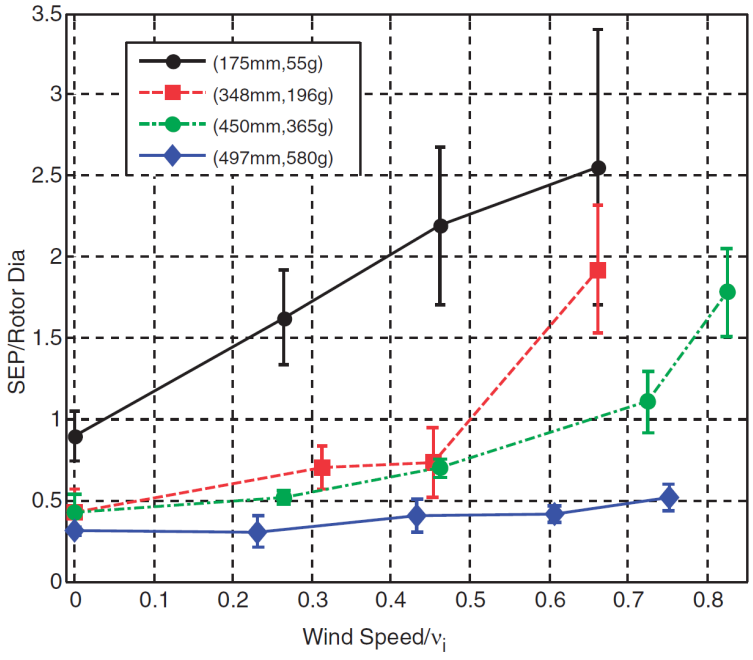

Figure 1.4: Non-dimensionalized average SEP for each coaxial helicopter, labeled with rotor diameter and mass.[1–3].

1.1.2 Types of MAVs

With the intent to overcome these intrinsic deficiencies of small scale flight, designers from differing backgrounds have produced multitudinous MAVs of varying form and function. Since DARPA issued its guidelines in 1997 many advancements have been made in electronics, control theory, materials, and the fundamental understanding of low Re aerodynamics. Coupled together with the rapid increase in COTS parts available on the consumer market, the MAV design space is no longer monetarily restricted to military projects or well-funded commercial endeavors that can afford bespoke components. Generally, these MAVs can be divided into 3 categories based upon the manner in which they produce lift: fixed-wing, flapping-wing, and rotary-wing. Each archetype possesses inherent benefits and drawbacks[57]. The subsequent sections briefly present the three aforementioned MAV archetypes along with some examples then concludes with the cyclocopter, a rotary-wing concept that has the potential to alleviate some of the detriments of micro-scale flight through a novel approach to lift generation.

1.1.2.1 Fixed-Wing MAVs

MAVs with fixed-wings are perhaps the oldest of the micro-sized flying devices. For many adults, playing with rubber-band-powered model airplanes as children growing up is an indelible experience. But the advanced systems of today are a radical evolution from these prototypical designs largely thanks to rigorous scientific study. In 1998, the MLB Company, in collaboration with UC Berkeley and funding from DARPA, developed what they call the Trochoid which was powered by a small gasoline engine (Fig. 1.5a)[58]. Several sizes were developed and the 20 cm size boasts a top speed of 60 mph with recorded controllable flights in 20 mph winds. Two years later, AeroVironment, also funded by DARPA, created the Black Widow MAV as part of an SBIR contract which set several world records[59]. This aircraft, shown in Figure 1.5b, was driven by a single propeller, weighed 80 g, and demonstrated an endurance of 30 minutes. Shortly after that, the Navy Research Laboratory designed a 129-gram MAV named the Micro Tactical Expendable (MITE) capable of carrying a 100 g payload (Fig. 1.5)[60]. This small flying wing design used two

propellers and was able to perform autonomous obstacle avoidance using an onboard color camera. Researchers at the University of Florida produced a circular planform flying wing with a 6-inch diameter that used flexible wings to improve flight stability and enhance structural durability (Fig. 1.5d)[61]. The UF device was able to achieve flight times of 15 minutes with speeds ranging from 15-25 mph.

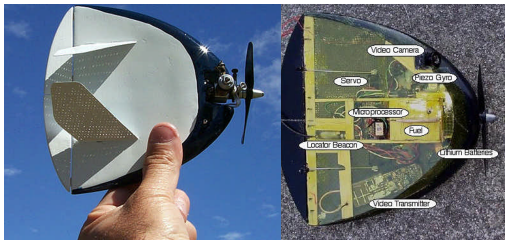

(a) Trochoid: 15 cm (left) and 20 cm (right)[58].

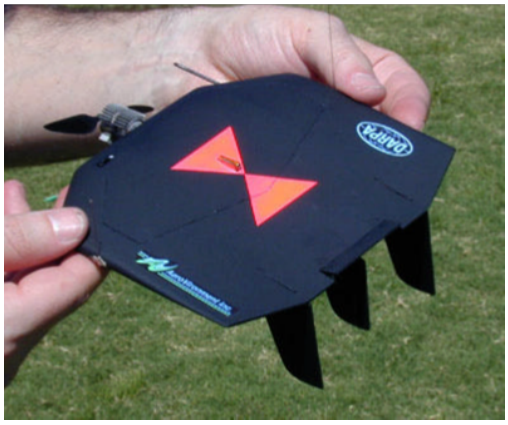

(b) Black Widow[59].

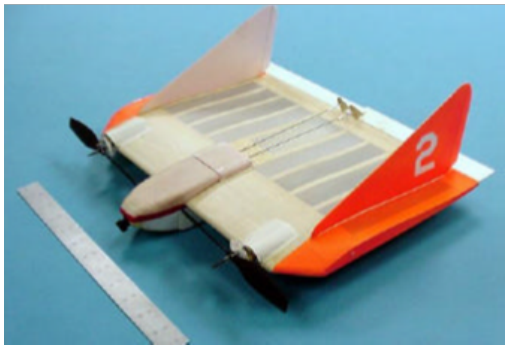

(c) MITE[60].

(d) UF's flexible wing MAV[61].

Figure 1.5: Examples of fixed-wing MAV designs.

Many of the early MAVs were fixed-wing designs because of the hardware available at the time. Compared to other types of MAVs, a fixed-wing design has advantages in both endurance and weight – forward flight is not as power intensive as hover and structures at these scales are

very stiff for their weight. But these vehicles cannot hover and have poor control authority at slow speeds which makes them ill-suited to operate in constrained environments that would require low-speed flight, tight turns or other demanding maneuvers. Payload carrying options are also limited because the capacity for many of the aforementioned designs is restricted by the internal volume of the wing.

1.1.2.2 Flapping-Wing MAVs

Inspired by the nimble flyers found in nature, many MAVs have been created with flapping-wings in attempts to imitate the enviable flight qualities airborne creatures possess. Accordingly, the types of flapping-wing aircraft mimic the various styles of flapping kinematics (or gait) found in nature. There are bird-like ornithopters, insect-inspired entomopters, and vehicles that flap like hummingbirds. Ornithopters seek to embody the forward flight endurance many birds and insects seem to effortlessly demonstrate while also maintaining their agility. Entomopters vary in design from those reminiscent of four-winged insects like hover-capable dragonflies to those resembling moths. MAVs modeled after hummingbirds are trying to achieve the extreme aerobatic adroitness and forward flight speeds the real ones are capable of. From a practical standpoint, an MAV that could replicate natural flight would have superior maneuverability and produce a lower sound signature than other types. But, aside from some simplistic toys, these craft are almost exclusively research projects due to the complex aerodynamics of flapping wings, limited endurance, and the difficulty of creating a reciprocating mechanism that can mimic biological systems with sufficient fidelity and reliability.

One such pioneering effort was the Microbat, created at UCLA in 2001 in collaboration with AeroVironment (Fig. 1.6a). Eponymously named for the morphological structure of its wings, the vehicle weighed 12.5 grams, flapped at a frequency just under 30 Hz, and achieved a maximum flight time of 42 seconds[62]. More recently, researchers at TU Delft developed several flapping-wing configurations they called DelFly (Fig. 1.6b). The heaviest of which weighed 21 grams, was hover capable, and was successfully flown outside and used as a test-bed for vision-based navigation algorithms[63]. Another endeavor from AeroVironment produced the Nano Hummingbird,

a 19 g aircraft with a wingspan of 16.5 cm that could hover for several minutes and fly forward up to 6.7 m/s (Fig. 1.6c)[64]. Separately, a team at Harvard were able to successfully fly a tiny, insect-inspired robot which has earned the name RoboBee. The first iteration was an 80-milligram two-winged device capable of roll, pitch, and yaw control that required tethered power to fly (Fig. 1.6d)[65]. An updated version weighs 90-milligrams and uses four wings while being powered by photovoltaic cells under intense artificial light (Fig. 1.6e)[66]. In Japan, research was conducted on a small flapping vehicle to investigate control by means of shifting the center of gravity (CG) (Fig. 1.6f)[67]. The battery was held in a lower portion of the vehicle which was pivoted side-to-side and fore-to-aft to generate roll and pitch moments. At Texas A&M, a robotic hummingbird was made and flown that utilized biomimetic wing kinematics coupled with aerodynamic center shifting to replicate and study hummingbird flight (Fig. 1.6g)[68]. As part of that effort it was used to examine the properties of flexible wings as well as to experimentally derive linear models of its flight dynamics and conduct a stability analysis.

1.1.2.3 Rotary-Wing MAVs

Lastly, there are rotating wing aircraft, the most well-known types are the scaled-down helicopter and the multicopter. MAVs employing single, coaxial, or multi-rotor configurations are particularly suited for hovering/low-speed flight. These designs exploded in popularity because of the benefits modern electronics provided. Readily available motor controllers, high-quality open-source software, and the advent of brushless motors enabled longer flight times and more stable platforms that could be used by a wider audience. More flight-worthy hardware in the hands of more people facilitated extensive end-user experimentation allowing companies and hobbyists to focus on developing more use-cases for MAVs rather than on how to make them work. The open-source software allowed people to modify handling qualities and tune the systems for different situations (*e.g.*, racing, aerobatics, or photography). As a result, the industry converged on accepted practices that could be used to adjust rotary-wing MAV flight characteristics without deep technical knowledge. Additionally, these aircraft are attractive to a broad user-base because they

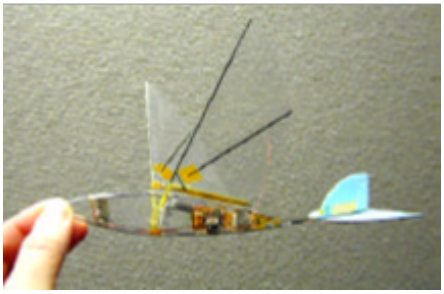

(a) Microbat[62].

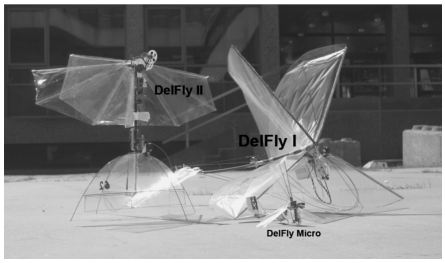

(b) The DelFly family of MAV[63].

(c) Nano Hummingbird[64].

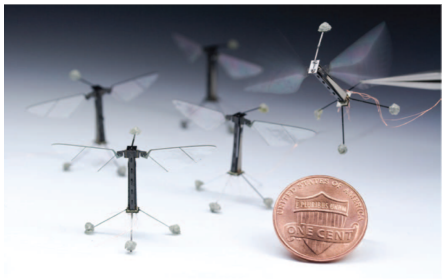

(d) Tethered, two-winged RoboBee[65].

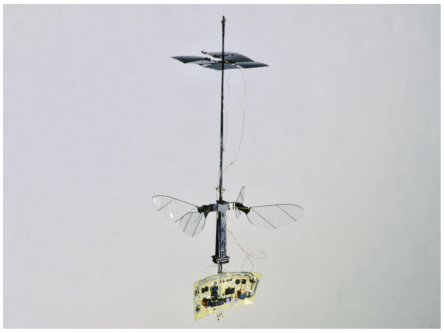

(e) Photonically powered, four-winged RoboBee[66].

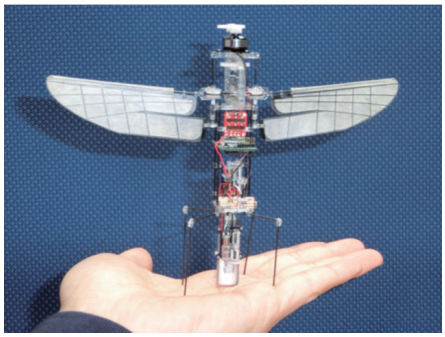

(f) Japanese flapping MAV[67].

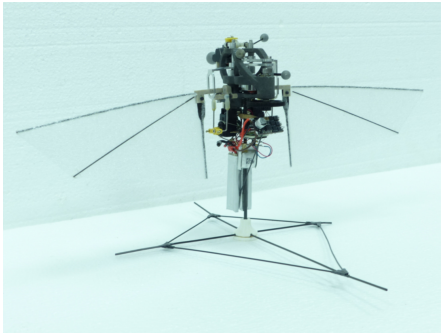

(g) Robotic hummingbird from Texas A&M[68].

Figure 1.6: Examples of flapping-wing MAV designs.

are fairly payload agnostic. Nearly any sensor package or item that is within weight budget can be affixed to a helicopter or multicopter without worrying about the payload's footprint. Since the flight speed is relatively low, there is no strict aerodynamic requirement for the payload to be loaded internally to the structure like with fixed-wing aircraft.

Remote-controlled (RC) helicopters exemplify the progression rotary-wing MAVs have made, moving from passive mechanical stability systems to computer augmented controls. One early research project into MAV-scale helicopters was conducted at the University of Maryland (UMD) that built a 100-gram MIcro COaxial Rotorcraft, dubbed MICOR, to investigate various control methods and overall feasibility (Fig. 1.7a)[69]. In the nearly two decades since then, micro-helicopters have gained acceptance in commercial and military markets. Figure 1.7b shows a popular RC model in inverted hover, a basic maneuver in the world of 3D helicopter aerobatics. From a military standpoint, both the UK and US militaries have tested the Black Hornet (Fig. 1.7c). A small, 18-gram helicopter equipped with a camera, night vision, and GPS navigation capabilities.

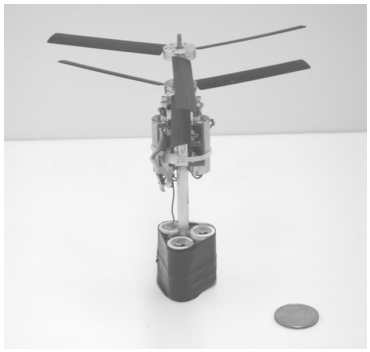

(a) MICOR (MIcro COaxial Rotorcraft)[69].

(b) mCPS demonstrating inverted hover[70].

(c) Black Hornet. Credit: FLIR

Figure 1.7: Examples of helicopter MAV designs.

Probably the most prolific of the MAV designs is the multicopter (or multirotor), an aircraft that uses several propellers distributed in a pattern to provide lift and control moments. Often the

only moving parts are the propellers and because of this mechanical simplicity they are robust with low service costs. A research project at Stanford in 2001 studied micro-scale propeller designs, powerplants, and stability augmentation leading to the development of the mesicopter, a 17-gram quadcopter (Fig. 1.8a)[71]. However, this aircraft had limited useful flight time owing to the power required by the brushed motors and the low-energy density batteries. For comparison, figure 1.8b shows a toy that can currently be bought from many retailers with a flight time of several minutes, indicative of the progress made in the field. There are also efforts to use these multicopters in transitioning aircraft to garner the benefits of both multirotors and fixed-wing aircraft. One example of this is the mini Quadrotor Biplane Tail-sitter, or QBiT, developed at UMD that can fly in a quadrotor mode then transition to forward flight to take advantage of its wings (Fig. 1.8c)[72]. The mini QBiT weighs 230 g and has no control surfaces but uses combinations of propeller thrust and torque for stability and control in both modes. Unfortunately the quad-biplane requires a maneuver to transition between hover and forward flight and back again, one that limits its uses in tight spaces.

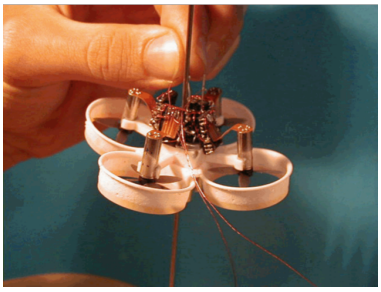

(a) Mesicopter[71].

(b) Cheerson CX-10. Credit: Cheerson

(c) Mini QBit[72].

Figure 1.8: Examples of multirotor MAV designs.

Finally, there is the cyclocopter, a promising solution to overcoming the deficiencies associated with standard rotors. Predominantly using cycloidal rotors, or cyclorotors, for lift generation and control, cyclocopters have the potential to be more maneuverable and gust-tolerant while also

being able to transition seamlessly from hover to high-speed forward flight. Enabled by modern technology and materials, recent research into the cyclorotor has yielded promising results and created the world's first flight worthy cyclocopter UAV. Building upon that, the ultimate goal of this project was to study the ability of cyclorotors to enhance MAV performance. A cyclocopter MAV can maintain the capabilities of other rotary-wing MAVs while also exhibiting the superior forward flight performance typical of fixed-wing types. In order to understand how that is possible a brief explanation of what a cyclorotor is and how it functions will be provided below followed by a short synopsis of cyclorotor research foundational to this work.

1.2 The Cyclorotor

The cyclorotor is a VTOL propulsion concept consisting of several blades that rotate about a horizontal axis with the blade span parallel to the axis of rotation (Fig. 1.9). The pitch angle (θ) of each of the blades is varied periodically as the blade moves around the azimuth of the rotor such that the blade is at a positive geometric angle of attack both at the top and bottom halves of its circular trajectory. The blade kinematics and aerodynamic forces on a functioning cycloidal rotor are shown schematically in Fig. 1.10. The maximum value of θ the blade attains is known as the pitch amplitude. Symmetric pitch kinematics mean that maximum geometric blade pitch is the same at the top and bottom, whereas asymmetric means they are different. The radial direction pointing towards this maximum blade pitch from the center of rotation is known as pitch phase, but the angle γ between the pitch phase and maximum resultant thrust is called thrust offset. By varying both the rotational speed (Ω) and the cyclic pitch phasing (Φ), the magnitude and direction of the net thrust vector of the rotor can be carefully controlled.

There are several advantages of the cyclorotor over conventional rotors, one of the most significant of them being the fact that all the spanwise elements of the blade operate at the same aerodynamic conditions, which allows all the blade elements along the blade span to be set at an optimum configuration. This is in contrast with conventional rotors, in which each blade element along the span experiences a different flow velocity, Reynolds number, and angle of attack. Experiments conducted at the University of Maryland have also shown that a cyclorotor may be more

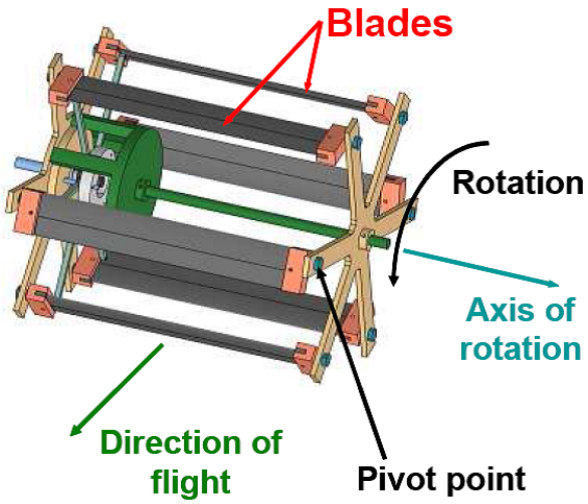

Figure 1.9: Cycloidal rotor model with key components identified[4].

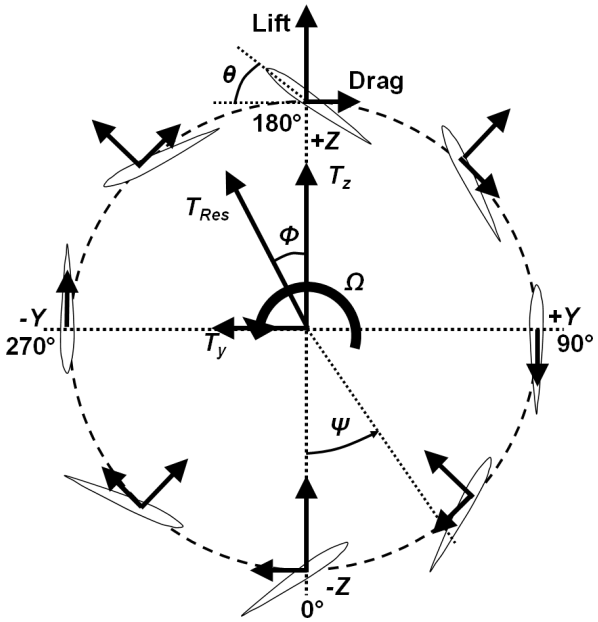

Figure 1.10: Blade kinematics and forces on a cycloidal rotor in hover[4].

aerodynamically efficient in terms of power loading (thrust per unit power) than a conventional rotor of the same scale and similar actuator area[73, 74]. Additionally, a cyclorotor is able to obtain the required thrust at a significantly lower rotational speed than an equivalent conventional rotor, and therefore has a reduced acoustic signature making it further advantageous for reconnaissance missions. Furthermore, since the blades are cyclically pitched once per revolution ($1/rev$), unsteady flow mechanisms may delay blade stall onset and in turn may augment the lift produced by the blades. Finally, since the thrust vector of a cyclorotor can be instantaneously set to any direction perpendicular to the rotational axis, the concept may also have better maneuverability compared to a conventional rotor based MAV. By vectoring its thrust a cyclocopter can transition from hover to forward flight or enter translational motion without changing attitude, further demonstrating its usefulness in highly constrained applications and indoor operations. More detailed information about the operating principles of a cyclorotor will be provided in Chapter 2.

1.3 Research on the Cyclocopter

Marie Antionette's dressmaker, Mademoiselle Bertin, is known for telling the court, "*Il n'y a de nouveau que ce qui est oublié*" which translates to, "There is nothing new except what has been forgotten." Cyclorotors are a poignant example of this wisdom. The concept of horizontally rotating wings for aerodynamic uses was heavily explored in the pioneering days of flight. Given the widespread application of paddle wheels to aquatic navigation it is unsurprising that a similar approach would be taken for air travel. When specifically applied for generating propulsive and lift forces these devices were called cyclogiros, now called cyclorotors. Up until around the 1960s there were only a few concerted efforts to make cyclogiros. However, most of these projects were not based on a scientific approach and almost all were full-sized aircraft. As a result, no flight-worthy cyclogiros were produced. With the success of the helicopter, development efforts were diverted into it as the primary VTOL technology and interest in cyclorotors foundered. For several decades a dearth of research left the cyclogiro as a novelty of a bygone era. But the challenges of small-scale UAV design once again created an impetus for designers to explore non-traditional lifting devices. Systematic studies on cyclorotors began again in 1998 and persist to this day in multiple research institutions and companies around the world. These efforts were more scientific in nature than previous attempts, methodically studying the fundamental elements of cyclorotor thrust generation using modern techniques. Because of this, great progress was made towards understanding the design of cyclorotors and flight capable cyclocopters were produced not long after.

In regards to early cyclorotor research, Ref. [5] is an extensive report commissioned by the U.S. Army in 1969 that reviews all of the literature their team could find (approximately 1200 references) related to "Horizontal-Axis Rotating-Wing Aeronautical Systems" (HARWAS), which encompasses more than just cyclorotors. Their references include "periodicals, journals, reports, newspapers, films, patents, and books, as well as interviews with technical researchers in the field of horizontal-axis rotating-wing aircraft systems." No vehicle using cyclorotors for propulsion was flown before the report was released. It identified as limiting factors low power density of

engines, lack of fundamental knowledge of HARWAS aerodynamics, and insufficient structural materials, coincidentally mirroring the deficiencies of current MAVs identified by contemporary scientists. The report also contains analysis of their findings which notes two preliminary designs they identified as promising. The first of which is a modification of an existing aircraft where the flaps are replaced with a HARWAS for short take-off and landing (STOL) scenarios (Fig. 1.11). The airfoil doesn't continuously rotate, but is placed in the slipstream to replace flaps and other control surfaces. The second is an aircraft using 4 cyclorotors as the source of propulsion and lift (Fig. 1.12) that was meant to combine the hover-capability of helicopters with the high-speed forward flight of fixed-wing craft. This was a purely conceptual design and further advancement in the application of cyclorotors to flying vehicles was limited due to the "total lack of research in this area."

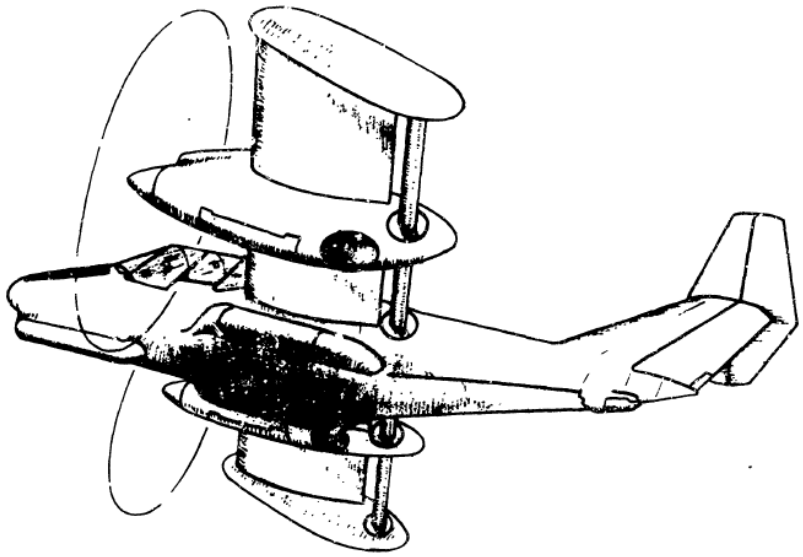

Figure 1.11: Deflected slipstream STOL aircraft utilizing rotating airfoil flap for slipstream and lateral control[5].

One of the earliest documented designs of a cyclogiro referenced by the report is the "Aerial Carriage" proposed by Sir William Congreve, who is also known for his rocket innovations(Fig. 1.13). But one of the first scientific studies of cyclorotors was done by Professor Kirsten at the

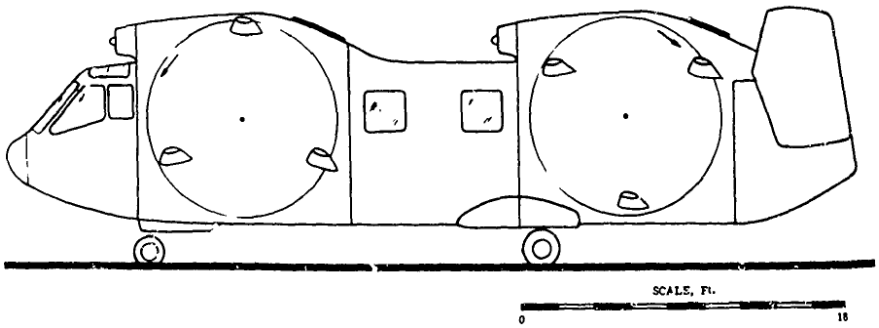

Figure 1.12: Cyclogiro transport aircraft designed for composite mission profiles[5].

University of Washington in the 1920s in collaboration with W. E. Boeing [7, 75, 76]. Kirsten's "cycloidal propeller" design used blades that rotated in the opposite direction to the rotation of the system at half of the angular velocity so that they only turned 180° for one complete revolution of the propeller (Fig. 1.14). Small and large experimental versions of this design were built and tested in a wind tunnel. These experiments revealed that the performance of the propeller heavily depended upon the ratio of blade chord to rotor diameter. After satisfactory wind tunnel results, a propeller was made that could produce 212 lbs of thrust at 225 RPM with the intention of equipping an airship, the *Shenandoah*, with several like it (Fig. 1.15). Unfortunately, the airship crashed and the project was halted with no further development. However, several aquatic cycloidal propellers were produced and a vessel outfitted with one was able to make combined trips totaling over 4000 nautical miles. An Austrian engineer by the name of Ernst Schneider was simultaneously developing a variant of the aquatic propeller and his company, Voith-Schneider Corp, bought the patent for Kirsten's cycloidal propeller and developed it into the Voith-Schneider Propeller (Fig. 1.16)[8]. To date, this is the only commercially successful application of cycloidal propellers.

Beginning around the same time, a Swedish engineer by the name of C. B. Strandgren conducted experiments towards building a full-sized aircraft powered by cyclogiros. From about 1924 to 1934, Strandgren constructed several experimental rigs, the largest of which had a diameter of 18 feet (Fig. 1.17)[9]. The plan was to create a single-seater aircraft powered by a 130 hp engine that utilized these rotors(Fig. 1.18). Although work progressed to the point of demonstrat-

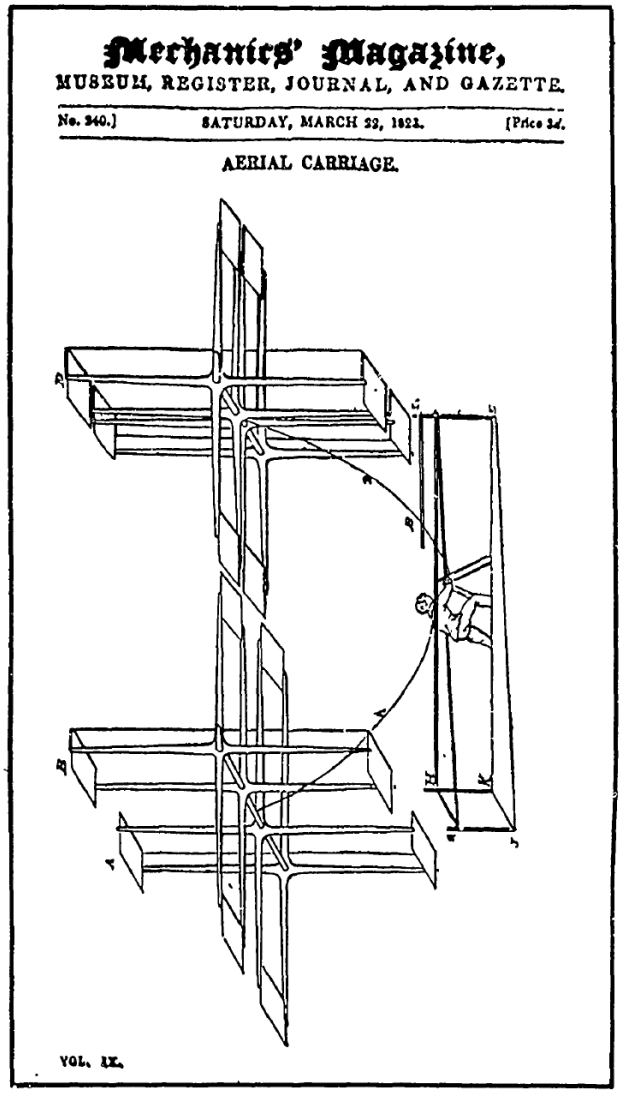

Figure 1.13: Early cyclogiro proposed by Sir William Congreve, 1828[5].

ing satisfactory performance for the cyclorotors themselves, the vehicle was never built or flown. Alongside this work, he also developed the first analytical model for cyclogiro lift production[77]. His model assumes a quasisteady aerodynamic flow over the blades and calculates the tangential and normal blade forces at each azimuthal location in the rotation. The total force is then obtained by integrating this result over one revolution and multiplying by the number of blades. Through his analysis he shows that the force produced can be changed in magnitude and direction by altering the phasing and amplitude of blade pitch kinematics. Extending this formulation, he further

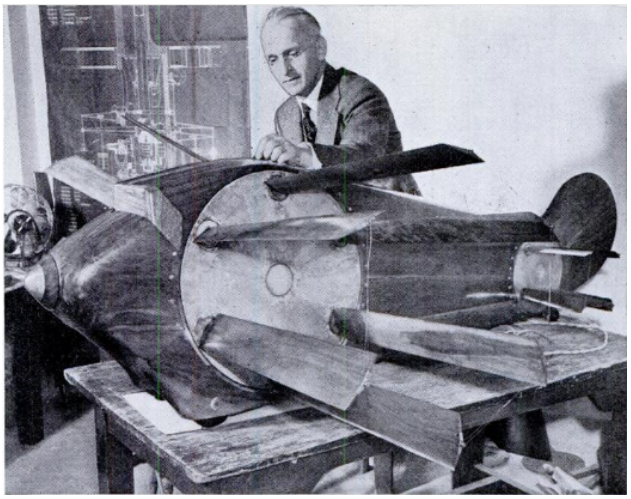

Figure 1.14: Professor Kirsten with a model of a cycloidal propeller driven airplane[6].

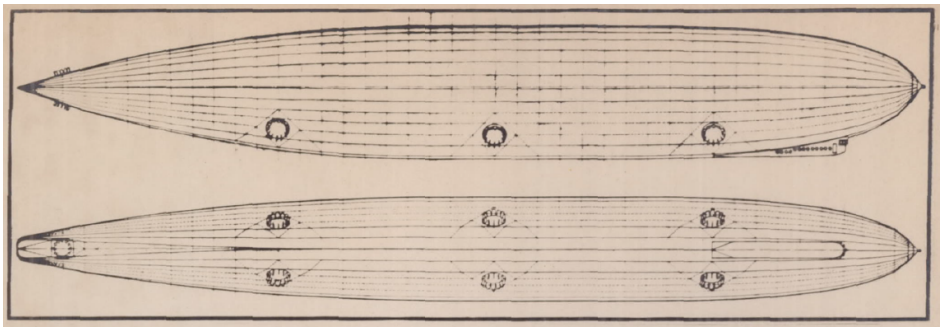

Figure 1.15: Airship "Shenandoah" (680.8 ft) equipped with cycloidal propellers[7].

demonstrates the ability of a cyclogiro to autorotate.

Almost concurrently in 1933, Wheatley was developing a separate simplified model of the cyclogiro using Blade Element Momentum Theory (BEMT). It was assumed that inflow through and across the rotor was constant, the blades did not interfere with each other, and the coefficient of drag was constant. The instantaneous lift and drag of the blade was calculated and were resolved into horizontal and vertical forces, which were then integrated over one revolution to obtain the net force produced. The tangential force was used to calculate the total power required. The simulations showed that high solidities are advantageous and autorotation is possible. A case study was performed on a 3000 lb gross weight aircraft and satisfactory performance was predicted. It

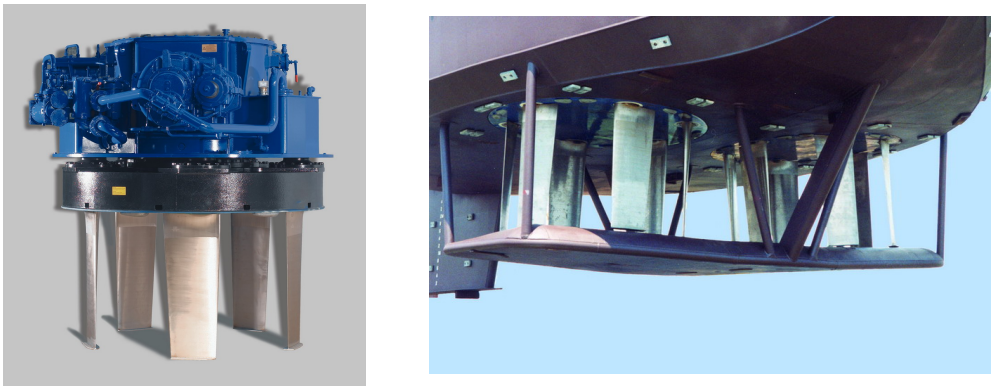

Figure 1.16: Voith-Schneider Propellers: Individual propeller (left) and installed on a ship (right)[8].

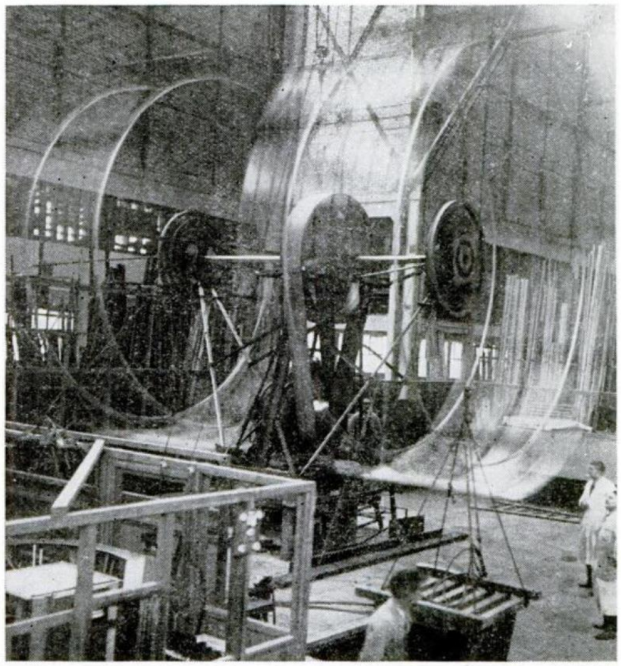

Figure 1.17: Full-size test of Strandgren's cyclogiro in France[9].

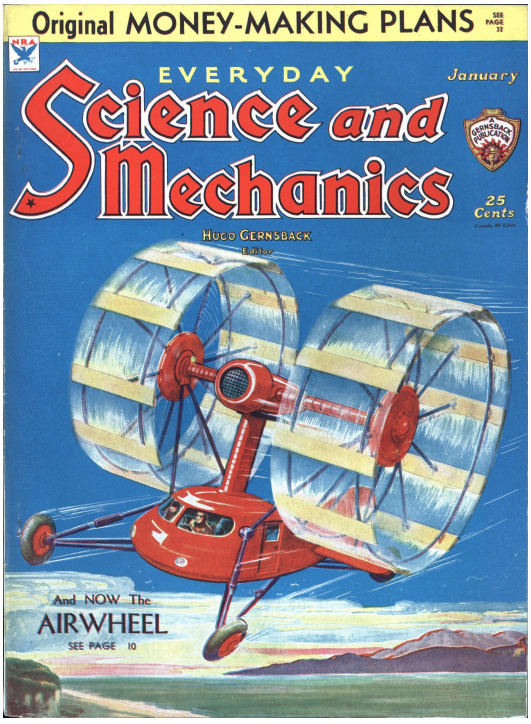

Figure 1.18: Everday Science and Mechanics magazine from January 1934 depicting Strandgren's vehicle concept.

was noted that the difficulty of cyclogiro construction lied in the large structural forces, complex control mechanisms, and gyroscopic moments.

To validate his model, in 1934 Wheatley constructed and tested an experimental cyclogiro having 4 blades of 0.312 ft chord and 8 ft in both span and diameter in the NACA 20-foot wind tunnel (Fig. 1.19)[10]. The rotor was mounted vertically in the wind tunnel and series of data were collected at sequentially altered pitch amplitudes and phases. Runs were done for both static and forward flight conditions of varying speeds. In the static case it was observed that the lift direction was offset by about 10° from the desired direction (*i.e.*, from the phase angle of maximum pitch), which was thought to be caused by the Magnus effect. In forward flight, it was seen that the horizontal force production and power are strong functions of blade pitching amplitude whereas vertical force is a strong function of pitch phasing. The variation in power required was correctly predicted by Wheatley's aerodynamic model, but the total power measured in the experiment was much higher. This discrepancy existed because profile drag was shown to be dependent on tip-speed ratio and not constant as had been assumed. The results were analyzed by applying them to a simulated aircraft employing the test rotor which resulted in lackluster performance and requiring a power of 0.15 hp/lb. One of the conclusions from this study was that the unsteady aerodynamics of oscillating airfoils required more research in order to fully understand the cyclogiro force production.

Over the next several decades there was sporadic interest in cyclogiro aircraft with some designs proposed by the military along with several patents being filed. But there was essentially no scientific research on cyclogiro again until 1998 when Bosch Aerospace was awarded an SBIR for their proposal to build a 600 lb cyclorotor-based UAV. Bosch developed a working prototype of their design as well as computer models based off data from the previously cited works[78]. Further work was done in collaboration with Mississippi State University's RASPET Flight Research Laboratory to refine this model using data from their own experiments and an updated inflow model that attempts to capture the effects of inflow within the rotor (Fig. 1.20)[79, 80]. Good agreement was found between the model and Wheatley's data ($\sim 10\%$) as well as their own test results ($\sim 5\%$). Although the power required was still under predicted and the value of C_{D_o} was adjusted to account for the rotating structure not capture by the model. Bosch eventually pivoted

Figure 1.19: Wheatley's 8 ft cyclogiro set up for testing in the 20 ft wind tunnel[10].

from UAV applications of the cyclorotor to airship control[81, 82]

One of the first low Reynolds number cyclorotor studies was conducted at the Israel Institute of Technology. A rotor was designed that would run at a Re of 40,000 while force and torque measurements were taken using a 5-axis sting balance (Fig. 1.21)[13]. The rotor could be fit with 2, 4, or 6 blades each with a chord of 21.9 mm and a span of 110 mm using a NACA 0015 airfoil. They noted from their experiments that the thrust coefficient is only weakly correlated

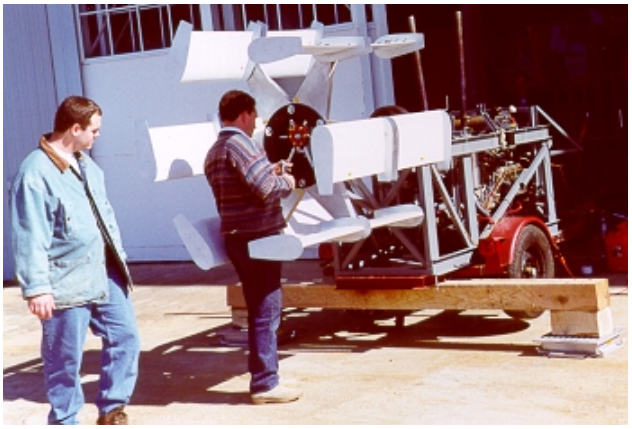

Figure 1.20: Engineers from Bosch working on their cyclorotor test rig[11].

to number of blades and is over-predicted by a simple quasi-steady model. Accompanying this experiment was a CFD simulation of a similar rotor at the same Reynolds number that agreed well with their experimental results, highlighting the inadequacy of the simplified theory (Fig. 1.22). A second follow-on study was conducted to refine these results using more appropriate measures to estimate force production[12]. Accurate time-averaged force estimation was achieved with simple momentum theory by accounting for a large Magnus effect and setting the thrust producing area of the rotor to half of its projected area. Error between the experiment and CFD was less than 5% for total force estimation and less than 20% for torque production. The rotor in the experiment experienced stall at 26° geometric maximum pitch for the 2-bladed and 32° geometric pitch for the 4-bladed, but the individual blades stalled at 8.6° angle of attack when accounting for aerodynamic conditions. The difference between rotor and blade stall can be explained by the reduction in angle of attack due to induced flow. The offset direction of thrust produced by the rotor lagged behind the phase of maximum pitch by anywhere between 10–40°. The researchers noted that the primary limitation for cyclorotors lies not in their aerodynamic performance but in their structural design because centrifugal forces can exceed aerodynamic forces by 2 orders of magnitude. The structure required to deal with these forces can prohibitively increase weight or parasitic drag.

In 2006, Yu *et al.* at the National University of Singapore performed optimization experiments on MAV-scale cyclorotors[83, 84]. Several rotors were built with various baseline diameters (120,

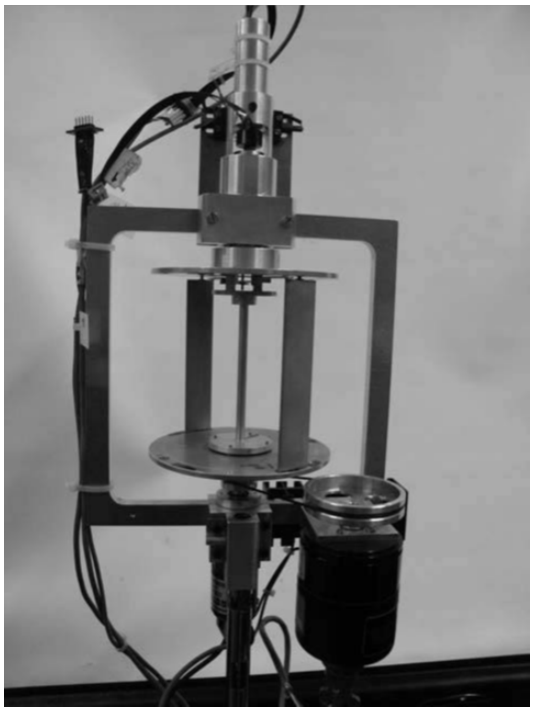

Figure 1.21: Two-bladed version of the rotor used during experiments at Technion–Israel Institute of Technology[12].

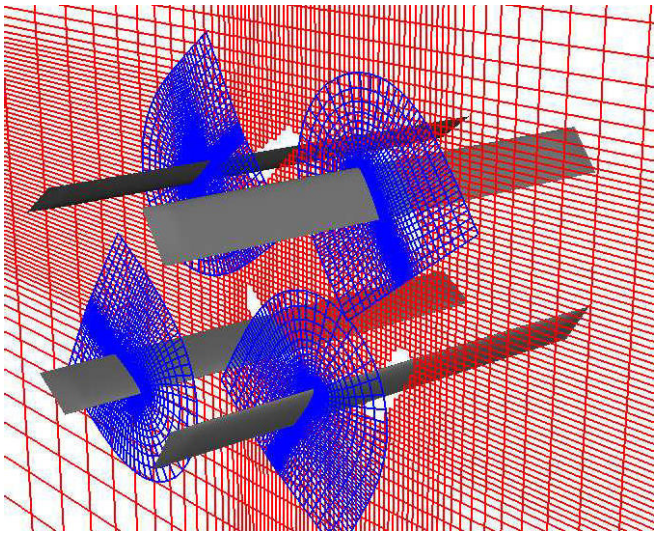

Figure 1.22: CFD mesh used for 4-bladed rotor analysis[13].

140, and 200 mm) and used a new 5-bar pitching mechanism that was simpler than a typical 4-bar linkage system. Different blade designs were tested including differing aspect ratios, taper ratios, and blades with winglets. Other tests were performed to examine the impact of blade airfoil section and pitching kinematics. In all cases, as expected, a reduction in disk loading increased power loading. A higher span to diameter ratio was found to be beneficial but a smaller radius meant a higher operating RPM which caused increased centrifugal loading and tip deflection. To counteract this effect, fishing line was tied between the blade tips as a way to reduce tip deflection with negligible weight. Winglets were not found to improve performance of the rotor. A rectangular planform blade had the highest performance with deteriorating results as taper ratio was increased. Based on these studies, a twin-cyclorotor MAV weighing 358 grams was built that could produce 520 grams of thrust, enough to hover; though it was never reported that this vehicle flew.

Breaking chronological continuity in favor of clarity, the following sub-sections present sev-

eral larger bodies of research conducted at institutions as cohesive units rather than attempting to describe individual papers in order.

1.3.1 Seoul National University

In 2003 at Seoul National University researchers began a multi-year program to study cyclorotors that included building several prototypes and conducting CFD analysis. To begin, the first proposed experimental setup was evaluated using a commercial CFD program called STAR-CD for the purpose of predicting performance and to understand the flow field around the rotor[14, 85]. It was revealed that the thrust offset from the phase of maximum blade pitch was not only due to the Magnus effect, but also because of the inflow inside the rotor. Airflow moving downwards increased the resultant inflow on the right half and decreased it on the left. These studies also identified the virtual camber effect, a byproduct of a straight blade rotating in a curvilinear flow. Because every point on the chord line is at a different radius relative to the center of rotation, each point has a different speed relative to the flow (Fig. 1.23). The variation of relative velocity along the chord line changes the blade angle of attack in a similar manner to camber in a rectilinear flow, becoming more pronounced as chord-by-radius increases. For the top blade this virtual camber is negative and for the bottom blade it is positive.

A test rig matching the specifications of the CFD analysis was built that consisted of a single cyclorotor driven by an electric motor mounted to a stand capable of measuring vertical and horizontal forces (Fig. 1.24). Rotor radius could be adjusted from 0.4 m to 0.45 m and 0.5 m. The blades measured 0.8 m in span with a 0.15 m chord. Tests were run while varying several other parameters: the number of blades, maximum pitch, and RPM. Good agreement was found between these experimental data and CFD. The total thrust produced by the cyclorotor was found to not be directly correlated to the number of blades (*i.e.*, a 6-bladed rotor did not produce three times the thrust of a 2-bladed rotor). Based off of these experiments an aircraft was designed that had a maximum gross takeoff weight of 50 kg with two cyclorotors of 1.4 m in diameter (Fig. 1.25)[15, 86]. The power plant was a 100 cc internal combustion engine capable of producing 16 hp, of which only 11 was needed to take off. Counter torque for the rotors was achieved by setting

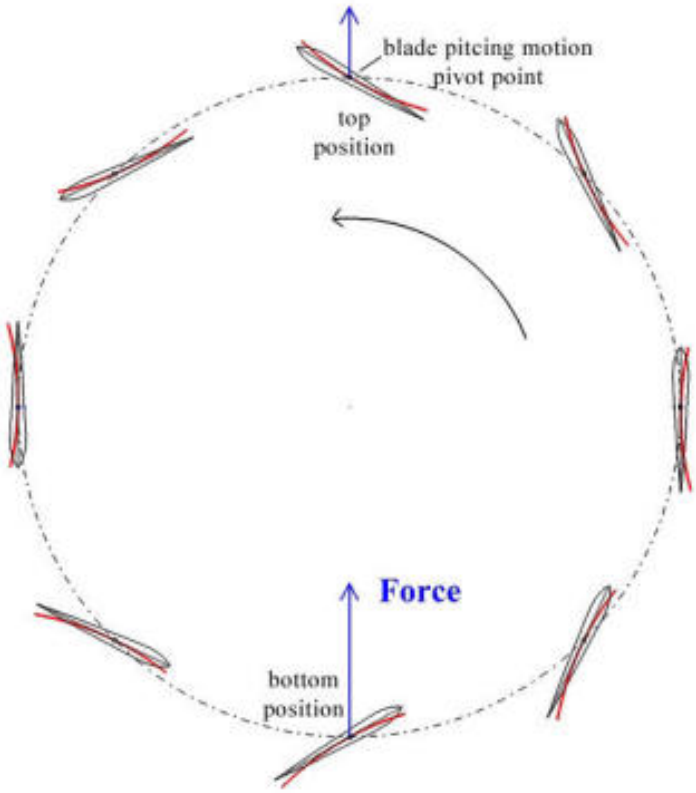

Figure 1.23: Virtual camber of blade by azimuthal position[14].

the CG below and aft of the rotation axis. It is unclear whether this vehicle was flown.

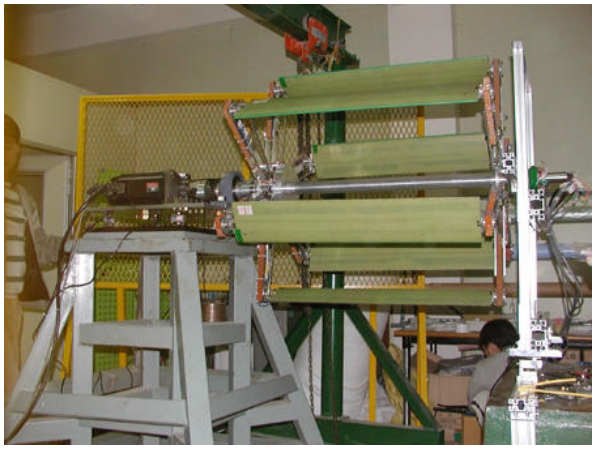

Figure 1.24: Rotor mounted on experimental test setup[14].

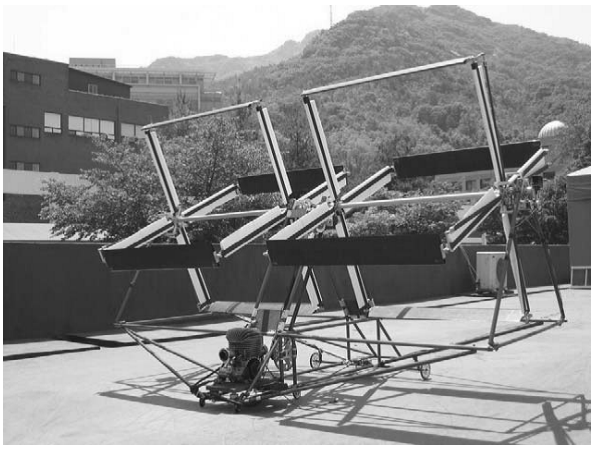

Figure 1.25: 46 kg twin-cyclcopter powered by 16 HP engine[15].

After that, multiple projects began to utilize cyclorotors for UAV ranging from 2.6 kg up to 114 kg as well as vertical axis wind turbines. First, a 2.6 kg MAV-scale cyclocopter was made to verify design principles (Fig. 1.26)[16]. No allowances were made for attitude control, but it could lift off while tethered to the ground and rotor torque was balanced using counter-rotation. A similar process of design and validation was applied to a quad-cyclocopter with 114 kgf of lift. The four cyclorotors had a diameter of 1.7 meters, a blade span of 1 meter, and a blade chord of 0.22 meters. The rotors operated at 450 RPM and consumed a combined 24.8 hp. This quad-cyclocopter was not flown, but was mounted to load cells to measure forces during operation.

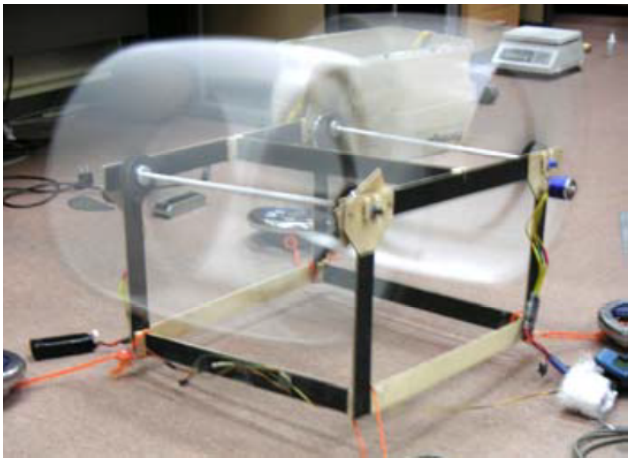

Figure 1.26: Tethered ground test of two-rotor cyclocopter[16].

From there, a reduced-sized quad-cyclocopter was developed with several changes, most notably elliptical blades for aerodynamic efficiency[17, 87, 88]. The overall blade and rotor design was done using 2D CFD then validated with 3D CFD. The blades used a NACA 0018 airfoil, had a span of 0.5 m and a maximum chord of 0.105 m. Each rotor measured 0.25 m in radius and had four blades (Fig. 1.27). Structural analysis of the system was conducted in MSC.NASTRAN. Unlike previous designs, the linkage system for blade pitching was located at mid-span and sandwiched inside the main rotor structure leaving the blade tips unsupported. However, this design reduced the parasitic drag created by rotating linkages and structure at both ends of the blades. Tethered

flight testing was conducted outside and hovering flight was achieved; although attitude control was unstable. Several years later an updated version of this quad-cyclocopter would demonstrate untethered, stable flight outdoors(Fig. 1.28)[18].

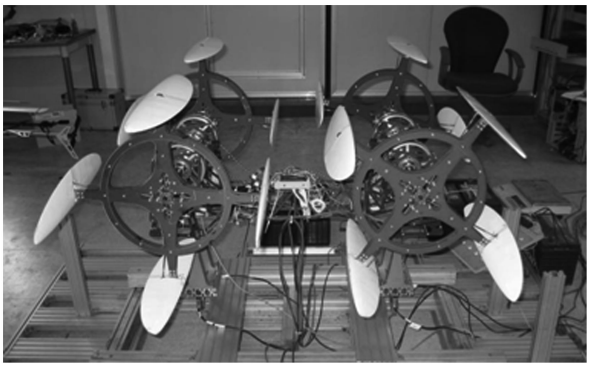

Figure 1.27: Assembled quad-cyclocopter ready on ground-test rig[17].

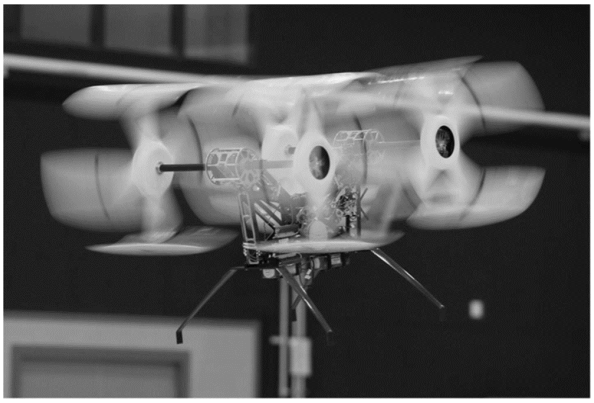

Figure 1.28: Upgraded quad-cyclocopter in free flight[18].

The latest cyclocopter developed at Seoul National University was a 110 kg twin-cyclocopter UAV (Fig. 1.29)[19, 89]. An existing commercial helicopter UAV was modified to accept two cyclorotors and the conventional tail rotor was rotated 90° so it pointed vertically up to balance the torque of the main rotors. The rotors were 4-bladed with a diameter of 2 meters, a span of 1.5 m, and an operating RPM of 420. The power plant used was the rotary engine supplied with the original UAV capable of 29 hp continuous output. Ground tests were done on a fixed stand initially and a maximum lift of 130 kgf was measured. Gains for the flight controller were tuned individually during tethered flights and it was found that roll and yaw are coupled because of the gyroscopic moment created by the cyclorotors. Through careful flight testing, stable hover was eventually achieved outdoors (Fig. 1.30).

1.3.2 University of Maryland

One of the most extensive and systematic studies of MAV cyclocopter flight began at the University of Maryland (UMD) in 2007. Sirohi, Parsons, and Chopra built a 6-inch diameter test rotor

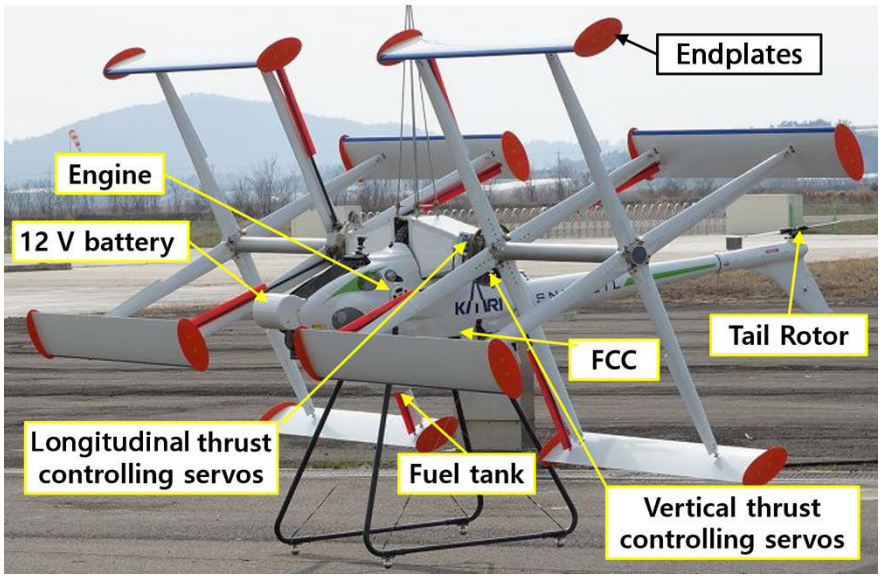

Figure 1.29: 110 kg twin-cyclocopter with parts labeled[19].

Figure 1.30: 110 kg twin-cyclocopter performing a stable hover with the tether slack[19].

to determine the effects of the number of blades, blade pitch angle, and rotational speed on thrust and power output (Fig. 1.31)[20]. Vertical force was measured by two load cells and the non-rotating center shaft was mounted to a torque cell allowing power to be calculated from torque and RPM. Measurements were taken at blade pitch amplitudes of 10°, 20°, 30°, and 40° for rotational

speeds ranging from 0 to 1200 RPM using 3 blades then repeated using 6 blades. The 6-bladed rotor produced only 30% more thrust than the 3-bladed case at the same RPM and configuration. The cause of this was discovered to be increased inflow from the additional blades, which reduced blade angle of attack thereby decreasing lift. No reduction in lift was observed for high angles of attack up to the 40° case indicating that dynamic pitching effects may be delaying stall. Accompanying the experiments, a model was developed to predict rotor performance based on double-multiple streamtube momentum theory in conjunction with a formulation of Wagner's function to account for unsteady aerodynamic effects. Pressure measurements were taken at center span around the rotor to quantify downwash to help validate the model. Thrust predictions correlated well with the 3-bladed case but were less accurate for 6 blades, possibly due to blade interactions, which were neglected. Power predictions were satisfactory for high rotational speeds, but poor for low RPM largely due to the substantial tare power of the system.

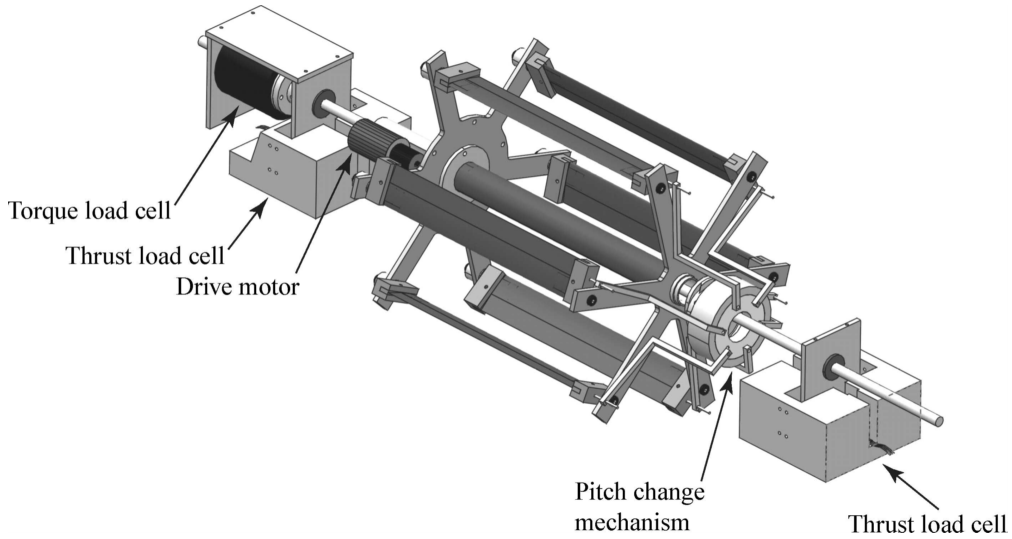

Figure 1.31: Cyclorotor test setup showing sensors and rotor components[20].

After that, Benedict *et al.* began conducting extensive parametric studies on an MAV-scale rotor for the purpose of optimizing thrust and power[4, 74, 90–93]. Up to this point, the few studies on cyclorotor had been not very systematic and therefore, the process and parameters to design one

for an actual flying vehicle were not well understood. Towards that end, a cyclorotor was created with weight and aerodynamic considerations in mind for eventual use on a flying vehicle. The goal was to produce a cyclorotor that could achieve power loadings comparable with or superior to conventional micro-rotors and then to utilize this optimal rotor on a cyclocopter. Using a test stand, shown in Fig. 1.32, that could measure thrust and torque, the following parameters were studied: rotational speed, blade airfoil profile, blade flexibility, blade pitching amplitude (symmetric and asymmetric), pitching axis location, number of blades with constant chord (varying solidity), and number of blades at a constant rotor solidity (varying blade chord). All rotors tested had a radius of 6 inches and two different blade dimensions were predominantly used. The first set of blades had a 6-inch span and 1-inch chord while the second set had a 6.25-inch span and 1.3-inch chord. The operating speed range of the rotor was from 400–2000 RPM. Figure 1.33 shows total thrust versus RPM for several different symmetric pitch amplitudes. The phase angle of the resultant thrust was found to increase as rotational speed increased (*i.e.*, with no mechanical change, the thrust vector tilts more as the rotor spins faster). No blade stall was observed at very high angles of attack, up to 45°. Blade flexibility was found to reduce thrust and increase power due to aeroelastic effects. Adding more blades was beneficial to power loading because more blades reduced the operating RPM for a required amount of thrust and the reduction in power from lowering the RPM was greater than the increase in power due to added profile drag. Asymmetric pitching was able to increase power loading and the effect was attributed to the virtual camber effect. And finally, shifting the pitch axis away from the leading edge improved performance with the ideal range being from 25–35% chord. These studies were able to dramatically improve the performance of the cyclorotor and reduce parasitic power. The optimal design found had 4-blades with a 1.3-inch NACA 0015 airfoil and had an asymmetric pitching of 45° at the top but 25° at the bottom, pitching about the 25% chordwise location.

During these experiments, flow field measurements were taken using Particle Image Velocimetry (PIV)[4, 94], the process for which is explained in more depth in Chapter 3. Flow through a cyclorotor is complex and was not very well understood; therefore, taking measurements was

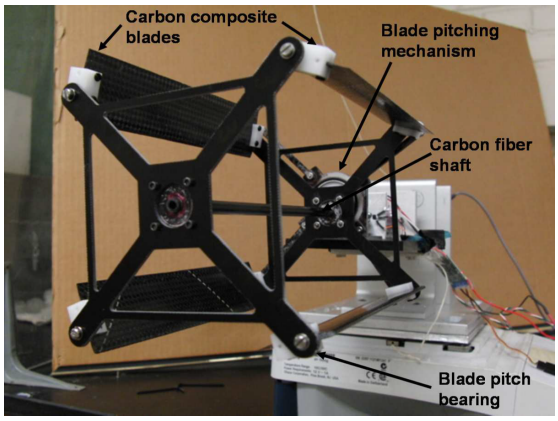

Figure 1.32: Test stand used to conduct parametric studies with components labeled[4].

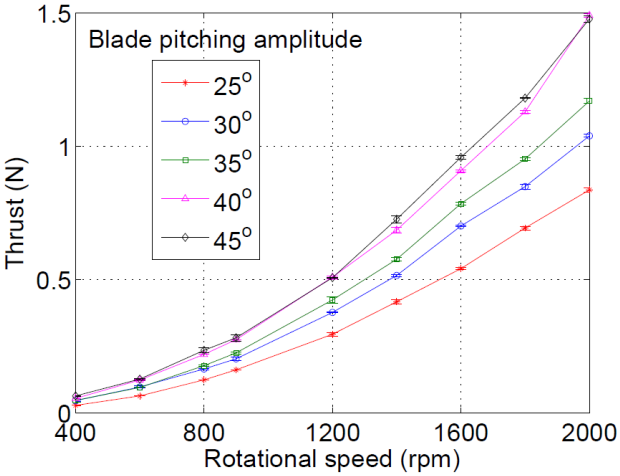

Figure 1.33: Cyclorotor forces versus rotational speed with NACA 0010 blades at different pitching amplitudes[4].

important to help understand phenomenon like the absence of blade stall and the skewed wake as well as to properly model the inflow. These spanwise and chordwise PIV measurements (Figs. 1.34 and 1.35, respectively) were the first ever on a cyclorotor and revealed the complex nature of flow within and around the rotor. The wake of each blade is characterized by a tip vortex on both ends that grows and dissipates after it is shed. Inside the rotor, the flow is highly rotational with different inflow velocities on the right- and left-hand sides. A large leading edge vortex was observed on the blades at maximum pitch angle and this flow structure was postulated to be instrumental to cyclorotor aerodynamics and delaying blade stall.

As a continuation of this work, an aeroelastic model was developed to accurately predict average thrust and blade loads[4, 95]. Previous analytical models of cyclorotors did not account for blade deformations; however, because of large centrifugal loads experienced by cyclorotor blades these must be included. Structural modeling was done using two methods 1) second-order non-linear finite element analysis and 2) a fully-nonlinear geometrically exact beam model using multibody based analysis (using software MBDyn). Finite element analysis was sufficient and accurate for stiff blades with low deflection, but the multibody model was necessary for flexible blades with larger deflections. The blade element based aerodynamic model used an unsteady at-

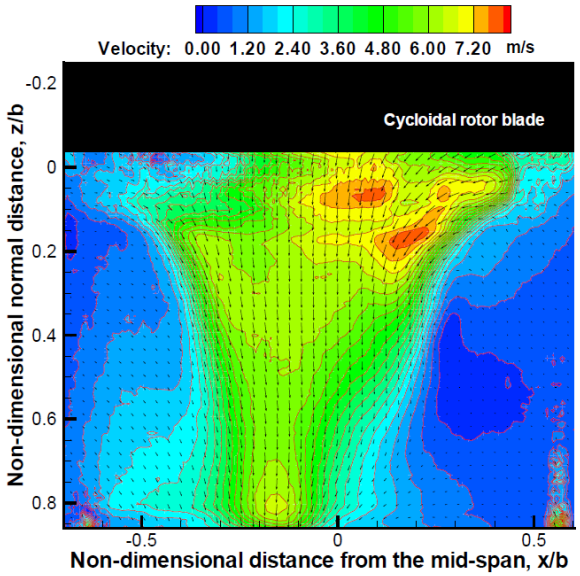

Figure 1.34: Time averaged velocity measurements showing the wake contraction of the cyclorotor[4].

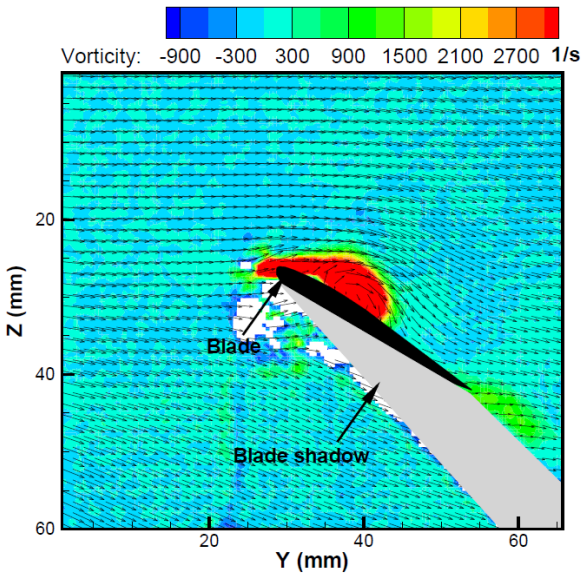

Figure 1.35: PIV measurements showing the leading edge vortex on top of the blade[4].

tached flow formulation based on the Wagner function and Duhamel's superposition principle to obtain the circulatory lift and moment for arbitrary variations in angle of attack. This formulation discretized the angle of attack as a series of step inputs over time and the response to each was then calculated using indicial response functions. Once the response was known, the unsteady loads could be obtained through superposition using Duhamel's integral. Inflow was calculated using a simple streamtube model of uniform inflow (Fig. 1.36a) and a double-multiple streamtube model that took into account the downwash from the upper half of the rotor impacting the lower half (Fig. 1.36b). Results were more accurate with the double-multiple streamtube model. Overall, the model accurately predicted the magnitude of force production for a wide range of variables (Fig. 1.37), but direction of thrust was off for some cases. Blade flexibility lowered thrust due to the reduction in geometric angle of attack resulting from nose-down torsional deformation in the upper half which is not compensated by the nose-up deformation in the lower half.

With an experimentally optimized rotor design and a more thorough understanding of cycloro-

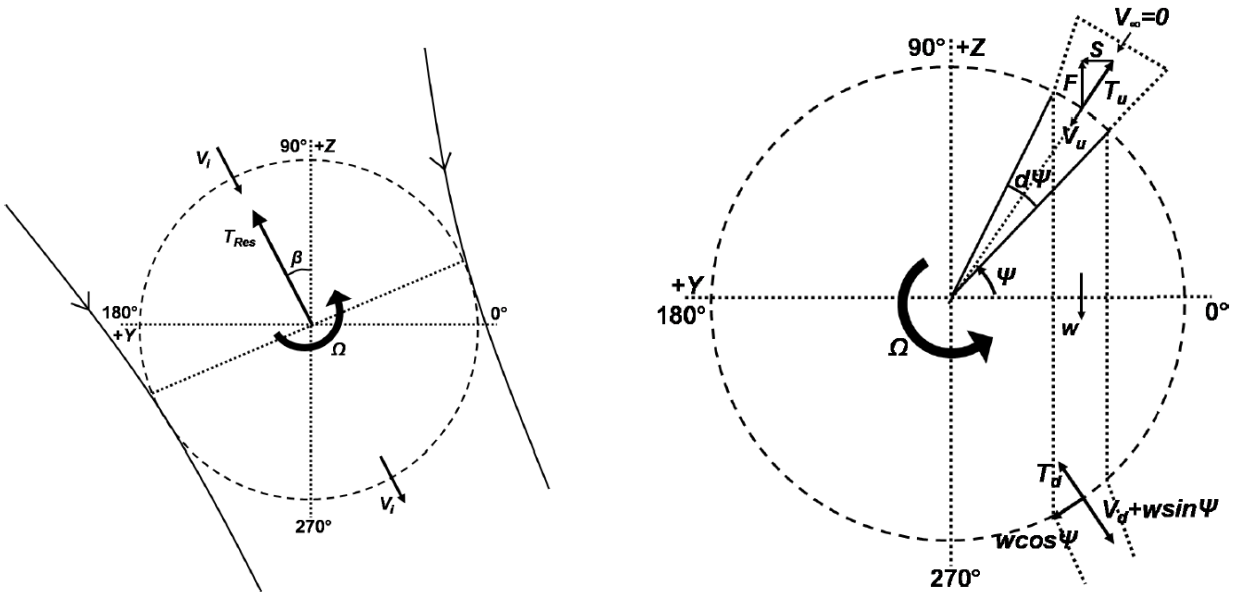

(a) Uniform inflow.

(b) Double-multiple streamtube inflow.

Figure 1.36: Schematic of the inflow models[4].

tor aerodynamics, a quad-cyclocopter was developed[4, 96]. Weighing a total of 809 grams, the vehicle had 4 cyclorotors in a "+" shape that were all driven by the same motor via a two-stage transmission (Fig. 1.38). The thrust of each cyclorotor could be vectored separately and different combinations of servo inputs were used for control and stabilization. By successively testing on a gimbal stand then in a tethered configuration the vehicle was safely trimmed and controller gains were tuned. Through tethered hovering flights it was proven that a cyclocopter could be trimmed and achieve hover using only thrust vectoring (Fig. 1.39).

Shortly after the flying the quad-cyclocopter, Benedict *et al.* began further improving the design of the cyclorotor. Additional experiments were performed to further investigate the impact of certain geometric parameters on cyclorotor performance including rotor radius, blade span, chord, and planform[73]. A strong correlation was found between performance and chord/radius ratio with the optimum value being quite high (0.5–0.8) depending on blade pitching amplitude. Both increasing the rotor solidity through blade chord while keeping the number of blades constant and shortening blade span were shown to improve power loading. Blade planform shape did not have a

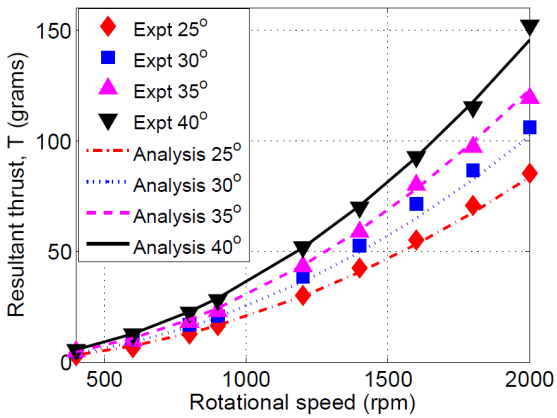

(a) Multiple streamtube model, 3-bladed rotor.

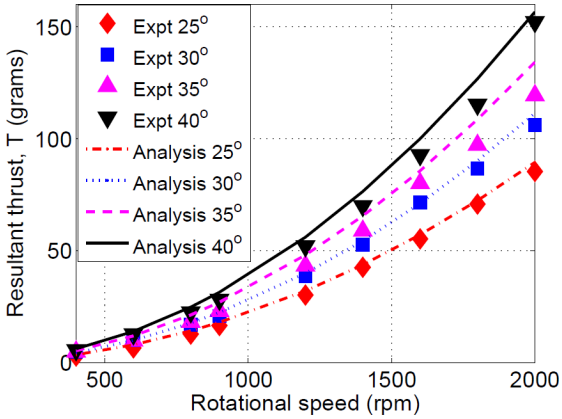

(b) Single streamtube model, 3-bladed rotor.

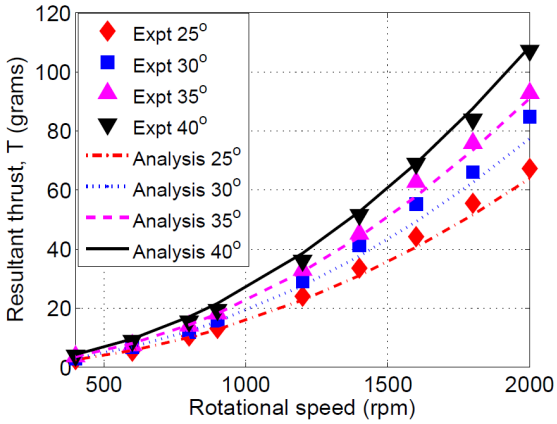

(c) Multiple streamtube model, 2-bladed rotor.

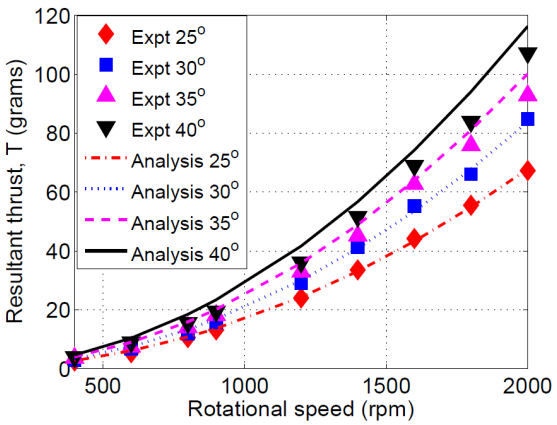

(d) Single streamtube model, 2-bladed rotor.

Figure 1.37: Comparison of predicted average resultant thrust obtained using single and multiple streamtube models with experimental data for 2-bladed and 3-bladed rotors[4].

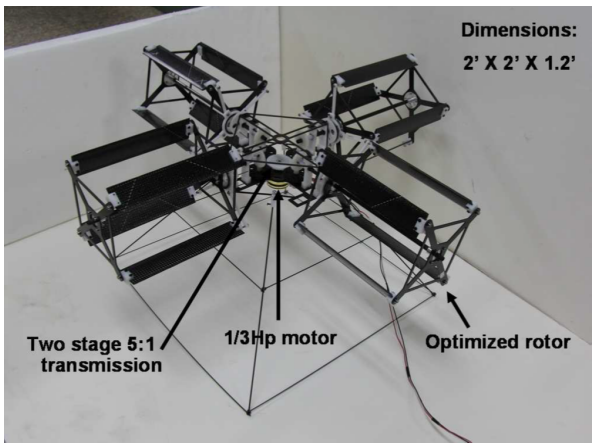

Figure 1.38: Quad-cyclocopter weighing 809 grams developed at UMD[4].

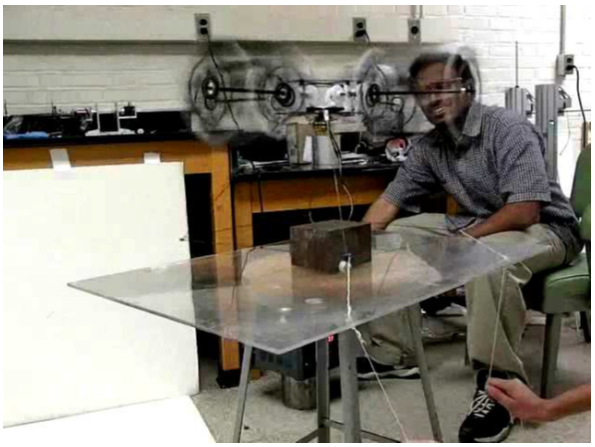

Figure 1.39: Tethered hovering of the quad-cyclocopter[4].

significant impact, although, trapezoidal blades with a small taper ratio had a slight advantage over rectangular blades. The fully optimized cyclorotor from this study had a higher power loading than a conventional micro-rotor at an equivalent disk loading (Fig. 1.40).

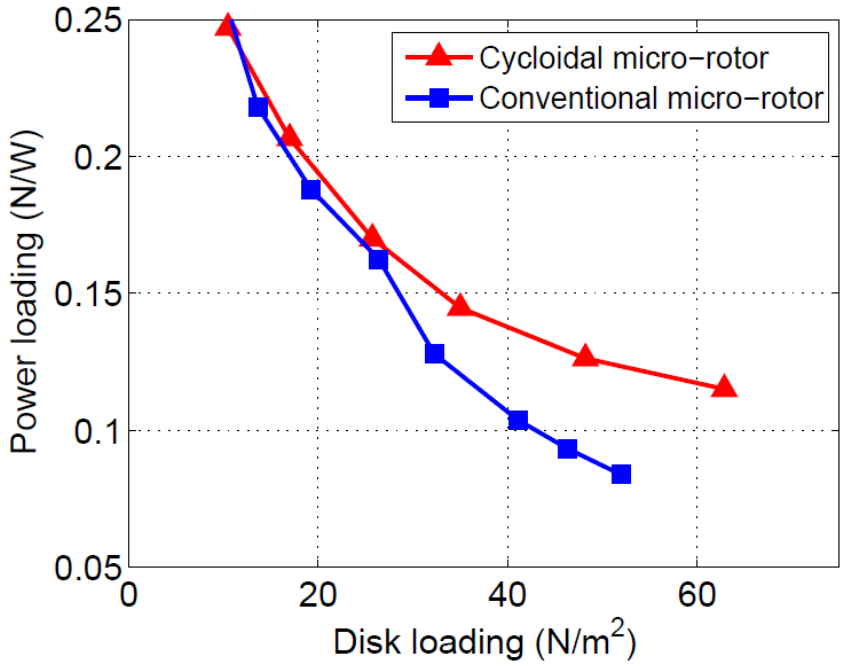

Figure 1.40: Power loading for experimentally optimized cyclorotor compared with conventional micro rotor[4].

Using these new insights, another rotor was designed in 2011 for use in a twin-cyclocopter configuration[21, 22]. The new design measured 5 inches in diameter and had a 4-inch span with 40° symmetric maximum blade pitch. Compared to the previous twin-cyclocopter, the structure of the end-plates was reduced and additional measures were added to reduce parasitic power during operation. Weighing only 30 grams,the rotor could produce 115 gram-force of thrust while spinning at 2400 RPM. Cyclorotors of this design were used to build two twin-cyclocopters, each weighing about 200 grams and utilizing individual motors for each rotor to allow for independent RPM control (Fig. 1.41). A single propeller was used to balance the cyclorotor torque on each. Employing only feedback gains on rate gyros, the twin-cyclocopter was able to lift off and stably hover under its own power. This cyclocopter was the first ever to achieve untethered, stable hover, achieving a historic milestone (Fig. 1.42)[97].

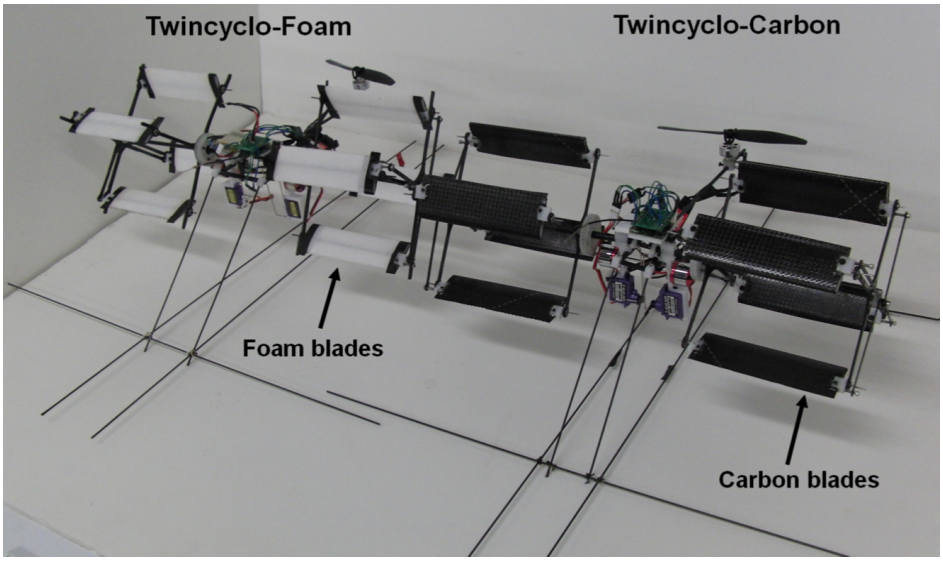

Figure 1.41: Twin-cyclocopters built with experimentally optimized rotors showcasing different blade manufacturing techniques[21].

Building on this achievement over the next several years, more research was conducted to understand the fundamental characteristics of cyclorotor aerodynamics with a focus on forward flight[23, 24, 98, 99]. The methods for these studies included wind-tunnel experiments, PIV mea-

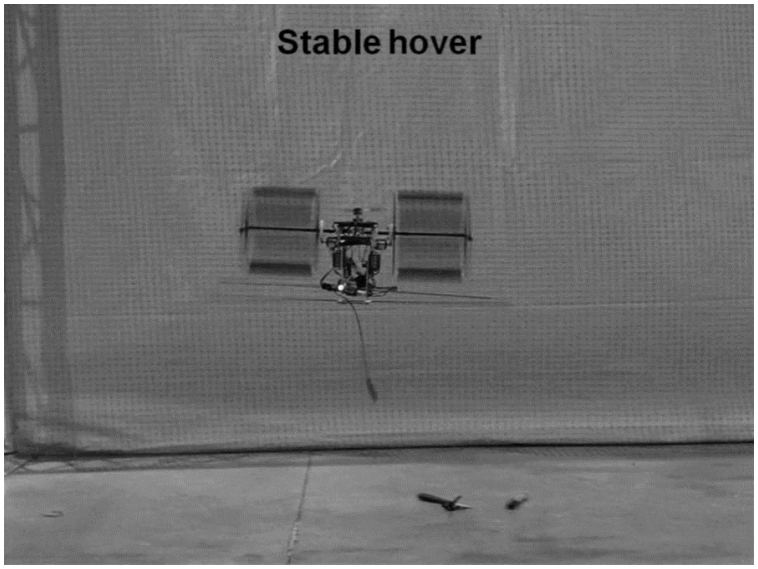

Figure 1.42: First stable, hovering, untethered flight of a cyclocopter based vehicle[22].

surements, and CFD analysis. Several parameters studied were chord/radius ratio (c/R), pitch axis location, blade pitch amplitude, pitch phase relative to incoming flow, and asymmetric pitching schedules. At all forward speeds, flow curvature effects played a profound role in force production. Flow curvature, or the combination of virtual camber and the virtual incidence angle, is predominantly a function of chord/radius ratio, pitch rate, and pitch axis location. Maximum power efficient c/R decreases with forward speed, but lift per unit blade area can be increased with enhanced flow curvature effects, creating a trade-off. The impact of virtual incidence angle, specifically on flow curvature, is dependent on the advance ratio (μ_{AR}), defined as:

$$\mu_{AR} = \frac{V_\infty}{R\Omega} \tag{1.1}$$

where V_∞ is the free stream velocity, R is cyclorotor radius, and Ω is the rotational speed in rad/s. At high μ_{AR}, lift increased as virtual incidence was decreased (*i.e.*, as blade pitch axis was moved towards the trailing edge). Another consequence of virtual camber is that spin direction of the cyclorotor becomes important during forward flight. Because of the virtual camber, the bottom blade experiences a greater overall change in lift than the top blade. Meaning that if the lower

blade is advancing, its gain in lift will be higher than the loss from the top blade, producing a net increase in thrust (Fig. 1.43). Otherwise, if the bottom blade is retreating the top will lose more lift than the bottom will gain, reducing total thrust. For this reason, cyclorotors should have a back spin relative to the direction of travel such that the bottom blade is advancing.

Wind tunnel data showed that at low phase angles power consumption could be reduced using asymmetric pitch kinematics suggesting that such pitch schedules could be advantageous for low speed flight. The reduction in power relative to symmetric pitching might be due to a more uniform azimuthal distribution of blade forces. Total asymmetry between top and bottom blade was limited by blade stall on the upstream blade ($\Psi \approx 0°$) in highly asymmetric pitch schedules.

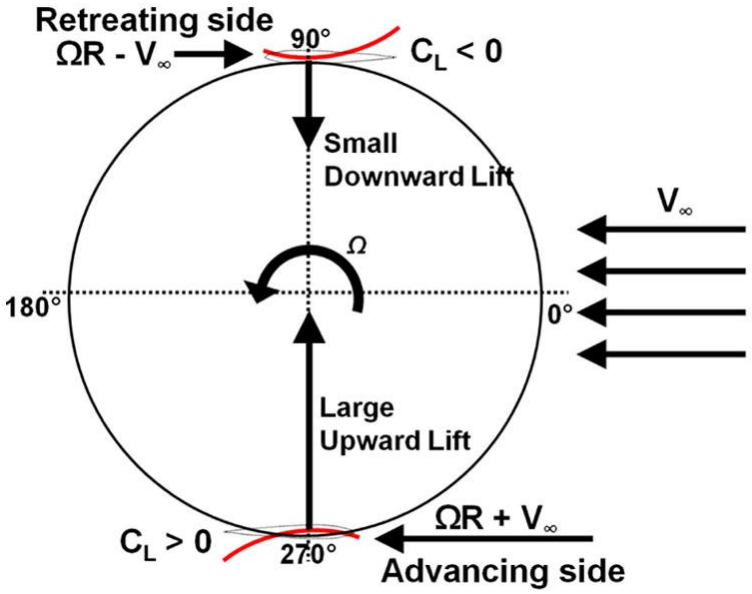

Figure 1.43: Physics behind lift production on a cyclorotor showing the impact of forward velocity[23].

Several other conclusions were drawn from these studies:

- Cyclorotors become more efficient at producing lift in forward flight, but less efficient at producing horizontal propulsive force (Fig. 1.44).

- If designed properly, separate pitching schedules for hovering and forward flight are not needed because the same kinematics can be used efficiently for both with a simple phase shift.
- Rotor power was primarily dependent on pitch amplitude and insensitive to phase angle for a wide range of advance ratios.
- Decreasing rotational speed led to significant reductions in power consumption (with the cube of RPM); however the minimum speed is governed by the onset of blade stall because of the lower inflow.
- PIV flow field visualization and qualitative 2D CFD analysis showed that constructive blade wake interactions can increase blade lift.

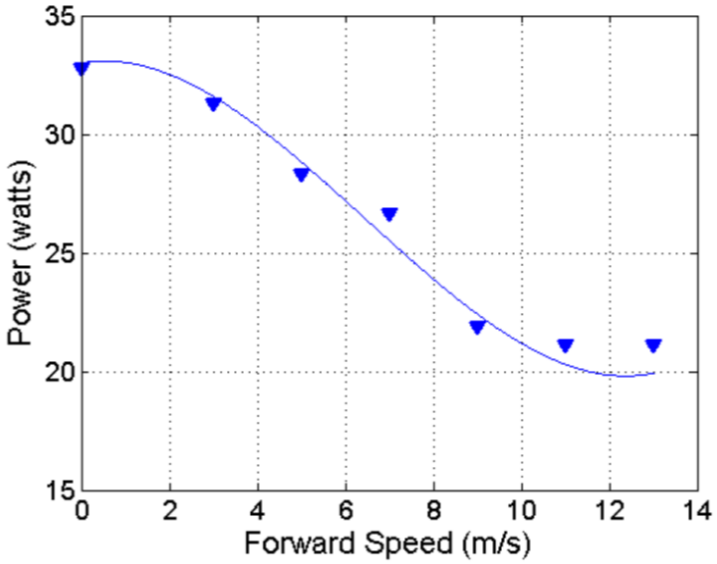

Figure 1.44: Maximum forward velocity with constant cyclorotor rotational rate of 1740 RPM for steady, level flight[24].

Concurrent with these forward flight experiments, several other hover capable cyclocopters were developed to study different aspects of cyclocopter flight. One such study was done by

Adams *et al.* at the Air Force Academy in collaboration with UMD into and the use of a cam-based cycloidal blade pitching mechanism[25]. The 535 gram twin-cyclocopter developed to test this system was the first cyclocopter to fly using cam-based blade pitching (Fig. 1.45). The cam relied on centrifugal force for engagement and could be moved in flight to change both the phase and magnitude of cyclorotor thrust without changing the rotor RPM. There are several advantages to this, the most obvious being that the power transmission system can be optimized to operate at its most efficient speed. Moving a cam also has less lag time and is more responsive than altering RPM because there is no need for a change in angular momentum. Furthermore, in forward flight the cam system can realize changes in pitch kinematics that are not possible with a 4- or 5-bar linkage system and can account for the increased horizontal flow resulting in more efficient operation. Flight testing of the 535 gram cyclocopter revealed extreme sensitivity between the roll-yaw gyroscopic couplings when moving the cams and confirmed the improved bandwidth of a cam system over a linkage system.

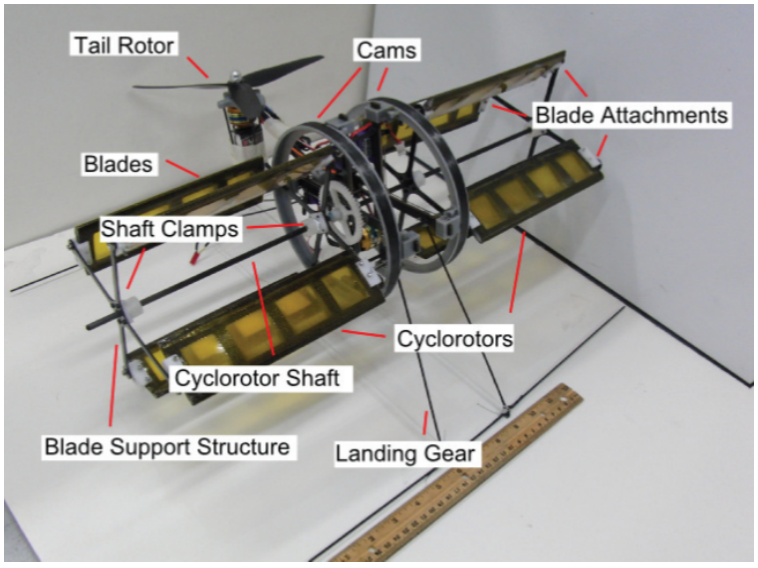

Figure 1.45: Cam controlled twin-cyclocopter[25].

Benedict *et al.* also devoted effort towards improving the previously described quad-cyclocopter.

The updated design weighs about the same amount, but mass was removed from the structure of the rotors and blades as well as the transmission system while motors were added to drive each rotor individually[26] (Fig. 1.46). The result is a more capable cyclocopter that can change the magnitude and direction of thrust for each rotor separately from the others for a total of 8 control inputs: 4 motor RPMs and 4 servo directions. The same "+" configuration was used and although angular momentum is balanced in trimmed hover, roll and pitch are coupled when commands are given meaning that all 4 rotor RPMs must be changed for a pure roll or pitch response. A PD controller was developed to fly the quad-cyclocopter that could compensate for the roll-pitch couplings. Differential RPM commands are used to control roll and pitch while thrust vectoring is used to command yaw.

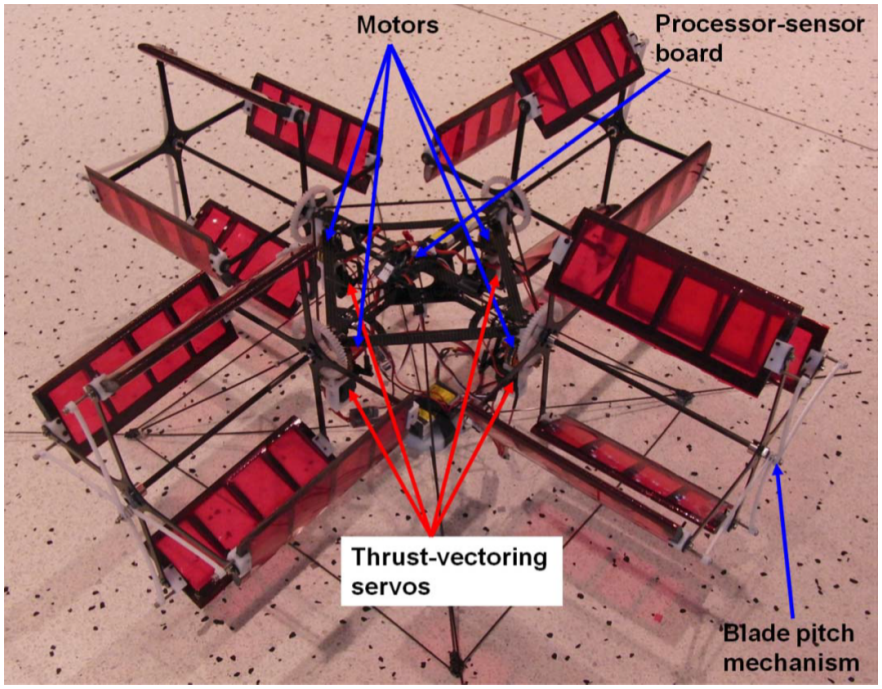

Figure 1.46: Quad-cyclocopter with independently driven rotors and thrust vectoring servos[26].

Subsequent to the cam-based design and the updated quad-cyclocopter, several other twin-cyclocopters were built at scales ranging from 350 down to 60 grams (Fig. 1.47)[100, 101]. These

design projects were focused on miniaturization of the cyclorotor concept. As such, they dealt with practical manufacturing and engineering considerations that arose from an applied design process. One notable observation was that cyclorotors typically comprised 24–34% of vehicle weight and produced low T/W ratios[101]. The root cause of this was the requirement for stiff blades to prevent torsional deflection and bending. The researchers noted that making the blades stiff added weight which greatly increased centrifugal loading. In turn, the rotor had to be made heavier to deal with the increased force; therefore lightweight blades were paramount to lightweight cyclorotors. To ameliorate the weight penalty of stiff blades, the designs for these smaller cyclocopters were such that the blade pitching axis was at the chordwise CG location to eliminate any torsional moments from centrifugal loads. This meant their structure could be lightened allowing for more minimal rotor structure and a less robust pitching mechanism. To further bring down blade weight, manufacturing techniques were modified to lower the total material needed to form the airfoil while maintaining stiffness. These improvements culminated in the 60-gram twin-cyclocopter whose rotors had a T/W ratio of 3, a significant improvement over the earlier, larger designs.

There were several other practical aspects of cyclocopter design that were addressed in the process of designing, building, and flying multiple vehicles. One of the most prominent was the interplay between mass distribution, CG location, and nose rotor design. These three things are interdependent and affect the handling qualities of the vehicle. Without empirical data to draw from, the cumulative impact was hard to predict and therefore, having several examples of flight-worthy vehicles was a good way to gather a qualitative understanding. The design methodology associated with such properties will be covered in Chapter 4, which heavily draws upon the lessons learned from these previous cyclocopters. Another area where practical discoveries were made was the flight testing process. The steps to safely prepare a vehicle for flight were improved over the years including streamlining the trimming and tuning process as well as creating additional test hardware like a single degree-of-freedom (DoF) stand and a gimbal stand for ground testing. The methodology adopted for preparing a cyclocopter for flight testing will also be discussed in detail in Chapter 4.

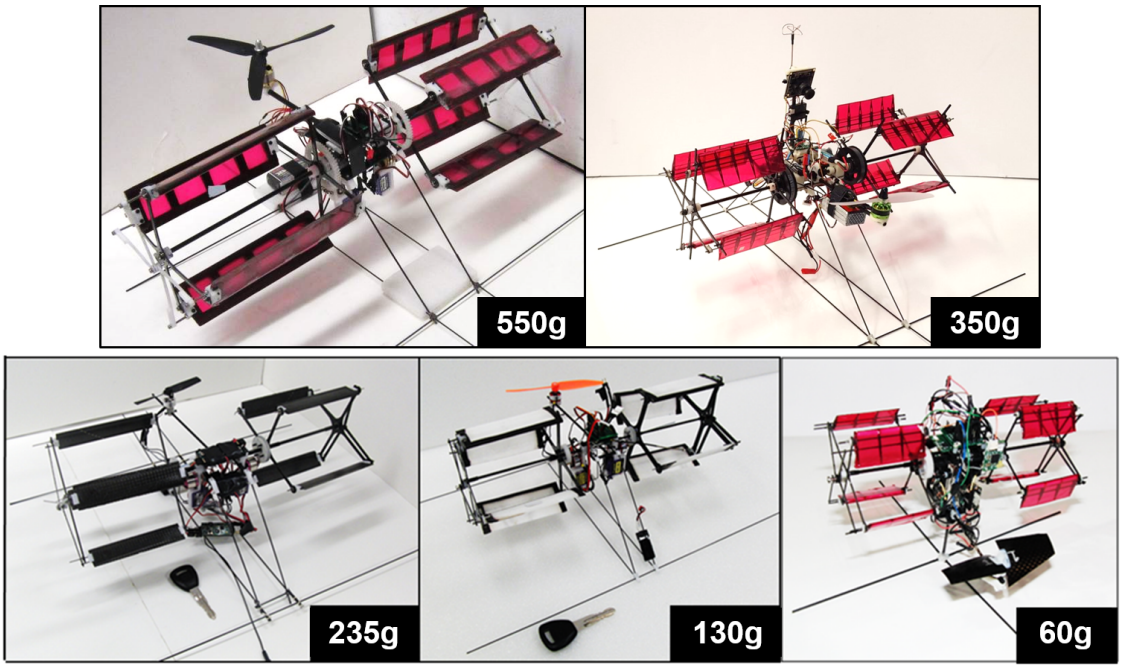

Figure 1.47: Hover-capable cyclocopters developed at UMD, ranging in size from 550 grams down to 60 grams[27].

Work on building and flying cyclocopters eventually lead into studies on their dynamics, flight characteristics, and controller design. A 550-gram cyclocopter, shown in Fig. 1.47, was developed and used in several projects revolving around these aspects. Its rotors had a diameter of 6 in, span of 6.25 in, and 4 blades with a chord of 2 in utilizing a NACA 0015 airfoil. It used $\pm 45°$ symmetric pitch kinematics. The first research study was conducted by Hrishikeshavan *et al.* to formulate a model of the bare airframe dynamics in hover[28]. Retro-reflective markers were attached to the vehicle that could be tracked by specialized VICON cameras. Motion tracking software would record the position and velocity of each marker and then calculate the position and velocity of the vehicle based on their relative orientation. By collecting data on specific maneuvers performed by the cyclocopter in flight, a linear model to describe the body dynamics can be extracted (Fig. 1.48). This process of using data to formulate a model of an unknown system is called system identification (SysID) and Chapter 5 will cover the specific details in more depth. The linear time-invariant (LTI) model derived for the system in hover revealed that the longitudinal mode and

heave modes were largely decoupled from the lateral and yaw modes, however, the latter two were highly coupled to each other. Pitch and roll were both unstable while yaw was neutrally stable. Based on the identified model, the control authority and gust rejection capability of the cyclocopter were then quantified using a control-theoretic framework that characterized the reachable states of the vehicle for a bounded control and gust disturbance input. The analysis showed negligible damping in the rate dynamics, which combined with the presence of gyroscopic coupling, gave the twin-cyclocopter high open-loop maneuverability potential. Results from this process were useful in comparing cyclocopter bare-airframe performance against data from similar analysis of other MAV platforms and showed that the twin-cyclocopter was significantly more maneuverable than a shrouded-rotor MAV.

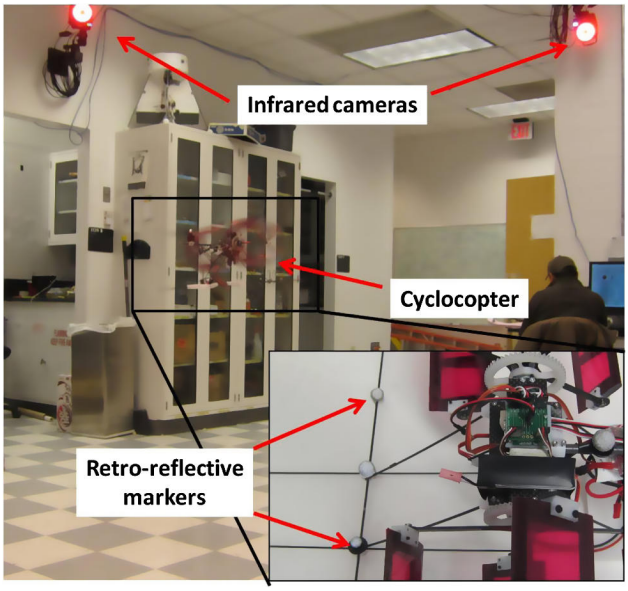

Figure 1.48: System identification setup used to create linear model showing reflective beacons and infrared cameras used to track them[28].

Further utilizing the 550 g cyclocopter, open-jet wind tunnel and free flight experiments were performed by Shrestha *et al.* to help develop control strategies to be used in forward flight that take advantage of the unique thrust vectoring capability of the cyclorotor[29]. The MAV was attached

to a 5-DoF stand via a ball-and-socket joint at the CG that permitted limited rotation (Fig. 1.49). Horizontal and vertical sliders allowed the vehicle to move within a constrained distance vertically within as well as parallel to the wind tunnel flow, but not perpendicular to it (Fig. 1.50). Care was taken to ensure the stand did not introduce excessive damping. A pitot probe was attached to the nose of the cyclocopter to measure flow velocity. With the wind tunnel on, the cyclocopter was given commands so that it maintained a level attitude and a fixed position on the sliders, only possible because of the cyclorotors' thrust vectoring capability. Testing through a series of increasing wind speeds revealed that the RPM required to maintain steady level flight initially increased but then decreased after a certain point (Fig. 1.51), thus verifying that cyclorotors possess aerodynamic advantages in forward flight. However, using thrust vectoring to induce forward velocity exacerbated the roll-yaw coupling already present. Additional mixing of the roll and yaw commands was necessary in order for the pilot to command pure body rates in either direction. The amount of mixing necessary depended on the phase angle of the thrust vectors and initial values for the flight controller were found while testing on the stand. Flight testing of the cyclocopter showed the control scheme derived in the wind tunnel experiments was valid in free flight up to 5 m/s, although some additional tuning was required. This was the first cyclocopter vehicle to demonstrate longitudinal translation using thrust vectoring.

After achieving stable and consistent performance, another system identification experiment was conducted on the 550 g cyclocopter, but this time in order to develop a model for forward flight rather than hover[27]. For this study the VICON motion capture cameras were set up in a large open space to allow the cyclocopter to develop forward speed before collecting data (Fig. 1.52). Critical to the system identification process was the excitation of vehicle frequencies using specific maneuvers. Because the regime of interest was forward flight, relevant maneuvers were only performed after the vehicle had reached a speed of 2 m/s. Although simple in principle, it was difficult to hit the target speed within the interrogation volume of the cameras and perform maneuvers without causing the vehicle to go unstable. Contending with such issues meant many iterations of data collection and only providing excitation the vehicle could recover from. The

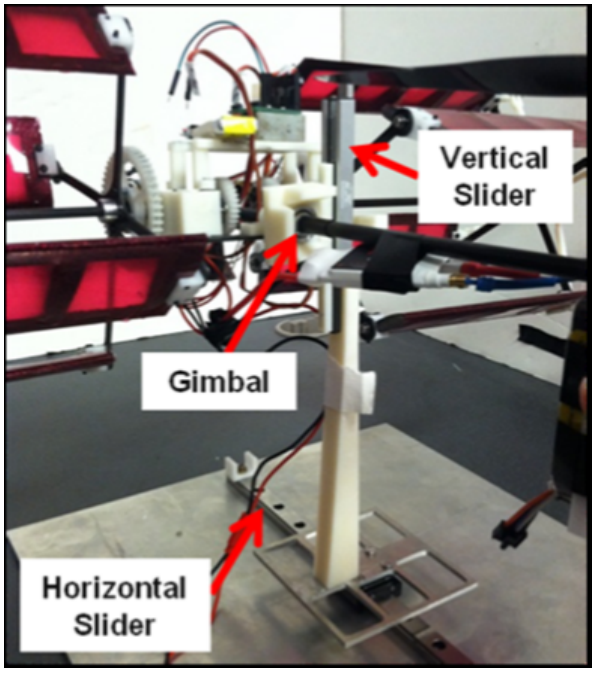

Figure 1.49: Cyclocopter on 5-DoF stand[29].

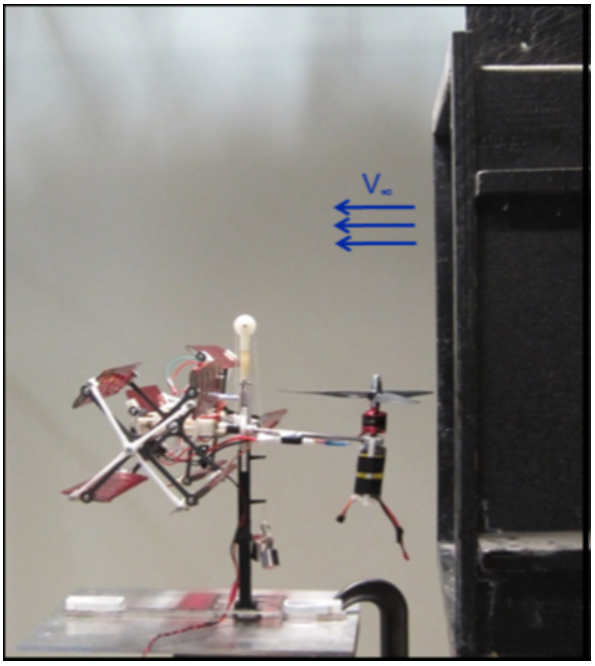

Figure 1.50: Wind tunnel testing setup for 550-gram cyclocopter[29].

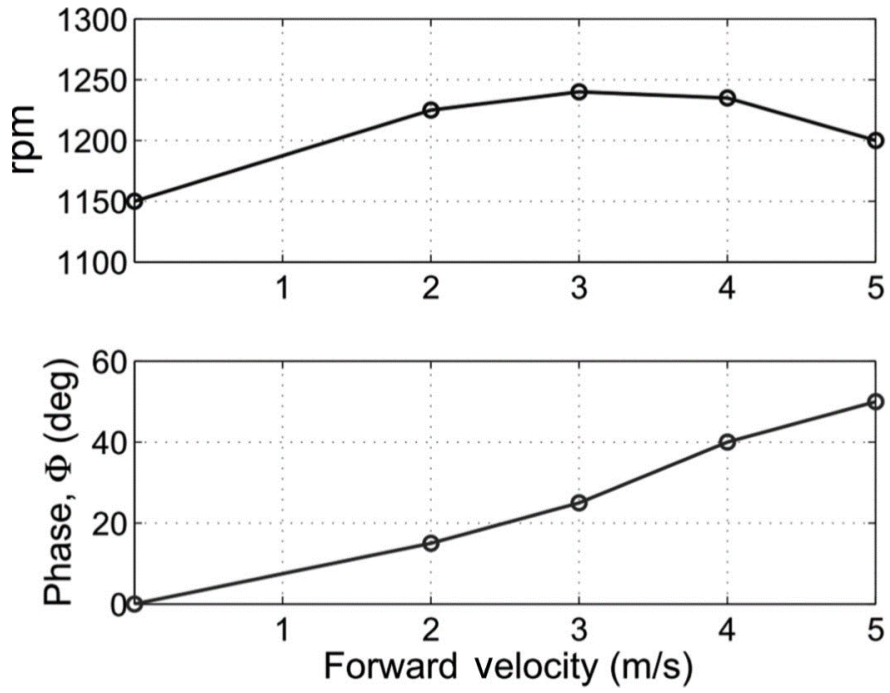

Figure 1.51: Controls inputs required to obtain trimmed free flight[29].

resulting model showed how even in forward flight the cyclocopter dynamics are dominated by gyroscopic coupling. The inherently unstable lateral-yaw mode present in hover became even more unsteady due to controls coupling at high phase angles further compounding the relationship between roll and yaw. Using thrust vectoring to command forward speed was demonstrated to be an effective controls technique. Real-time data showed that the twin-cyclocopter responded quickly to thrust vectoring commands, reaching top speed less than 2 seconds after the command was given, and then returning to a hovering state quickly after the phase command was removed. Also indicated in the model was a resistance to longitudinal disturbances in forward flight. A positive wind gust would result in a pitch up moment which would slow the vehicle back to its trimmed airspeed. However, these disturbances would excite the lateral-yaw mode as well (Fig. 1.53).

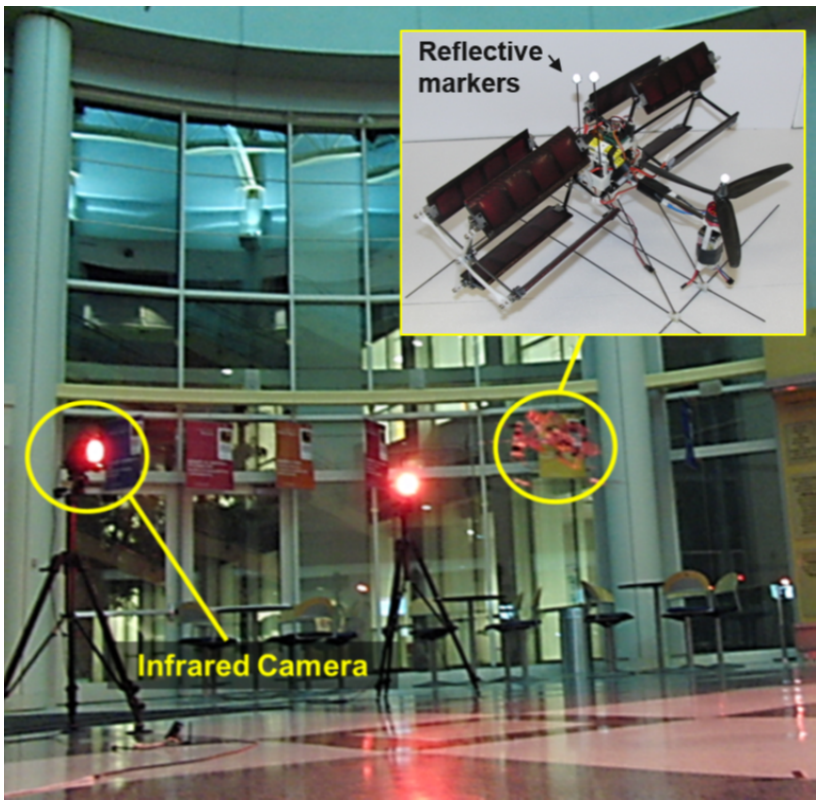

Figure 1.52: Motion capture testing setup for forward flight model determination[27].

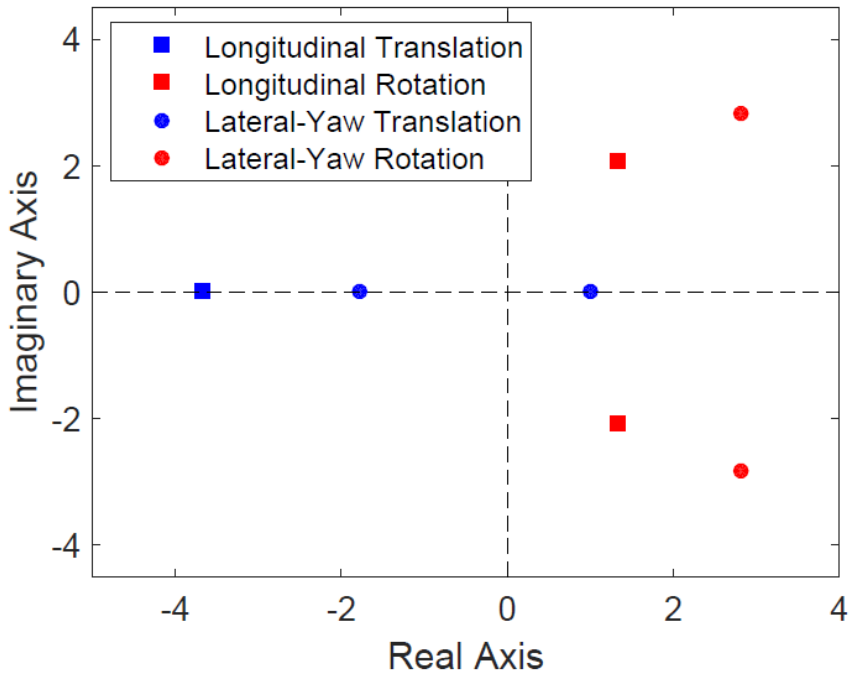

Figure 1.53: Pole location for the twin-cyclocopter in forward flight showing stability in translation, but instability in rotation[27].

Follow-on research was performed by Shrestha *et al.* on the same vehicle to investigate the disturbance rejection capabilities of the cyclocopter through a series of experiments in the wind tunnel and in front of a synthetic gust generation device. A calibrated pitot probe designed to operate at low speeds continuously measured free stream velocity throughout the experiment. Two controls approaches were tested — a traditional closed-loop system where the controller responds to disturbances and another incorporating real-time flow measurement whereby the controller reacts before a disturbance is felt. First, the maximum gust perturbation that the cyclocopter could reject was determined by mounting it to a 1-DoF rotational stand and placing that in the wind tunnel air stream. Then the vehicle was subjected to successively increasing edgewise flow until control saturation was reached and the vehicle could no longer maintain a level attitude. The process was conducted for both longitudinal and lateral directions. Longitudinal stabilization was achieved using thrust vectoring while lateral control was performed with differential RPM of the cyclorotors. Because the wind tunnel was controlled by an electric motor, only ramp flow changes

could be commanded, but the highest longitudinal and lateral ramp disturbances that could be sustained were 10 m/s and 6.5 m/s, respectively. After that the cyclocopter was mounted to a 6-DoF stand for use in the synthetic gust generation environment which consisted of several blade-less fans behind shutters that could be instantly opened or closed, allowing the creation of step gust profiles (Fig. 1.54). Disturbance rejection performance was quantified by using the motion capture system to command the cyclocopter to hold position; displacement from the commanded point was the performance metric. Separate tests were run where forward velocity was controlled through pitch attitude or by thrust vectoring (Fig. 1.55), the latter being far more effective at maintaining the desired position for a given gust (Fig. 1.56). Additionally, incorporating *a priori* knowledge of the flow gathered from the onboard pitot probe greatly increased disturbance rejection capabilities (Fig. 1.57). Crosswind scenarios were considered as well and performance deteriorated at higher side-slip angles due to the reduced disturbance rejection capability along the lateral axis.

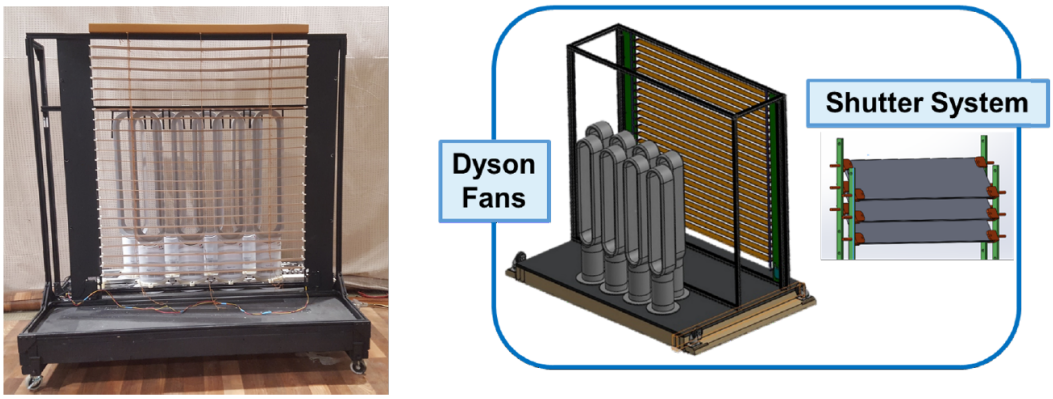

Figure 1.54: Synthetic gust generation device with shutter system[27].

More recently, Shrestha *et al.* created a 1010 gram quad-cyclocopter to investigate the potential of cyclocopters for use in multi-modal locomotion: aerial, aquatic, and terrestrial (Fig. 1.58)[27]. Being able to switch between these would allow a vehicle to conserve energy, traverse longer distances, and maneuver through confined spaces. The cyclocopter used four cyclorotors in an "H" configuration where the fore and aft rotors are spun in opposite directions from each other to

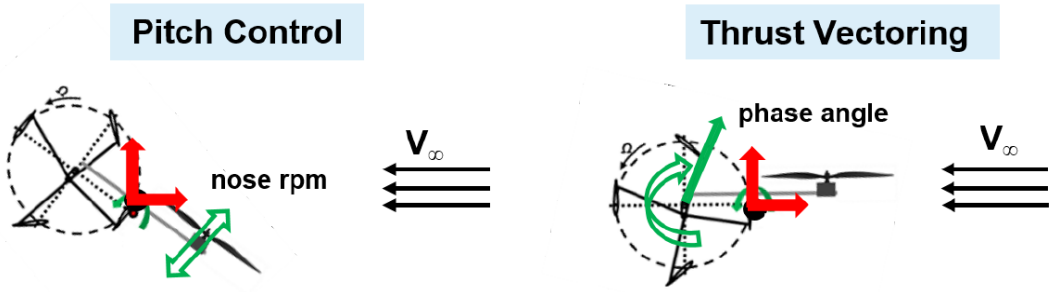

Figure 1.55: Pitch control vs. thrust vectoring control[27].

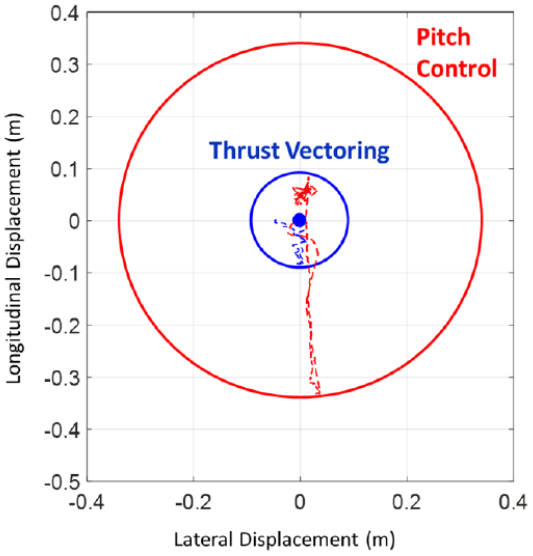

Figure 1.56: Displacement for a 2.8 m/s gust for pitching and thrust vectoring control methods[27].

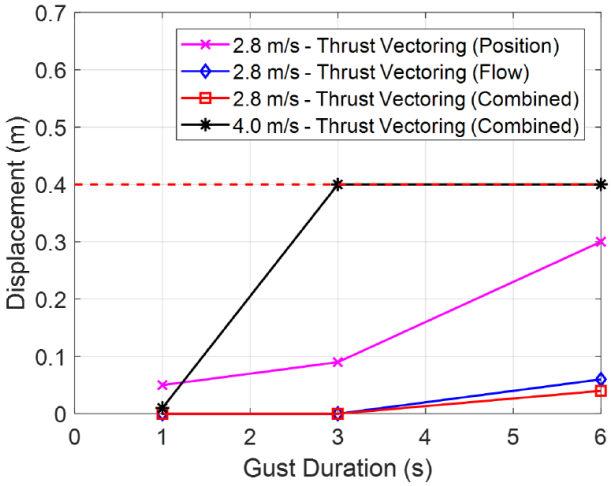

Figure 1.57: Displacement vs. gust duration for 2.8 m/s and 4 m/s guts using different feedback types[27].

balance torque. The cyclorotor end-plates are modified to act as wheels by having a circular outer frame. Both inboard and outboard end-plates were fixed to the driven shaft to maintain alignment in terrestrial mode. A titanium rod ran through the rotating shaft to the eccentric piece at the outermost end allowing for thrust vectoring. Retractable landing gear was added that enabled the vehicle to lower or raise itself from the ground when transitioning between aerial and terrestrial modes while also serving as pontoons for the aquatic mode. Locomotion in terrestrial mode is accomplished by having all the cyclorotors all rotate in the same direction, except to turn which

was achieved through differential rotor speeds. During aquatic movement, the cyclorotors operate with a high phase angle so that they generated primarily horizontal (propulsive) thrust. Operational testing demonstrated successful mobility in each mode along with transitions between all three. Power consumption was greatly reduced in terrestrial and aquatic modes when compared to aerial operation.

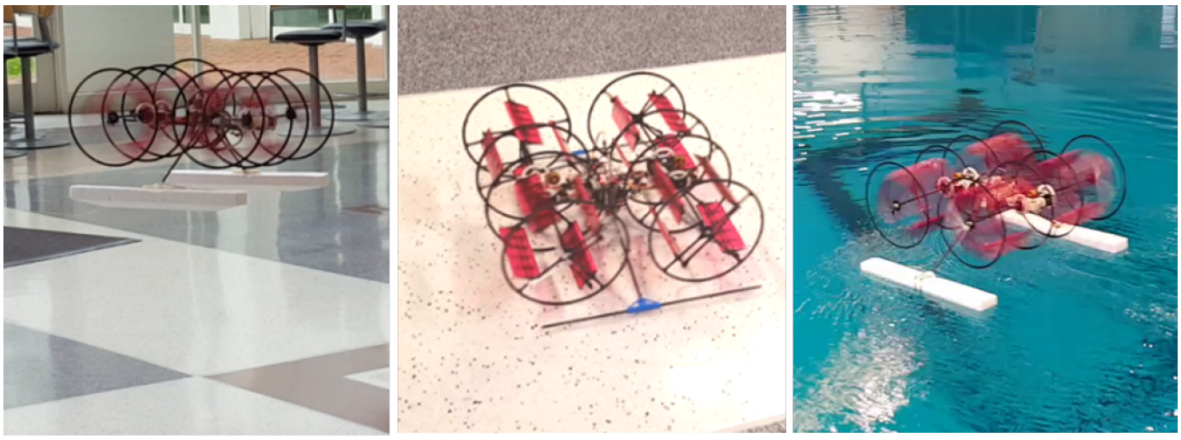

Figure 1.58: Quad-cyclocopter demonstrating aerial, terrestrial, and aquatic modes[27].

Not mentioned in the previous paragraphs is the work at UMD to study the application of cyclorotors to vertical axis wind turbines, which is outside the scope of this work[102–104].

1.3.3 Texas A&M University

In 2014, Benedict moved from UMD to Texas A&M University as a faculty member and cultivated a research group named the Advanced Vertical Flight Laboratory (AVFL) the purpose of which was to study the cyclocopter and other unconventional S/VTOL concepts. Presented in this section are several projects focused on MAV cyclocopters conducted since the inception of the AVFL in parallel with the topical research. Not included are several cyclorotor studies pertaining to their use on larger cyclocopter UAVs, in vertical axis wind turbines, and on underwater vehicles.

Halder and Benedict developed a standalone aeroelastic model consisting of an unsteady aerodynamic model coupled with a fully geometrically exact beam model[105]. The focus was on

capturing the aeromechanics of a cyclorotor employing moderately or highly flexible blades. The aerodynamic model incorporated various physics of cyclorotor operation including nonlinear dynamic virtual camber, the effect of near and shed wakes, and leading-edge vortices. From a design standpoint, deflections are inevitable due to the high transverse loading, but lightweight blades are critical to an efficient rotor as previously mentioned. Therefore, understanding the interplay between blade bending, torsional deflections, and aerodynamic performance is imperative to an optimized design. In order to validate the model, experiments were conducted on cyclorotors with blades of varying flexibility; data from which showed that, with increasing blade flexibility rotor thrust decreases while power consumption increases, greatly reducing power loading. When experimental data was compared with model predictions it was found that a second-order nonlinear structural model under-predicted thrust because it over-predicted bending deflections and axial twist. However, when using the geometrically exact model, the predictions matched experimental results well. Analysis showed that torsional deflection decreased geometric pitch from the prescribed angle, commensurately decreasing thrust in the upper half. The study also revealed that bending deflections did not directly impact thrust a considerable amount, but bending curvature created large nonlinear moments which increased twist, the primary reason for thrust reduction.

Reed *née* Walther *et al.* performed experiments to understand the unsteady aerodynamic phenomena on cyclorotor blades operating at ultra low Re ($\sim$18,000) using a combination of force and flowfield measurements as well as CFD[30]. A single blade was affixed to a rotating arm by a servo and load cell then suspended into water to match the Reynolds number of significantly smaller rotors (Fig. 1.59). The rotation of the arm and actuation of the pitch-control servo were coordinated by a computer to prescribe various pitching kinematics. The water was seeded with $\sim$10-μm-diameter glass beads to allow for PIV measurements of the flowfield, the setup for which is shown in Fig. 1.60. Instantaneous blade fluid dynamic forces and moments were measured by the six-axis load cell for both symmetric and asymmetric pitching schedules: 15°, 30°, 45° symmetric and 7 different asymmetric cases with a peak-to-peak amplitude of 60°. The maximum power loading found was attained by using blade pitch angles of 35° top and 25° bottom, which

reduced the power required and increased thrust produced over the other schedules that were tested (Fig. 1.61). A more uniform distribution of drag with respect to azimuthal location is responsible for this increase — drag was nearly equal between the upper and lower halves (Fig. 1.62). The 2D CFD analysis of the airfoil correlated well with both force and flowfield measurements (Fig. 1.63), although slightly better agreement was found in the upper half of rotation than the lower half where it over-predicts forces. Overall, the top half of rotation produced less thrust than the bottom because of the difference in virtual camber.

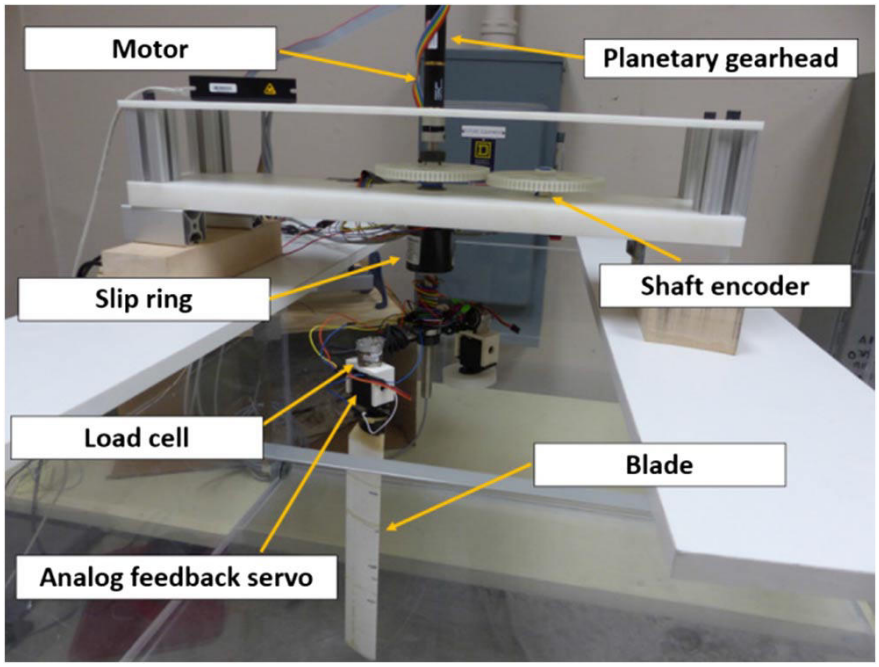

Figure 1.59: Single-bladed cyclorotor test rig in water tank[30].

Using a similar experimental approach, dynamic and static pitching cyclorotor cases were then compared in order to isolate the unsteady aerodynamic phenomena from steady effects[31]. Symmetric dynamic pitching of $\pm 5°$–$\pm 45°$ (in 5° increments) was compared with static pitch cases run in the range of -45° – +45°. Dynamic blade force coefficients were almost double the static ones, which meant that the unsteady mechanisms greatly increased force production thus allowing cyclorotors to produce large amounts of thrust at relatively low rotational speeds. For the dynamic

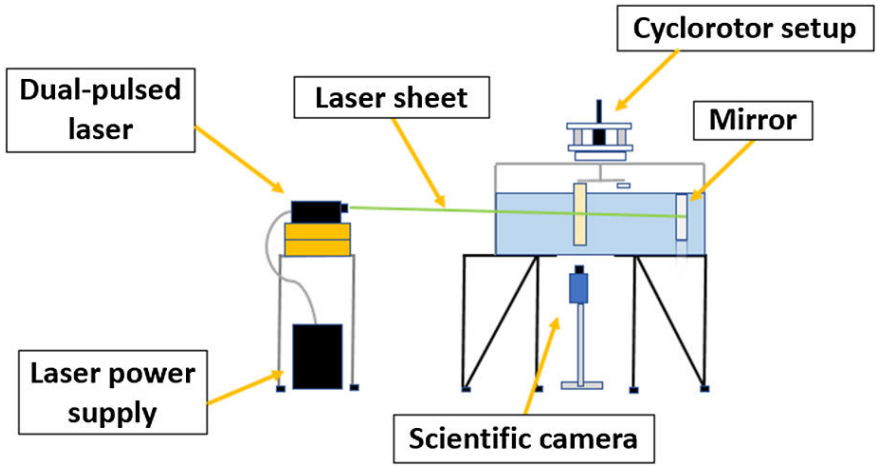

Figure 1.60: Schematic of hydrodynamic PIV setup[30].

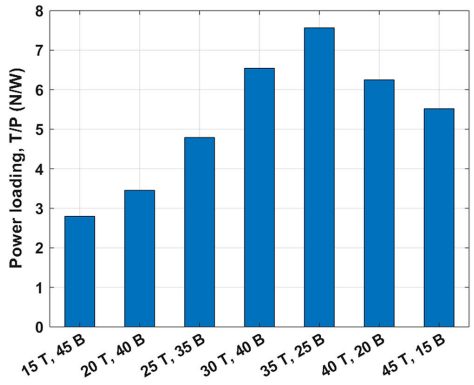

Figure 1.61: Cycle-averaged blade power for each 60° peak-to-peak asymmetric pitching case[30].

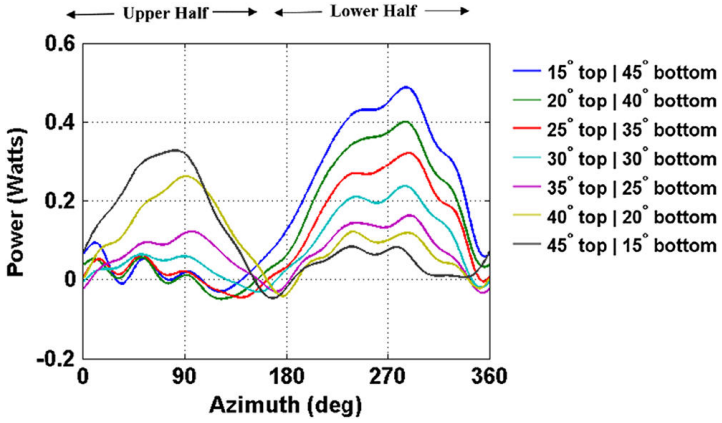

Figure 1.62: Measured instantaneous blade power vs azimuth for 60° peak-to-peak asymmetric pitching[30].

cases, blade lift monotonically increased up to 45° pitch amplitude; however, for the static cases, flow separated from the leading edge after around 15° with a large laminar separation bubble (Fig. 1.64). Large asymmetry was observed in lift and drag coefficients between upper and lower halves of the trajectory because the dynamic stall process during the upper half differed significantly from that in the lower half. This was because dynamic stall vortex development was based on maximum pitch and pitch rate, which varied based on azimuthal location. In both halves the strong leading edge vortex delayed stall to very high angles of attack, enhancing lift. Even so, the higher pitch

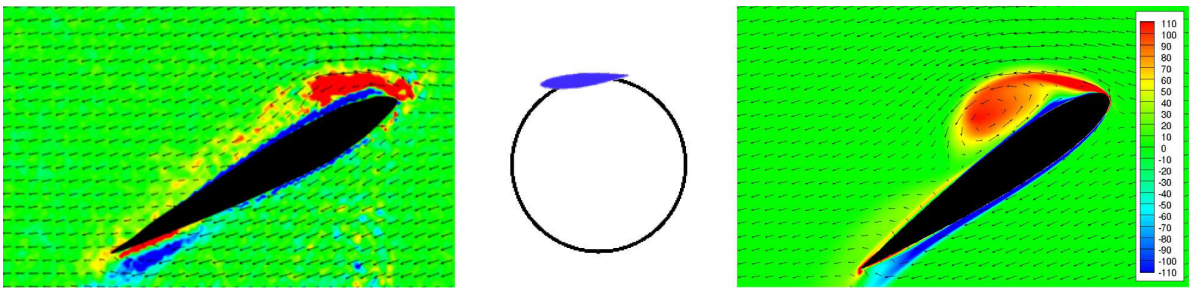

Figure 1.63: Representative results comparing PIV (left) to CFD (right) for 35°/25° top/bottom asymmetric kinematics[30].

amplitude kinematics saw a reduction in Figure of Merit (FoM) due to higher dynamic drag coefficients. Measured resultant forces were mostly normal to blade chord for dynamic pitch cases indicating that the pressure force, as opposed to the viscous force, is dominant on a cyclorotor blade even at these low Reynolds numbers.

A third study likewise using Re matching via water submersion was conducted by McElreath *et al.* to analyze the formation, strength, and convection of cyclorotor tip vortices with a focus on isolating how blade aspect ratio impacts 3D flowfields[32]. Understanding tip vortex behavior will aid in the reduction of unsteady blade loads and induced vibrations in future designs. Shed tip vortices also impact cyclorotor aerodynmamic performance through interactions with blades in the lower half of rotation. Motivated by the previous studies that indicated significant variations in radial force, and hence lift, with blade AR, force data and flowfield measurements using two views of PIV were taken 1) fixed inertial view enabling investigation of vortex development at varying vortex ages 2) blade fixed view to allow investigation of early blade tip vortex development (Fig. 1.65). Over the four aspect ratios and multiple pitching kinematics tested, several relationships became apparent. Aspect ratio did not affect vortex convection trajectory, but it did affect the rate of downward convection, vortex size, swirl velocity, and decay rate. Higher AR blades generated weaker vortices with reduced swirl velocity and faster decay. Decreasing blade aspect ratio decreased radial force coefficients (lift) as relative 3D-effects increased leading to higher swirl velocity of shed tip-vortices, which when coupled with shorter blade spans, resulted in higher in-

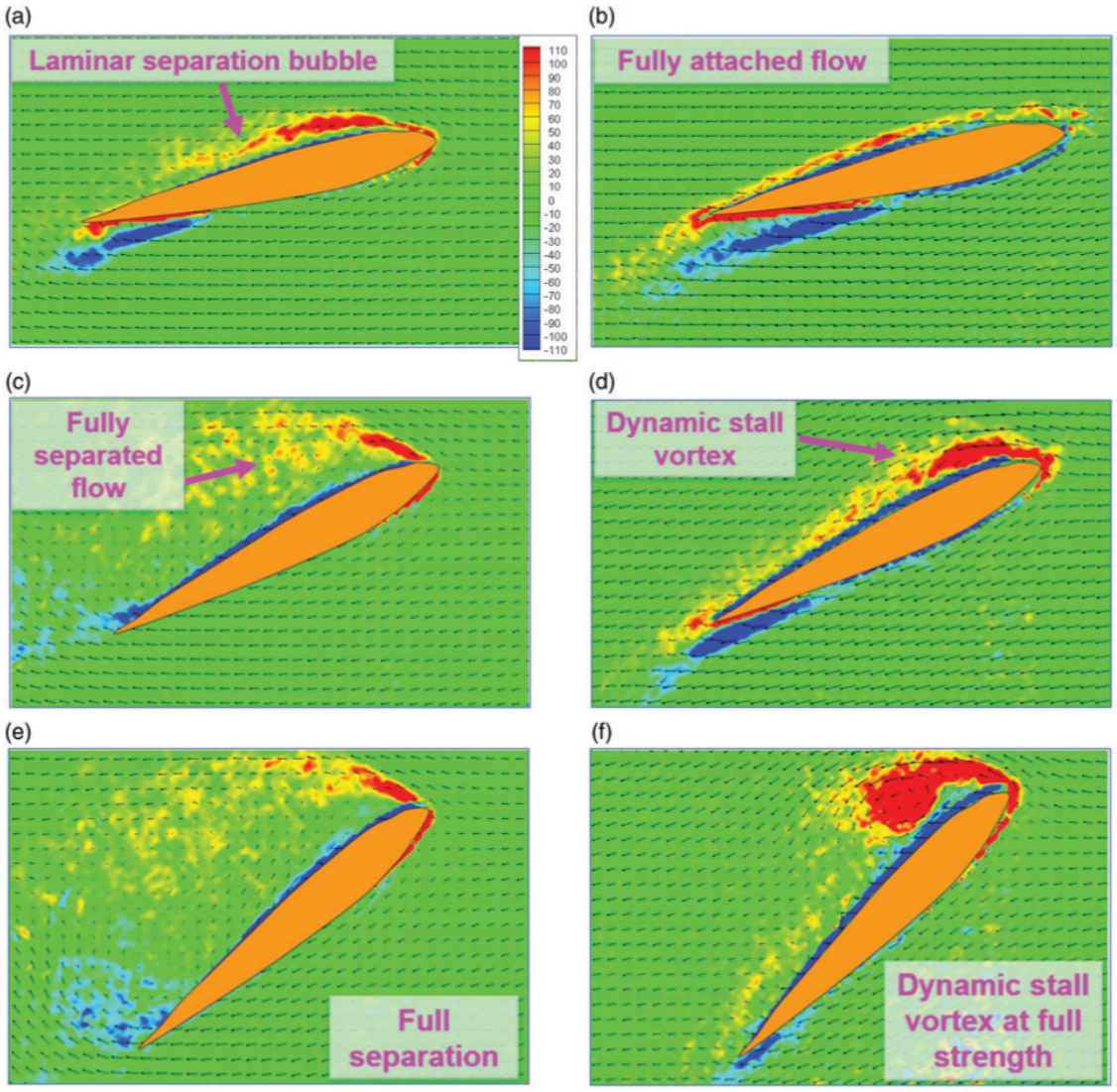

Figure 1.64: Static (left column) vs dynamic (right column) PIV comparison for 15°, 30°, and 45° kinematics at maximum pitch angle[31].

duced downwash along the blade and lower radial force per unit span. Tip vortex strength varied by azimuthal location which lead to periodic variation in the induced flow velocity on the blade with vortex strength being higher in the lower half than the upper half (Fig. 1.66). Counter-intuitively, shed tip vortices did not immediately begin to decay as they do in fixed wing applications, but rather peak swirl velocity grew initially indicating that the cyclorotor blade might have provided additional energy immediately after shedding.

In addition to the experimental work continuing in the AVFL, Halder and Benedict incorporated

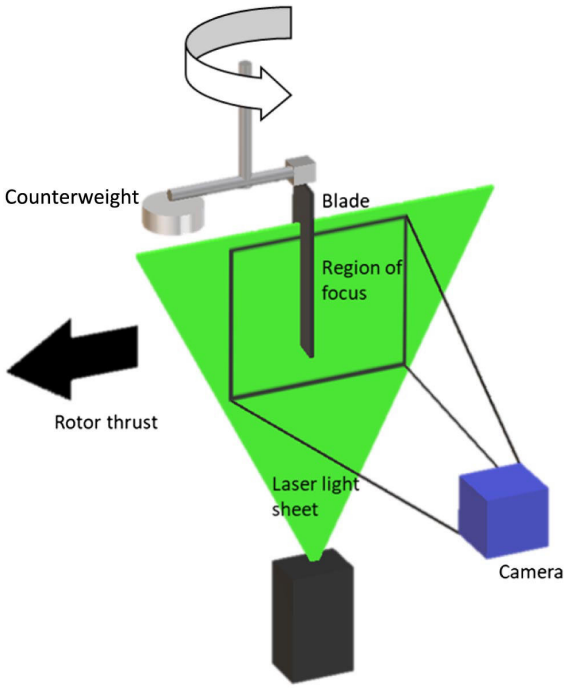

Figure 1.65: Diagram of PIV setup for flowfield measurements of cyclorotor blade tip vortex[32].

the previously described aeroelastic model (Ref. [105]) into a coupled trim model of a twin-cyclocopter in forward flight[33, 106]. Its constituent parts included a blade structural model, blade aerodynamic model, vehicle drag model, nose rotor drag model, and trim equations for a twin-cyclocopter. Blade aeroelastic response and vehicle trim equations are solved together by simultaneously updating control inputs and blade responses. The twin-cyclocopter modeled had five control inputs (mean and differential RPM, mean and differential phase of cyclorotors, and RPM of nose rotor) to balance three moments and two forces (Fig. 1.67). Lateral forces were zero for all phases of flight. Alternatively, mean and differential pitch amplitude of cyclorotors could be adjusted to control lift instead of RPM. Forward flight in the model was performed at a level body attitude with forward propulsion provided by cyclorotor thrust vectoring. The model was validated with previously published data on the performance of twin-cyclocopters at different forward speeds from Ref. [24]. Once validated, the model was used to understand trim behavior of an MAV-scale cyclocopter in forward flight and how trim is affected by parameters such as gross weight, max pitch amplitude, operating RPM, and longitudinal CG location. A comparison of

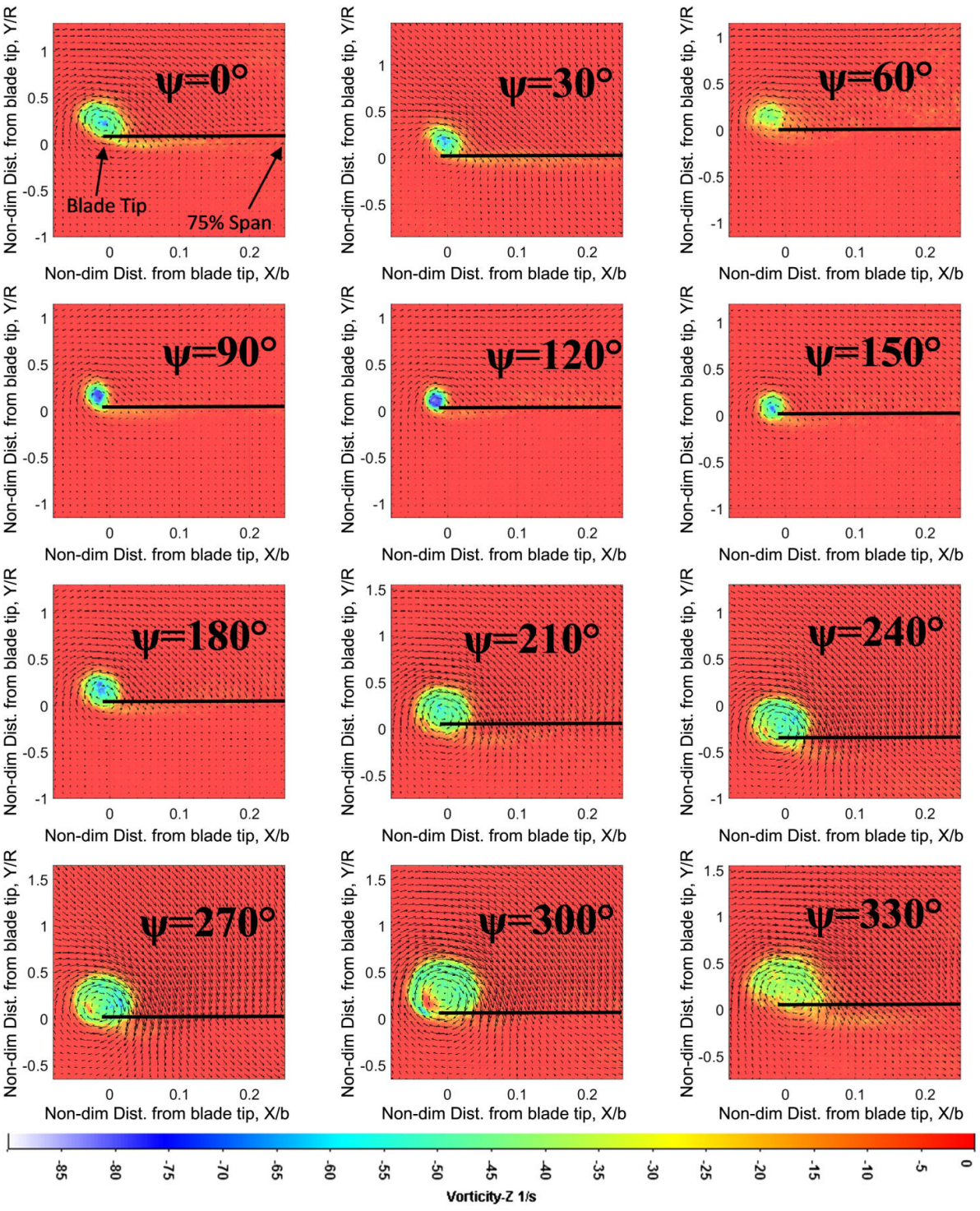

Figure 1.66: Tip vortex tracking along the azimuth[32].

RPM- to pitch-amplitude-based control schemes was also performed. One major finding was that the CG of the vehicle should be placed as close to the cyclorotor axis as possible to reduce power

(Fig. 1.68). Furthermore, data showed that increasing pitch amplitude permitted higher forward speeds with only a marginal increase in power; however, there was a moderate rise in hover power (Fig. 1.69).

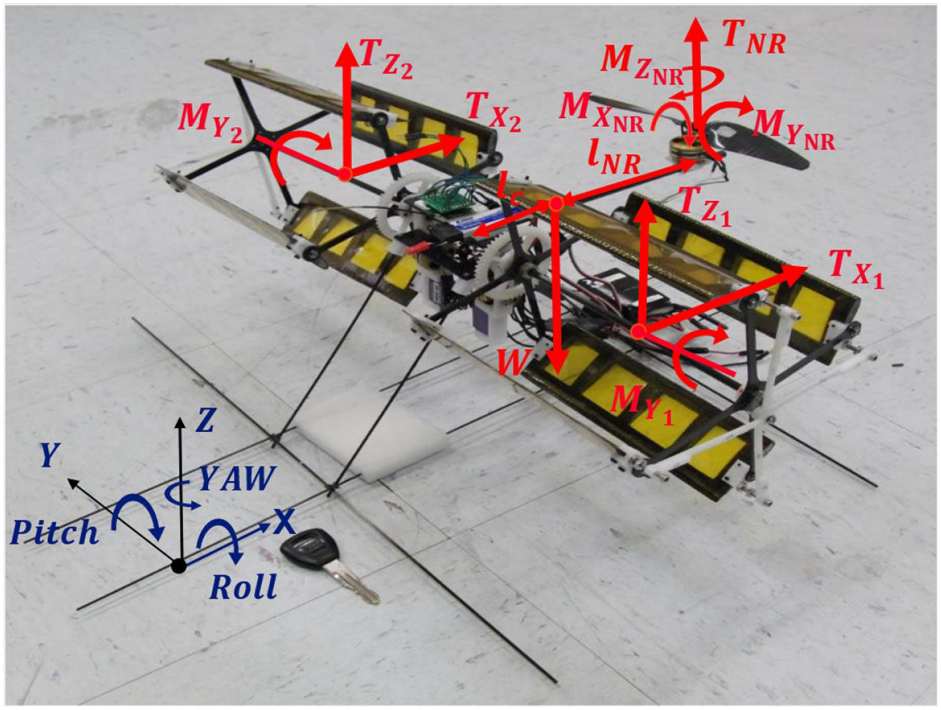

Figure 1.67: Forces and moments on a twin-cyclocopter in forward flight[33].

1.4 Research Goals and Paper Outline

While not exhaustive, the presentation of previously conducted research outlines a clear progression in the maturation of cyclorotor technology. In a flurry of flight-oriented research in the 1930s some experimental and analytical work was done on cyclorotors to study the feasibility as a concept and a couple of attempts were made to construct full-scale cyclocopters. However, it was not until the explosion of interest in UAVs and MAVs that the cyclorotor saw great strides towards a realized aircraft. Shifting focus to smaller vehicles was more conducive to the inherent nature of the cyclorotor. A greater understanding of function and design led to even more capable rotors which, in turn, permitted more accurate models. Growing beyond mere understanding,

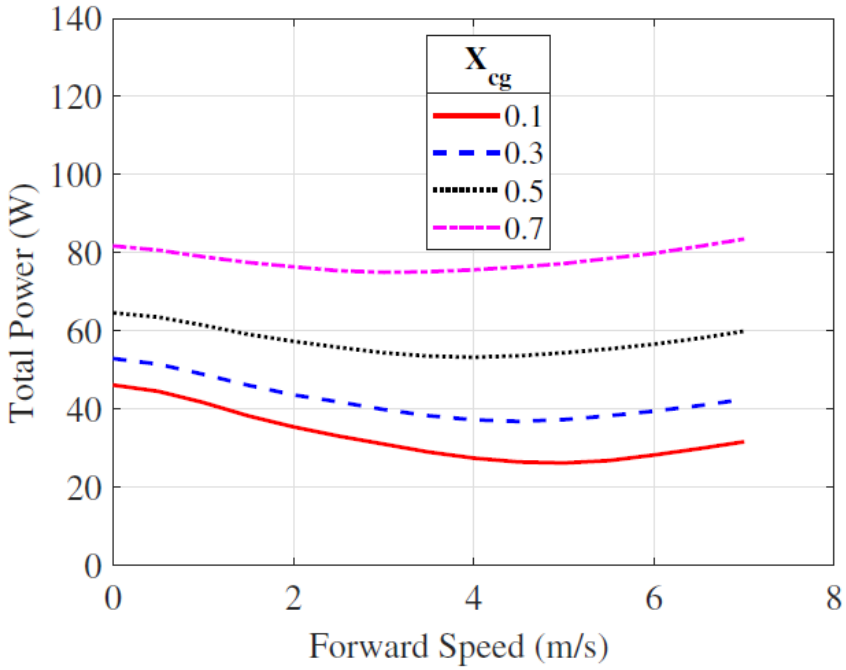

Figure 1.68: Variation of required total power for twin-cyclocopter in forward flight for different longitudinal positions of CG[33].

parametric studies of cyclorotor design explored the operational space from a practical standpoint enabling the construction of fledgling flight-worthy cyclocopters. With a proven design process, more types, sizes, and configurations of cyclocopter could be built and used to collect valuable empirical data. In the years hence, more refined vehicles have been used to investigate cyclocopter dynamics, build both empirical and analytical models, and develop controls techniques. Mere hovering experiments gave way to forward flight projects and the more advanced, validated models are now currently helping to render the previously required experimental design process unnecessary, reducing overhead and saving time. The research described in the remainder of this paper began shortly after hover-capable cyclocopters had come to fruition and was ongoing up to the publication of this document. This thesis will follow the organization laid out below, provided with a short description and justification of each chapter.

Through a design-oriented approach, this dissertation expands on the existing body of cyclorotor research by investigating aspects of cyclorotor physics, design, and performance to quantify

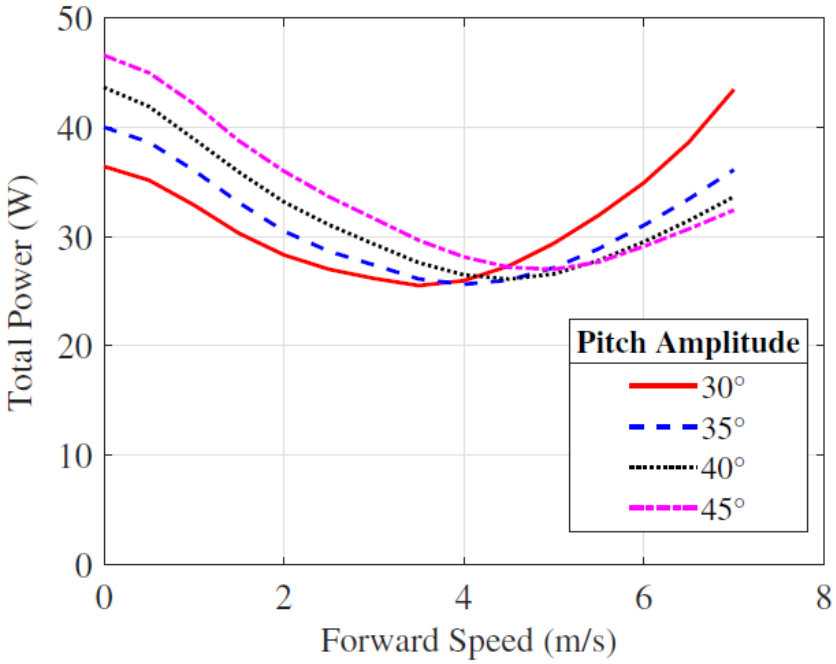

Figure 1.69: Total vehicle power required in forward flight for varying speeds and pitch amplitudes[33].

how such a device affects the capabilities of MAV at smaller scales (Re ∼11,000). There was limited data on cyclorotor performance at that regime and understanding of the physics was tentative at best; therefore, previous trends could not be relied upon to build or validate a model. Consequently, an experimental approach was chosen over a computational one. Moreover, most flyable cyclorotor designs were scaled and augmented versions of one another, but simply scaling down a larger rotor was not the optimal solution and hence a new, more suitable cyclorotor design was developed. Chapter 2 covers this development process and the resulting rotor design along with the parametric studies conducted to investigate its performance.

Flowfield measurements taken via particle image velocimetry proved invaluable to understanding the complex flow phenomena through and around cyclorotors, especially at ultra-low Reynolds numbers. They were also indispensable for generating and validating analytical models. As such, PIV was necessary as part of this research in order to explain the behavior of the cyclorotor and any cyclocopters built from it, especially owing to the unique design and scale of the rotor. Chapter

3 explains the setup and procedure for the PIV experiments and the key insights gained from them. These were the first flowfield measurements taken of a cyclorotor with cantilevered blades with elliptical planform, both of which made the flow highly 3-dimensional.

No flight-capable cyclocopter had been built at scales less than 50 grams and operated at such low Reynolds numbers ($< 20,000$); therefore, in order to study the performance of cyclocopters at those scales one had to be developed. Chapter 4 details the design and development process of building the world's smallest twin-cyclocopter as well as an exploration of different vehicle configurations and flight testing procedures. These vehicles gave valuable insight into the performance and characteristics of MAV-scale cyclocopter flight unattainable except through practical experience. Up to this point, the few flying twin-cyclocopters had all used a similar design and configuration, most poignantly the single nose rotor layout. A single nose-rotor cyclocopter was built while alternative nose rotor designs were considered, one of which, a coaxial-nose configuration, was incorporated into a second flying cyclocopter. Covered in this chapter will be the general design philosophy, cyclorotor integration, vehicle hardware, telemetry, and flight control system of two twin-cyclocopters followed by an explanation of the flight testing process from ground tests to stable flight. Multiple control strategies were used and qualitatively compared as well.

Chapter 5 explains the system identification procedure used to generate a linear model of the open-loop body dynamics of a twin-cyclocopter. Aside from the two described in the literature review and the one presented in this paper, there are no other linear models derived from functioning, flyable cyclocopters. These models are valuable because they can be used to compare the vehicles to each other and to other MAV concepts. They can also be used for developing model-based controllers. Discussed in this chapter are the experimental setup, the process used to collect data, and the analytical methods used to calculate the model. Additionally, important findings from the model are given along with explanations of the underlying physics.

As part of the objective to study cyclorotor application, a third cyclocopter MAV was developed, a quad-cyclocopter, which is discussed in Chapter 6. Using a scaled version of the rotors from the twin-cyclocopter, this effort is a validation of the design process and parametric studies.

It also offered the opportunity to study control strategies and compare flight qualities between the twin- and quad-cyclocopters because of their similar rotor designs and sizes. Forward flight experiments were also performed that showcase the unique ability of cyclocopter to use thrust vectoring for propulsion while facilitating the comparison of thrust vectoring versus pitching translation for both the twin and quad. Because there are few systematic looks into cyclocopter flight outside of a hovering regime, these experiments provided empirical insight necessary to expanding the capabilities of MAV cyclocopters.

The final chapter, Chapter 7, concludes the thesis with a summary of key findings and proposals for future work.

2. Micro-Cyclorotor Design and Parametric Study

In the endeavor to understand the aeromechanics, dynamics, and control of cyclocopter MAVs at a scale that has never been studied before (gross weight around 30 grams), a new design had to be created, one that was more suited to the flow regimes and fabrication processes associated with micro-scale aircraft. Many of the successful, flying UAV cyclocopters shared common design elements; however, in the effort to scale down the cyclocopters concept even further, it was quickly realized that merely shrinking down these rotors was not a feasible approach. To align with DARPA's challenging vision of an MAV from 1997 the existing designs had to be made smaller, more portable, and more capable. With that in mind, a new concept was generated based on these goals and engineered specifically with material selection, fabrication, and aerodynamics in mind. Figure 2.1 shows this concept that uses a unique cyclorotor, blades, and shape-factor. One of the driving principles was to keep everything as compact as possible so the final design would be palm-sized and keeping all hardware inside the lateral footprint of the rotors would make the body more aerodynamic as well. The body cowling would reduce parasitic drag of the rotors and structure by shrouding rotating parts and enclosing the linkage system within the rotor. Additionally, shielding the cyclorotor and nose propeller in this way would also minimize exposure of rotating parts thereby limiting the chance of striking something in confined spaces as well as increasing performance by creating a duct for the nose propeller.

Establishing a concept first is important to identify constraints and requirements, plus it gives future design efforts a more concrete direction. To align with the objectives of the project, two physical parameters were identified as primary determinants of all other system variables: size and weight. Setting these as initial conditions for the MAV restricts hardware options and forces innovation to meet project goals rather than accepting bloat associated with unconstrained engineering. Since the cyclorotors themselves would be the largest structure on the vehicle their size would by extension determine the size of the vehicle; therefore, a radius of 1 inch was imposed. Establishing an initial weight limit was more complicated than eye-balling it and using esoteric

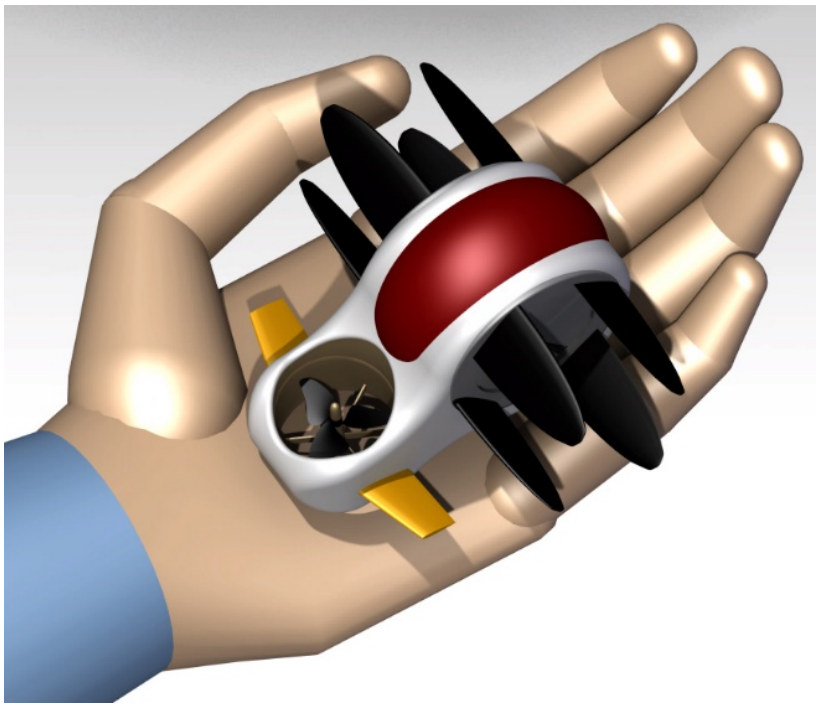

Figure 2.1: Conceptual drawing of a micro-scale cyclocopter.

intuition. Rather it required analysis of past data to determine the proper makeup of a cyclocopter of this size. Based on trends from the UMD studies for rotor size, performance, vehicle weight, and Reynolds number plus a survey of available COTS parts a reasonable, but still demanding, upper limit was set. Figure 2.2 shows previous vehicles by weight versus Reynolds number with the conceptual target in comparison. It is also important to note that all the previous cyclocopter designs from UMD followed the exact same template, excepting the 800 gram quad-cyclocopter.

By looking at the smallest COTS parts on the market and comparing that to the mass fraction breakdowns of the other UMD cyclocopters (Ref. [27]), it was concluded that a maximum vehicle weight of 30 grams was achievable with some improvement to the cyclorotors to increase the $Thrust/Weight$ (T/W) ratio. From there it was assumed that the required thrust would be evenly split between the two cyclorotors and nose propellers, meaning each cyclorotor must produce 0.1 N of lift. With a rotor radius already set, the performance could be predicted by assuming other cyclorotor dimensions that should closely approximate an optimal rotor according to the data,

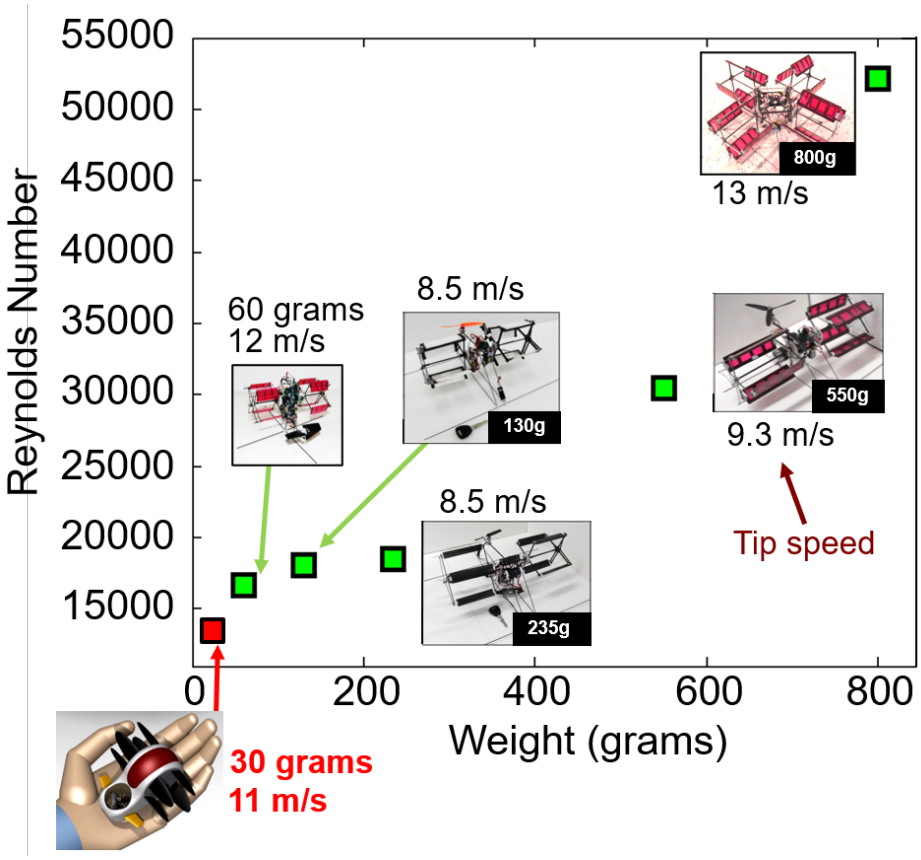

Figure 2.2: Range of cyclocopter UAVs developed at the University of Maryland by weight and Re with micro-cyclocopter concept for comparison.

meaning a c/R ratio of 0.8, 4 blades, and an aspect ratio between 1 and 2. Thus configured, a tip speed of approximately 11 m/s and a Reynolds number of around 11,000 at and operating speed of $\sim$4000 RPM were calculated. Summarizing the initial design parameters:

- Maximum Vehicle Weight < 30 grams
- Cyclorotor Radius = 1 inch
- Cyclorotor Thrust > 0.1 N
- Cyclorotor Speed $\approx$ 4000 RPM

The first step in realizing this concept is to develop and build the cyclorotors because they are the heart of the system. As such, all of the factors that affect the performance of the cy-

clorotor need to be carefully tailored to the specific application in order to generate high quality experimental data. And since these same rotors will be used throughout this study it is imperative that they are well characterized and sufficiently optimized. This chapter will cover cyclorotor design, blade design and manufacturing, and parametric studies conducted in order to develop high thrust-to-weight ratio cyclorotors to be used on the MAV. The series of parametric studies carried out investigated performance based on the number of blades, blade size, pitching kinematics, and blade aspect ratio. The Chapter is subdivided into three sections as follows:

- Cyclorotor and Pitching Mechanism Design – Covers the design and development of the micro-cyclorotor along with the discussion about its unique properties.
- Blade Design and Manufacturing – Discusses how the small blades are manufactured and the challenges associated with that process.
- Cyclorotor Performance – Presents the various parametric studies conducted along with results obtained and discussion of pertinent findings. The culmination of these studies is the final optimized micro-cyclorotor design.

2.1 Cyclorotor and Pitching Mechanism Design

The primary challenge in designing and building a cyclocopter of this scale was creating lightweight, yet efficient rotors that can produce the required thrust. Building off of knowledge gained from previous studies, a lightweight cyclorotor was designed that is different from any previously built cyclorotor (Fig. 2.3). The rotor uses cantilevered blades with a semi-elliptical planform shape to reduce rotor weight (by eliminating the shaft and the additional tip end-plate) and improve aerodynamic efficiency (by reducing induced drag). It also uses lightweight blades constructed in a way that is only possible at this size. As a baseline design, a rotor radius of one inch was chosen in order to keep the size and weight of the rotor low, as well as reduce the overall cross-sectional profile of the craft and thus fit well within the targeted vehicle size. The construction of rotors this small was challenging because of the tight tolerances needed for the small

moving parts that would allow the pitch mechanism to function while also keeping the designed pitch kinematics. As an example, a change of 0.25 *mm* will cause a change of a couple degrees in the pitching kinematics, affecting rotor performance.

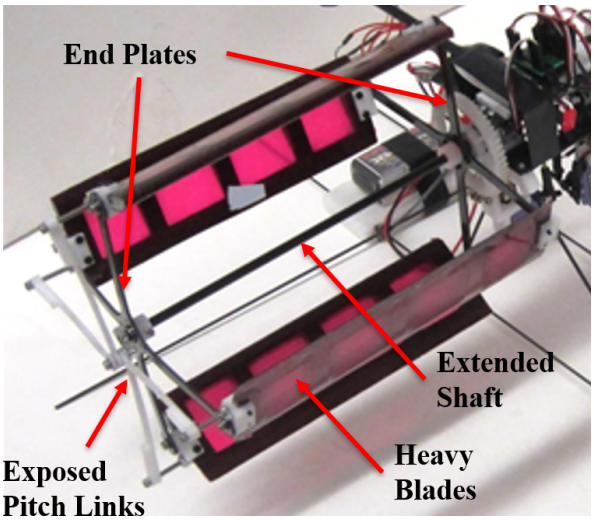

(a) Large-scale cyclorotor[28].

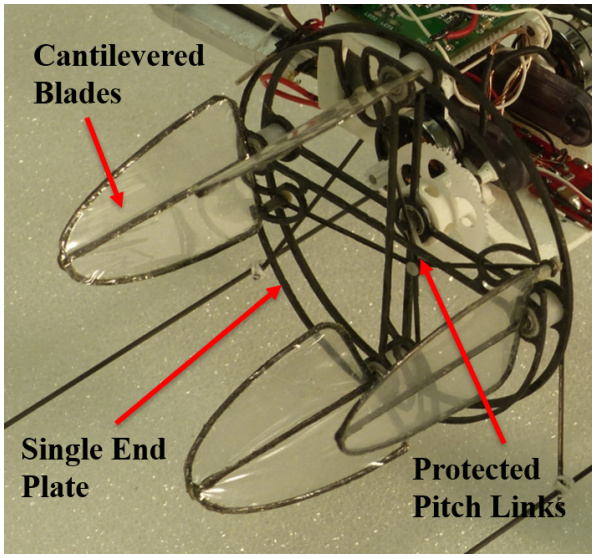

(b) Micro-scale cyclorotor.

Figure 2.3: Primary differences between larger cyclorotors and the micro-scale rotor.

Because the blades were cantilevered, the end plate had to be designed to accommodate the pitch links at the root of the blades, and different blade root loads. For this reason, a single end-plate-based rotor was developed, which was designed to resist flexing under the centrifugal loads experienced during high-speed rotation. As shown in Fig. 2.4, the end-plate was made of two separated carbon fiber frames connected with spacers made from Delrin®, which also house the two root pitch bearings for each blade. This resulted in a lightweight end-plate with high stiffness. The stiffness, as mentioned previously, tends to increase as the structures are scaled down and this vehicle design leverages that to reduce weight. The carbon fiber frames are made out of 1/32" thick laminate. It has been shown that deflection of the blades at the root can reduce thrust by up to 40 percent; therefore blade-root stiffness is equally critical and the carbon fiber frames were

made thicker at the attachment points to provide the necessary support[21]. Figure 2.5 shows early testing of the micro-cyclorotor with a Mylar sheet covering the front frame to illustrate how the linkage system could be shielded inside the rotor, but performance was not appreciably modified in this configuration so Mylar was not added to the front frame of later rotors.

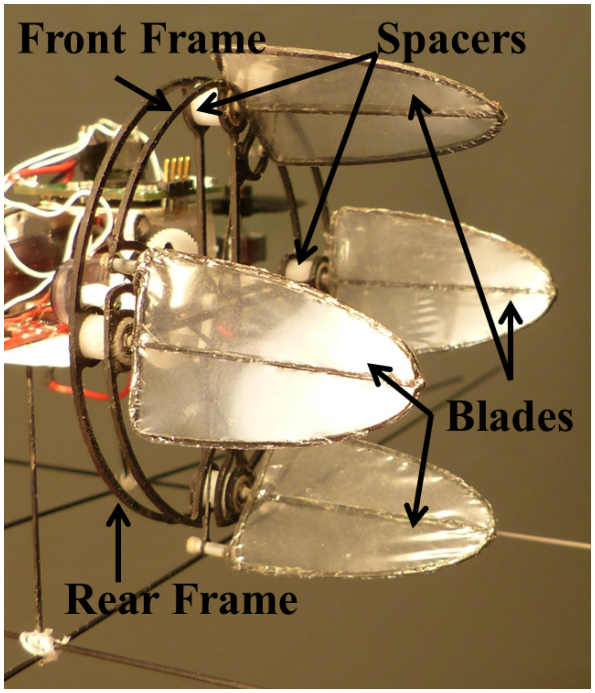

Figure 2.4: Micro-scale cycloidal rotor.

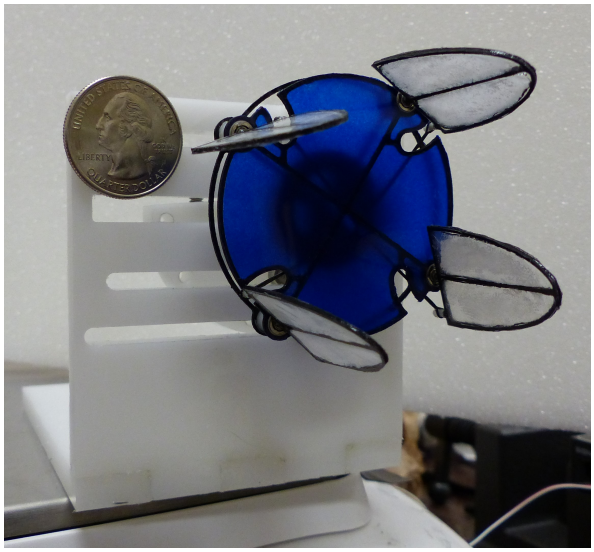

Figure 2.5: Cyclorotor with Mylar cover on front frame.

The cyclorotor utilizes a passive blade pitching mechanism which is based on a 4-bar linkage system where the blade pitching is kinematically coupled to the rotation. Figure 2.6 shows the four different lengths in the cyclorotor that form the mechanism: L_1 is the rotor diameter (25.4 mm), L_2 the pitch offset; L_3 the linkage length, and L_4 the distance between blade pivot and linkage attachment (8.3 mm). L_1 and L_4 were fixed; therefore, modifications of the kinematics were achieved through adjusting L_2 and L_3. The system can be seen in operation in Ref. [97].

It is interesting to note that the pitching kinematics created by this mechanism are only an approximation of the perfectly sinusoidal pitching shown in Fig. 1.10. This is due to the relative

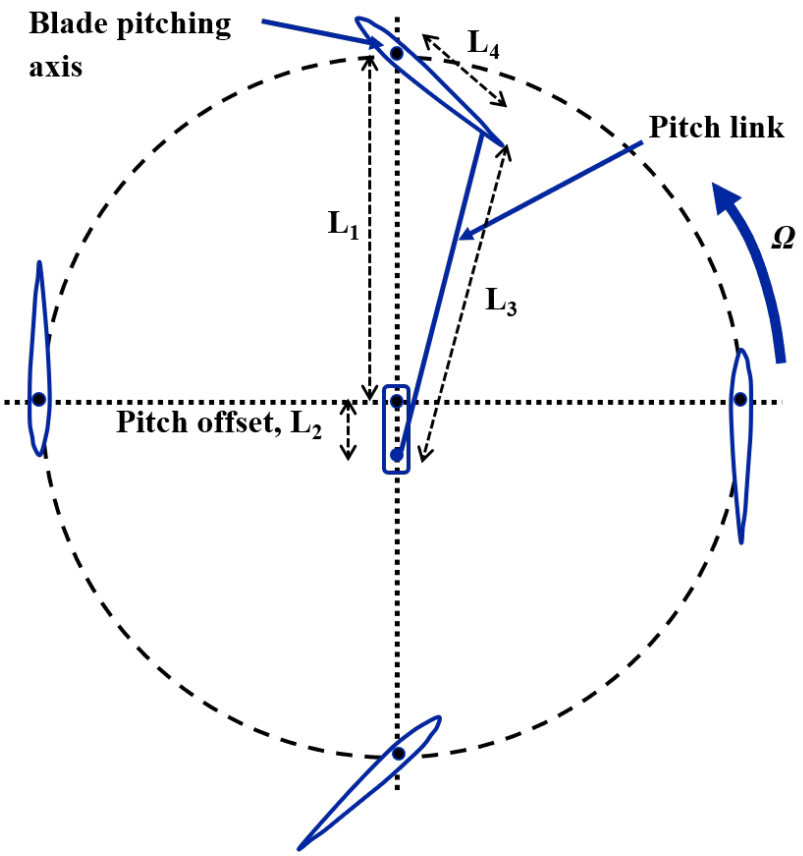

Figure 2.6: Schematic showing four bar passive pitching mechanism[22].

lengths of L_1, L_2, L_3, and L_4 and is particularly exaggerated at these small scales. Figure 2.7 shows a drawing of the cyclorotor in which the pitch angle deviation caused by the real 4-bar linkage system can be seen. The top and bottom blades are at the prescribed $\pm 45°$ pitch angle, but the right and left blade are not tangential to the rotor as would be the case with sinusoidal pitching. Such a small difference might not appear too dramatic, however, a clear divergence can be seen when considering the angular velocity (Fig. 2.8) and angular acceleration (Fig. 2.9) graphs, which are far from perfect sine waves. The effect this deviation from harmonic pitching has on thrust and power are not fully understood. However, since both lift and drag are functions of not only pitch angle but also angular velocity and acceleration it warrants further study.

Designing the pitching mechanism presented its own set of challenges due to its small size. Figure 2.10 shows an exploded view of the rotor and pitching mechanism with several of the parts

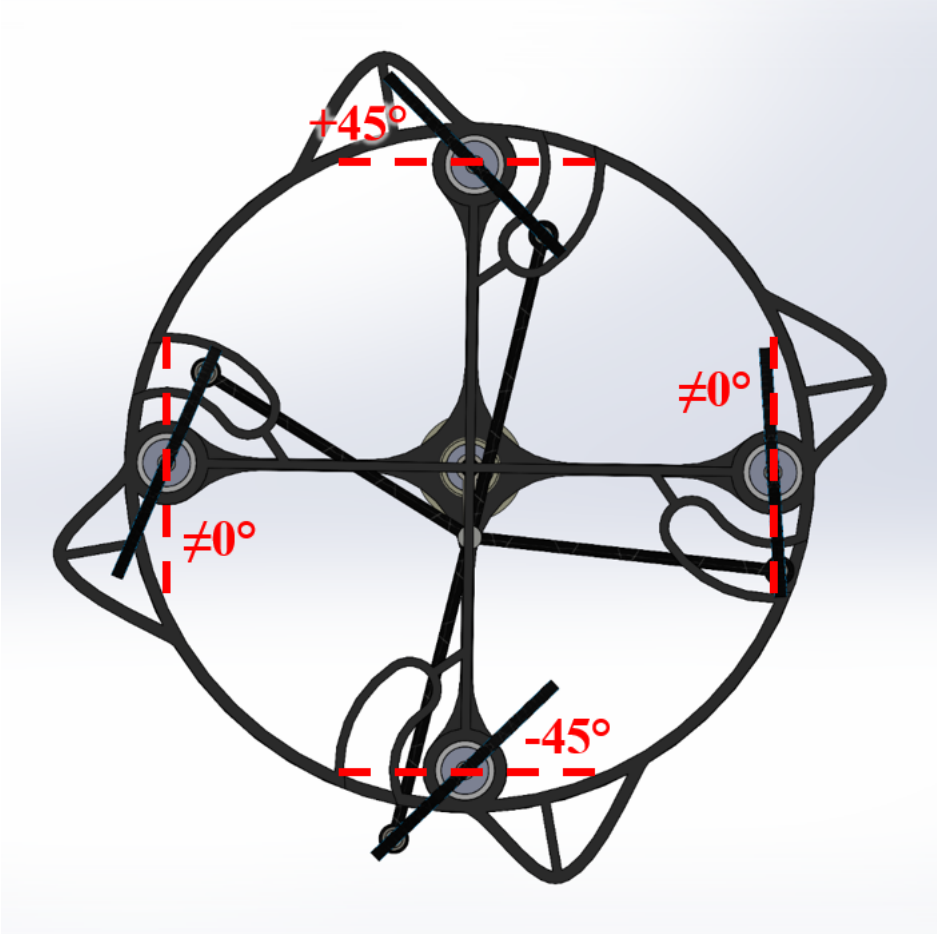

Figure 2.7: Drawing showing the imperfect blade angles at 0 and 180 degrees azimuth.

labeled accordingly. One of the important considerations in any cyclorotor configuration utilizing a 4-bar mechanism is the fact that the pitch linkages must be hinged to the pitch offset beyond the end of the main rotor shaft in order to avoid interference. For this cantilevered rotor design, the blades were mounted on the front carbon fiber frame, resulting in a root offset for each of the blades from the end of the main rotor shaft by the Delrin® spacer (see Fig. 2.4). This allows the pitching linkages to run in the space between the carbon fiber frames directly from the end of the main rotor shaft to the blades. By positioning the pitching links between the frames in this manner they were protected during vehicle crashes. The pitch links themselves were made of unidirectional carbon fiber prepreg and were manufactured using a Teflon™ base mold together with a silicone mat to compress the fibers into the mold, thus achieving the desired shape. This process, outlined in the

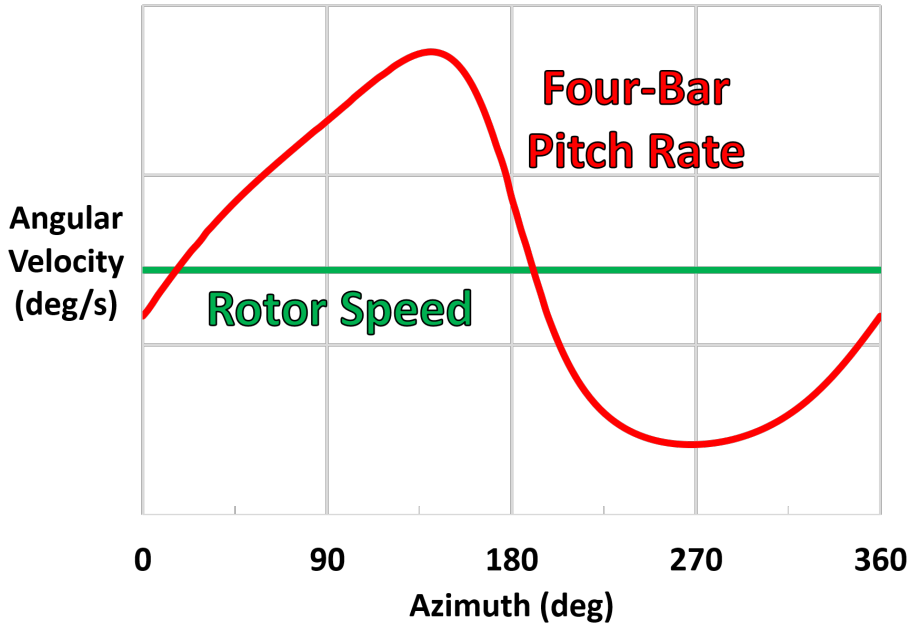

Figure 2.8: Angular velocity of blade by azimuth with the rotational speed of the rotor shown for reference.

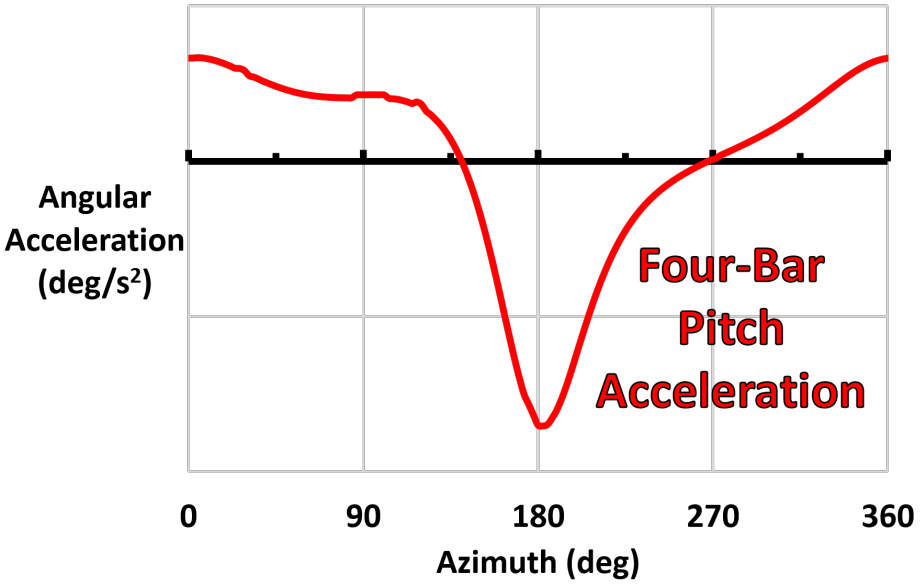

Figure 2.9: Angular acceleration of blade by azimuthal location.

subsequent sections on blade design, allowed the production of parts of consistent quality that were too delicate to fabricate with other methods. The resulting linkages weighed 0.01 grams each and

since all of the carbon fibers were aligned in the direction of loading they were very strong in that direction. Later, after the parametric studies, it was discovered that the linkages had an elongation of 0.018 in (0.45 mm) after they were removed from the Teflon™ mold, thus altering the pitch kinematics slightly. However, the elongation amount was consistent across different lengths of linkages meaning it had the same impact on all units made. Furthermore, other sources of error and tolerance stacking within the linkage system were of the same order and so all pitch kinematics described in the remainder of this paper for the micro-cyclorotor will refer to nominal prescribed values.

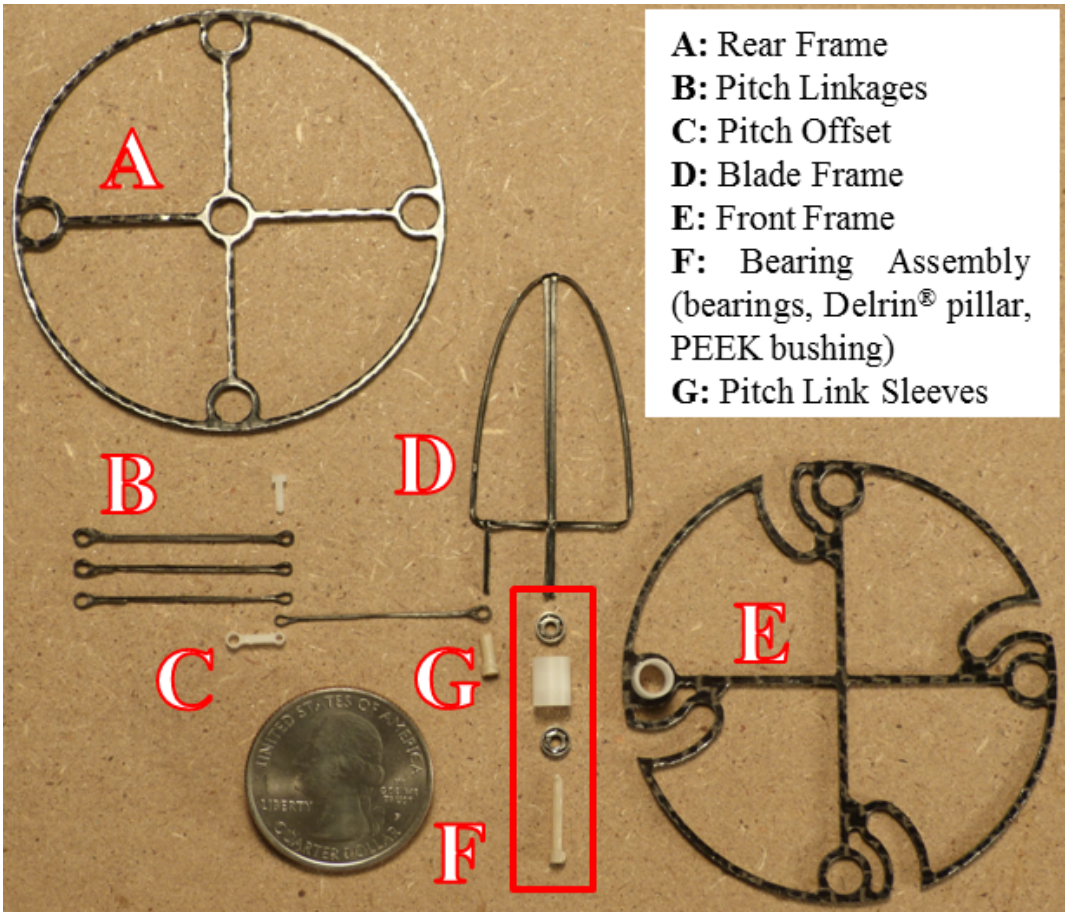

Figure 2.10: Exploded view of the rotor, pitching mechanism, and blades with parts labeled accordingly.

The bushings that interfaced between the blade frames and blade bearings that allowed the blades to freely pitch, were milled from PEEK plastic (for abrasion resistance). The central pitch offset was machined out of Delrin® and was glued onto the shaft with a plastic-bonding cyanoacrylate adhesive. After fabrication, the pitch link sleeves were fastened to the ends of the blade frames, creating a hinge between the blades and pitch links that allowed free and smooth rotation of the pitching mechanism. The fully assembled cyclorotor weighed 2.5 (half of which was the steel bearings) grams and is shown in Fig. 2.11.

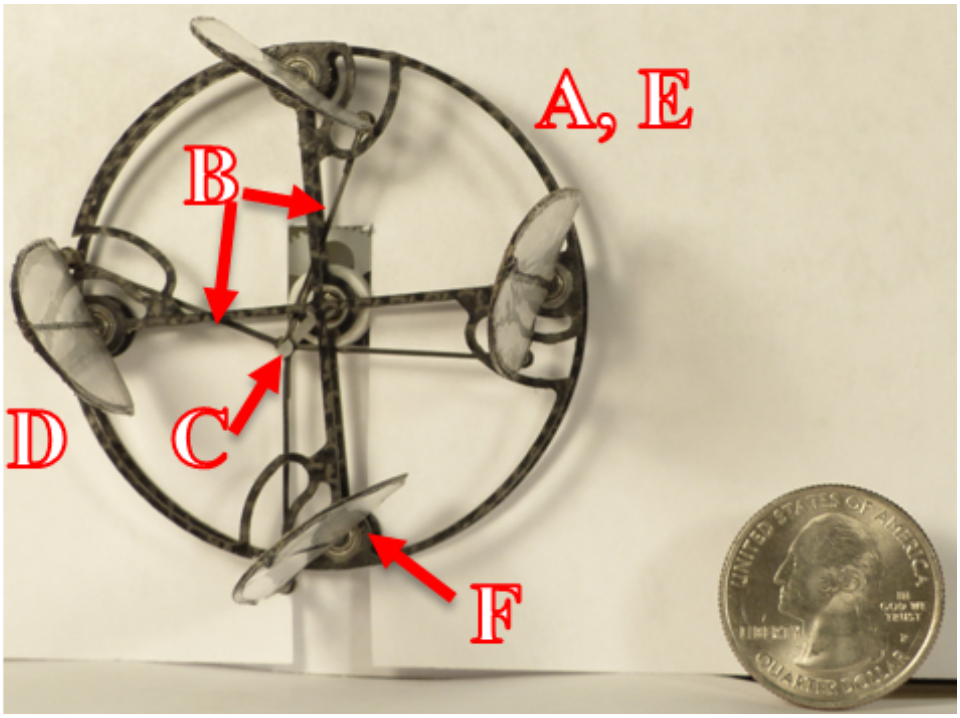

Figure 2.11: Fully assembled rotor for the twin micro-cyclocopter.

Through operation and data collection, several common points of failure were successively identified and rectified to improve cyclorotor reliability and consistency. Perhaps the improvement that increased reliability the most was the addition of protective fins onto the Front Frames[E] to shield the leading edge of the blades at large pitch angles (Fig. 2.12). Without this structure the blade's leading edge was the outermost radial point of the cyclorotor meaning that if the vehicle

collided with anything or flipped-over, the delicate blades were absorbing the brunt of the impact. This caused the blades to break and had to be changed often. Adding material to the front frame so that it extended past the arc swept by the leading edge greatly reduced the frequency of blade failures. After the blades were no longer the primary failure point it was noted that the Rear Frames[A] were the next most common element to break while the Front Frames almost never failed. Using fillets at the locations where the majority of breakages occurred strengthened these junctures and alleviated this issue in all but the most violent of crashes. This small amount of material might seem trivial, but it was initially decided to pare down the frames as much as possible to reduce weight in order to meet the targeted limit.

The third most noteworthy change was a redesign of the Pitch Link Sleeves[G]. Occasionally, a pitch linkage would slide up or down too far and get caught in the front frame or on the Pitch Offset[C] during rotation and break. Instead of a smooth cylinder, a notch was machined into the sleeve to ensure a limited range of motion in either direction (Fig. 2.12). To install the linkage, the tail of the loop was separated from the main length, wrapped into the notch, and then re-glued. In conjunction, the Delrin® pillars[F] were re-machined to make the separation between the frames more consistent, addressing the same issue. Weight added by the sum of these improvements was 0.6 grams, making the improved rotor weigh 3.1 grams total.

2.2 Blade Design and Manufacturing

The hallmark of the micro-cyclorotor was the cantilevered blades. The blade design was biologically inspired, utilizing a symmetrically pitched, flat-plate airfoil. This design was chosen because of the low operating Reynolds number of approximately 11,000 and because constructing an airfoil at these scales was too impractical to implement. For the blade geometry, a semi-elliptical planform was selected because it is known that this shape improves aerodynamic efficiency. Manufacturing these blades proved to be one of the most difficult tasks. Initially, blade frames were machined out of 1/32" carbon fiber laminate and Mylar was glued on either side. However, blades created through this method proved to be too flexible. Solving this deficiency required devising a specialized fabrication technique that ensured consistency and reproducibility in creating strong,

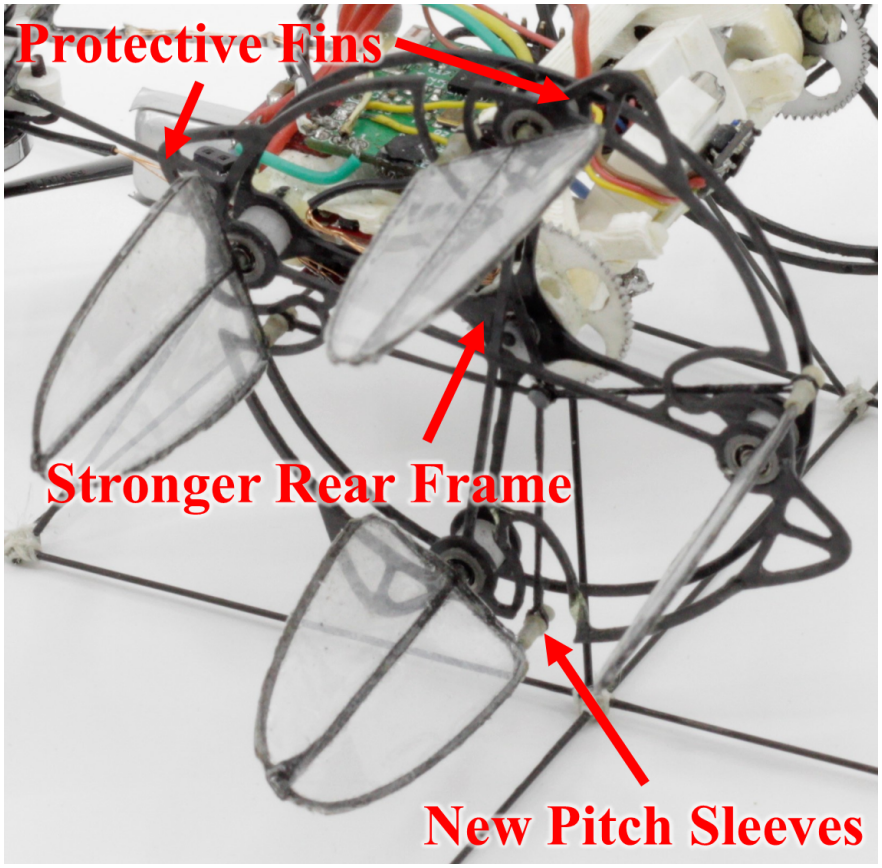

Figure 2.12: Micro-Cyclorotor with several improvements labeled.

lightweight blades. The method developed to accomplish this was to employ a layup technique using a Teflon™ mold and silicone compress, which resulted in the successful fabrication of stiff, light-weight blades. This was the same process used to manufacture the pitch linkages, and ensured that the unidirectional carbon fiber material would bond sufficiently to the carbon fiber rods used for the pitch axis and pitch link pegs. The Teflon™ material was chosen for the mold because it would not bond with the carbon fiber when heat treated, was heat resistant, and was strong enough to maintain the mold shape under clamping pressure. Figure 2.13 shows the step-by-step process employed to produce blades using this method.

First, a strip of unidirectional carbon fiber was laid into the Teflon™ mold so that it made a complete loop (Fig. 2.13a). Then 0.7 mm diameter carbon fiber rods for the pitch axis and pitch link pegs were laid in their respective slots. The pitching axis of each of the blades was carefully

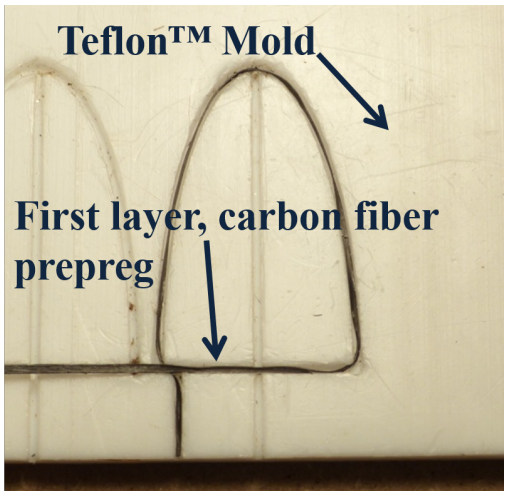

(a) Looping the unidirectional carbon fiber around the blade mold.

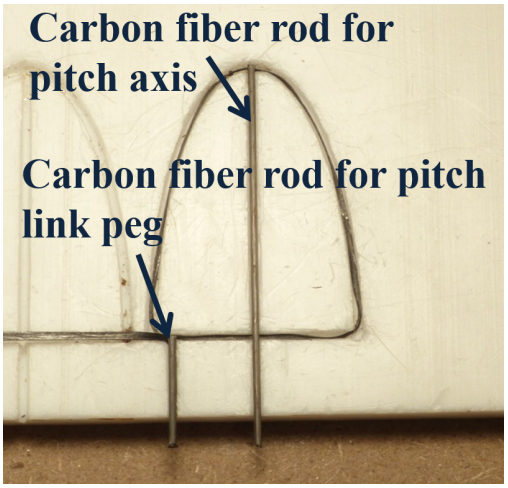

(b) Inserting the carbon fiber rods for the pitch axis and pitch link pegs.

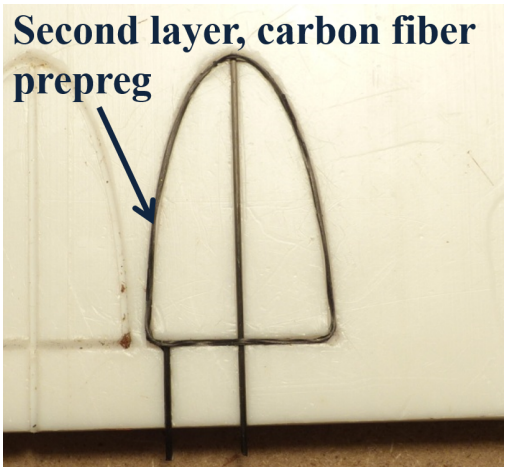

(c) Looping the second layer around the mold.

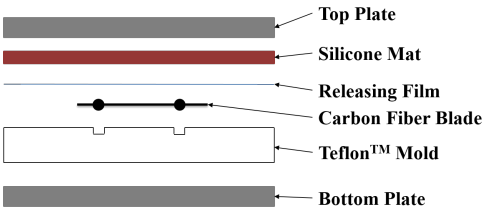

(d) Schematic showing the constitutive layers of the blade layup.

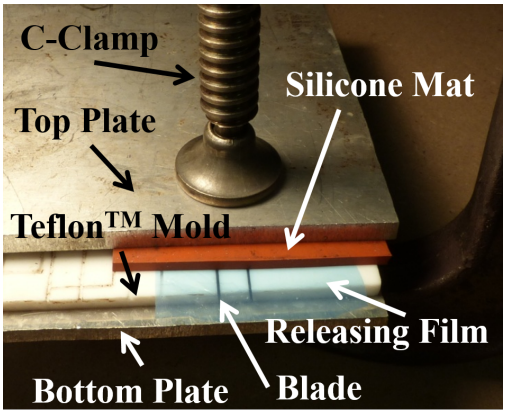

(e) Full layup with all components of mold.

Figure 2.13: Multi-step process for manufacturing cyclorotor blades.

positioned at exactly the chordwise center of gravity location in order to reduce the pitching moment on the blades due to centrifugal loads (Fig. 2.13b). After that, another complete loop around the mold was made with the unidirectional strip so that the rods were sandwiched between layers of it (Fig. 2.13c). This was then stacked, as shown in Fig. 2.13d, and clamped tightly together. The aluminum plates evenly applied the clamping pressure. The flexible, heat-resistant silicone sheet transferred the pressure to the carbon fiber and pushed it into the mold without developing damaging pressure points. The anti-stick/releasing film prevented the carbon fiber from bonding with the silicone. When the full mold layup was completed (Fig. 2.13e), it was cured at 350° F for 135 minutes. After the curing was finished and the cured epoxy and frame had cooled to room temperature, a 3 micrometer thick Mylar sheet was added to both sides of the now complete frame using a spray-on contact cement, effectively creating a closed surface within the frame shape. After trimming the excess, a heat gun was used to stretch out the Mylar thereby removing any imperfections. The resulting blades weighed 0.1 grams and were produced 4 at a time, but the quality, strength, and weight were consistent and therefore this method was used for manufacturing all blades. The one shown in the figure had a maximum chord of about 0.8 inches and a span of 1.3 inches.

2.3 Rotor Performance

2.3.1 Setup for Performance Measurements

In order to maximize the thrust and the aerodynamic efficiency of the rotor design, a series of systematic experiments were conducted to compare the performance of various rotor configurations. The goal of these studies was to obtain the blade size, pitch amplitude, number of blades, and blade aspect ratio that produced the highest thrust at a fixed rotational speed and best thrust/power ratio (or power loading) at the operating thrust. To accurately measure the cyclorotor performance (vertical force, side force, and mechanical power), a 3-component force balance was constructed and calibrated. This force balance was then used to measure the small forces produced by the 3-gram cyclorotors developed for the 30-gram twin micro-cyclocopter. The complete force balance is shown in Fig. 2.14, with key components labeled. As can be seen, the balance was composed

of several Transducer Techniques GSO-100 100-gram load cells that measured the two orthogonal components of thrust (T_X and T_Z) with high resolution ($\pm$0.01 N), and a Transducer Techniques RTS-5 5 in-oz reaction torque sensor that measured the torque generated by the rotor. In addition, a Hall-effect switch was used to measure the rotor RPM in real time. Mechanical power was calculated from the torque and rotational speed measurements.

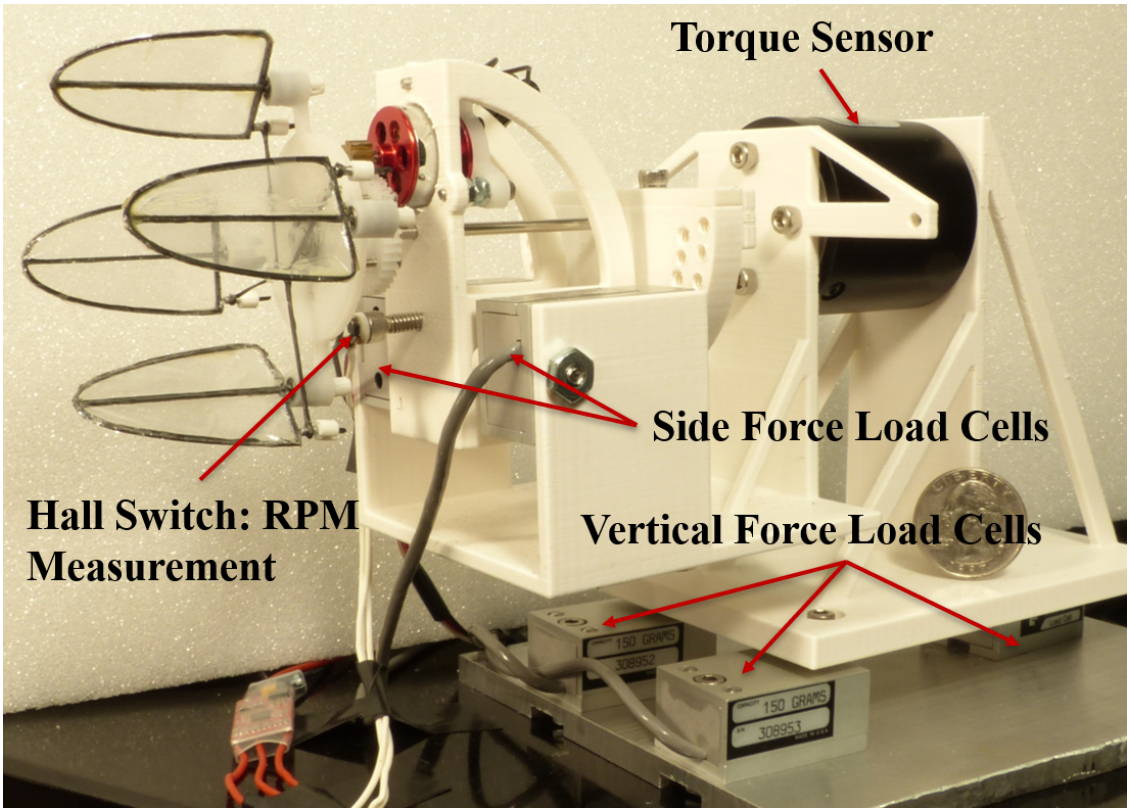

Figure 2.14: Custom built 3-component force balance for the micro-scale cyclorotor[34].

For the parametric studies, the rotor frames and end plates were replaced by a single end plate machined out of Delrin® as opposed to carbon fiber in order to improve modularity in the design. Since the total aerodynamic power measurements included the induced and profile power of the blades and also the parasitic power of the end plate and linkages, tare tests were conducted with just the end plate (no blades) to measure the parasitic power, which was around 15% of the total

power. The parasitic power was subtracted from the total power to obtain pure blade power, which is what is presented in the paper. The results from the experimental parametric studies using the 3-component balance are presented in the subsequent sections.

2.3.2 Effect of Blade Size

The first step was to analyze the effect of blade size on rotor performance. The goal of comparing these different blade sizes was to explore which size would provide the maximum thrust for the lowest weight penalty. To this end, a set of three blades with identical planform, but scaled to different sizes, was built and tested. These blades were called Wing 1, Wing 2, and Wing 3, and are shown in Fig. 2.15. Table 2.1 gives the relevant parameters of these wings. After testing, it was proven that Wing 3 was unable to withstand the inertial loads because of its weight and it suffered from large deflections at the required RPM; therefore, limited data was collected at low rotational speeds. Wing 1, on the other hand, was lightweight enough to rotate at 4000 RPM, but was too small to generate sufficient thrust. Wing 2, however, was able to produce the necessary thrust at the targeted RPM, and was subsequently chosen as the baseline design. Fig. 2.16 plots the variation in thrust with rotational speed for Wing 1 and Wing 2, demonstrating that the larger wing can produce the required thrust at a reasonable rotational speed. Aside from the aspect ratio tests, the rest of the studies were conducted using Wing 2 while changing other rotor parameters.

Table 2.1: Dimensions for Different Wing Sizes

	Weight g	Root Chord mm	Span mm	Area mm^2
Wing 1 (small)	0.12	17.3	27.9	378.9
Wing 2 (medium)	0.14	20.4	33.0	529.3
Wing 3 (large)	0.22	23.5	38.1	704.6

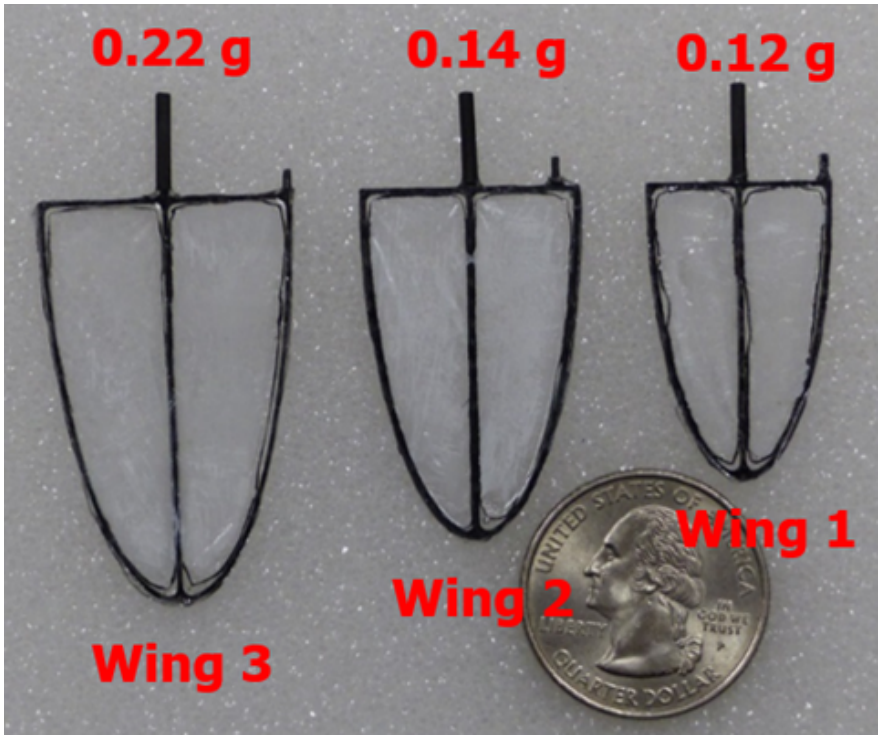

Figure 2.15: Three different blades tested.

2.3.3 Effect of Pitch Amplitude and Number of Blades

A set of measurements was taken for 2-, 3-, 4-, and 6-bladed cyclorotors at different pitch amplitudes. The thrust produced by 2-, 3-, 4- and 6-bladed cyclorotors with pitch amplitudes of $\pm 35°$, $\pm 40°$, $\pm 45°$, and $\pm 50°$ is presented in Figures 2.17 to 2.20, respectively. Measurements were performed for all of the pitching kinematics shown in Table 2.2. L_1 and L_4 are kept constant for all experiments. Therefore, by changing L_2 and L_4 in conjunction, the blade pitching amplitude could be varied while keeping the blade kinematics symmetric between upper and lower halves. It can be seen from these results that for all pitch amplitudes, thrust increased with the number of blades, which is not surprising by itself, but the specific variation requires further explanation.

To understand the effect of number of blades further it was important to isolate the effect of blade area and investigate how the thrust produced per unit area of the blade varied with number of blades. This can be shown more clearly by examining the non-dimensional thrust coefficient, C_T, normalized by rotor solidity, σ, for a specific rotational speed. C_T and σ are defined below:

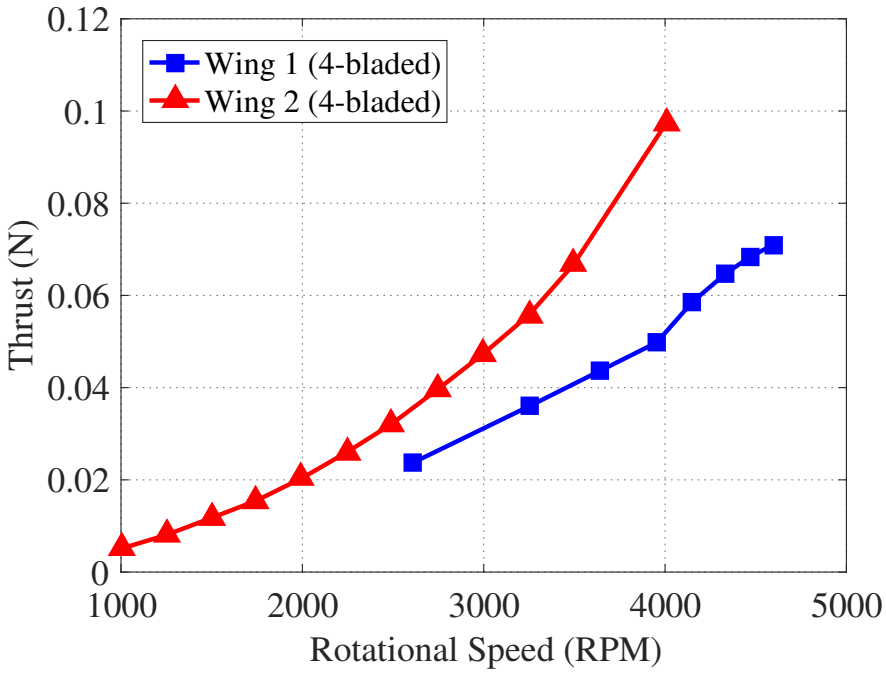

Figure 2.16: Thrust vs. rpm for two different wing sizes on a 4-bladed cyclorotor.

Table 2.2: L_2 and L_3 Lengths for Specified Kinematics

Pitch Amplitude	L_2 mm	L_3 mm
$\pm 35°$	4.73	26.28
$\pm 40°$	5.31	26.18
$\pm 45°$	5.84	26.06
$\pm 50°$	6.32	25.95

$$C_T = \frac{T}{\rho A_{dia}(\Omega R)^2} \tag{2.1}$$

$$\sigma = \frac{N_b c}{2\pi R} \tag{2.2}$$

where T is thrust, ρ is the density of air, A_{dia} is the projected area $diameter \times span$ of the cyclorotor, Ω is the rotational speed of the rotor, R is rotor radius, N_b is the number of blades and

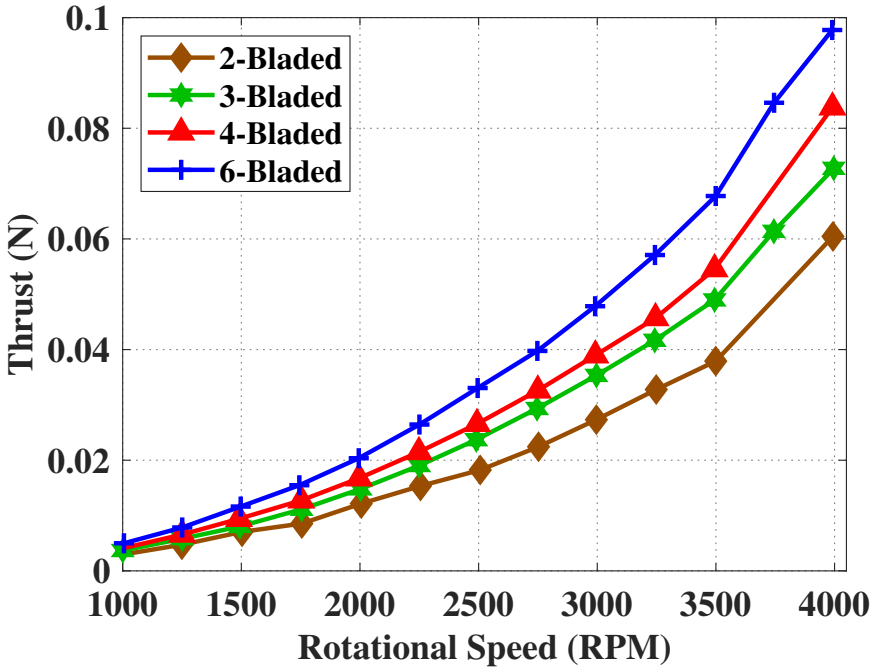

Figure 2.17: Total thrust versus rpm for multiple rotor configurations at 35° pitch amplitude.

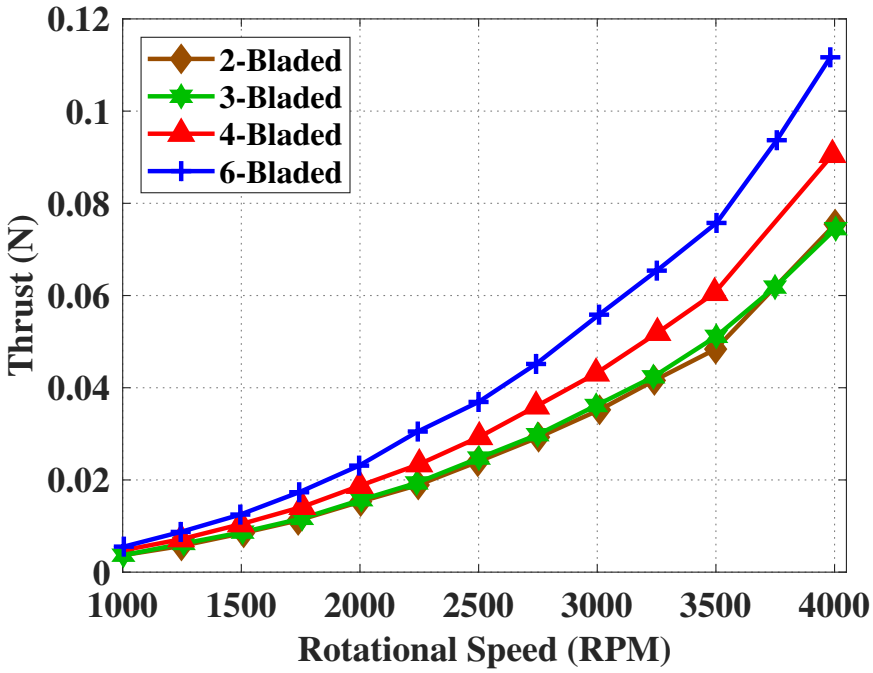

Figure 2.18: Total thrust versus rpm for multiple rotor configurations at 40° pitch amplitude.

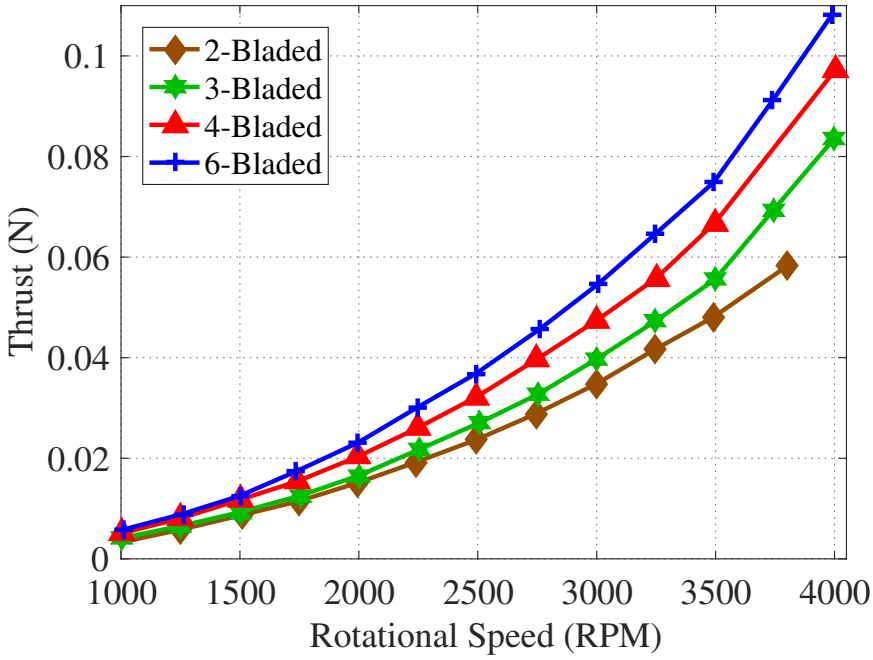

Figure 2.19: Total thrust versus rpm for multiple rotor configurations at 45° pitch amplitude.

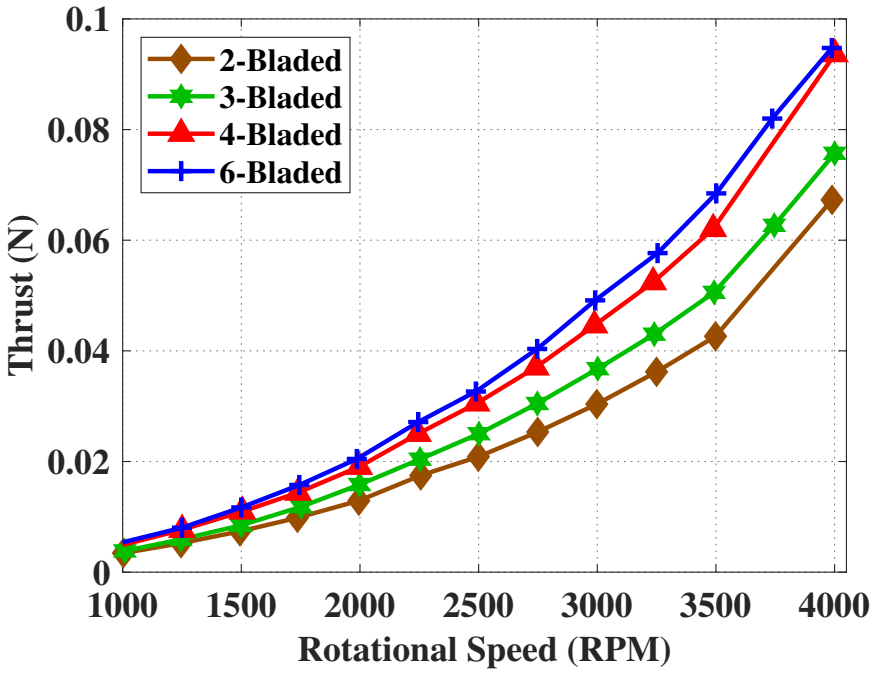

Figure 2.20: Total thrust versus rpm for multiple rotor configurations at 50° pitch amplitude.

c is average blade chord. Figure 2.21 plots the variation of thrust per unit blade area C_T/σ as a function of blade pitch amplitude for 2-, 3-, 4-, and 6-bladed cyclorotors at a rotation speed of 3500 RPM. An interesting observation from this graph is that even though the total thrust increased with the number of blades, the thrust per unit blade area decreased with increasing number of blades. From Fig. 2.21 it can be seen that the 2-bladed cyclorotor had the highest C_T/σ followed by 3-, 4- and 6-bladed rotors in that order. The reason for this is the fact that as the number of blades was increased for a fixed pitch amplitude and rotational speed, the absolute thrust increased, which increased the inflow velocity. For a fixed pitch amplitude, the higher the inflow velocity, the lower the angle of attack. Therefore, the blades on a rotor with higher number of blades produced more inflow (due to higher thrust), which reduced the blade angle of attack leading to lower blade lift. A secondary reason for the reduction in blade lift with higher number of blades could be the interference between the blades.

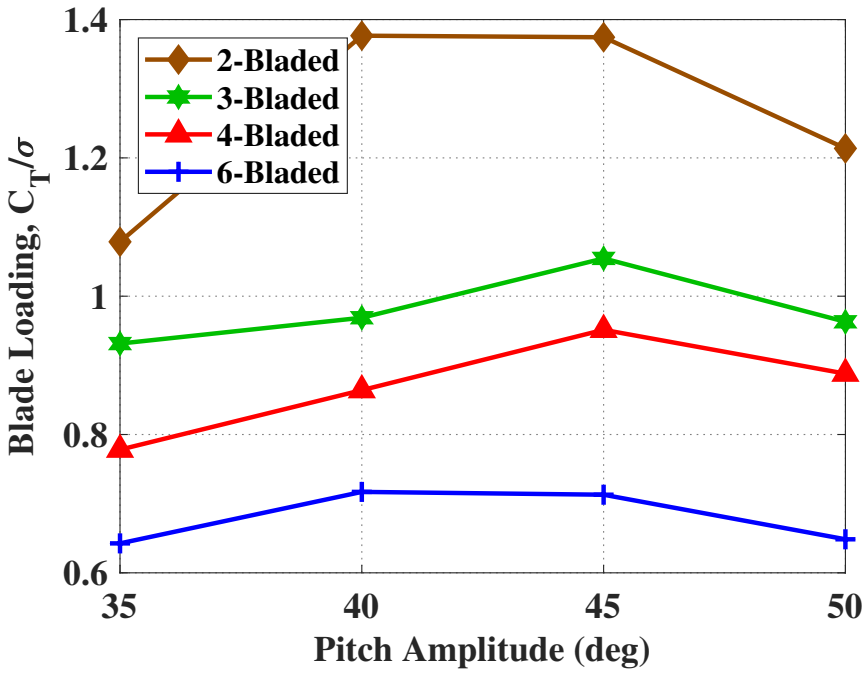

Figure 2.21: Blade loading versus pitch amplitude for multiple rotor configurations.

Figure 2.21 also shows the effect of pitch amplitude on thrust. For 3- and 4-bladed cyclorotors, it is interesting to see that the thrust increased with pitch amplitude all the way up to 45° and dropped when it was increased to 50°. For the 2- and 6-bladed cases, the thrust increased till 40°, and then stayed constant from 40° to 45° and further dropped when increased to 50°. These results are consistent with the previous findings that have found large pitch amplitudes (40°–45°) produce the greatest amount of thrust for cyclorotors [21]. The reason for the blades not stalling at such high pitch amplitudes was because of dynamic stall (or the leading edge vortex) and flow curvature effects inducing dynamic camber on the blades [107]. These phenomena will be further investigated using PIV based flowfield measurements in a subsequent chapter.

When considering performance, it is also important to consider rotor efficiency, or power loading (thrust per unit power). For a rotor, the power loading has to be compared at the same disk loading so that the ideal induced power is the same. Disk loading is thrust divided by actuator area and for the cyclorotor the rectangular projected area, A_{dia}, was chosen as the actuator area. The power loading for cyclorotors using different numbers of blades at different pitch amplitudes are compared in Figures 2.22 to 2.25.

Figure 2.22 compares the power loading for a cyclorotor with different numbers of blades for a pitch amplitude of 35°. It can be seen that the power loading increased dramatically from 2 to 3 blades; however, it dropped slightly for 4- and 6-bladed rotors. For the 40° pitch amplitude case (Fig. 2.23), again there was a dramatic increase in power loading from 2- to 3-bladed rotor, but it stayed constant from 3 all the way up to 6 blades. Figure 2.24 shows that, for the 45° amplitude, power loading increased substantially from 2- to 3- to 4-blades, but then decreased for the 6-bladed rotor. The 50° pitch amplitude shown in Fig. 2.25 shows a clear difference in power loading with varying number of blades. 2-bladed has the lowest power loading followed by 3-bladed, 4-bladed, and 6-bladed with the highest power loading. A possible reason for the increased efficiency with number of blades could be because of the lower operating RPM; the decrease in profile power due to the reduction in RPM may have outweighed the increase in profile power because of higher solidity.

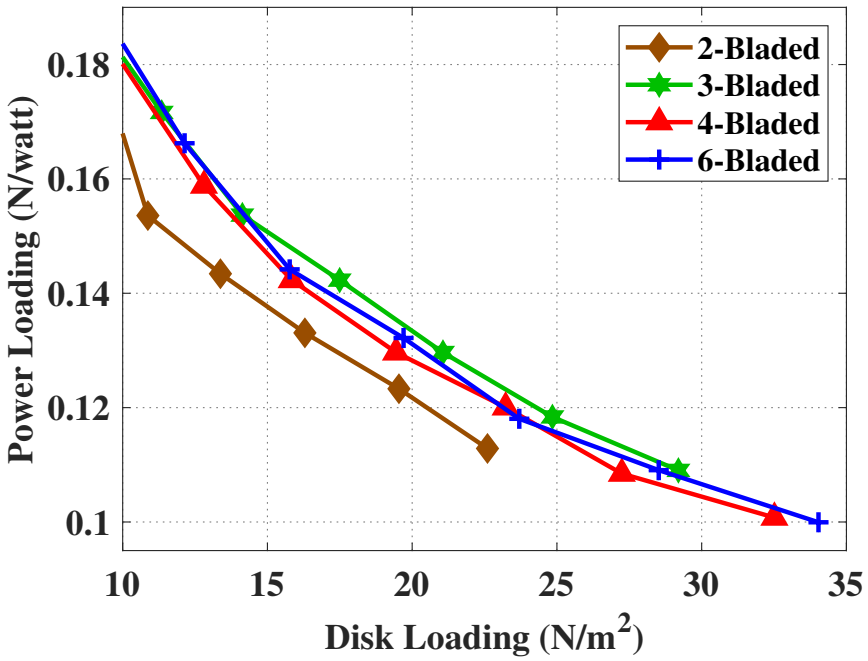

Figure 2.22: Power loading versus disk loading for multiple rotor configurations at 35° pitch amplitude.

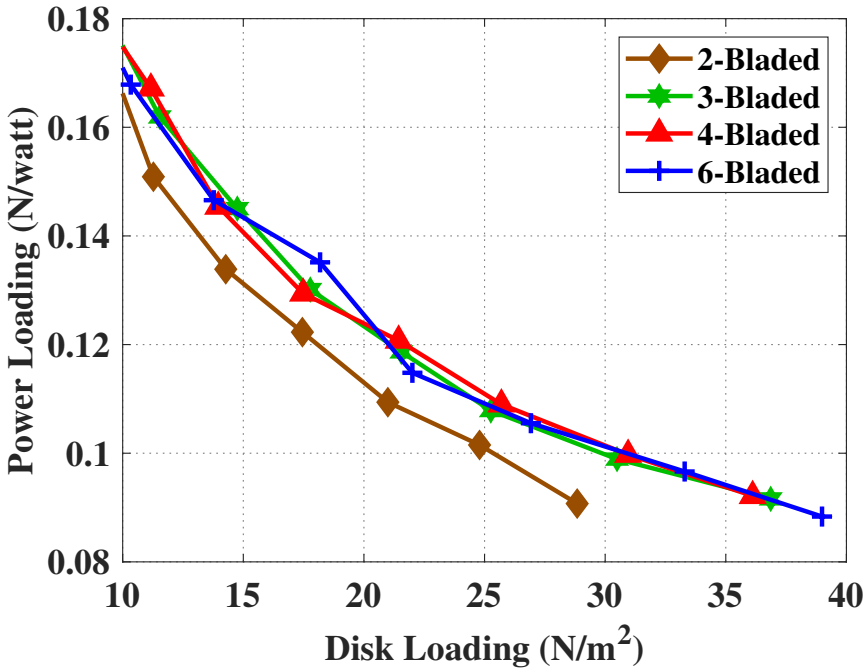

Figure 2.23: Power loading versus disk loading for multiple rotor configurations at 40° pitch amplitude.

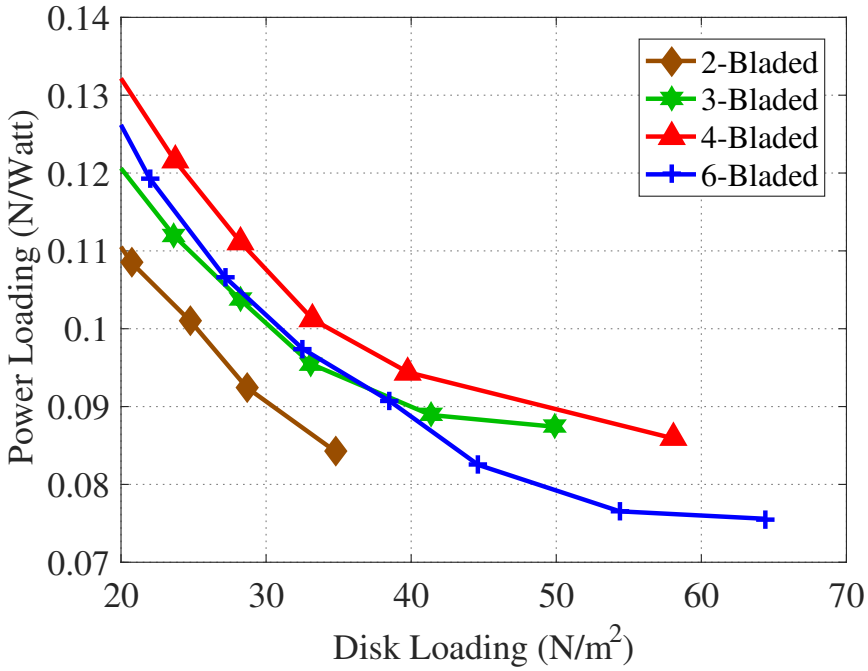

Figure 2.24: Power loading versus disk loading for multiple rotor configurations at 45° pitch amplitude.

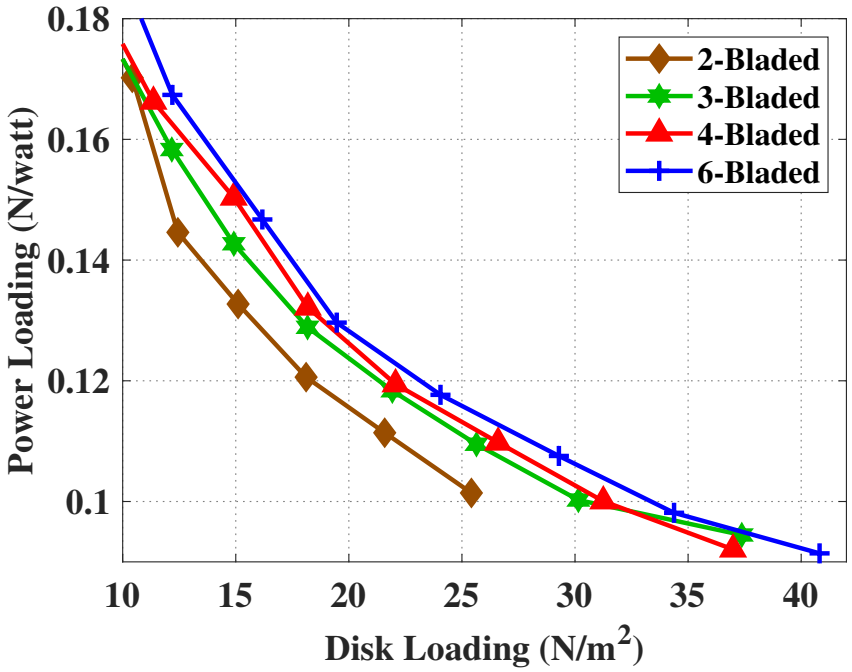

Figure 2.25: Power loading versus disk loading for multiple rotor configurations at 50° pitch amplitude.

To understand the effect of blade pitch amplitude on power loading for a fixed number of blades, Figs. 2.26 and 2.27 compare the thrust and power loading for a 4-bladed cyclorotor operating at different pitch amplitudes. Lift was highest at 45° amplitude which is consistent with previous studies that have found large pitch amplitudes (40°–45°) produce the greatest amount of thrust for 4-bladed cyclorotors[73]. Efficiency was lowest at 35° then increased at 40° and 45° followed by a slight decrease to the 50°. Once again, this reinforced the observation that a cyclorotor performs best at high pitch amplitudes, especially at MAV-scale Reynolds numbers.

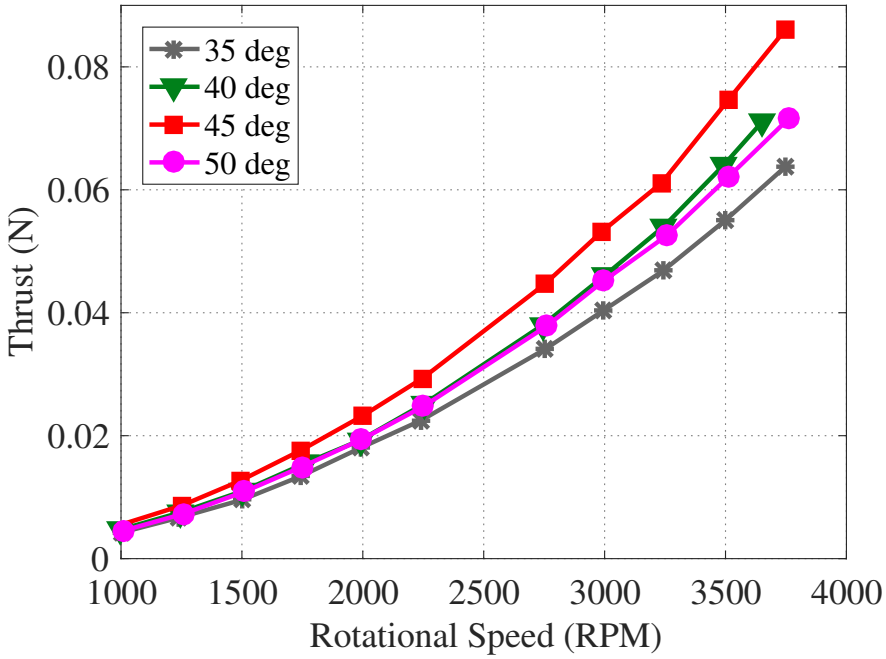

Figure 2.26: Thrust vs. RPM at different blade pitch amplitudes for a 4-bladed cyclorotor using Wing 2.

2.3.4 Effect of Blade Aspect Ratio

For the aspect ratio study, flat plate blades with elliptical planforms and 3 different aspect ratios, $(blade\ length)^2/(blade\ area)$, were tested, as shown in Fig. 2.28. The three aspect ratios were 1.181, 1.618 and 2.196. These aspect ratios were obtained by varying the semi-major and minor

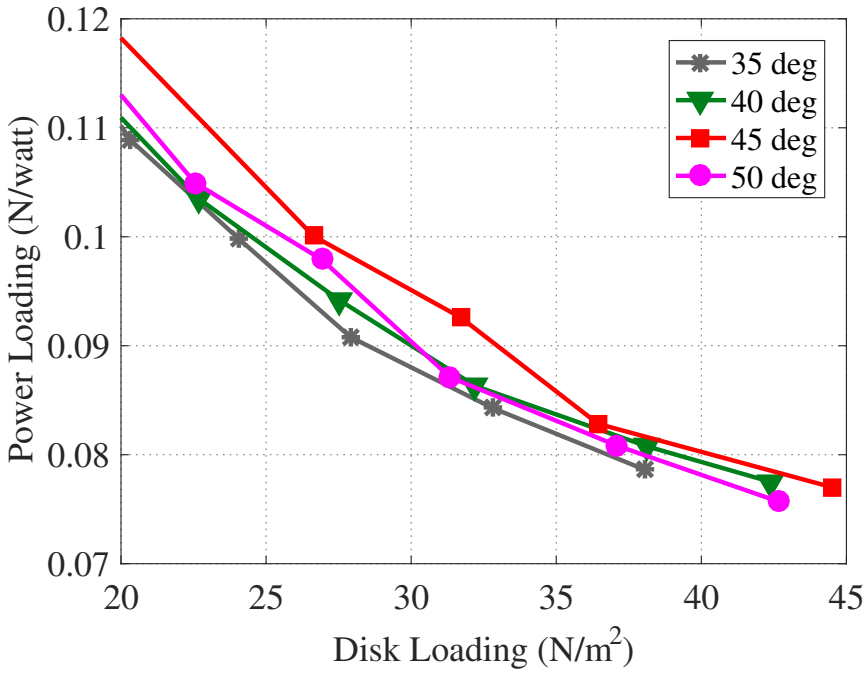

Figure 2.27: Power loading versus disk loading for a 4-bladed rotor with different pitch amplitudes.

axes of the ellipse such that the blade area stayed the same. The baseline cyclorotor blade had an aspect ratio of 1.618 and span of 33 mm and this was the one used in the number of blades and pitch amplitude studies mentioned in the previous sections. The blades with aspect ratios of 2.196 and 1.181 will be referred to as the high and low aspect ratio blades, respectively. The three sets of blades were tested in a 2-bladed configuration with a symmetric pitching of 45°. Figure 2.29 shows the variation of thrust with rotational speed for cyclorotors with the three sets of blades. As seen from the figure, the blades with the lowest aspect ratio (1.181) produced the lowest thrust while the medium (1.618) and high aspect ratio (2.196) blades produced almost equivalent thrust. This is an interesting result considering all three blades had the same planform area. The power loading for the cyclorotors using the three blades is shown in Fig. 2.30, which shows a clear difference between the three aspect ratio blades. The low aspect ratio (1.181) produced the least power loading followed by the highest aspect ratio (2.196) and the baseline blades with the medium aspect ratio (1.618) having produced the highest power loading. This is slightly counter intuitive

from a fixed-wing aerodynamics perspective because one would expect the increased aspect ratio to have the highest efficiency. The reason for this would depend on the chord/radius of the blade [107] and also the complex unsteady 3D aerodynamics on low aspect ratio cyclorotor blades which are not fully understood at this point.

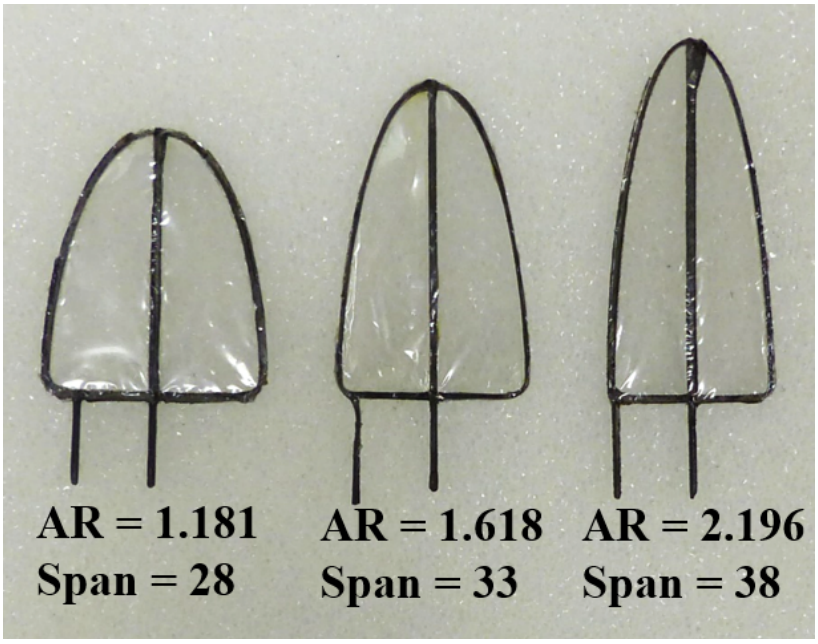

Figure 2.28: Blades of constant area and varying aspect ratio. Span dimensions are in mm.

2.4 Final Cyclorotor Design

Based on these results, a blade pitch amplitude of 45° and a 4-bladed rotor configuration were chosen as the final design. The 2- and 3-bladed cyclorotors were unable to produce the required thrust at the target RPM regardless of pitch amplitude. The 6-bladed rotor produced the most thrust; however, the extra blades added weight to the rotor and, as seen from Fig. 2.24, the 4-bladed one was more efficient for an equivalent level of thrust. The chosen rotor configuration outperformed all of the others that were tested and it produced the required thrust of 10 grams (0.1 N) at the target operating RPM of about 4000, expending 1.13 watts of mechanical power, as shown in Figs. 2.31 and 2.32.

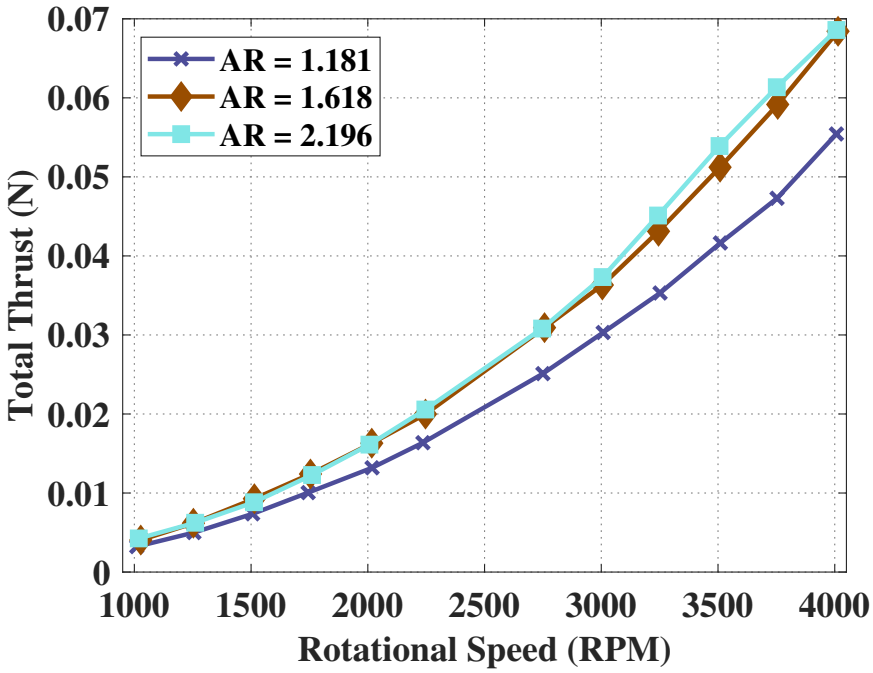

Figure 2.29: Thrust vs. RPM for varying aspect ratio for 45° pitch amplitude.

With blade size, geometry, and number of blades determined, the final analysis conducted on the blades and rotor setup was an evaluation of blade deflection, possibly from either a weak root boundary condition or bending along the span of the blade. The method used to qualitatively evaluate deflection was an experiment conducted using a strobe light (Fig. 2.33), which was flashed in synchronization with the rotational frequency of the rotor. This gave the appearance that the rotor was stopped, and when the amount of deflection experienced by the rotor was qualitatively compared to that of the stationary rotor, there was minimal deflection observed at the operating frequency of 4000 RPM. Based upon these results, it was concluded that bending deflections did not substantially reduce rotor efficiency.

2.5 Concluding Remarks

This chapter focused on the parametric studies performed on a micro-scale cyclorotor. Because of the small size (rotor radius of 1 inch), the cyclorotor investigated operated at ultralow Reynolds numbers (Re 11,000) and also utilized a blade design completely different from previous studies.

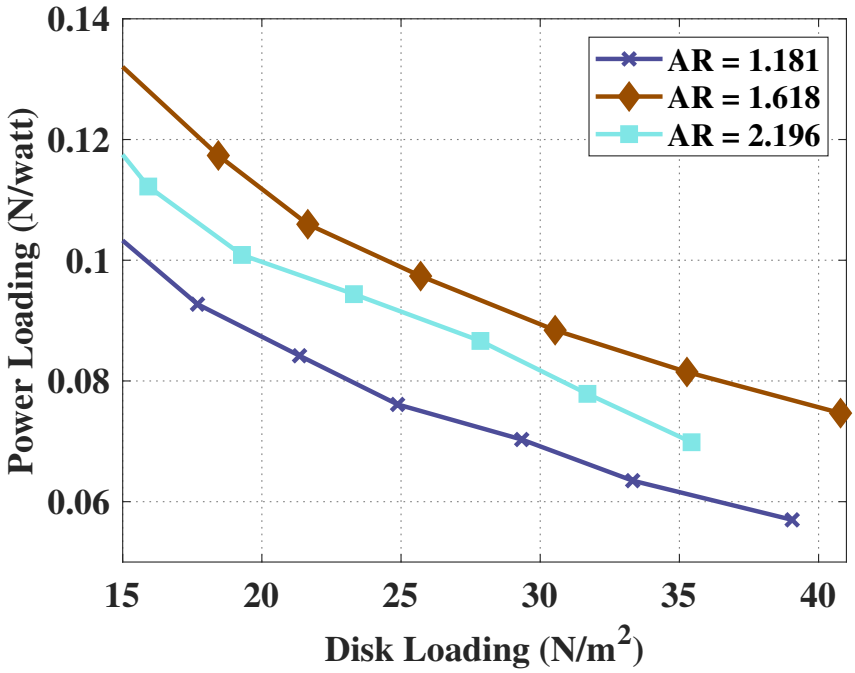

Figure 2.30: Effect of aspect ratio on power loading.

The micro-scale rotor incorporated a low aspect ratio cantilevered blade with flat plate airfoil and elliptical blade planform, which meant that 3-dimensional effects would be more prominent. A highly sensitive, miniature 3-component balance was developed to measure the vertical and horizontal thrust, torque, and rpm with varying blade size, number of blades, pitch amplitude, and blade aspect ratio. The final rotor configuration chosen used 4 elliptical blades with a root c/R ratio of 0.8 and a low aspect ratio at $\pm 45°$ pitching. The original cyclorotor by itself weighed 2.5 grams and was capable of producing 10 grams of thrust at 4000 RPM giving it a T/W ratio of 4, higher than any previous cyclorotor. Some conclusions that can be drawn from these results are as follows:

- Even though the total cyclorotor thrust increased with increasing number of blades, the thrust per unit blade area (C_T/σ) decreased with increasing number of blades. The reason for this is the increased inflow due to higher thrust with larger number of blades leading to a lower effective angle of attack.

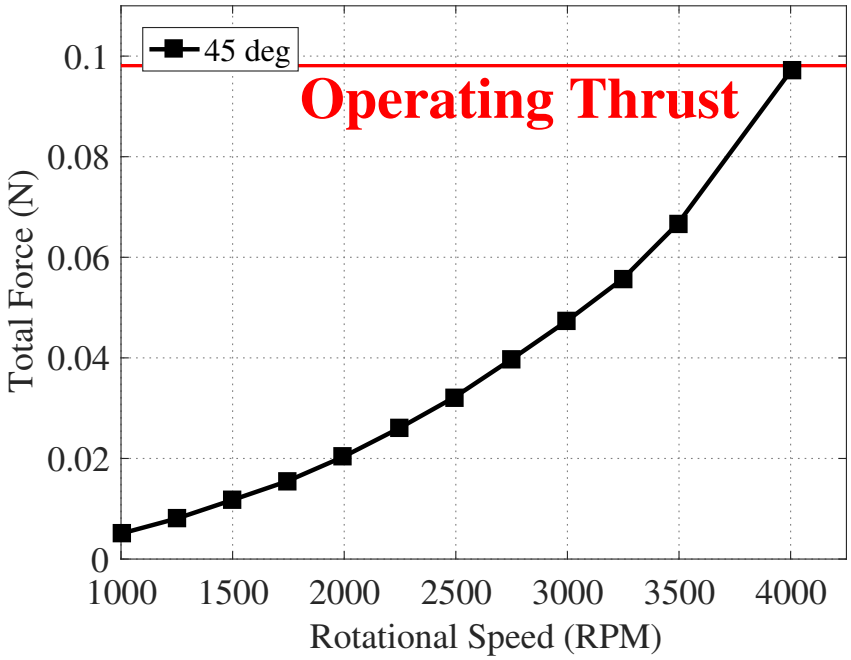

Figure 2.31: Thrust produced by final rotor design.

- Consistent with the previous findings at higher Reynolds numbers, large pitch amplitudes (40°–45°) produced the greatest amount of thrust for cyclorotors. The reason for the blades not stalling at such high pitch amplitudes could be because of the leading edge vortices (dynamic stall) similar to what is seen on flapping wings.

- The highest power loading was achieved with higher number of blades (4–6 blades), high pitch amplitude (40°–45°), moderate aspect ratios, and high chord-by-radius ratios (=0.8).

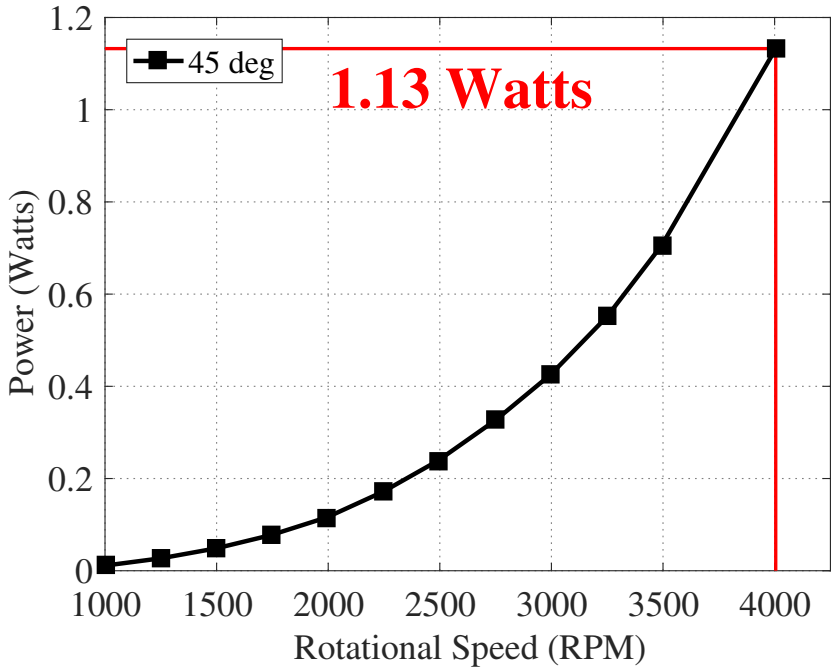

Figure 2.32: Mechanical power required by final rotor design with operating power labeled.

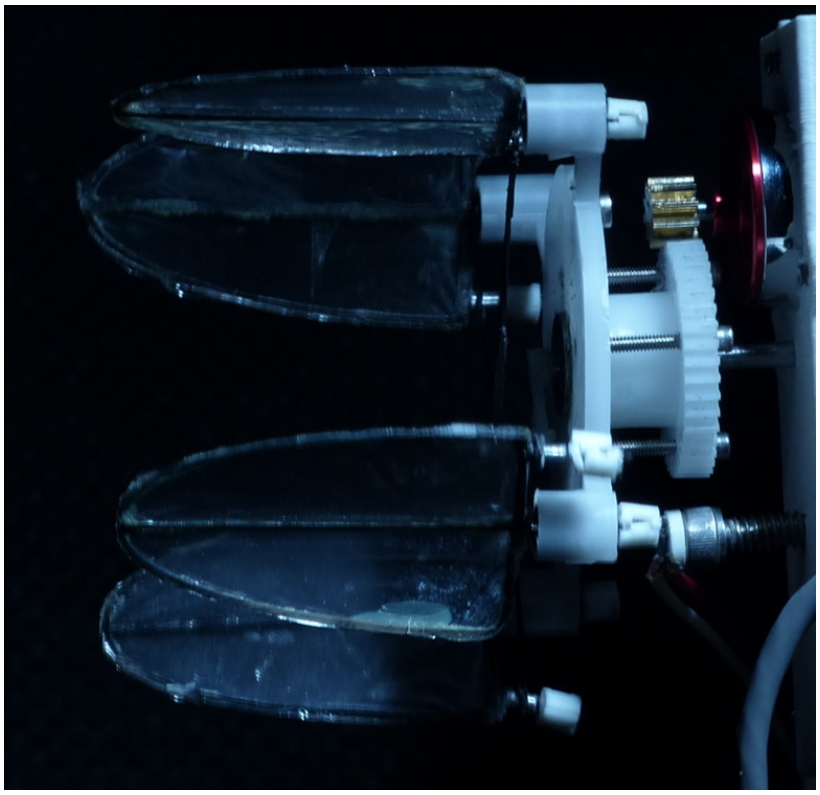

Figure 2.33: Strobe light analysis of blades during operation at 4000 RPM showing minimal deflection.

3. Cyclorotor Flowfield Measurements

After the cyclorotor design was finalized for use on the flying test vehicles and its performance systematically characterized, flowfield measurements were taken inside and around the rotor to better understand the complex flow of this low Reynolds number device. Measuring flowfields involve collecting data on different properties (*i.e.*, velocity, temperature, pressure, *etc.*) and is used for a wide variety of purposes in many fields including turbine engine analysis and aquatic vessel development. Although the literature is limited on flowfield measurements of cyclorotors, they have been indispensable for research efforts by giving definitive insight into cyclorotor aerodynamics. A deeper understanding of the flow structures, vortex development, and wake formation of cyclorotors enabled more accurate modeling and having high-fidelity measurements of a physical system is crucial to validating numerical simulations. Similarly, due to the unique nature of the micro-cyclorotor, greater knowledge of the 3-dimensional flow in and through the rotor was required before the predictive capabilities of computational models for low Reynolds number cyclorotors could be improved. Moreover, data on flow conditions pertaining to the boundary layer formation, vorticity, blade interactions, and inflow distribution was almost entirely lacking in this regime.

This chapter covers work done to take velocity measurements of the flow through the optimized micro-cyclorotor by using a technique called particle image velocimetry (PIV). PIV is a process that uses a laser sheet to illuminate a plane in the fluid medium which has been impregnated with tiny particles to form a suspension (*e.g.*, fog in air or microscopic glass beads in water). In the case of 2D PIV a high resolution camera orthogonal to the plane then quickly takes two pictures with a precise time interval between of the illuminated specks in the laser sheet. The principle is that the particles are small enough and the time interval short enough such that all motion observed between the two images is caused by movement of the medium and not drift of the particles. It is also assumed that the particles are too small to affect the properties of the fluid. Moreover, a minimum particle size is required to generate enough reflected light for camera to capture. A PIV

cross-correlation software is used to calculate the velocity vector of each particle and generate a velocity field.

3.1 Setup for Particle Image Velocimetry Measurements

To obtain the PIV data, the cyclorotor was removed from the 3-component force balance and was fixed to a rigid mount in a room with quiescent air. Only 2 blades were used in the PIV experiments to facilitate data collection and reduce shadows in the laser sheet which, in turn, reduced the number of blade interactions and complexity of the internal flow. Using 4 blades would create large sections inside the rotor where data could not be collected. Nevertheless, other than the removal of blades, the hardware used was identical to that used for the vehicles described in later chapters resulting in an accurate representation of the aerodynamic conditions in hovering flight. The rotor and mount were painted black and a black background was added to avoid laser reflections off the rest of the rig. The PIV setup was a pulsed Nd:YAG laser sheet and a synchronized, 5.5 mega-pixel sCMOS camera. The laser pulses were also synchronized with rotor rotation using the Hall-Effect sensor and a programmable timing unit such that phase-locked measurements could be made at different phasing angles or azimuthal locations of the blade as the rotor rotates. For all PIV measurements, the laser was adjusted so that the sheet was as thin as possible in the area of interest. A thin sheet ensures that only particles in the plane of interest were lit up. Mineral oil fog was used to seed the testing area with sub-micron sized smoke particles that reflected the laser sheet and allowed the camera to capture the light reflected from particles. To mitigate blade shadows, which would create voids in the measurements, a mirror was used to reflect the laser light back to illuminate the shadow regions. Areas where the smoke particles cannot be distinguished from the background were masked out during processing, which can be seen as black in the PIV images. Two images were taken micro seconds apart and the relative movement of the particles from one to the next was used along with a cross-correlation software (LaVision Davis) to calculate the flow velocity vectors. A low F-number (large aperture) was selected for the camera lens to minimize the focal length. This was done so that only the seed particles in the laser sheet were in focus, which reduces extraneous vectors.

Two sets of PIV measurements, (1) chordwise and (2) spanwise, were made in orthogonal directions. In the chordwise direction, flowfield measurements were taken by aligning the laser sheet perpendicular to the blade and rotor axis at the 60% spanwise location for a full rotor revolution (schematic shown in Fig. 3.1). For these measurements, the camera view was normal to the laser sheet, which was along the rotor axis. The goal of the chordwise measurements was to capture the evolution and shedding of leading/trailing vortices on the blade and the inflow/wake inside and around the rotor, which would aid the development of 2D inflow models in the future.

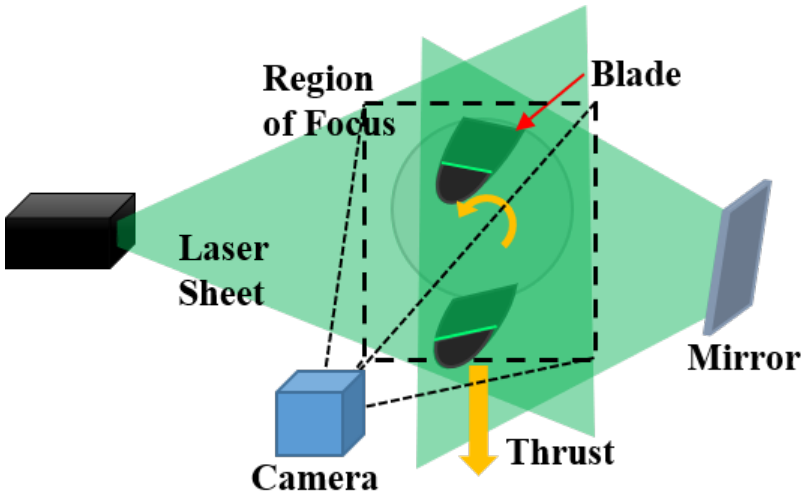

Figure 3.1: Experimental setup for chordwise PIV measurements at fixed blade-span location.

The setup for the spanwise measurements is shown in Fig. 3.2. The laser and camera have been rotated by ninety degrees such that the laser sheet is oriented along the axis of the rotor and bisects the rotor vertically into left and right halves. The goal of the spanwise measurements was to capture the development of blade tip and root vortices and the accompanying 3-dimensional flow features as the rotor rotates.

3.2 PIV Results

All the PIV measurements were conducted on a 2-bladed cyclorotor using medium aspect ratio (AR=1.618) blades at a pitch amplitude of $\pm 45°$. For the chordwise measurements, the setup

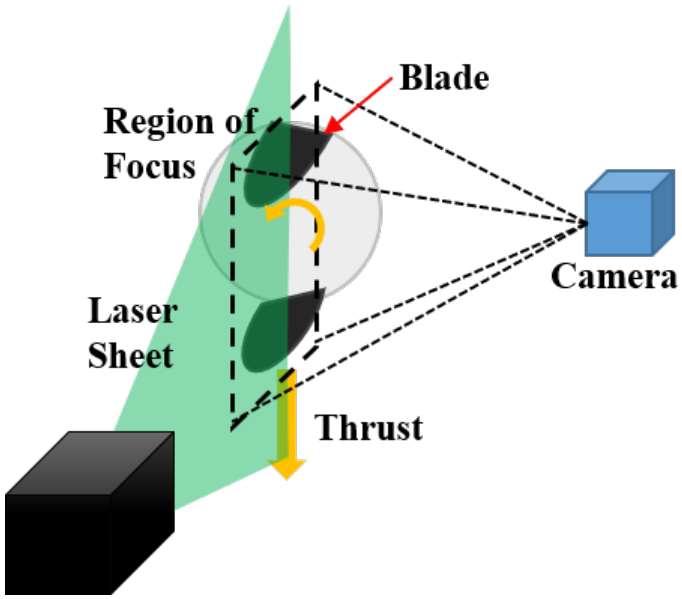

Figure 3.2: Experimental setup for spanwise PIV measurements.

shown in Fig. 3.1 is used to capture flow field features in an interrogation plane normal to the blade span and the axis of rotation and intersects the blades along the chord at a chosen spanwise location. For these experiments, the plane is positioned at the 60% spanwise location. Phase-locked images were captured during a full revolution of the rotor at 19° azimuthal intervals with the rotor operating at 3200 rpm (Re 9000). Taking data throughout the entire revolution was necessary for a thorough understanding of the flow because the blade sees unique conditions at every point. For each of these tests, one hundred image pairs were captured at every azimuthal location (20 azimuthal locations in total), and the calculated velocity field from each of the image pairs was averaged across all 100 image sets, resulting in a clean flowfield calculation. Each pair of images was taken at 20 microseconds between images, which gave the smoke particles enough time to move spatially within camera interrogation frame, but not too much so that correlation was lost between frames. Figures 3.3 and 3.4 show the results from the chordwise measurements. To be concise, only half of the location images are shown, which corresponds then to azimuthal resolution of 19° for half of a revolution, because there is a twice per revolution (2/rev) cycle due to the number of blades. The regions that are masked out (colored in black) are the blades,

pitch-links, and some other areas where background reflection led to spurious vectors.

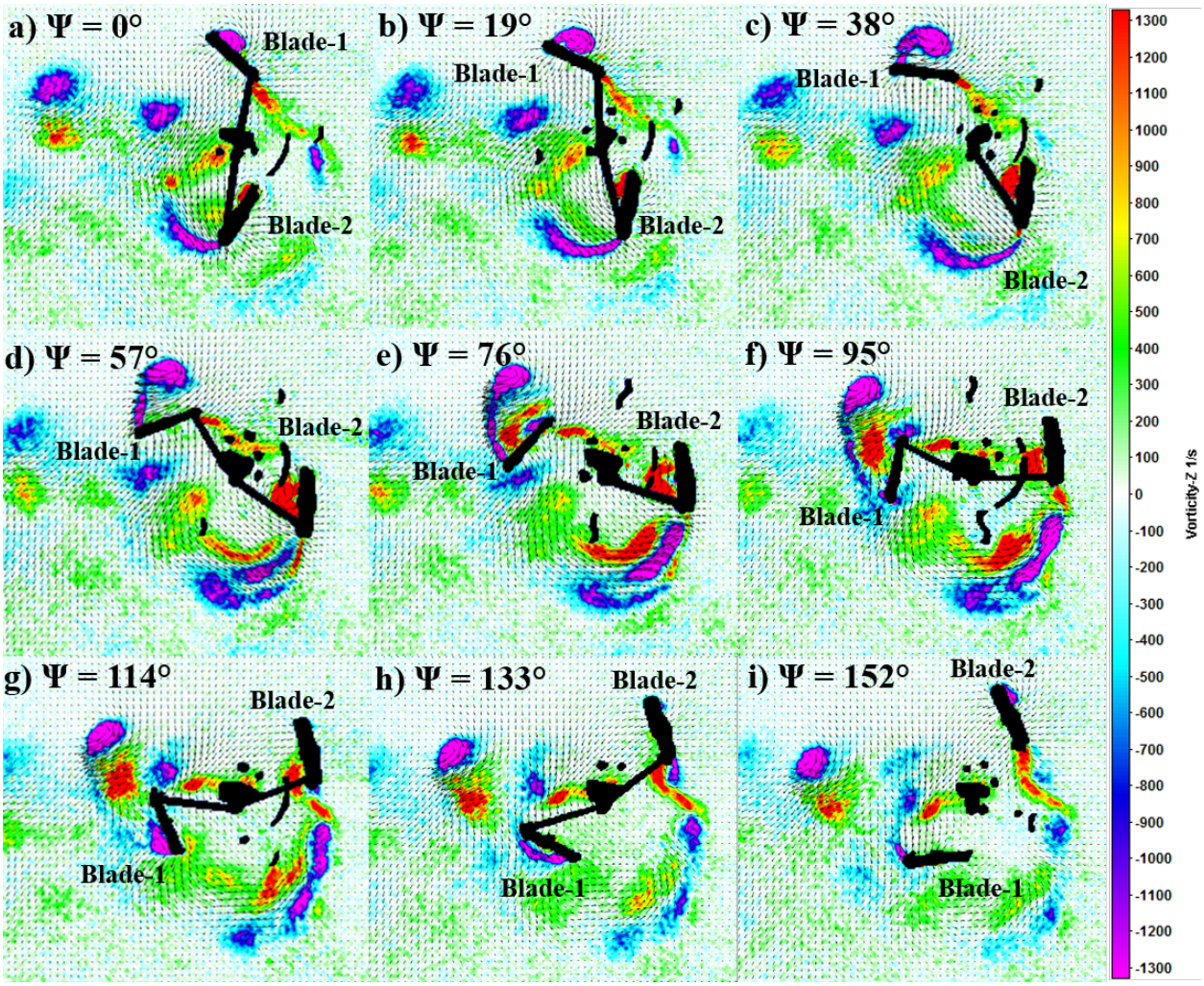

Figure 3.3: Chordwise PIV measurements at 3200 rpm and 60% span for incremental azimuths (Ψ).

For the spanwise measurements, the configuration in Fig. 3.2 was used. Here, the interrogation plane cut the blades lengthwise along the entire span, meaning it was coincident to the axis of rotation, bisecting the rotor vertically into left and right halves. For this case, the images were captured at 20 different wake ages at 9.5° resolution across one-half of a rotor revolution since the rotor has two blades and the second half of the revolution will be a duplicate of the first. Similar to the first data set, the rotor was operated at 3200 rpm, and 100 images pairs were captured at each

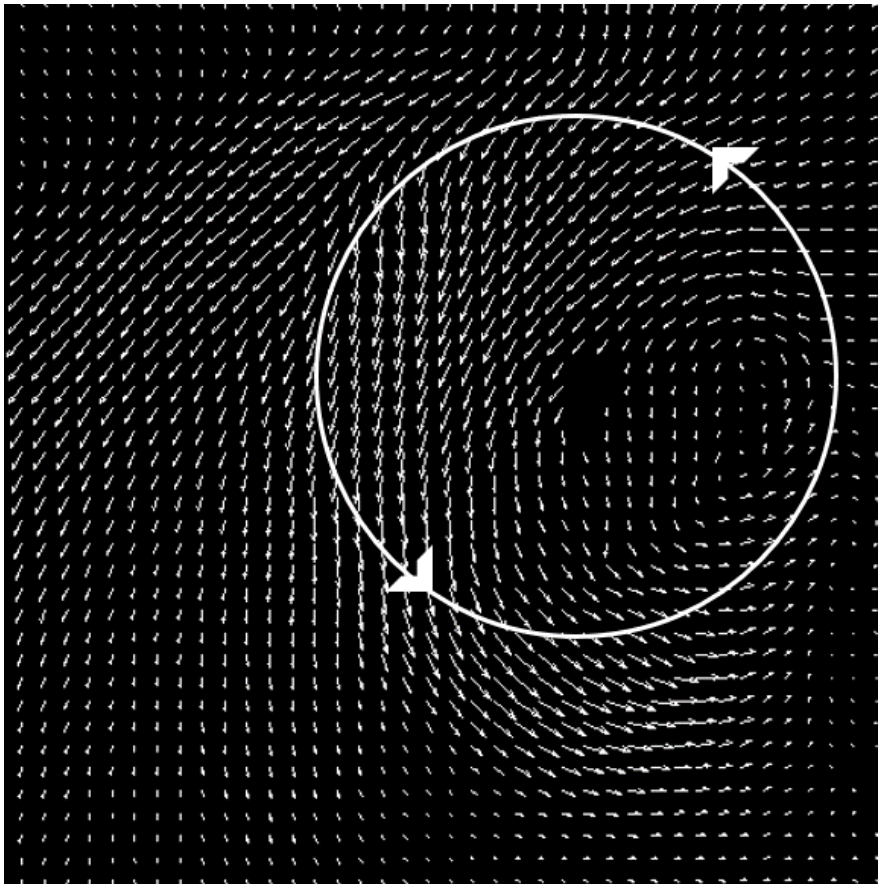

Figure 3.4: Time averaged vertical velocity for chordwise measurements.

phase location. The flowfield results after PIV calculation are shown in Figs. 3.5 and 3.6. For both results, the background contour represents vorticity with purple representing negative or clockwise vorticity, and red representing positive or counter-clockwise vorticity. The black vector arrows show the direction and magnitude of the calculated velocity field. A video generated from the PIV images captured for both spanwise and chordwise measurements are provided in Ref. [108].

3.2.1 Chordwise Flowfield Measurements at 60% Span

For the chordwise PIV measurements shown in Fig. 3.3, strong leading edge vortices (LEVs) and trailing edge wakes can be seen on the blades both at the top (blade-1) and bottom (blade-2) of their circular trajectory (Fig. 3.3a). Figure 3.3a corresponds to 0° phase angle. As seen from the blade at the top (blade-1), leading edge vortex and trailing edge vortices had opposite vorticity. For

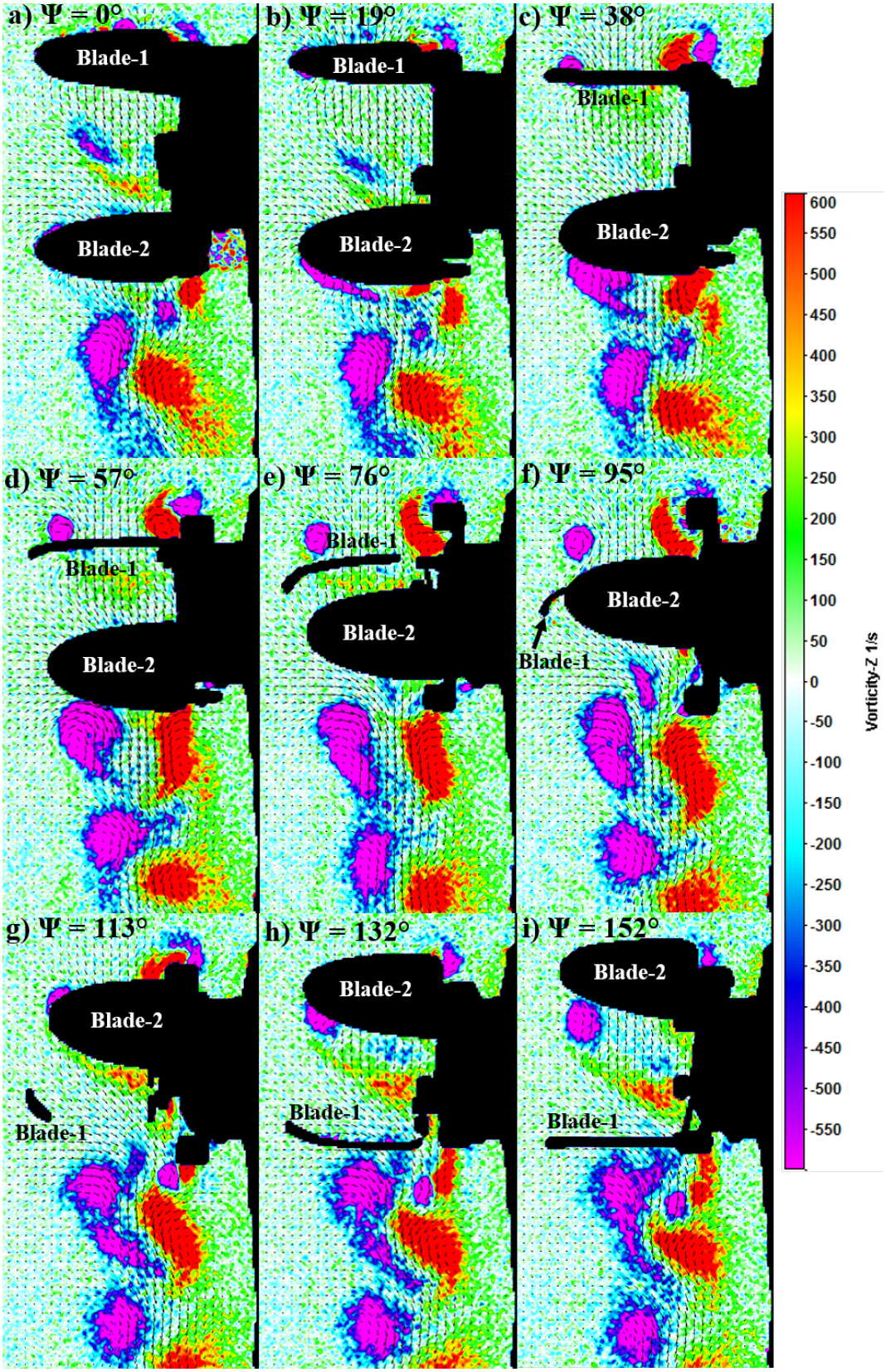

Figure 3.5: PIV spanwise measurements at 3200 rpm with laser bisecting rotor vertically.

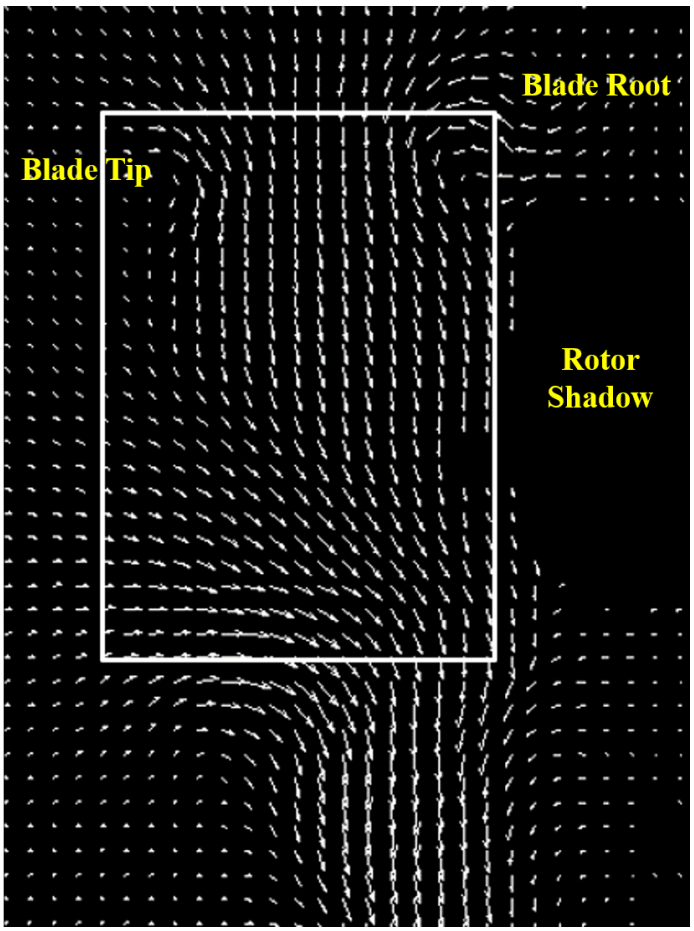

Figure 3.6: Time average vertical flow velocity for spanwise wake age measurements.

the leading edge vortex, vorticity was in the clockwise direction (purple) and for the trailed wake or shear layer it was counter-clockwise (red). Also, as expected, the sense of vorticity was reversed for the blade at the bottom (blade-2) (LEV is red and trailed wake is purple). It is interesting to note that the vortex on the top blade was larger for this particular azimuthal location ($\Psi = 0°$). One would expect the flowfield on the upper and lower blades to be similar because they have the same pitch angle, however, this was not the case because of the flow curvature effects which would virtually camber the blades in opposite directions in the upper and lower halves and also because of the effect of wake interaction from the upper half to the lower half[107]. As the blades progressed, the leading edge vortices on both the top and bottom blades gained in strength and at an azimuthal location of approximately $\Psi = 19°$ (Fig. 3.3b), the LEV on the upper blade

(blade-1) started to shed. At this location it was interesting to see the curved trailed wake for the lower blade (blade-2), clearly showing that a planar wake assumption is not true for a cyclorotor blade. At $\Psi = 38°$ (Fig. 3.3c), the LEV on blade-1 was completely separated from the blade; even so, the LEV on blade-2 was still intact and growing in strength at this azimuthal location. The fact that the vortices had maximum strength past the 0°phase could be one reason why maximum lift production on the blade could be delayed, which could result in the thrust vector being slightly tilted from the vertical.

Moving on to the next azimuthal locations, $\Psi = 57°$ and $76°$ (Figs. 3.3d and 3.3e), blade-1 moved away from the shed LEV and there was also a detached shear layer extending from the leading edge of blade-1 to the shed LEV. At this point, the LEV from blade-2 also shed. Of special importance is the fact that the size of these vortex structures are comparable to the blade chord. Moreover, in Figs. 3.3e and 3.3f it appears as if the shed LEV from blade-1 interacted with the blade to produce another vortex structure with opposite vorticity, resulting in two vortices with clockwise (purple) and counter-clockwise (red) vorticity on top of blade-1. In Fig. 3.3f, the trailing wake of blade-2 shows vorticity in two different directions. The reason for this is not clearly known at this point. In Fig. 3.3g ($\Psi = 114°$), the counter-rotating vortex pairs shed from blade-1 interacted with each other creating a complicated flowfield around them, where the flow velocity between the vortices was greatly increased. At this point, a new LEV started forming on blade-1. Figures 3.3h and 3.3i show the dissipation of the previously shed vortices and trailed wake. Another important phenomenon observable in all these figures is the extremely complex and dynamic nature of the inflow inside the rotor. The direction and magnitude of the inflow varies dramatically from one blade azimuthal location to another.

The flowfield measurements at the different phases or azimuthal locations were averaged to obtain the time-averaged (averaged over a revolution) velocity vectors, which are shown in Fig. 3.4 where the circle shows the blade trajectory. A significant observation from this figure is the highly skewed nature of the inflow inside the rotor, with the wake even re-circulating on the right side of the rotor. Also, the downward velocity on the left side is significantly higher than the right

side. Previous studies at higher Reynolds numbers (Re 30,000) have shown skewed wake on a cyclorotor[91], but not to the extent seen on the present meso-scale cyclorotor operating at much lower Reynolds numbers (Re 11,000). In the parametric studies, the skewed wake manifested as a tilt of the resultant thrust vector from the vertical (tilt angle, Φ shown in Fig. 1.10) as high as 50° in some cases. A lack of downward velocity below the rotor in the data revealed that the wake contracted so quickly and dramatically that almost all of the downwash from the micro-cyclorotor occurs in-board of the 60% span location, which is corroborated by the spanwise measurements explained below.

3.2.2 Spanwise Measurements

The phase averaged data for the spanwise measurements shown in Fig. 3.5 revealed that the flow on the blade was almost completely 3-dimensional with strong tip and root vortices. The wake from the upper blade was fully contracted at approximately midway through the rotor before it impinged on the bottom blade. This wake interaction heavily influenced the flowfield and aerodynamic conditions, especially on the inboard sections on the lower blade. Thus, the top blade tip and root vortices, which were shed and convected downwards, were pushed towards the inboard sections of the bottom blade, generating a highly 3-dimensional flow. The direction of rotation is such that the top blade (blade-1) is going into the page and bottom blade (blade-2) is coming out in Fig. 3.5a. Figure 3.5a ($\Psi = 0°$), shows the shed tip (purple) and root (red) vortices. Even though it may appear as if these vortices were shed from blade-2, these were actually the vortices shed from blade-1, when it was around $\Psi = 56°$ (see Fig. 3.5d). In Fig. 3.5b ($\Psi = 19°$) the shed tip and root vortices convected further down. Figure 3.5c ($\Psi = 38°$), shows the formation of strong tip and root vortices on blade-2 and blade-1. Even on blade-1 the inflow was highly 3-dimensional and varied along the span of the blade because of the downwash from the root and tip vortices. At $\Psi = 57°$ (Fig. 3.5d), the tip and root vortices were completely shed from both blade-1 and blade-2. It is interesting to see that the vortices shed from the upper blade (blade-1) were more concentrated compared to the vortices from the bottom blade (blade-2). This was also seen with regard to the leading edge vortex in Fig. 3.3. This could be because of the fact that the inflow was

much cleaner in the upper half compared to the wake interference and other factors in the lower half. In fact, in Fig. 3.5d, one can see three sets of tip and root vortices. The lower-most, and the most diffuse one, was the one shed by blade-1 in the previous cycle when it was in the bottom half. The ones right below blade-2 had just been shed from it. The vortices at the top had just been shed by blade-1 in the upper half and aged the least. Figures 3.5e to 3.5i ($\Psi = 76^\circ - 152^\circ$) show the convection and diffusion of the three tip-/root-vortex pairs. Of particular interest is that since the tip and root vortices were very close and rotated in the opposite direction, they increased the flow velocity in between them. In addition to that, the two vortices interacted with each other resulting in a spatially oscillating (or undulating) wake under the rotor bounded by the vortices.

The flowfield measurements at the different phases or azimuthal locations were averaged to obtain the time-averaged (averaged over a revolution) velocity vectors, which are shown in Fig. 3.6 where the rectangular box shows the position of the cyclorotor. The results clearly show the contraction in the wake after crossing the upper half so that mostly the inboard sections of the lower-half blade are affected by the wake from the upper half. Furthermore, the wake changes in direction and contracts even more after crossing the lower half. Unexpectedly, and not observed in other cylorotor studies, was a small component of inflow velocity along the axis of rotation between the blades. The cantilevered design had no end plate at the tip of the blades which permitted axial flow as opposed to previous cyclorotor designs, which had an endplate at the blade tip to support the blade. Leaving the cyclorotor end open allowed air to be drawn into the cyclorotor due to the pressure differential. A mechanism akin to a centrifugal pump might be contributing to the axial inflow as well, but the physics behind this phenomenon are not fully understood at this point. Figures 3.4 and 3.6 together demonstrate the three-dimensionality of the inflow in a cyclorotor.

3.3 Concluding Remarks

Covered in this chapter were the PIV-based flowfield velocity measurements on a micro-scale cyclorotor configured identically to the final design in Chapter 2 but with 2 blades instead of 4. Phase-locked flowfield measurements were conducted using Particle Image Velocimetry (PIV) techniques in two different orientations, chordwise and spanwise. The chordwise measurements

had the laser plane normal to the axis of rotation and examined the evolution of leading edge vortices and the trailing edge wake at 60% span location from the root. The spanwise measurements had the laser plane parallel to the axis of rotation, bisecting the rotor vertically into left and right halves. From this study the following conclusions were drawn:

- PIV measurements showed that the flowfield on the present meso-scale cyclorotor was highly 3-dimensional and unsteady, characterized by the growth and shedding of leading edge vortices (LEVs) and non-planar trailing vortex sheet, strong root and tip vortices, which interacted with each other to create an undulating wake, highly skewed inflow, and strong interaction of the slip stream from the upper blade on the lower blade.

- Large re-circulation velocities were observed inside the rotor which caused a differential in blade flow conditions between the right and left half of the rotor, contributing to the skewed wake.

- Downwash created by the low aspect ratio, cantilevered elliptical blades was heavily contracted just beneath them in both the upper and lower halves which meant that the majority of blade interactions occurred at interior spanwise locations leaving the blade tips exposed to relatively clean air.

- Low pressure inside the rotor was drawing more fluid mass axially through the open end of the cantilevered cyclorotor design, only possible because of the lack of an end plate at the rotor tip.

4. Twin-Cyclocopter Design and Development

Once the cyclorotor design process in Chapter 2 had been finalized, and the PIV experiments were conducted, work began on building and realizing a 30-gram cyclocopter that incorporated the final cyclorotors to align with the initial conceptual drawing (Fig. 2.1). Being based off of previous, larger cyclocopter designs, the concept was a single-nose rotor twin-cyclocopter created to conduct experiments with the goal of understanding the flight dynamics of cyclocopters at small scales. It was determined that an experimental approach was the best method to confidently investigate the potential benefits of cyclorotor-based MAV given the lack of validated models for conducting accurate simulations. This chapter covers the development and flight testing process for a twin-cyclocopter along with subsequent improvements including the exploration of alternative twin-cyclocopter configurations for improved handling.

4.1 Twin-Cyclocopter Configuration

A twin-cyclocopter is an MAV that uses two co-rotating cyclorotors and a nose rotor to counteract the nose-down torque and augment thrust. Initially developing a twin-cyclocopter, as opposed to a quad-cyclocopter, was done to compare the vehicle characteristics to previous cyclocopter designs both qualitatively and quantitatively using flight test data and the experiments described in Chapter 5. The first twin-cyclocopter built is shown in Fig. 4.1 with key components labeled. There are five control inputs on this twin-cyclocopter, 3 motor RPMs and 2 servos directions. The motors determine how much lift is produced and the servos provide for the thrust vectoring capability of the cyclorotors. The over-actuated nature of this configuration allows it to command instantaneous accelerations in more directions than a typical quadcopter potentially increasing its maneuverability and gust tolerance, but this needs to be investigated further to fully reap the benefits.

Depending on the location of the center of gravity, thrust production will be spread between the three lift producing devices in different proportions. Setting nose rotor lift first determined the

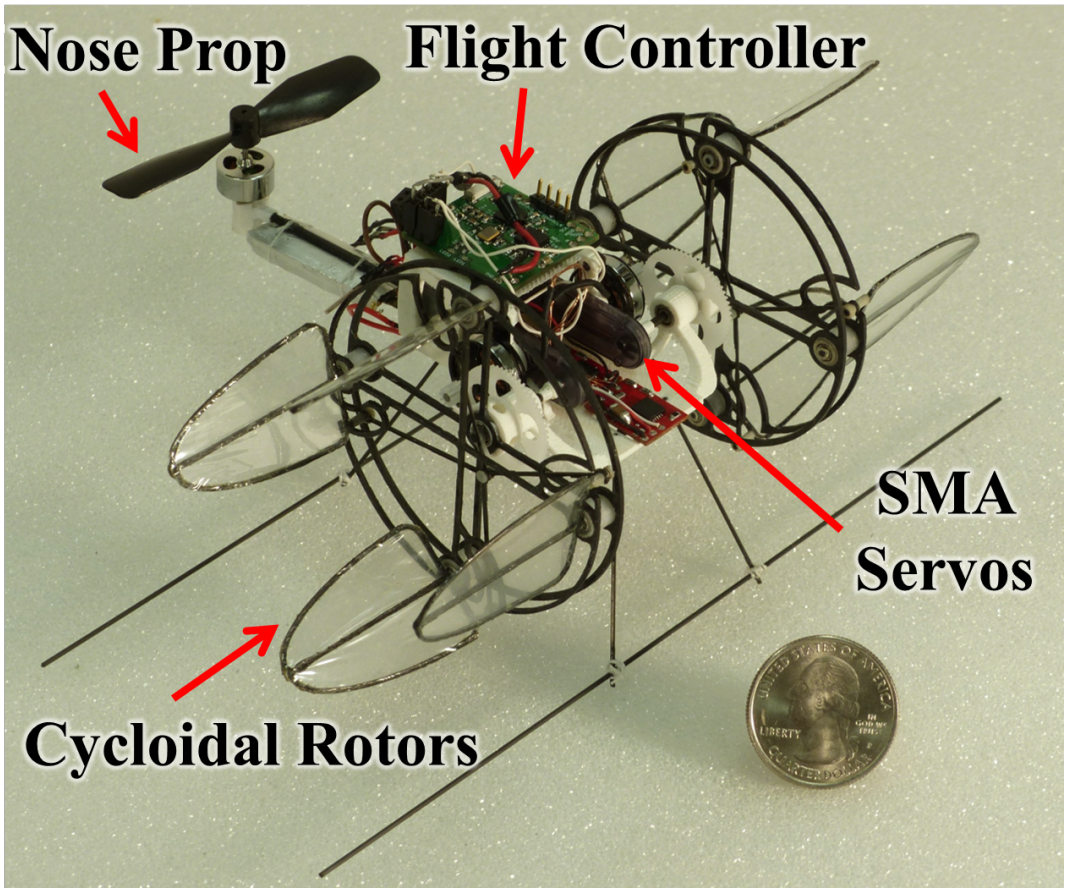

Figure 4.1: 29-gram micro-scale twin-cyclocopter

distance between CG and propeller. Placing the nose rotor closer to the CG required it to produce more thrust, but loading the nose too much would increase the motor weight and reduce the control effectiveness of the cyclorotors. Alternatively, extending the nose rotor too far made the vehicle excessively sensitive to changes in the nose rotor lift. Although the balance of forces and torques in hover was a simple statics problem, the interplay between thrust ratio, CG placement plays a significant role in the flight quality.

The initial vehicle was configured such that lift was evenly split in hover between the three thrust vectors where each was producing one-third of the total, meaning the required nose rotor thrust to counteract the torque of the main rotors was set to around 8 – 10 grams (0.08 – 0.1 N). This value was determined by the availability of micro-scale hardware and the weight breakdown of the cyclocopters that had been developed previously. Several lightweight propellers were selected and

tested over a range of rotational speeds using the motor that would be on the vehicle. Differences between propellers of similar diameter were minor and all could meet the thrust requirement so the one with the highest figure of merit was chosen.

4.2 Vehicle Integration

Using two cyclorotors in the configuration previously described, a flight-ready vehicle was constructed as shown in Fig. 4.1. Maintaining total weight below 30 grams was a primary focus of this first iteration so careful attention was given to every component to reduce weight. This is smallest cyclocopter ever built in the history. Small size also meant the cyclorotors would be operating at ultra-low Reynolds numbers, approximately around 11,000 at the operating rpm. The lightweight airframe, which functions as an anchor point for all electrical and mechanical subsystems, was designed to hold the components in a compact configuration, thus minimizing the profile of the craft. It was rapid prototyped from ABS (Acrylonitrile Butadiene Styrene) plastic and featured carbon fiber rods extending outwards that functioned as landing gear. The thrust vectoring of each cyclorotor was actuated by means of a Toki Biowire SmartServo RC-1 shape-memory alloy based servo actuator weighing 1 gram. The rotors themselves were each driven by a 2.5-gram brushless HobbyKing AP-02 7000kv brushless, outer-runner motor at a 6.7:1 gear ratio. Both the motors and actuator servos were powered by a 160 mAH single cell LiPo battery weighing $\sim$3.7 grams. The nose rotor used a hexTronik 7700kv brushless motor and the 57X20 propeller from the Sky Buddy RTF R/C plane. The speed controllers on the vehicle were XP-3A ESCs. The total weight of the first prototype was approximately 29 grams. Table 4.1 gives a breakdown of the system components by weight. Overall, the vehicle has a footprint of 5.65 in wide by 5.75 in long and stands 3.2 in tall, excluding the landing gear.

A subsequent iteration was done that improved upon the first design. Apart from the updated cyclorotors that were described in Chapter 2, the airframe was redesigned to be smaller and lighter while orienting everything in a more compact package. It also re-positioned the flight controller to be located at the CG. The Toki Biowire shape-memory alloy (SMA) servos were found to have a limited service life under the constant unidirectional torque experienced during cyclorotor opera-

Table 4.1: Component Weight Breakdown of 29-gram Cyclocopter.

Component	Weight g	Total %
Motors + Transmission	7.5	26
Cyclocrotors (Combined)	5.5	19
Structure + Wires	4.6	16
LiPo Batteries	4.9	17
Electronics	4.1	14
Nose Rotor + Motor	2.4	8
Total	29	100

tion and were replace with Hobbyking HK-5320 digital servos. When new, the SMA servos could perform without issue, but over time the servo's ability to hold position deteriorated introducing large variations into thrust vectoring which made flights unstable. The Hobbyking servos weighed 1.7 g each, but through shaving down the case and other weight saving measures only weighed 1.25 g when installed. The nose structure was changed from a single 1.5 mm carbon fiber tube to two 1 mm carbon fiber rods. This created a more rigid nose preventing excessive vibrations during flight and giving a more stable mounting platform for the battery. Transmission gear ratio was changed from 6.7:1 to 5:1 for 20% more maximum thrust at a 9% penalty to electrical power loading ($thrust/power$, see Table 4.2). Gear testing was performed on a mass balance so data accuracy was not as high as the performance measurements in Chapter 2, but it was adequate to make an engineering determination. Finally, the 160 mAH and 80 mAH 3.7 V LiPo batteries used to power the motors and flight controller were replaced by a single 240 mAH 3.85 V LiHv (Lithium-ion Polymer High-voltage) that was used to power all electronics. The culmination of these upgrades resulted in the vehicle shown in Fig. 4.2, which weighed just over 30 grams. Eventually, the propeller itself would be swapped for one with a slightly larger diameter to generate more thrust because the smaller one was inadequate for balancing the pitch torque when the battery voltage dropped under load.

Another effort worth mentioning is the investigation into different transmission systems, namely belt vs. gears. A larger motor than was required served as the power system for the parametric stud-

Table 4.2: Gear ratio testing results for AP-02 and 1 in radius cyclorotor.

Pinion-Wheel Teeth	Gear Ratio	Max RPM	Max Thrust	Max Electrical Power	Power Loading
	g		g	W	N/W
12-60	5	4350	12	4.7	25.2
11-60	5.45	4200	11	4.4	24.7
12-70	5.83	4000	10	4.2	23.4
10-60	6	3975	10.1	4.0	24.6
11-70	6.36	3800	9.3	4.0	22.9
9-60	6.67	3925	9.5	3.4	27.7
10-70	7	3750	8.7	3.4	25.4
9-70	7.78	3500	7.7	3.1	24.6

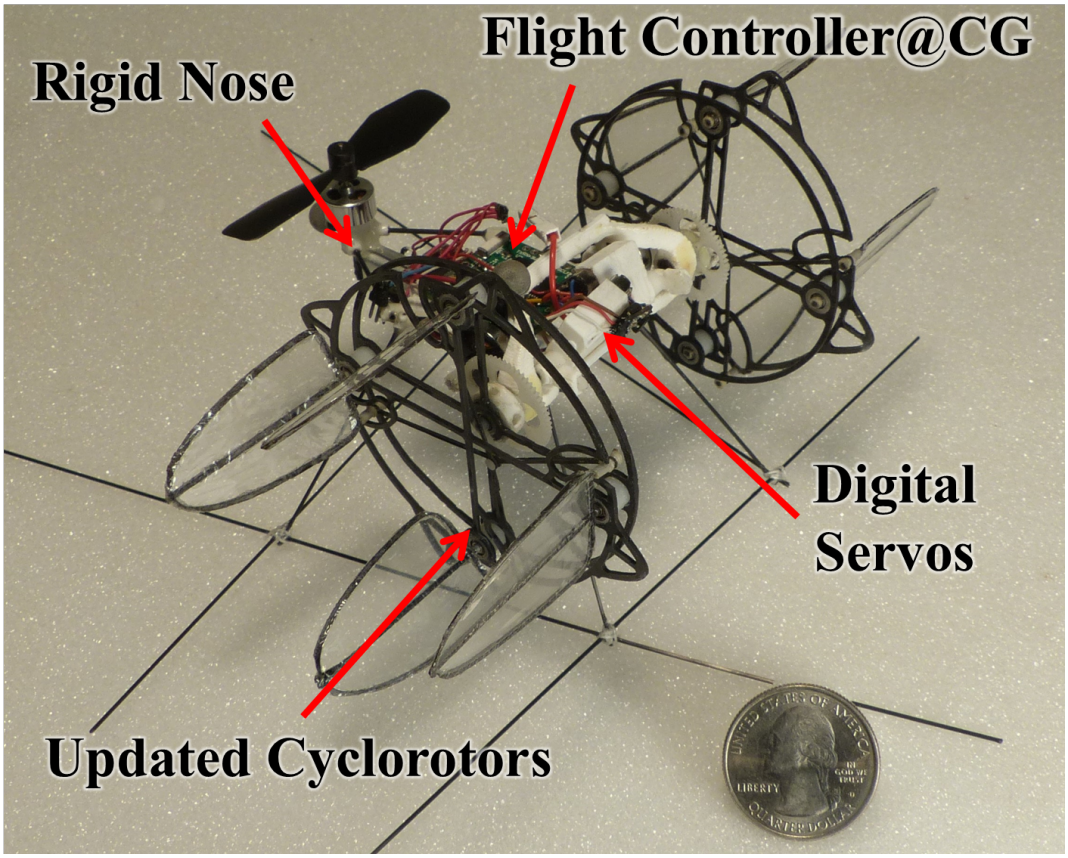

Figure 4.2: Second iteration of micro-scale twin-cyclocopter.

ies and PIV experiments, but the motor and transmission components were too heavy to be used on the MAV. The HobbyKing AP-02 and hekTronik 7700kv mentioned above were both tested

using micro gears from Didel and pulley systems made in-house. The hekTronik 7700kv proved under-powered for this application. COTS parts for belt drives at this size were limited so different sizes of pinions and pulleys were 3D printed. Although a belt-drive transmission system would allow more freedom in motor placement, the pulley systems tested proved ineffective because of restricted belt engagement and large belt tensions required to function properly. As a result, the gear combination that could produce the required RPM at the lowest power draw was chosen.

4.3 Vehicle Telemetry

Attitude stabilization was implemented onboard using a flight controller called ELKA-R – a custom-built, embedded processor-sensor board which can be seen in Fig. 4.3 and on the vehicle in Fig. 4.1. It weighed 1.7 grams and was powered by a single 1-cell 3.7-volt LiPo battery. The flight controller housed an STM32 microprocessor with a 32-bit ARM Cortex F4 core for high-end onboard computational tasks. The MPU-9150 inertial measurement unit (IMU) integrated on the board included tri-axial gyroscopes, accelerometers, and magnetometers. Wireless communications were serviced by an on-board nRF24L01 chip, a low-power 2.4 GHz RF transceiver. The flight controller had a sensor update rate of 500 Hz. It was also capable of streaming vehicle attitude and actuator controls data to the base station and receiving pilot commands at 50 Hz (Ref. [109]). The flight controller was capable of sensing vehicle attitude and angular rates and sending corrective signals to the servos for stabilization by varying the pulse width input to the motors and servos.

To communicate wirelessly with the onboard controller, the operator used a LabVIEW interface which included a wireless 2.4 GHz data link with nrf24L01 transciever. The base station LabVIEW program allowed the operator to control the vehicle, modify the feedback gains, change the sensitivity of pilot inputs, and record attitude data transmitted by the onboard processor. The LabVIEW program received pilot inputs through the use of a DX6i Spectrum transmitter which was hardwired to the base station. The program then connected to the microcontroller through a wireless radio link and used this connection to send the control inputs and receive the vehicle attitude and rate data. The data processing and inner-loop feedback control calculations were

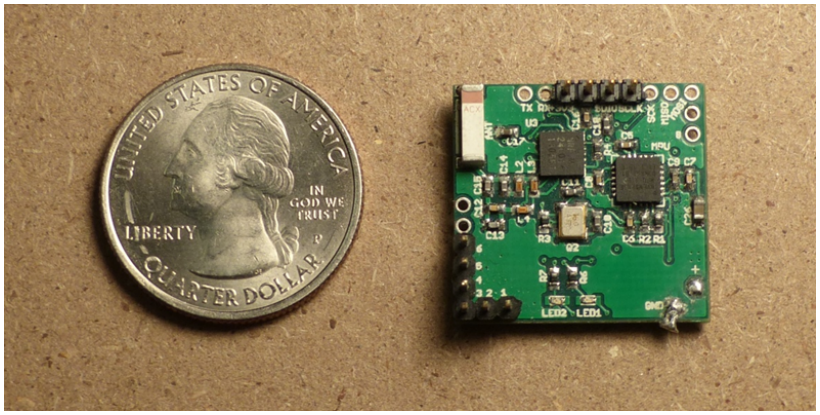

Figure 4.3: Custom-built 1.7-gram kinematic autopilot with U.S. quarter for size comparison.

performed onboard by the microprocessor.

The on-board gyros measured the pitch (q), roll (p), and yaw (r) angular rates while the accelerometers recorded the tilt of the gravity vector in the body frame. The vehicle attitude could then be extracted by integrating the gyro measurements with time. However, it was known that this leads to drift in attitude measurements (Ref. [110]). Accelerometers on the other hand offered stable bias, but were sensitive to vibrations and in general offered poor high frequency information (Ref. [111]). Therefore a complementary filter was incorporated to extract the pitch and roll Euler angles using a high-pass filter for the gyros (4 Hz cut-off) and a low-pass filter for accelerometers (6 Hz cut-off). The rotational vibrations were filtered out since they are sufficiently higher than the body dynamics. On-board inner loop feedback was implemented using a cascaded proportional-integral-derivative (PID) controller, shown in Fig. 4.4, that has an inner PID loop on the attitude rates (p, q, and r) and and outer loop with proportional gains only on pitch and roll Euler angles (θ and ϕ) — a PPID loop. Heading data was not available so yaw Euler angle was not measured or used for feedback.

4.4 Attitude Control

Control of the vehicle was accomplished in two ways: varying the RPM of the drive motors for either the main rotors or the nose rotor (changes thrust magnitude) and rotating the offset link in the pitching mechanisms, which changes the blade pitch phasing (thrust vectoring). The

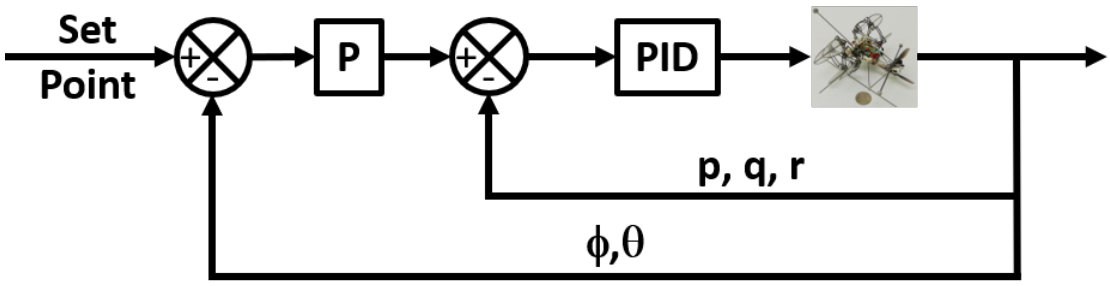

Figure 4.4: PPID feedback loop architecture for flight testing operations.

arrangement of components that rotates the offset linkage is shown in Fig. 4.5 and the effect on thrust direction is shown in Fig. 4.6. Modulating the rotor RPMs and cyclorotor pitch offset link angle provided complete control over rolling, pitching, and yawing motion. Because of this ability to instantaneously change the magnitude and direction of the thrust vectors from the rotors, the cyclocopter possesses additional levels of agility and maneuverability over traditional rotorcraft. For roll control, the RPM of each of the main cyclorotors was changed differentially to increase the thrust of one rotor while decreasing that of the other rotor, effectively creating a moment about the longitudinal axis of the vehicle (Fig. 4.7). To control pitch, the RPM of the nose prop was varied to either increase or decrease the thrust created and generate a moment about the lateral axis due to the offset of the nose prop from the CG (Fig. 4.8). Finally, yawing moments were generated by rotating the pitch offset links in unison which tilted the thrust vectors of the main rotors in opposite directions, creating a moment about the vertical axis of the vehicle (Fig. 4.9).

An important consideration of twin-cyclocopter flight was the gyroscopic coupling present between roll and yaw degrees of freedom when either a roll or yaw control input was given. Because both main cyclorotors were rotating in the same direction about the lateral axis (counterclockwise when viewed from the starboard side of the vehicle), any force which caused rotation about either the longitudinal or vertical axis would result in a gyroscopic moment 90° out of phase. Thus, if the vehicle was rolled, for example, to the right, a positive yawing motion (clockwise when viewed from above) would be introduced. This phenomenon was experimentally measured in Ref. [28]

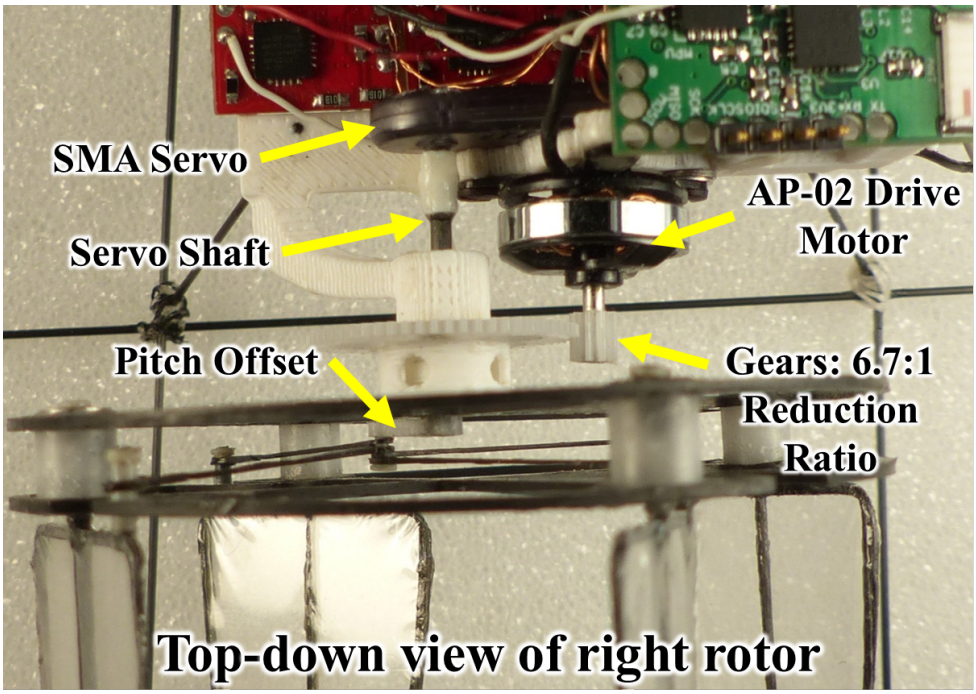

Figure 4.5: Top-down view of the linkage rotation system on the twin-cyclocopter.

and will be explored more later in Chapter 5. To compensate for this coupled behavior between roll and yaw, the flight controller was programmed to automatically send a portion of the loop output to the coupled DoF via a feed forward gain. Additionally, because of the single nose propeller, there was an unbalanced vertical torque resulting from it that generated a constant yaw motion while also introducing more couplings between pitch and the other degrees of freedom, albeit not as strongly as the cyclorotor torque due to the relatively smaller torque and angular momentum of the nose rotor. Dealing with this required a specific process for trimming and tuning.

It is interesting to note that there is little discussion of the unbalanced nose propeller torque in prior experimental studies of single-nose twin-cyclocopters. References [21, 22] briefly mention it, but scant few others do. Having consulted with the researchers at UMD they confirmed that the nose torque did not manifest a noticeable yaw during flight so the thrust vectors were pointed vertically and the unbalanced torque was counteracted by the natural damping of the system and controller feedback. However, the micro-cyclocopter experienced substantial yaw torque and cou-

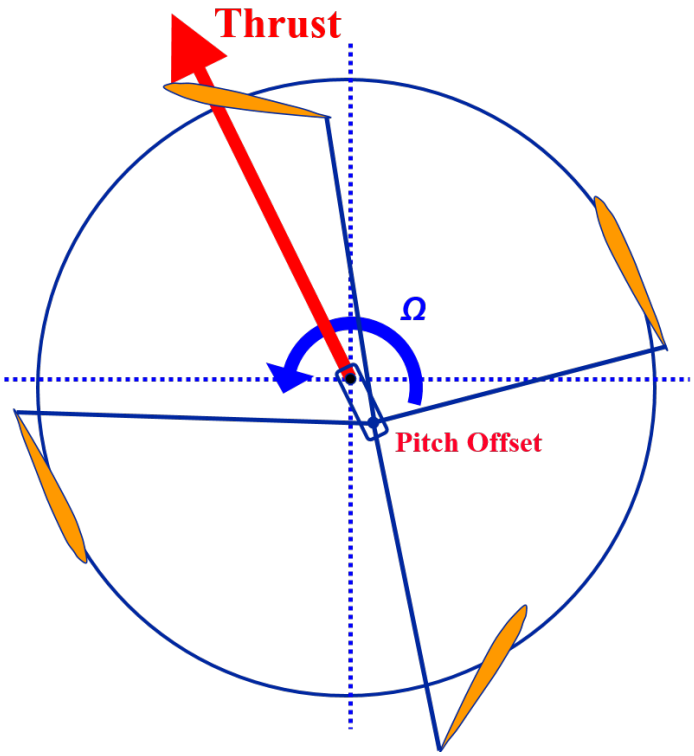

Figure 4.6: Thrust vectoring achieved through rotation of the pitch offset[22].

plings from the nose propeller which will be discussed later in this chapter.

4.5 Hovering Flight Testing

Since the flying qualities and behavior of this vehicle were largely unknown and initially unpredictable, an important flight testing consideration was safety of the vehicle during crashes. In order to prevent destruction of the airframe and reduce maintenance requirements, an $8ft \times 8ft \times 8ft$ safe enclosure was utilized to conduct flight tests in (Fig. 4.10). The sides were covered by a 90-micron thick plastic sheet to retain the vehicle within the enclosure during flight and offer a soft impact should the vehicle collide with the walls. Additionally, a sheet of plastic suspended from the edges of the frame a few inches off the ground provided assurance in case of a crash landing. The vehicle took off from the center of the suspended sheet, which provided a stable platform for vehicle lift-off. As expected, flying in this enclosure substantially reduced the number of mechanical breakdowns and improved the efficiency of flight testing operations. For additional safety

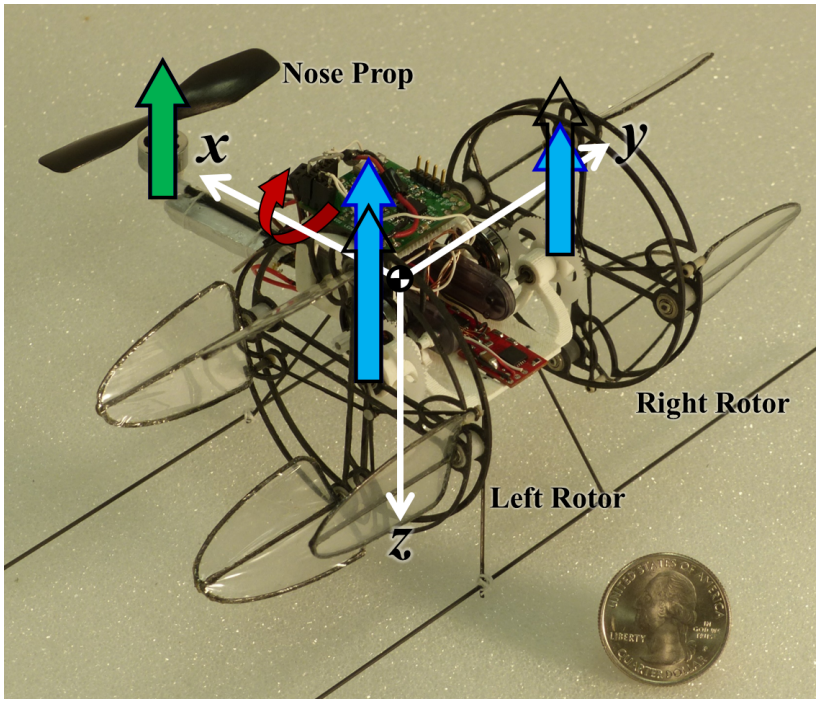

Figure 4.7: Differential cyclorotor thrust used to control roll.

during testing two measures were implemented in the controller: an automatic motor shut-off if an unrecoverable attitude was reached and an emergency stop for the motors.

The feedback method used to stabilize the vehicle was an experimentally tuned PID controller which stabilized the vehicle about a set point. Thus, it was important to trim the vehicle about the desired flight condition in order to appropriately utilize the controller feedback. For the initial flight tests, the desired flight condition was hover; therefore, effort was first focused toward modifying the direction of the individual main rotor thrust vectors until they were vertical. Ensuring the thrust vector is vertical was important because it eliminated coupling between roll and yaw trim inputs which would complicate the trimming procedure for the vehicle. Ensuring vertical cyclorotor lift was done on a smooth surface by powering only one cyclorotor then changing the corresponding servo position until no yaw motion was observed from the body. This method was found to be consistent and repeatable.

Next, roll and pitch had to be trimmed in successive hopping flights with no feedback until the MAV took off vertically. Roll was trimmed by introducing a constant offset between the cycloro-

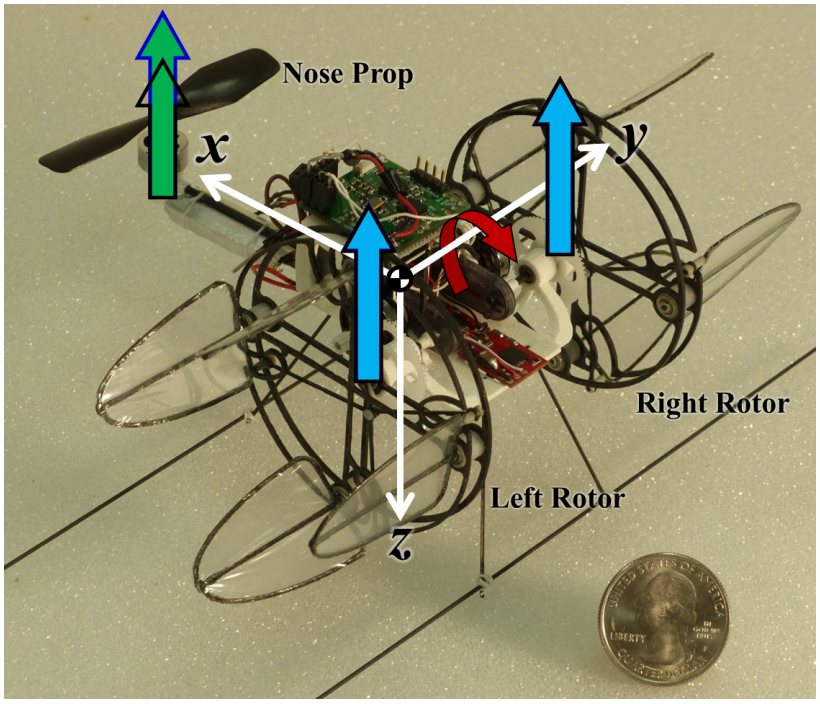

Figure 4.8: Nose rotor thrust being augmented to control pitch.

tor RPMs and pitch was trimmed by small adjustments to the nose rotor RPM so that it generated enough thrust to balance out the moment from the rotating rotors and supplement the lifting force. A vertical ascent with all lift vectors vertical meant that the cyclorotors were producing approximately the same amount of thrust and that the ratio between cyclorotor and nose propeller thrust was balanced. Even so, the vehicle would still yaw from the nose torque which necessitated that yaw trim be introduced by equally tilting the thrust vectors in opposite directions to counter the yaw torque.

There was one issue that required special attention because multiple trim states exist for hover, but only one would allow controlled flight. The trim methodology devised would converge on the proper solution, but because of the small size, some imperfections in thrust vector direction or magnitude would still exist resulting in a slight rolling or yawing motion. Because of the over-actuated nature of the twin-cyclocopter trim state was indeterminate. For example, a counterclockwise (CCW) yaw could be caused by the left thrust vector pointing too far backwards or the right thrust vector pointing too far forwards. Which thrust vector to adjust would be unclear. However, when

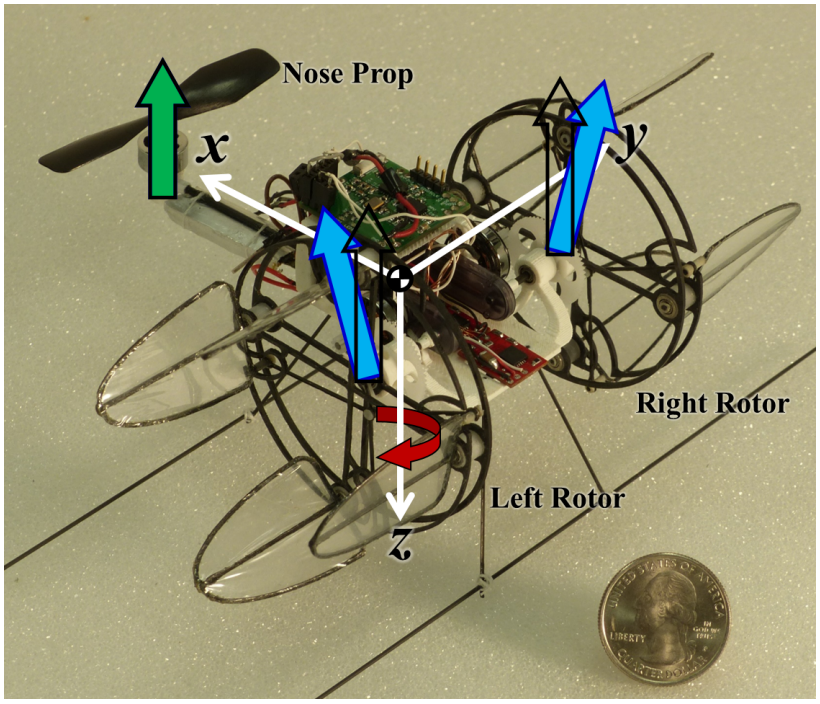

Figure 4.9: Thrust vectoring of cyclorotors used to achieve yaw control.

Figure 4.10: Flight space enclosed by Mylar walls to facilitate safe testing.

applying a symmetric trim to both vectors the result for each situation would differ. Figure 4.11 illustrates this dilemma. The same yaw trim creates a roll right response in one and a roll left in the other. By noting how the vehicle responds to trim inputs the current trim state can be resolved and the appropriate correction deduced. Proper trim is when both thrust vectors are the same magnitude and skewed the same amount from vertical to counteract nose rotor torque.

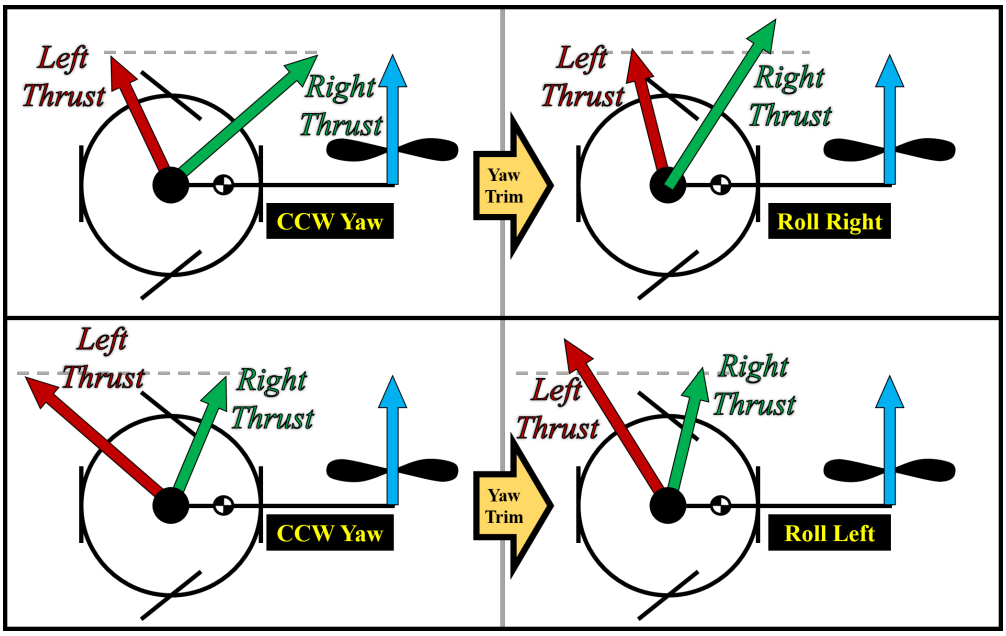

Figure 4.11: Counter-clockwise motion caused by indeterminate, imperfect trim.

After sufficiently trimming the vehicle, the next step was to introduce feedback gains in order to provide the additional level of control necessary beyond a human pilot's capability in order to stabilize the vehicle during hover. The inner feedback loop was configured for two different modes of pilot control 1)rate mode and 2)angle mode. In the rate mode, pilot commands (*i.e.*, the transmitter sticks) set a desired body angular rate for the inner PID loop. In angle mode, pilot commands were translated to a desired attitude angle by the outer proportional gain which become the inputs for the rate mode PID loop. Consequently, for flight testing with on-board stabilization, the inner PID loop on body angular rates had to be tuned first. Roll and pitch rate

proportional gains were introduced first which allowed the vehicle to achieve a marginal level of stability. Yaw rate proportional gains were then introduced later when the vehicle could stably hover, but still experienced undamped yaw. The rate proportional gains had the effect of slowing down the vehicle dynamics and allowed further trimming. After that the integral and derivative gains would be tuned by gradually increasing them until the desired flight characteristics were achieved. A fully tuned rate PID loop was sufficient to stabilize the vehicle, but flying within the constrained test space proved difficult due to drift. For this reason adding feedback on roll and pitch angles was necessary and significantly reduced pilot workload.

With a fully trimmed and tuned flight controller, a stable hover could be maintained at the center of the flight cube. In this state feed forward gains for the roll-yaw coupling could be added until a pure motion resulted from the associated pilot input. Gyro data of a short flight test is shown in Fig. 4.12 and the Euler angles are provided in Fig. 4.13. A video showing a few successful, stable flights is shown in Ref. [108]. The on-board feedback control system was able to restrict the angular rates and the vehicle did not deviate from level flight by more than ± 10 degrees in roll or pitch. The data begins at 2 seconds because that is when the hover begins after takeoff. The large spike around 7 seconds in the roll gyro and the associated smaller spike in the pitch gyro (Fig. 4.13) are when the throttle was reduced for landing.

4.6 Alternative Twin-Cyclocopter Configurations

While maintaining a point hover was not an issue for the micro-cyclocopter, maneuvering presented more of a challenge because of the unbalanced nose propeller torque which caused two main problems. The first was that cyclorotor thrust vectors had to be tilted to oppose nose yaw moment. Having the cyclorotor lift already skewed, any roll command given would introduce both rolling and yawing moments through differential thrust adding to the inherent gyroscopic coupling. Conversely, yaw commands would not generate any rolling moments, causing asymmetry in the controls. Secondly, the unbalanced nose torque introduced gyroscopic roll-pitch coupling that was not significant on larger vehicles. As a result, there existed a cascading gyroscopic coupling between all three rotational degrees of freedom.

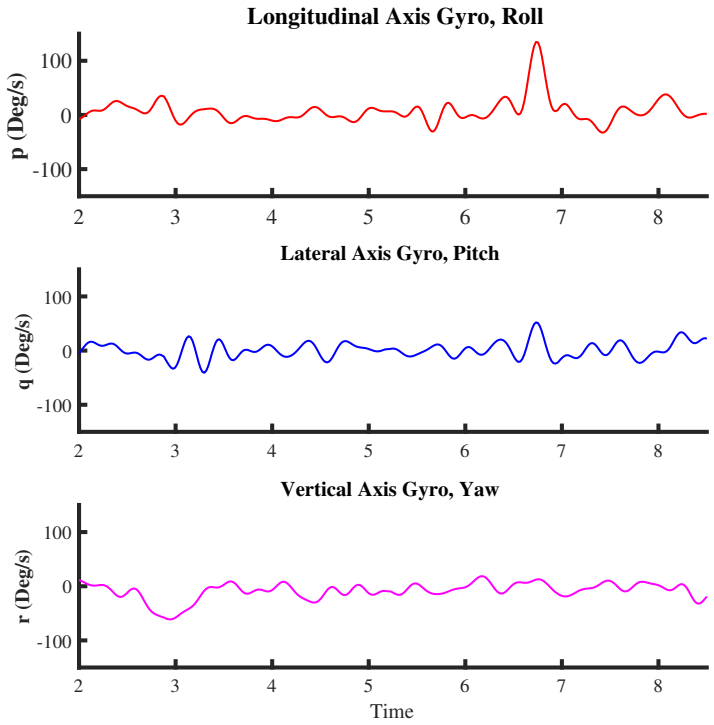

Figure 4.12: Angular rates for hovering flight test.

These two issues and the difficulties they caused in maneuvering the aircraft made flight testing based system identification studies difficult. The specifics of this isssue will be discussed further in Chapter 5, but nonetheless, ways of addressing the unbalanced nose torque to improve flight quality had to be explored if a linear model was to be derived from flight tests. One method was the complete elimination of the nose propeller altogether in favor of two additional cyclorotors in an "H" configuration quad-cyclocopter (presented in Chapter 6). An alternative was to use a second, counter-rotating propeller to balance the angular momentum in one of two possible layouts: coaxial or tandem (Fig. 4.14). Both required minimal alteration to the twin-cyclocopter hardware, but a coaxial configuration was chosen because of the difference in possible control schemes (Fig. 4.14a). Having two propellers meant two potential controls combinations, simultaneous or differential. In the tandem configuration (Fig. 4.14b), simultaneous control would result in a pure pitch moment, but differential would produce a coupled moment in both the roll and yaw axes because of

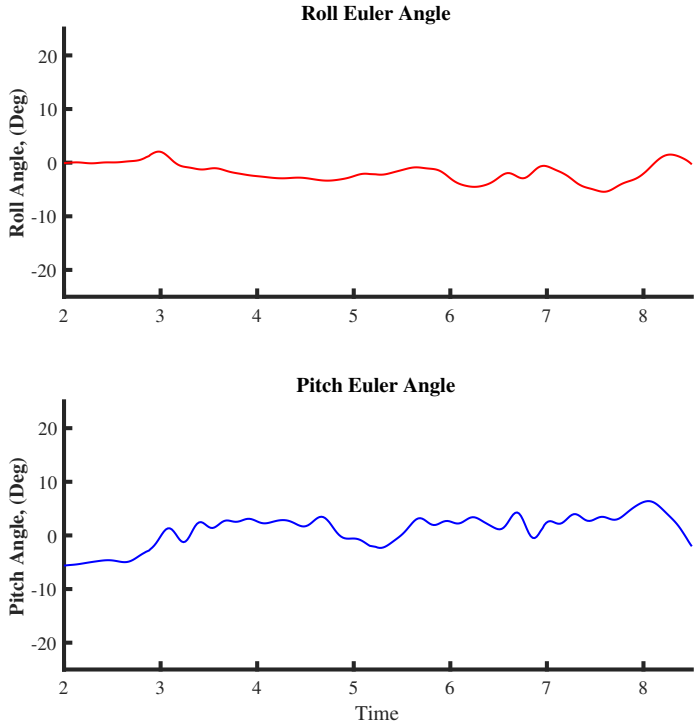

Figure 4.13: Euler angles for hovering flight test.

the offset distance between the propellers and the resulting uneven angular momentum, ultimately defeating the purpose. The coaxial configuration did not create collateral couplings — simultaneous and differential control of the coaxial propeller could impart pure pitch and yaw moments, respectively.

Creating a coaxial-nose twin-cyclocopter was done by swapping out the single nose propeller with two Hobbyking AP-02 motors in opposition (Fig. 4.15), which is the only difference between it and the improved single-nose iteration. A weight breakdown of this 33-gram vehicle is shown in Table 4.3.

4.7 Coaxial-Nose Cyclocopter Attitude Control

The control scheme for the coaxial-nose twin-cyclocopter incorporated different means of controlling pitch and yaw, without changing roll control methodology. The addition of a second nose

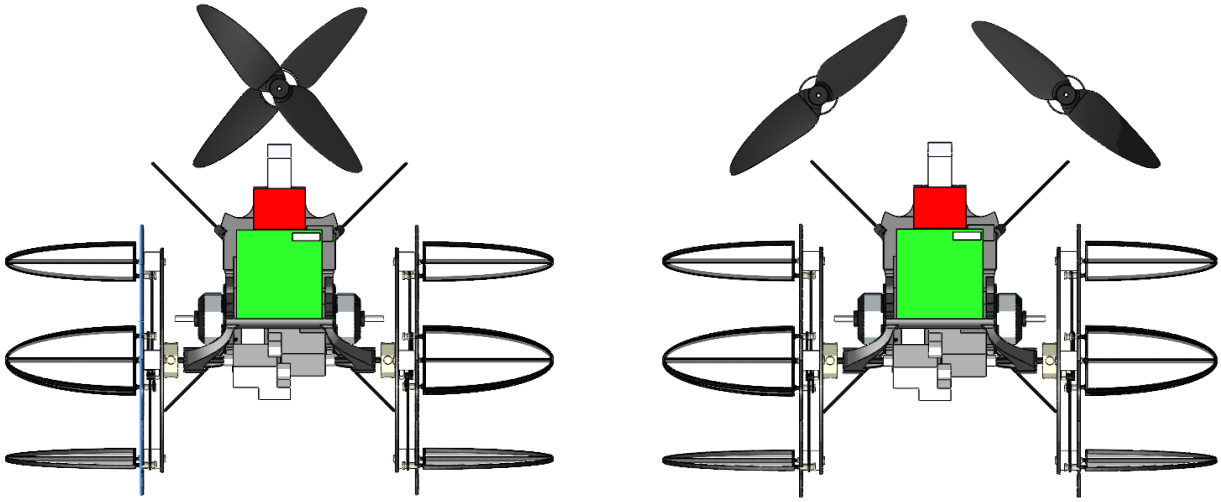

(a) Twin-cyclocopter with coaxial nose propellers.

(b) Twin-cyclocopter with tandem nose propellers.

Figure 4.14: Possible configurations of twin-cyclocopters with balanced nose torque.

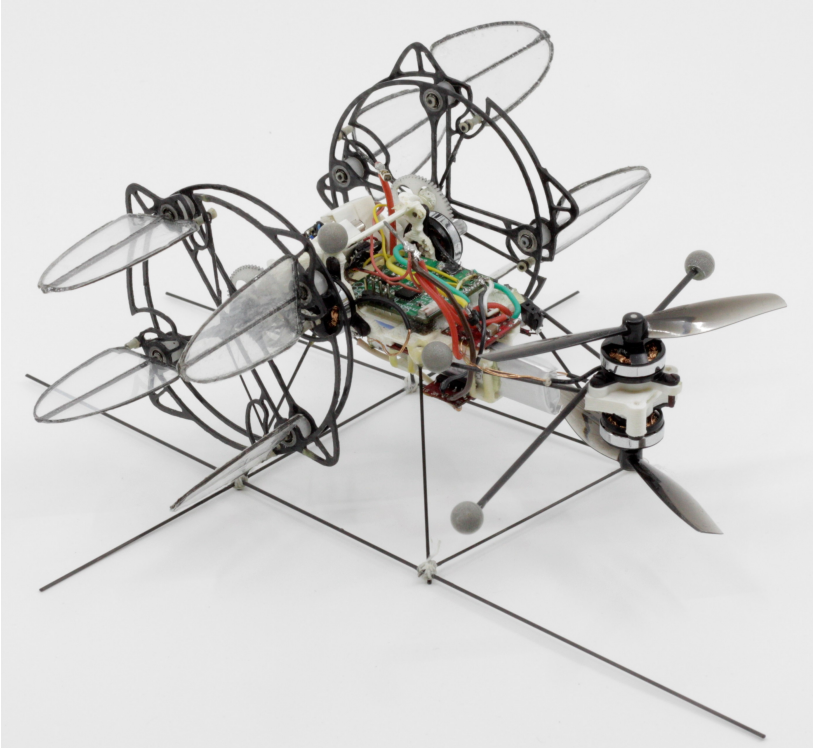

Figure 4.15: Micro twin-cyclocopter with coaxial nose propellers.

Table 4.3: Component Weight Breakdown of 33-gram Twin-Cyclocopter.

Component	Weight (g)	Total (%)
Motors + Transmission	7.5	23
Cyclorotors (Combined)	6.2	19
Structure + Wires	4.3	13
LiHv Batteries	4.9	15
Electronics	4.5	14
Nose Rotors + Motors	5.6	17
Total	33	100

propeller meant that not only could angular momentum be balanced, but also that yaw could be commanded in either direction while maintaining a constant amount of thrust. To achieve this, the RPM of one of the coaxial motors was increased while the other was decreased (Fig. 4.16). The upper nose rotor spins counterclockwise so an increase in its RPM increases the clockwise reaction torque on the body. The opposite holds true for the lower rotor. The correct ratio of change between upper and lower propeller to generate a pure yaw was tuned in flight. Pitch control still relied upon nose rotor thrust, but was now augmented by a equal but opposite change in cyclorotor thrust to maintain total lift (Fig. 4.17). This had the added benefit of changing cyclorotor torque to aid in pitching.

4.8 Coaxial-Nose Flight Testing

Like the single-nose twin-cyclocopter, flight testing with the coaxial-nose configuration began on the ground, trimming the vehicle first. By eliminating the propeller torque there was no need to use thrust vectoring to balance the single rotor torque, meaning that hover trim demanded perfectly vertical thrust vectors. To facilitate setting this, a single-axis yaw stand was first used to balance the torque of the coaxial nose rotors (shown with vehicle mounted in Fig. 4.18, rotation axis runs vertically through CG). Fortunately, the RPM offset between upper and lower propeller remained nearly constant across all throttle settings so no modifications were needed in flight. Then, on the same stand, servo positions were individually adjusted at hover throttle until the vehicle experienced no yawing motion. This implied that the thrust vectors were vertical. From the trim

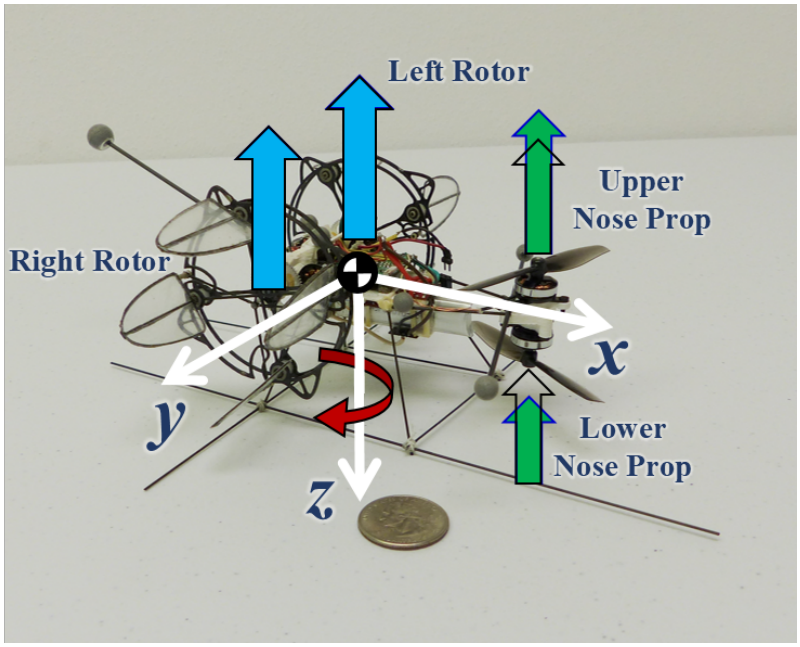

Figure 4.16: Differential RPM of nose propellers being used for yaw control.

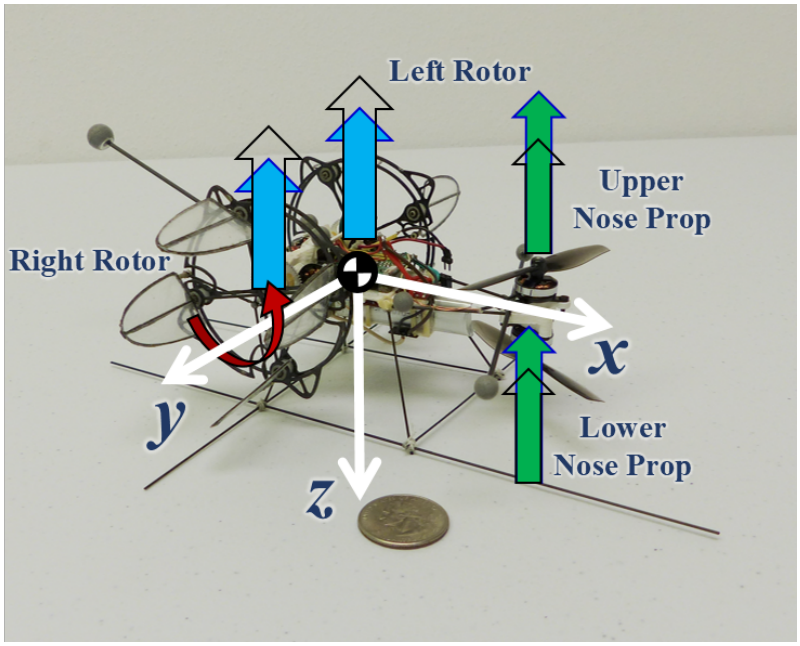

Figure 4.17: Pitch control achieved via coordinated use of nose propellers and cyclorotors.

setting attained in this manner only minor subsequent adjustments were required to reach full trim in flight.

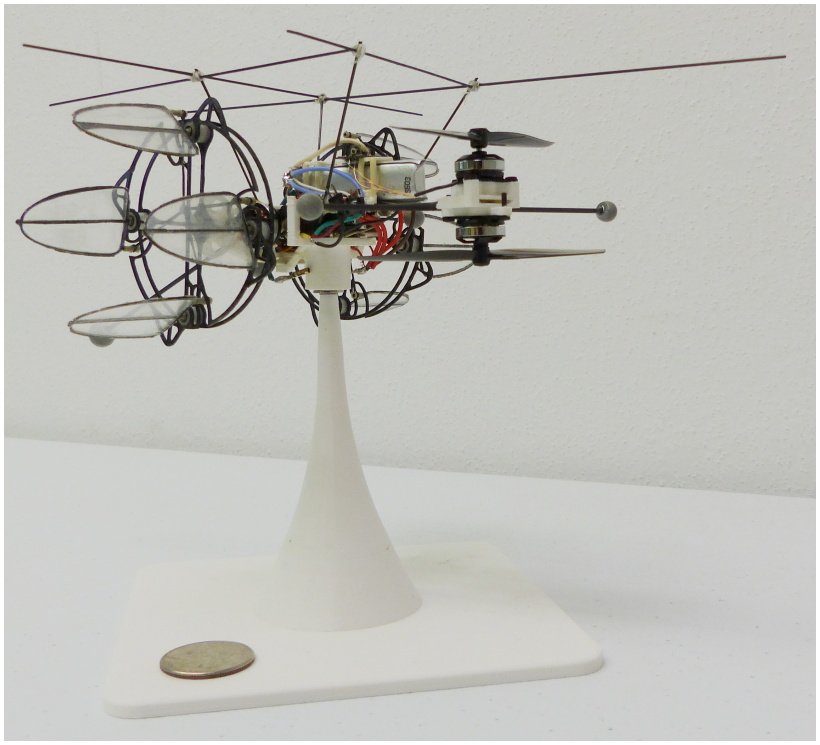

Figure 4.18: Micro-cyclocopter mounted upside-down on single axis yaw stand.

Once all lift vectors were perfectly vertical the aircraft was mounted to a balance to take calibration data on the motors. From this data relations were derived that dictated how nose rotor thrust should change relative to cyclorotor thrust in order to maintain a constant thrust along with the corresponding signal needed in the controller code. Nose rotor data was also used to maintain a constant lift when commanding yaw. Throttle sweeps were performed while taking measurements of rpm, lift, and current draw while using an electrical power supply to prevent voltage drop. Thrust versus RPM data for the cyclorotors was taken from the 3-component balance experiments described in Chapter 2. To account for the drop in battery voltage during flight two separate experiments were conducted at two different voltages, one to simulate a full battery and the other one for low battery voltage, which were then averaged to get an estimate valid over the entire duration of flight. Simple polynomial equations were then fit to the data to be used in the code. An example set of data for the top nose propeller can be seen in Fig. 4.19 showing calibration measurements with fit lines.

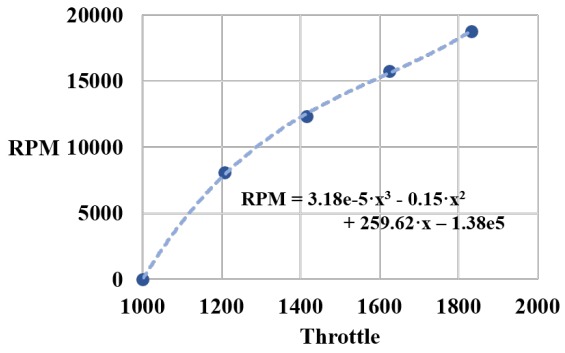

(a) Throttle versus RPM data with third-order polynomial fit.

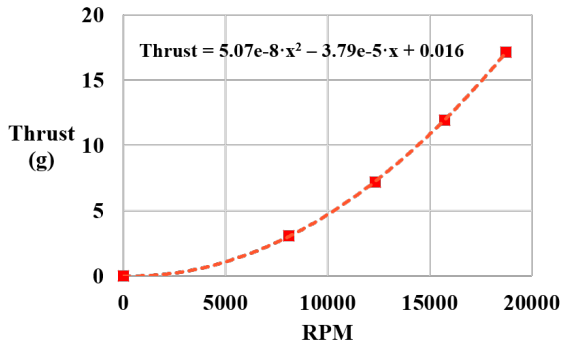

(b) RPM versus thrust with quadratic fit.

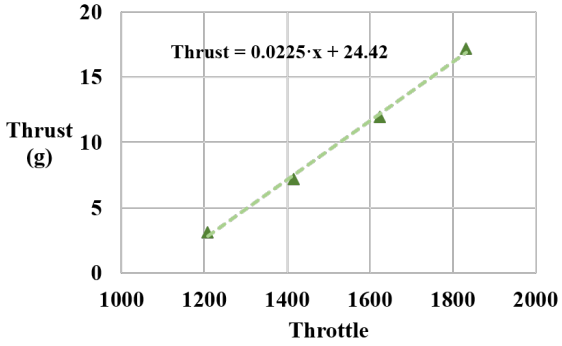

(c) Throttle versus thrust with linear fit.

Figure 4.19: Plots of calibration data with fit lines used in the flight controller.

Next, hopping flights with no feedback were performed and then gain tuning proceeded in a similar manner to the single nose rotor vehicle. As was expected, roll and yaw gains were almost identical. Once fully tuned, a comparison of the new pitch control technique to the old one was performed. The method utilizing cyclorotors and nose propellers together for thrust control was far more sensitive and precise, requiring much lower gains than using nose propellers alone. Simulating a pitch signal revealed that, when using combined pitching, the command sent to the cyclorotors was nearly twice the size of that sent to the propellers. Cyclorotor lift and torque has to be compensated by the nose rotor lift; therefore, reducing cyclorotor RPM greatly increased the effectiveness of the nose rotor lift. Furthermore, cyclorotor motor torque could be changed much faster than nose propeller lift because the torque of the electrical motors could be changed

at the speed of the electrical signal whereas changes in nose propeller lift had a delay from the spool-up/braking time required to change the angular momentum. In regards to yaw gains, differential propeller torque used separate gains from thrust vectoring yaw control and was tuned last but noticeably improved flight quality. Although either method could be used independently, incorporating both simultaneously produced the best results because of the natural hardware filtering that occurred between the servos and nose motors. Thrust vectoring had a slower response because of the physical travel of the servo but could exert a greater moment on the body. Whereas differential torque responded almost instantaneously because electrical motors yet was limited in magnitude by the motor torque. Therefore, any yaw perturbation or command was passively bifurcated between the servos acting as low pass filters responding to large amplitude changes and the nose motors acting as high pass filters damping high frequency motion.

Lastly, feed forward gains were introduced to eliminate gyroscopic coupling with an additional gain on yaw commands to adjust nose differential calibration. Flight quality of the coaxial-nose twin-cyclocopter was dramatically improved and maneuvers were more controllable, intuitive, and uncorrupted by coupled motion. Figure 4.20 shows the MAV in flight.

4.9 Concluding Remarks

Through careful management of weight, the world's smallest cyclocopter was built weighing only 29 grams, just under the weight estimate derived in the conceptual phase. The design, development, and flight testing of this vehicle demonstrated that the cyclorotor concept can be applied at small scales. The control strategy implemented on a custom flight controller used combinations of cyclorotor pitch phasing and motor rotational speeds to stabilize and maneuver the vehicle. Flight testing revealed the highly coupled nature of the twin-cyclocopter. A second micro-cyclocopter was built to investigate mechanical methods of decoupling modes and controls. Several key conclusions of this study are as follows:

1. The cyclocopter at these scales required low latency between state measurements and control outputs due to the inherently fast vehicle dynamics. The vehicle was able to achieve stable

Figure 4.20: Coaxial-nose micro-cyclocopter in flight.

hovering flights by using an inner stabilization loop implemented on a custom-built on-board flight controller at 500 Hz and an outer loop with pilot commands at 50 Hz. It was seen that higher feedback gains were needed for pitch than roll or yaw.

2. At these scales, the torque from the nose propeller had a greater impact on vehicle dynamics and caused coupling in rotational motion about all three body axes resulting in non-linear behavior.

3. A coaxial-nose propeller was used to eliminate nose torque thereby decoupling pitch from roll and yaw. Using a modified control strategy, the MAV with a coaxial-nose was more well-behaved, requiring only linear feed forward gains to compensate for gyroscopic couplings.

4. Controlling pitch utilizing cyclorotor motors and nose propellers was more effective than

only use nose propellers allowing feedback gains to be reduced.

5. Yaw control via thrust vectoring and coaxial torque modulation were used together on the same vehicle. The relative control authority and actuator response times between the thrust vectoring servos and coaxial motors acted as natural hardware filters such that thrust vectoring was tuned to high-amplitude/low-frequency responses and coaxial motor modulation was tuned for low-amplitude/high-frequency responses. Being able to individually tune each control method for a different range of responses improved performance.

5. Twin-Cyclocopter Hovering Flight Dynamics

Developing flight capable vehicles was a necessary step for experimentally extracting the flight dynamic models. Using a flying cyclocopter as the foundation for the model instead of taking a theoretical approach ensures that as long as the modeling technique is rigorously performed, it will capture the real physics, including the impact of factors such as CG location, inertia properties, and aerodynamic forces. The method chosen was a process called system identification, which entails providing known inputs to a plant and recording the corresponding outputs. Then numerical methods are used to populate an assumed model structure that relates control inputs to measured states. A linear or non-linear structure can be used, but a non-linear one requires more knowledge of the system due to the myriad of possible relations between controls, states, and their derivatives. For that matter, linear system identification is sufficient to capture complex flight dynamics as demonstrated by its use to describe F-18s, experimental NASA aircraft, helicopters, multicopters, flapping wing robots, and more[27, 52, 55, 68, 112–118]. A model derived in this fashion can be used to understand phenomena observed in flight, predict performance metrics, improve vehicle design and control, and make comparisons to other aircraft. The only other cyclocopter that has been modeled through system identification weighed 550 grams, had significantly different cyclorotors, and only used one nose propeller[28]. Being less than $1/10^{th}$ the weight, the 33-gram cyclocopter exhibits faster dynamics, a greater degree of gyroscopic coupling, and unexpected responses to benign commands. Of particular interest in this study were how scaling down the cyclocopter concept and changing the vehicle design impacted the inherent dynamics. Quantifying these observations in a linearized time-invariant (LTI) model through a systematic flight testing procedure is the focus of this chapter.

The single-nose configuration was subjected to a similar investigation but, for reasons explained later, proved difficult to collect quality data on mainly because of its poor handling qualities. It was this degraded performance that prompted the addition of the coaxial nose to enable the completion of system identification experiments. To date, this is the only coaxial-nose rotor

cyclocopter built, making it a prime subject for study.

5.1 Experimental Methodology

Linear system identification involves perturbing the vehicle from a trim state, recording the response, and estimating the parameters in linearized equations of motion to model system response with the vehicle states. The condition of interest in this experiment was hovering flight. Perturbations were provided for by pilot commands used to excite the system's modes. Reference 114 explains the process of linearizing the non-linear aircraft equations of motion about a desired equilibrium point using Taylor Series expansion. The result is the familiar linear state space equation:

$$\dot{\mathbf{x}} = A\mathbf{x} + B\mathbf{u}$$

A contains the aerodynamic coefficients representing the body dynamics and B is comprised of the control coefficients that characterize the response to inputs. $\mathbf{x}$ is the state vector and $\mathbf{u}$ is the control vector defined as:

$$\mathbf{x} = \begin{bmatrix} u & v & w & p & q & r & \phi & \theta & \psi \end{bmatrix}'$$

$$\mathbf{u} = \begin{bmatrix} \delta_{lat} & \delta_{lon} & \delta_{dir_{TV}} & \delta_{dir_{\Delta T}} & \delta_{thr} \end{bmatrix}'$$

where the state vector $\mathbf{x}$ consists of the translational velocities and angular rates in the body frame and the Euler angles for a 3-2-1 rotation. The cyclocopter body axes were defined as shown in Fig. 5.1 where the coaxial propeller was considered the front of the aircraft. Data from the on-board flight controller was used for computing angular rotation velocities, accelerations, and Euler angles except yaw. Integrating the on-board accelerometers to calculate body axis translational velocities would accumulate unacceptable error; therefore, a 6-camera VICON motion capture system (Fig. 5.2) tracked vehicle motion via reflective beacons attached to the body (the small grey spheres shown in Fig. 5.1). The interrogation volume of the VICON system was approximately 15

feet square at the base and 7 feet high. A $15' \times 15'$ suspended sheet of mylar protects the vehicle in the event of a crash. Inertial position [X_i, Y_i, Z_i] and Euler parameter data [β_0, β_1, β_2, β_3] were recorded during flight and sent to the base station to be synced with data from the flight controller. A small adjustment of about 30 ms was needed to account for latency between the Vicon data and onboard sensors. With this information, the time history of inertial position could be used to calculate all vehicles states. VICON and the flight controller had very close agreement; therefore, VICON data was only used for translational states and yaw Euler angle.

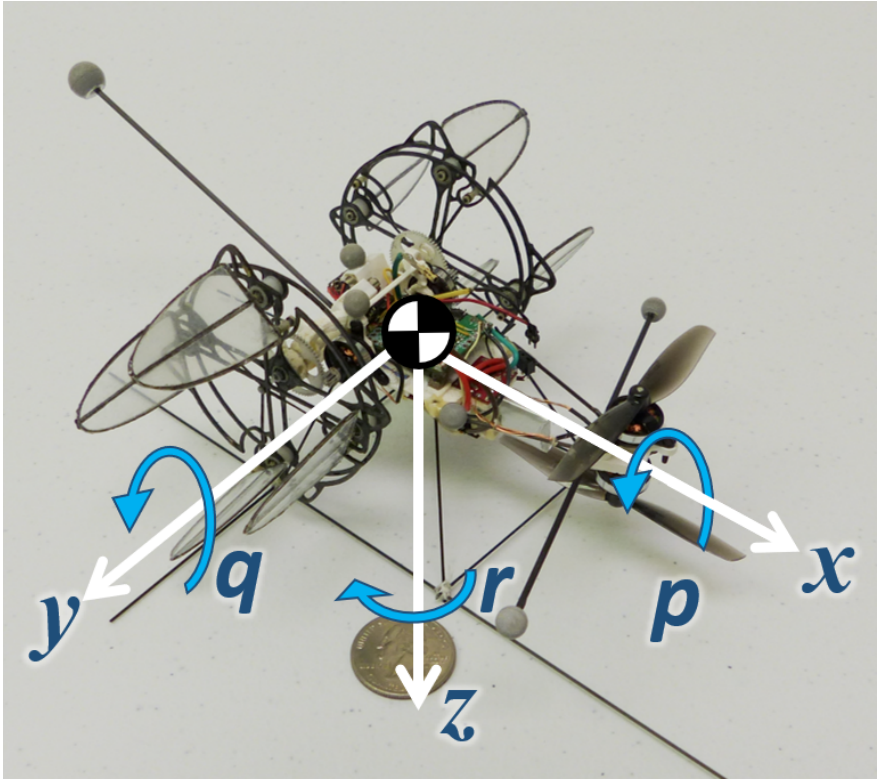

Figure 5.1: Micro-cyclocopter with body axis frame shown and corresponding positive body angular rates.

u is made of the 5 utilized control inputs: roll, pitch, thrust vectoring yaw, differential torque yaw, and throttle. The values were scaled to be in the range of [-1,1], which allows the results of this experiment to be compared to other models regardless of the actuator type. Each one

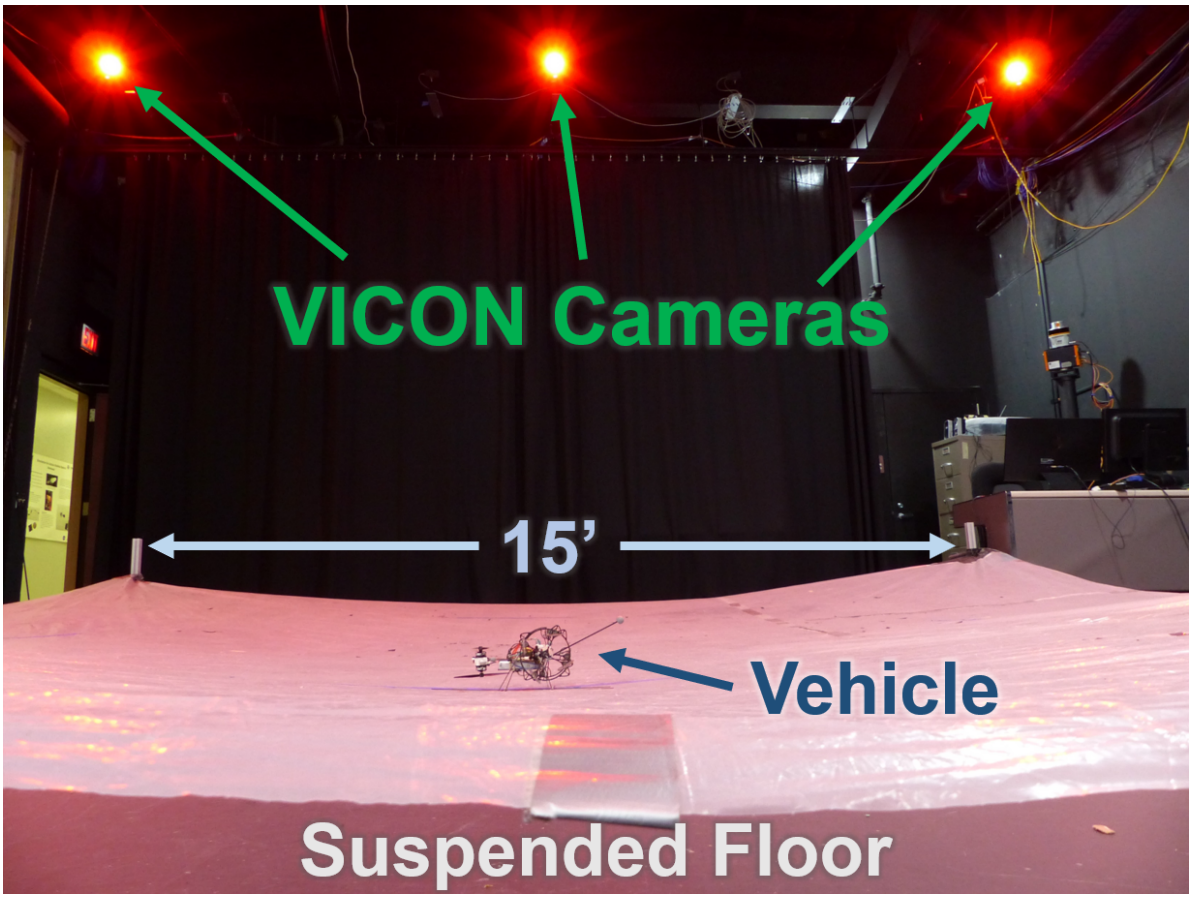

Figure 5.2: Flight space with suspended floor and Vicon cameras.

was a combination of the pilot commands and stabilization loop feedback in order to extract the open-loop behavior of the MAV. A model built using total actuator input in **u** will reflect the bare airframe dynamics of the micro-cyclocopter agnostic of the controller used. All motion from actuator inputs will be described by the B matrix and A will contain only coefficients related to aerodynamic forces and moments. Closed-loop analysis could be done to understand the behavior of the aircraft+controller system, but that was not the goal of this experiment.

5.2 Vehicle Preparation

Modifications had to be made to the micro-cyclocopter to increase model accuracy and comport with assumptions of the linear model.

5.2.1 Feedback Loop

First, the control loop had to be altered. The formulation assumed that states were always being driven to a constant value, but angle proportional gain directly violated this by driving the vehicle to a non-zero attitude during commands. An altered loop structure, shown below in Fig. 5.3, removed this complication by setting the desired attitude angles to zero, always driving the vehicle towards level attitude. Pilot commands were then added onto the output of the PPID loop as a perturbation. Additionally, derivative gains on rates had to be set to zero. The model assumes that state derivatives (translational and angular accelerations) are linear combinations of the states. Angular rate derivative gains violate this assumption by feeding back on angular accelerations making them functions of themselves.

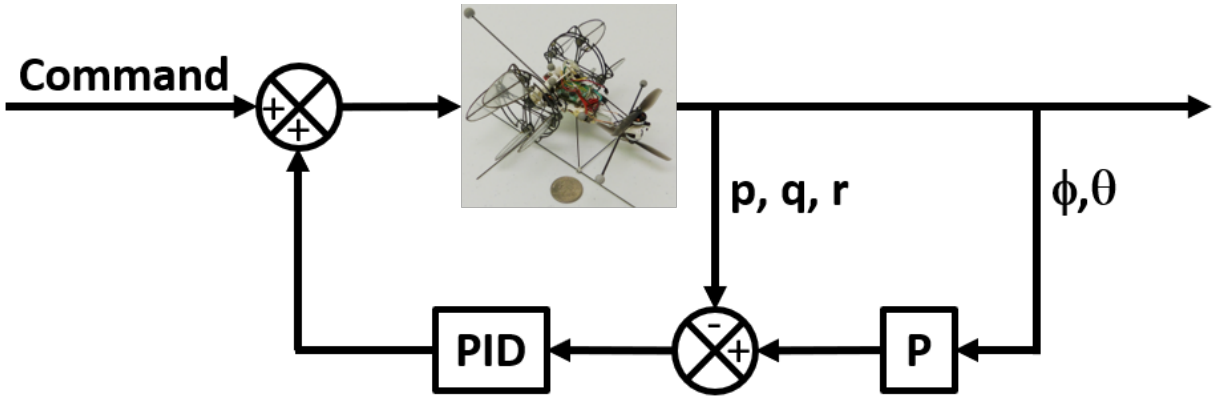

Figure 5.3: Feedback loop architecture for system identification experiments and data collection.

Furthermore, closed-loop feedback has poor signal-to-noise ratio between computer and pilot inputs which could obscure vehicle dynamics and ruin parameter correlation so controller gains were lowered as much as possible. By experimentally reducing gains slowly it was found that the cyclocopter was passively stable in roll and yaw so it could be flown with no feedback for those degrees of freedom, which was the ideal situation for extracting the natural dynamics. Pitch, being unstable, required feedback to stabilize but gains were reduced from typical flight values as much

as possible and no integral or derivative gains were used. Of the 14 feedback gains normally used to fly, only 2 were used while collecting data and all feedforward gains were removed, greatly reducing the impact of the controller on vehicle behavior.

In the case of the single-nose configuration, feedback gains could not be reduced very much for two reasons. First, the vehicle was naturally unstable unlike the coaxial-nose one so values could not be lowered too much. Second, even slightly lowered gains allowed excessive drift making it difficult to collect sufficient data before the aircraft left the VICON interrogation space. Drift for the single-nose was exacerbated by the canted cyclorotor thrust vectors. Combined, control signals remained relatively high, reducing model correlation and hiding pilot commanded perturbations in the noise unless they were large. Commands that could raise the signal-to-noise ratio high enough often sent the vehicle into an unrecoverable state[119].

5.2.2 Control Combinations

Also removed from the controller were the various actuator combinations described in the previous chapter that could obscure natural vehicle responses. Both control augmentations that relied on calibration equations were removed. One maintained a constant total thrust during pitch maneuvers by altering cyclorotor and nose propeller signals. Accordingly, pitch control was now solely achieved through nose propeller RPMs as shown in Fig. 5.4. The other balanced upper and lower coaxial nose propeller thrust when yawing to prevent a corollary pitch. Without this the controller would change the upper and lower propellers by an equivalent amount in response to a yaw command. Flight data would subsequently capture the full effect of the actuators on all degrees of freedom.

5.3 Data Collection

An essential part of system identification is perturbing the system about the trim point to excite the modes. The perturbations given to excite the micro-cyclocopter were given by the pilot rather than generated by a computer because it was imperative to prevent the craft from going unstable and human inputs tend to contain a broader spectral character[115]. Various input methods were

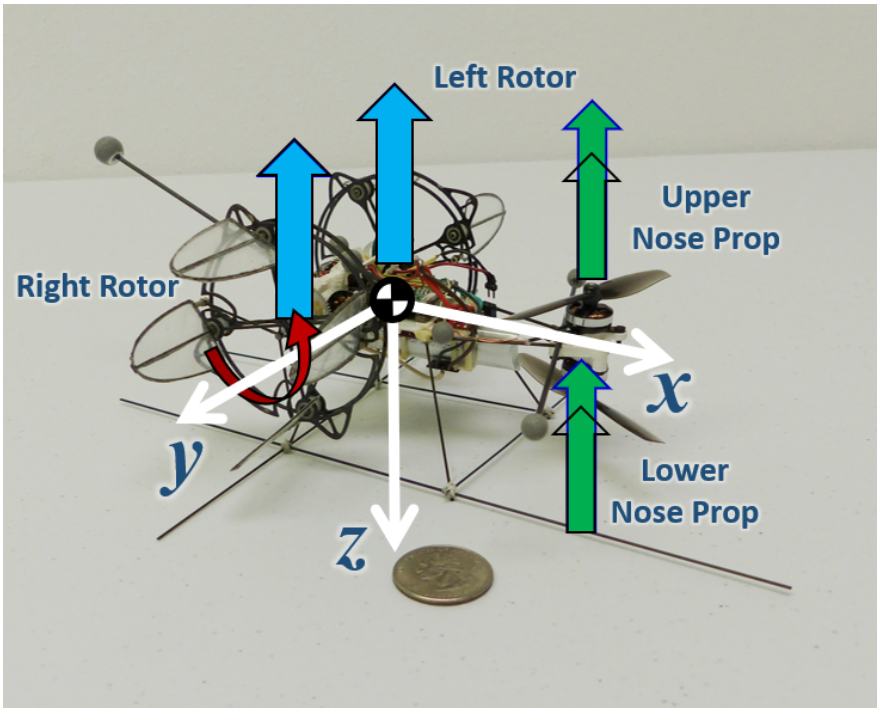

Figure 5.4: Coaxial nose being used to generate a positive pitching moment.

compared: doublets of differing periods, frequency sweeps, and impulses. No benefit was observed in data quality or model accuracy by using more complicated inputs so simple impulses were the preferred method of excitation. A sample of flight test data can be seen in figs. 5.5 to 5.8. The data was filtered using a 4^{th} order Butterworth filter with a 6 Hz cutoff frequency. It is easy to identify the location of control inputs (or perturbations) and the associated vehicle response, not only in the corresponding mode, but in the other modes as well (*e.g.*, a yaw response can be observed when a roll input is given). These data are all from the same flight test for the same period of time. Within these flight data periodic motion in roll and yaw can be seen that was not associated with any control input (Fig. 5.6). Resembling a falling leaf or a pendulum, this motion was part of the open-loop dynamics and developed naturally from a stationary hover. It was noted in flight testing that increasing throttle damped this mode out and eliminated it during vertical climb. Conversely, a descent seemed to induce this motion.

All perturbations for roll, pitch, yaw, and heave were attempted in a single flight to excite all

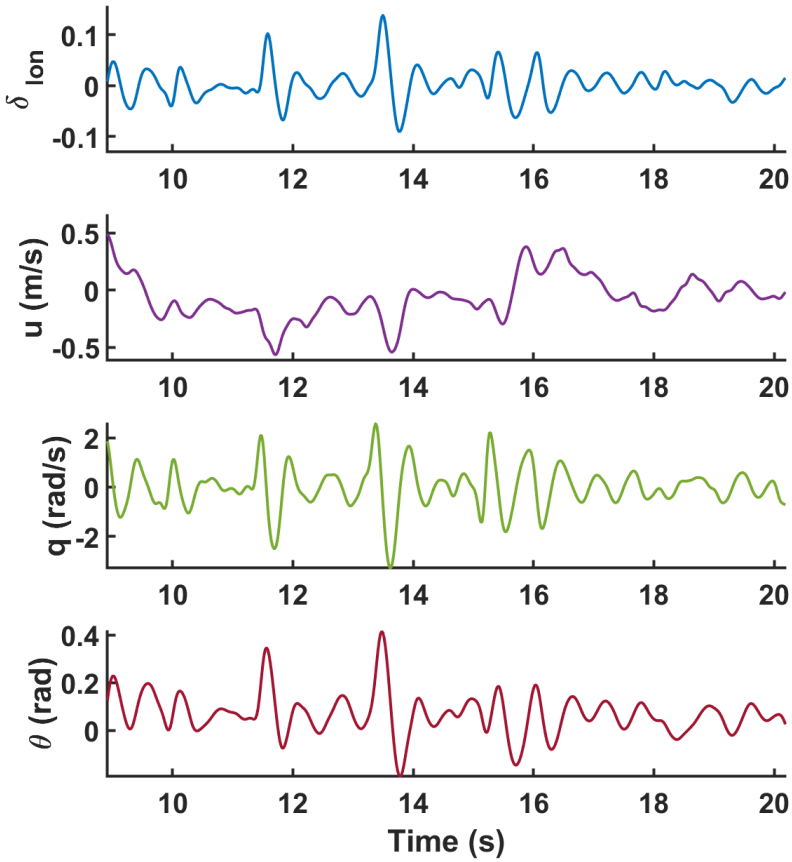

Figure 5.5: Representative example of longitudinal perturbation data.

modes, guaranteeing that any cross-correlation or couplings manifested in the data. If a set of flight data didn't contain all perturbations it was still used to generate matrix parameters, but cross-terms for the unexcited modes were weighted less compared to those generated by full data sets. This was another reason why the single-nose configuration was difficult to model — the vehicle would drift out of the interrogation space before all perturbations could be provided.

5.4 Results

Over 50 sets of data were collected in this manner and analyzed using the SIDPAC® code. Time history data of each element in **u** and **x** is known as a regressor. Finding the non-zero entries in the A and B matrices associated with each state was done using the SIDPAC® software suite

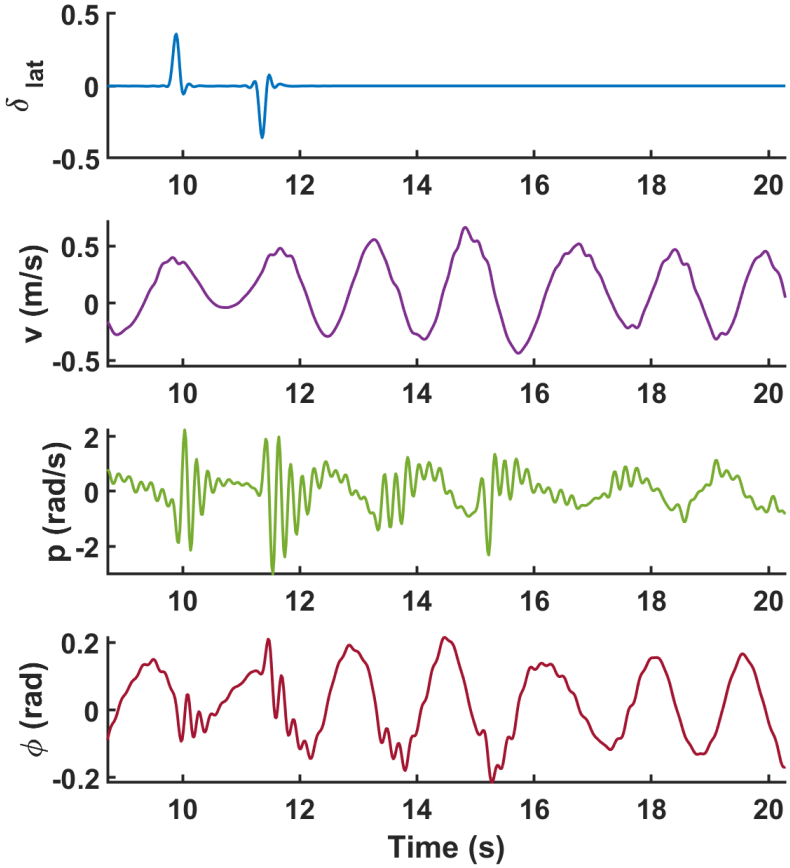

Figure 5.6: Representative example of lateral perturbation data.

developed by Dr. Morelli for MATLAB®[120]. Time domain methods were used because space constraints and the system's marginal stability limited performance of frequency sweeps and other maneuvers with enough spectral content for frequency domain analysis[114]. SIDPAC® relates the regressors to time history of a particular state derivative through a linear combination using a least squares fit to calculate the coefficients, the A and B matrix parameters. Through a process known as stepwise regression, the parameters were chosen in each row of the matrix by including or excluding a given regressor in the linear combination. To help the researcher select meaningful and well-correlated coefficients, the code returns two primary quality metrics. One is F-ratio and the other is coefficient of determination (R^2). F-ratio is a measure of how well variance in the data

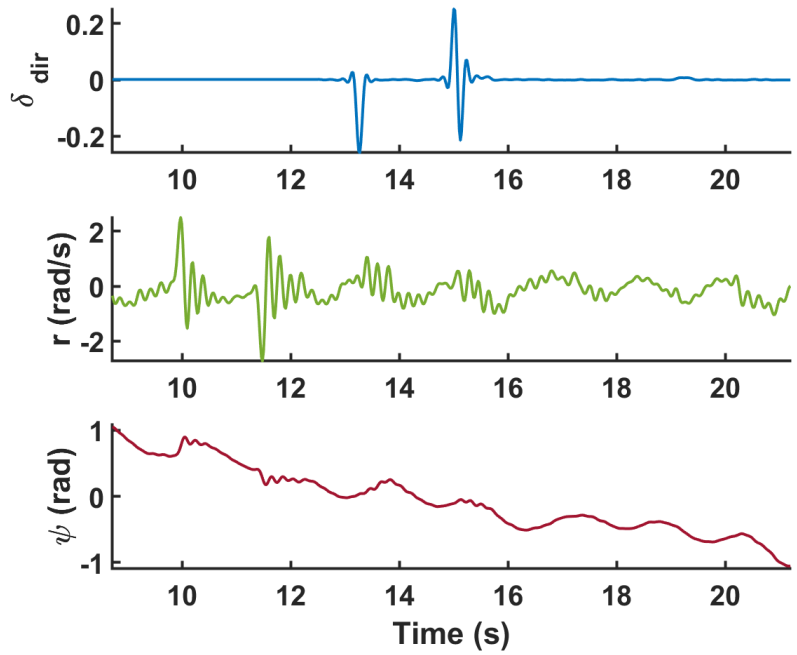

Figure 5.7: Representative example of directional perturbation data.

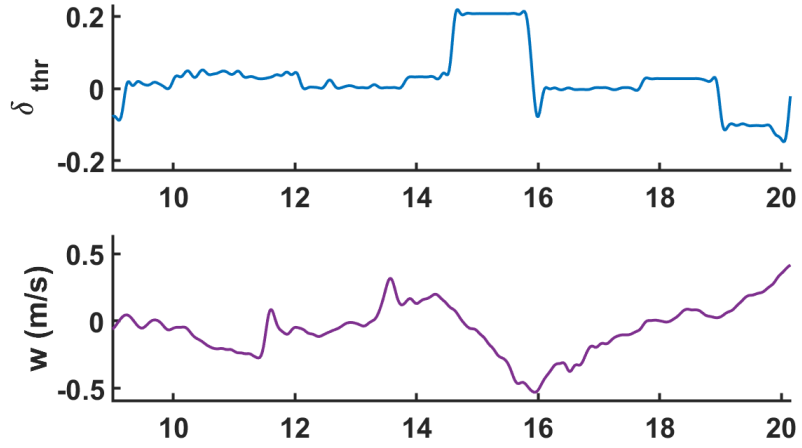

Figure 5.8: Representative example of heave perturbation data.

is explained by a regressor. A value above 20 gives a 95% confidence level that changes in the state are correlated with changes in the regressor. If a selected regressor generated a value less than this,

it was excluded. Coefficient of determination quantifies error between the state derivative data and a model composed of the selected regressors. It is expressed as a percentage between 0 and 100 — higher is better. However, consideration of these metrics required some engineering judgment and knowledge of the system to appropriately determine which parameters to include. Both metrics change as regressors are added or removed and there is no hard cut-off for R^2 values nor does a high F-ratio always mean a parameter should be included. Certain elements of the matrix can be excluded based on vehicle symmetry and drift. Experimental idiosyncrasies can also induce a correlation where there is none. On the other hand, there were several times when a parameter did not appear well correlated for a set of data, but in the aggregate emerged often enough that it was included in the averaged results.

It was this fusion of an academic prudence and quantitative investigation that produced the model structure shown below. The associated values for these parameters are shown in table 5.1. The discerning reader might wonder how the two values for yaw control, $\delta_{dir_{TV}}$ and $\delta_{dir_{\Delta T}}$, were separated in the controls matrix given that they excite the same vehicle mode. One half of the experiments were run with one type of yaw control and the other half with the other type. A matrices extracted from both were very similar, as was expected, and the only differences in the B matrices were the indicated parameters. Because of the linear nature of this analysis they can be combined into one B matrix.

$$
\begin{pmatrix} \dot{u} \\ \dot{v} \\ \dot{w} \\ \dot{p} \\ \dot{q} \\ \dot{r} \\ \dot{\phi} \\ \dot{\theta} \\ \dot{\psi} \end{pmatrix} = \begin{bmatrix} X_u & 0 & 0 & 0 & 0 & 0 & 0 & -g & 0 \\ 0 & Y_v & 0 & 0 & 0 & 0 & g & 0 & 0 \\ Z_u & 0 & 0 & 0 & Z_q & 0 & 0 & 0 & 0 \\ 0 & L_v & 0 & L_p & 0 & L_r & 0 & 0 & 0 \\ M_u & 0 & M_w & 0 & M_q & 0 & 0 & 0 & 0 \\ 0 & N_v & 0 & N_p & 0 & N_r & 0 & 0 & 0 \\ 0 & 0 & 0 & 1 & 0 & 0 & 0 & 0 & 0 \\ 0 & 0 & 0 & 0 & 1 & 0 & 0 & 0 & 0 \\ 0 & 0 & 0 & 0 & 0 & 1 & 0 & 0 & 0 \end{bmatrix} \begin{pmatrix} u \\ v \\ w \\ p \\ q \\ r \\ \phi \\ \theta \\ \psi \end{pmatrix}
$$

$$
+ \begin{bmatrix} 0 & 0 & 0 & 0 & 0 \\ 0 & 0 & 0 & 0 & 0 \\ 0 & Z_{lon} & 0 & 0 & Z_{thr} \\ L_{lat} & 0 & 0 & 0 & 0 \\ 0 & M_{lon} & 0 & M_{dir_{\Delta T}} & M_{thr} \\ N_{lat} & 0 & N_{dir_{TV}} & N_{dir_{\Delta T}} & 0 \\ 0 & 0 & 0 & 0 & 0 \\ 0 & 0 & 0 & 0 & 0 \\ 0 & 0 & 0 & 0 & 0 \end{bmatrix} \begin{pmatrix} \delta lat \\ \delta lon \\ \delta dir_{TV} \\ \delta dir_{\Delta T} \\ \delta thr \end{pmatrix}
$$

Having derived a linear model it is important to see its predictive capabilities. To that end, a set of data not included in the averaged model was used to recreate state derivatives with it. figs. 5.9 and 5.10 show the measured derivatives with the model output overlaid. In general, the model tracks well, particularly larger disturbances. There is a slight amplitude mismatch in the higher frequency content, but overall the model does a good job of predicting vehicle dynamics giving confidence in the conclusions drawn from it.

Table 5.1: Parameter Values for Coaxial-Nose Twin-Cyclocopter

Parameter	Value	% STD
Longitudinal Mode		
X_u	-0.60	25
M_u	4.25	38
M_w	4.71	44
M_q	-1.75	43
M_{lon}	-248.84	11
$M_{dir_{\Delta T}}$	-41.46	33
M_{thr}	21.16	43
Lateral Mode		
Y_v	-0.50	32
L_v	-19.55	36
L_p	-2.73	29
L_r	18.60	24
L_{lat}	76.77	45
Directional Mode		
N_v	-11.83	32
N_p	-11.14	19
N_r	-2.35	26
N_{lat}	-33.45	45
$N_{dir_{TV}}$	50.88	59
$N_{dir_{\Delta T}}$	25.51	40
Heave Mode		
Z_u	-0.48	37
Z_q	-0.30	52
Z_{lon}	5.47	40
Z_{thr}	-2.81	37

5.5 Discussion

Many things can be learned from analyzing the derived model. One of the best places to start is the structure itself. An emergent pattern across lateral and directional equations show that they are gyroscopically coupled by the cyclorotors. Longitudinal and heave modes also contain a common set of parameters. But the lack of shared terms between these mode pairs shows that they are decoupled from each other. This is proven by a deeper analysis of the model and in the Eigenvalue analysis of the A matrix, shown in Table 5.2.

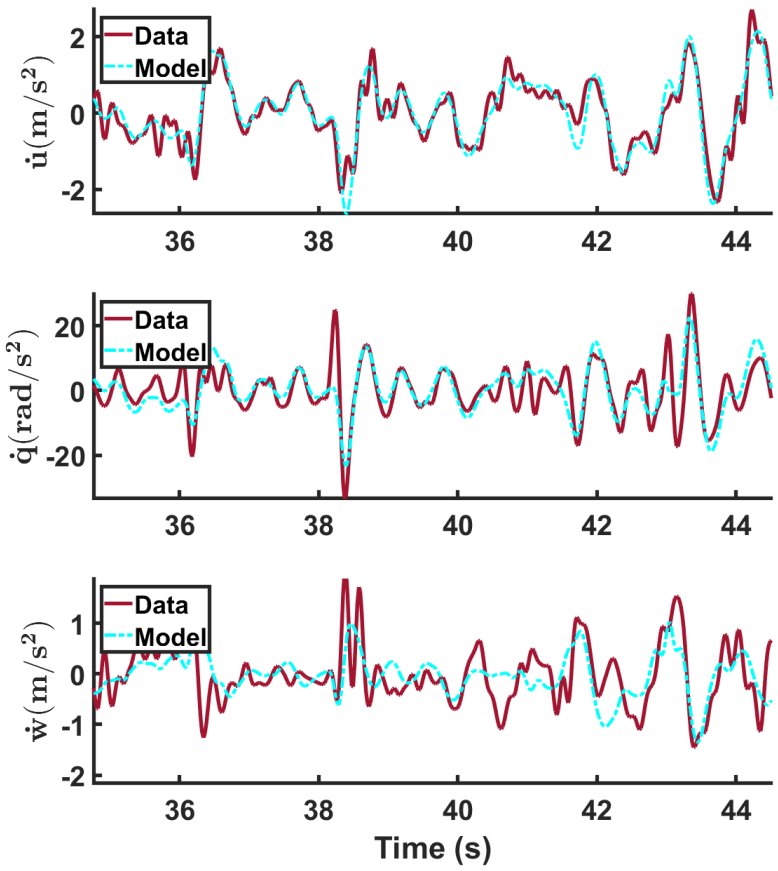

Figure 5.9: Sample of longitudinal data with model prediction.

Table 5.2: Eigenvalues for open loop dynamics

Mode	Eigenvalue	Frequency (Hz)
Lateral: p	-2.18 $\pm$ 13.89i	2.24
Lateral, Directional: v, p, r	-0.61 $\pm$ 3.58i	0.58
Longitudinal: u, q	0.74 $\pm$ 3.11i	0.51
Longitudinal: u, q, θ	-4.33	—
Longitudinal, Heave: u, w	0.50	—

There are two open-loop stable lateral oscillatory modes (one high frequency and one low), an unstable oscillatory longitudinal mode, a stable longitudinal mode, and a neutrally stable transla-

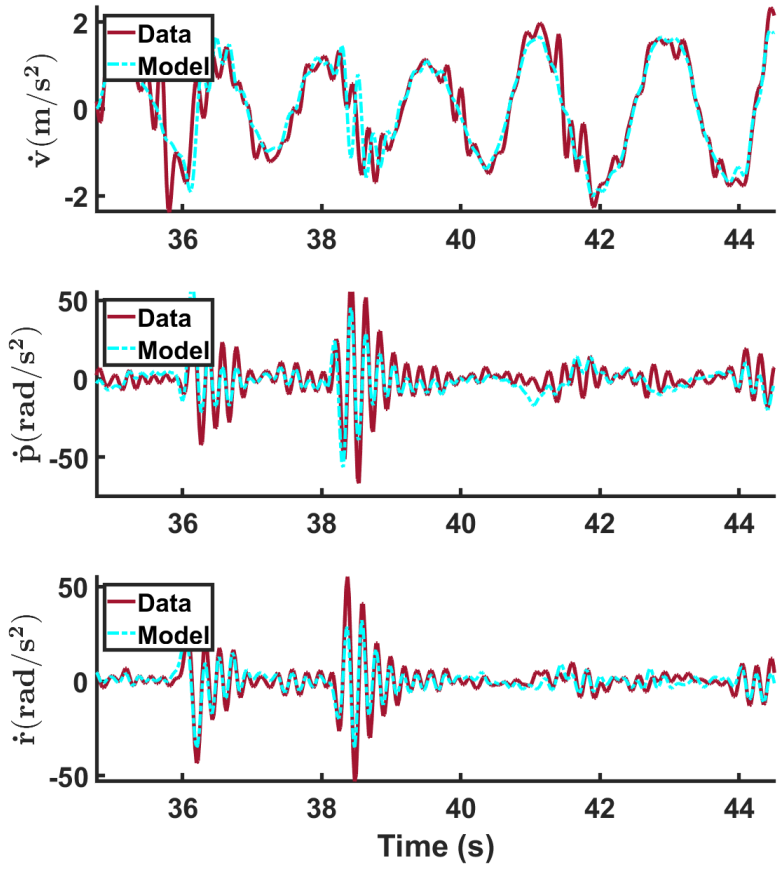

Figure 5.10: Sample of lateral data with model prediction.

tional mode. Of additional interest is the impact of the feedback gains on flight stability and these modes. Taking the same gains used during data collection and plugging them into the formula, $A - BK$, the closed-loop poles can be calculated. A comparison of the open and closed loop poles is plotted in Fig. 5.11. It can be seen that the gains on pitch shift the longitudinal modes barely into the stable region, validates that feedback gains were reduced as much as possible. The lateral/directional modes remain unchanged because there were no gains in those degrees of freedom.

The two gravity terms in longitudinal and lateral translations represent acceleration in those directions due to a non-zero attitude and were recovered with high accuracy during modeling. The bottom three rows of the matrix are kinematic relations between body frame angular accelerations

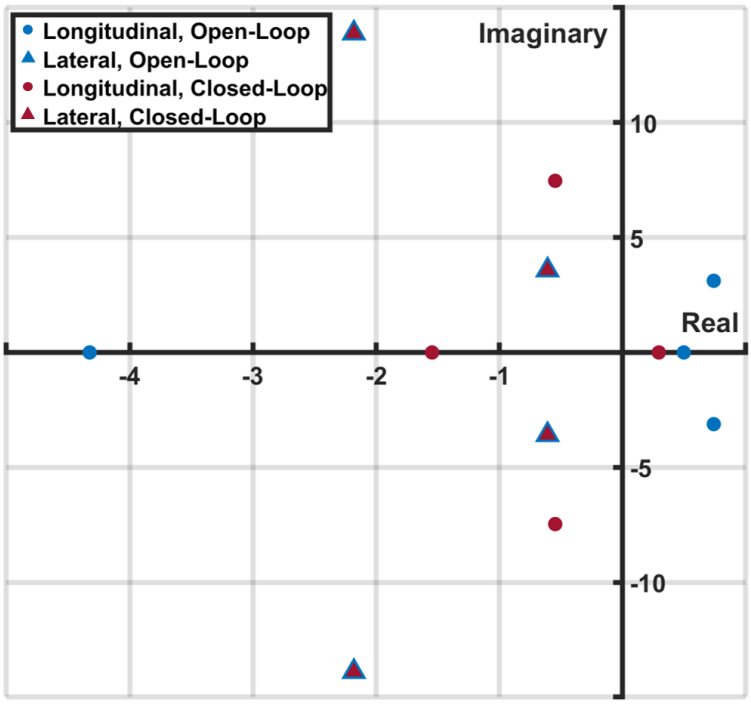

Figure 5.11: Pole plot showing open-loop poles and the impact of gains on stability.

and the change in Euler angles. To reflect the linear nature of the model these are set to 1, but real values were consistently above 0.95 indicating that the vehicle remained within the linear region of the small angle approximation. Next, each mode will be discussed individually in a bit more detail.

5.5.1 Longitudinal Mode

The previously mentioned efforts to decouple pitch from other modes of flight by balancing the vertical-axis nose propeller torque are apparent in the isolated nature of this mode. Absence of an M_p term demonstrates that there was no gyroscopic coupling between roll and pitch from a vertical angular momentum. The corresponding term in lateral mode, L_q, is also missing. The most characteristic feature about this degree of freedom is its instability. The singular unstable mode for this model is present here, hence the need for feedback control during flight. Explanations for the M_u and M_w terms in the A matrix are readily apparent. The positive M_u is caused by the resulting

moment from the increased nose-propeller lift in edge-wise flight. And the M_w parameter can be explained by a change of inflow during vertical motion. With a positive w perturbation (vehicle descent), the inflow velocity through the propeller decreases resulting in an increased angle of attack and thrust. Increased thrust at the nose prop will create a pitch-up moment (Fig. 5.12).

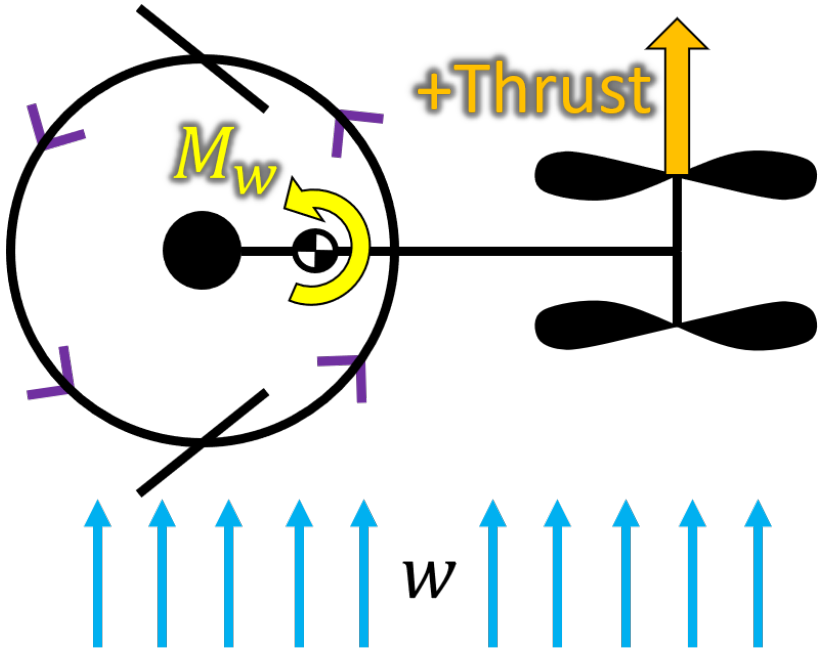

Figure 5.12: Schematic showing free flow for a positive w velocity and the resulting moment.

5.5.2 Lateral and Directional Mode

Gyroscopic coupling present in these modes is a well documented characteristic of cyclorotors because of their angular momentum. The off-diagonal terms, L_r and N_p, being nearly an order of magnitude higher than the damping terms along the diagonal shows how much vehicle motion was driven by this effect.

More interestingly, one characteristic unique to this cyclocopter MAV was learned through these efforts, revealed by the L_p term. Other twin-cyclocopters that have been built and flown were open-loop unstable in roll [28]. The vehicle in this study however, was stable in the roll

degree of freedom and it is the negative L_p term that was responsible. The physical cause is not fully understood, but it is hypothesized that the reason lies in design differences between the cyclorotors. Most prominently, the micro-cyclorotors possessed cantilevered blades open on one side rather than doubly-supported blades with rotating plates at each end. Being open at the blade tip permitted axial flow into the cantilever cyclorotor whereas it is blocked in the previous double-endplate design by the spinning structure. Evidence of this can be seen in the spanwise flowfield measurements that were presented in Chapter 3. A small amount of inflow that was parallel to the axis of rotation was induced by the cantilevered design (Fig. 5.13). Along with the transverse inflow, this axially ingested air made a 90° turn and aligned with the downwash of the rotor. Added lateral flow due to sideslip might increase lift by increasing mass flow through the rotor. As the vehicle rolled (ϕ) a lateral velocity (v) developed. This sideslip velocity forced more air into the open end of the rotor that was then acted upon by the blades. This increased mass flow might have augmented lift for the windward cyclorotor and decrease lift for the leeward one. Because both lift vectors are vertical, such a phenomenon would lead to a pure rolling moment opposite the sideslip direction, producing a stabilizing mode similar to what dihedral angle does for a fixed-wing aircraft. This could have been the origin for the low frequency roll mode witnessed in Fig. 5.6 that has a period of about 2 seconds.

Along with this low frequency mode there was an accompanying, naturally occurring high frequency one. The presence of both was a complicating factor during normal flight testing operations, specifically feedback gain tuning. If feedback was too low there was not enough control to damp out the low frequency mode. But too much feedback led to the excitation of the high frequency mode. Consequently, roll and yaw gains had to be tuned carefully in the balance between these limits.

5.5.3 Heave Mode

A couple of intriguing things can be seen in the heave degree of freedom. First is the lack of a damping term (Z_w) along the diagonal which means that vertical damping was so small that it did not appear in the linear analysis. Second is the presence of a vertical force in forward flight (Z_u)

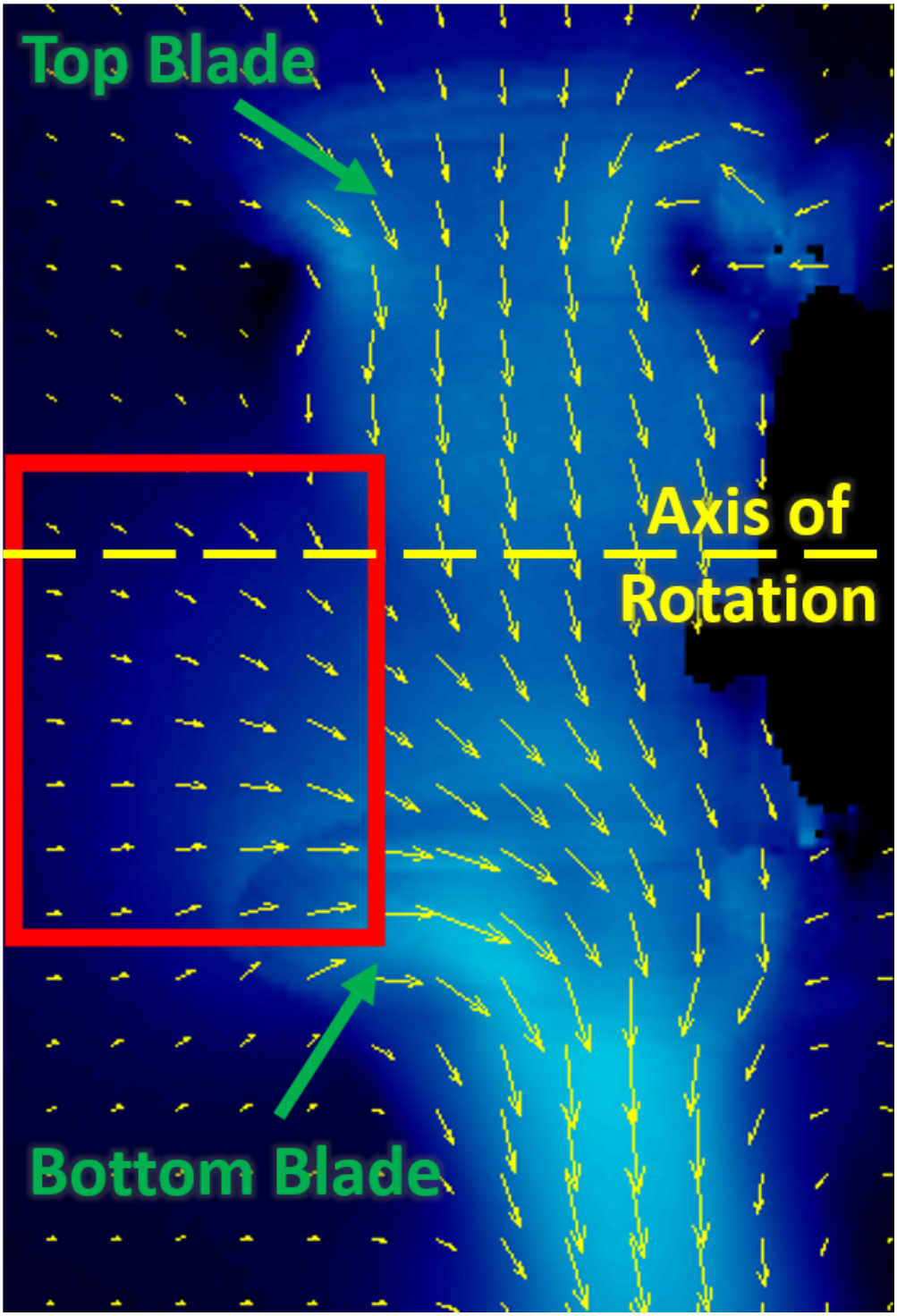

Figure 5.13: PIV snapshot with region of induced axial flow shown inside the red box.

caused by virtual camber. As discussed in Chapter 1, Fig. 5.14 (reprinted here for convenience) shows how this changes the effective chordline of the rotating blades at top and bottom locations, represented by the red lines. When subjected to a forward velocity (u) the top blade experiences a larger change than the bottom one. The outcome is a greatly increased lift on the lower blade and slightly decrease the lift on the upper one, producing a net positive lift. If the direction of flow is reversed (*i.e.*, the cyclocopter moves backwards) total lift is reduced.

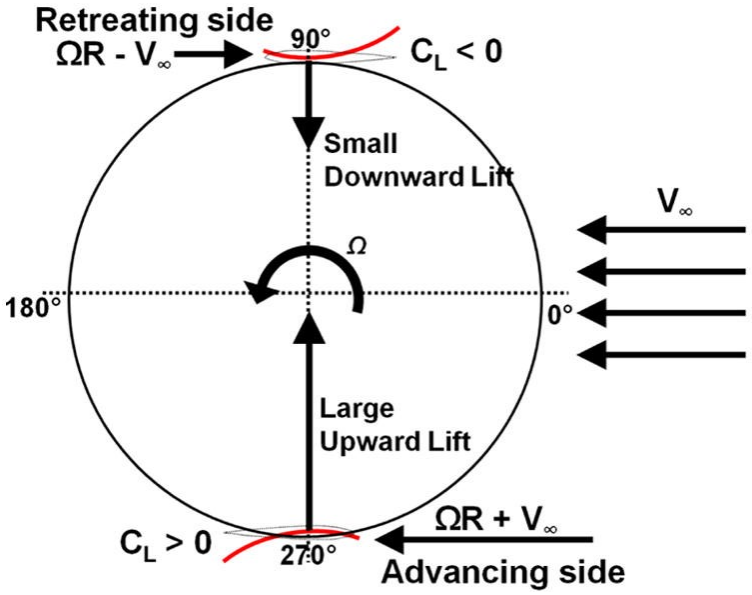

Figure 5.14: Cyclorotor experiencing increased lift in forward flight[23].

Naturally, an increased lift in the rear of the vehicle should cause a negative pitching moment. However, there was actually a positive pitching moment (M_u) in response to forward flight which must mean that some other physics was having a greater impact. Besides the increase in nose lift from edgewise flight, wake interaction could be responsible. When in forward flight ($+u$) the downwash of the upper propeller could be pushed away from the lower one, resulting in a cleaner flow and increased lift and hence, a positive pitching moment (Fig. 5.15). In the backward flight ($-u$) the body of the vehicle and the cyclorotors could be creating turbulent flow that moved towards the nose, interacting with the propellers and reducing lift which would cause a negative

pitching moment.

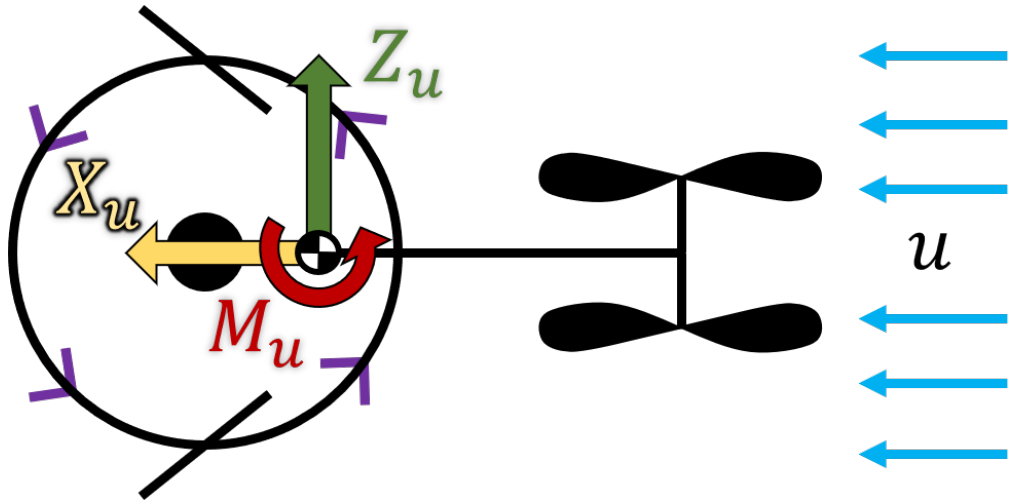

Figure 5.15: Total effective forces and moments created by a forward velocity.

5.5.4 Control Methodology

There are several important insights that can be gained from the extracted control parameters as well. Taking a look at the B matrix, the most obvious thing to note is the relative magnitude of pitch inputs (M_{lon}) with respect to all other entries. Being substantially larger means pitch was more sensitive to controls. A second peculiarity is the presence of M_{thr} which represents a pitching moment when throttle command was given. This reflects the varying response rates of the cyclorotors relative to the nose propellers. The torque and lift of the cyclorotors responded faster than the lift of the nose rotors. It is for this reason that using combined nose rotor and cyclorotor RPM changes was a more effective pitch control. Because only nose rotor lift was used for pitch, there was a heaving motion associated with it (Z_{lon}). In normal operation, when properly balanced by the calibration equations, total thrust would not change. Similarly, when using differential torque to control yaw, pitch commands were modified by calibration equations to eliminate the accompanying torque ($M_{dir_{\delta T}}$).

One parameter that might seem counter intuitive is N_{lat}. There should have been no yaw torque produced by a roll command considering measures were taken to ensure cyclorotor thrust vectors were vertical. But roll was controlled by differentially changing the RPM of the cyclorotors. Cyclorotor thrust vector direction varies with RPM as a byproduct of the rotational nature and flow interaction within the rotor. On larger cyclorotors the phase difference between maximum pitch amplitude and lift is around 15°, but for the micro-cyclorotor this phase was 45° at operating RPM consequently enhancing the impact of any RPM changes. Therefore, a varying RPM tilted the lift vectors and is the reason why the yaw moment generated by a roll command (N_{lat}) is approximately the same magnitude as the thrust vectoring yaw control itself ($N_{dir_{TV}}$).

Although the model was formulated for hovering flight, several coefficients hint at increased forward flight performance if thrust vectoring is utilized for translation. Simultaneously tilting the lift vectors forward or backward would result in an almost pure longitudinal translation. As explained earlier, forward velocity (u) would increase lift production because of virtual camber (Z_u) and reduce power consumption of the cyclorotors (see Fig. 1.44). The vehicle would also attempt to pitch up (M_u); therefore, nose rotor RPM could be reduced as well. The net effect could make translational forward flight via thrust vectoring an energy efficient mode for the cyclocopter.

5.5.4.1 Yaw Control Comparison:

When only using differential torque to control yaw, the number of actuators was reduced to 4, as the servos are only holding a position. But in the thrust vectoring case all 6 actuators were used. The only apparent downside to the differential torque method seemed to be reduced yaw effectiveness ($N_{dir_{\Delta T}} < N_{dir_{TV}}$) and the introduction of a pitching moment when giving a yaw command ($M_{dir_{\Delta T}}$), the effect of which can be ameliorated in the control software. So for a minimal increase in controller complexity and vehicle weight, the performance of a twin-cyclocopter can be greatly enhanced by a using coaxial nose instead of a single propeller.

5.6 Concluding Remarks

In this chapter the hovering flight dynamics of a 33-gram micro twin-cyclocopter were investigated by the formulation of a linear, time-invariant dynamic model. This twin-cyclocopter had a unique design and configuration that made it distinct from other flight-capable cyclocopters and significantly improved handling qualities as a result. The developed LTI model encapsulates many of these benefits in a simplified set of equations representing a complex dynamical system. A mode and frequency analysis was done on the system of equations that showed two stable modes and one unstable oscillatory mode. Altogether, a couple of predominant lessons were learned from this study, which are enumerated below:

1. The coaxial-nose micro-twin cyclocopter was inherently stable in roll and yaw with two oscillatory modes. It was the first cyclocopter flown to exhibit these properties and to have flown stable without feedback stability augmentation in the roll mode.

2. Balancing the vertical angular momentum caused by the nose propeller thoroughly decoupled longitudinal and heave modes from lateral and directional modes.

3. Lateral and directional modes were dominated by gyroscopic couplings.

4. Smart control techniques can take advantage of the coupled nature of the cyclocopter to improve performance.

5. Forward flight using thrust vectoring could be an energy efficient mode for the cyclocopter.

6. Micro Quad-Cyclocopter Development

Alongside the endeavor to balance yawing torque using a coaxial nose rotor, balancing pitching torque with additional cyclorotors was also investigated. Eliminating vertical angular momentum with the coaxial nose rotor had a demonstrably positive impact on cyclocopter handling quality without the need to develop an entirely new vehicle; therefore, a more extensive design program was conducted to created a vehicle with all angular momenta balanced. Nose rotors on the twin cyclocopter served the dual purpose of countering the cyclorotor reaction moment and providing extra lift, however, counter-rotating cyclorotors could perform the same functions instead. There are many cyclocopter configurations that can lead to zero total angular momentum by using multiple cyclorotors of the same size rotating at the same speed or several sizes of cyclorotors at different speeds. From the possible options, only those that used one size of cyclorotor were considered for this study to avoid developing two different cyclorotors for a single vehicle.

6.1 Quad-Cyclocopter Configuration

Available cyclorotor configurations were then limited to two options, either a “+" or an “H", which have both been documented in previous literature (Fig. 6.1). In the “+" configuration (Fig. 6.1a) the opposing rotors spin in opposite directions. While in hover or low-speed flight this produces a highly mobile vehicle capable of longitudinal and lateral translation with no change in body attitude. However, with respect to oncoming air flow one rotor is forward-spinning while the other is back-spinning, which causes a thrust differential as advance ratio increases because of the virtual camber effect similar to advancing and retreating sides of a conventional helicopter rotor. The “H" configuration (Fig. 6.1b) sacrifices lateral translation ability for improved forward flight speed and performance. Opposing rotors now spin in the same direction while the front and back pairs counter-rotate. Rotation is such that the outermost blades are descending and the innermost blades are ascending, which is necessary to help with pitching moment. Consider a nose-up pitch maneuver. To generate a pitch-up moment the RPM of the front rotors is increased,

while that of the rear rotors is decreased (Fig. 6.2). Not only does this change the cyclorotor lift, but it also imparts a torque on the body due to the change in RPM. When the rotors are spun towards the center (Fig. 6.2a), the torque change resulting from the increase to front RPM and decrease to rear RPM results in a nose-down pitching moment, opposite the intended direction. If torque magnitude is high enough, the vehicle may even briefly pitch down before pitching up. By spinning the cyclorotors away from the center (Fig. 6.2b), reaction torque is now in the desired pitching direction and works in concert with the lift differential to pitch the vehicle[35].

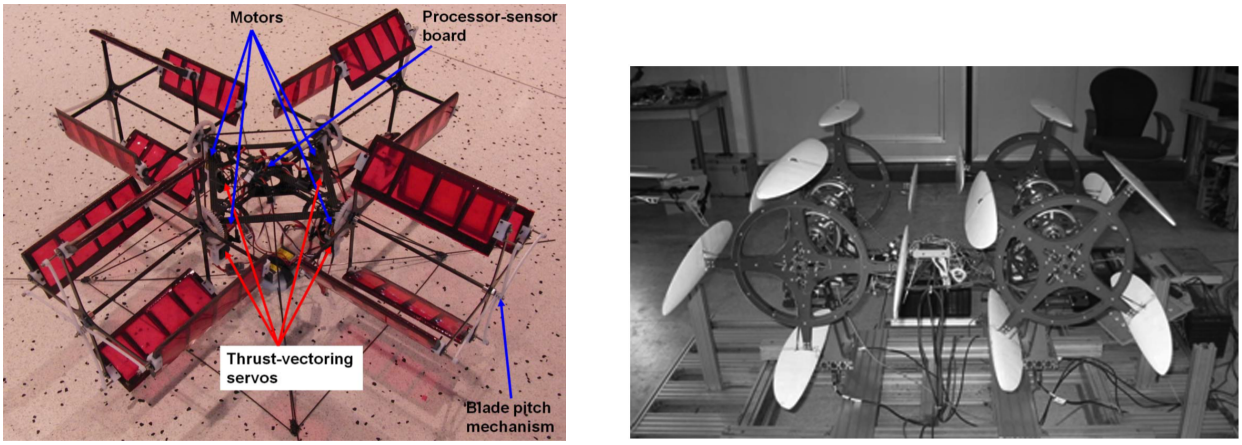

(a) “+" arrangement[26]. (b) “H" arrangement[17].

Figure 6.1: Two possible configurations of quad-cyclocopter.

Alternatively, if carefully designed, all four cyclorotors can spin in the same direction and the CG can be placed appropriately to counteract all pitching moments as demonstrated by CycloTech GmbH (Fig. 6.3)[121]. Forward flight would then increase lift equally on all four cyclorotors, but pitch attitude becomes integral to trim.

Ultimately, the counter-rotating “H" configuration was chosen for development because of the increased forward flight performance over the “+" arrangement and the fact that the ability to freely change pitch attitudes is not allowed by the co-rotating design. The 58-gram quad-cyclocopter is shown in Fig. 6.4 next to the other cyclocopters developed during this project. Stability and

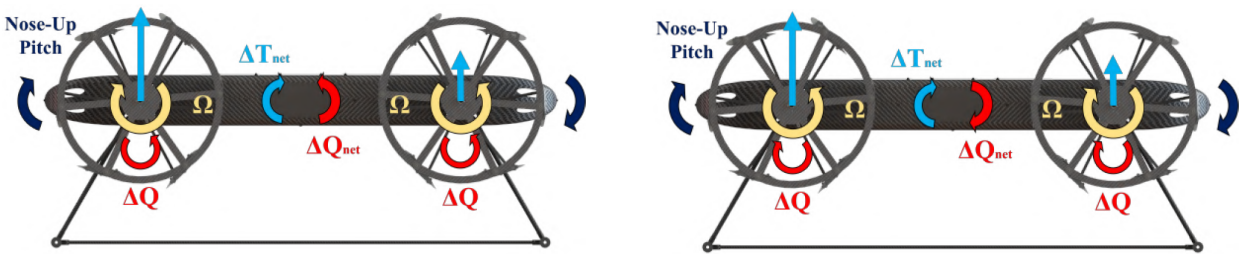

(a) Inward rotation of cyclorotors with opposing reaction torque and lift differential pitching moment.

(b) Outward rotation of cyclorotors with cooperating reaction torque and lift differential pitching moment.

Figure 6.2: Effect of possible cyclorotor spin directions in a quad-cyclocopter performing a nose-up pitching maneuver.[35].

Figure 6.3: 83 kg quad-cyclocopter developed by CycloTech with 4 co-rotating cyclorotors[36].

control were achieved through 8 independent actuator parameters (4 motor RPMs and 4 servo angles), which made it an over-actuated system and provided the quad-cyclocopter several unique capabilities as discussed in the subsequent sections. Development began by following a similar process as the twin-cyclocopter, starting with an initial concept and survey of available COTS parts followed by an estimation of total vehicle weight from the selected hardware. By mirroring the existing twin-cyclocopter about its lateral mid-line a quad-cyclocopter could be created. However, an aircraft produced in this manner would weigh more than the lifting capacity of 4 of the existing

cyclorotors. As a result, new cyclorotors capable of more thrust had to be designed.

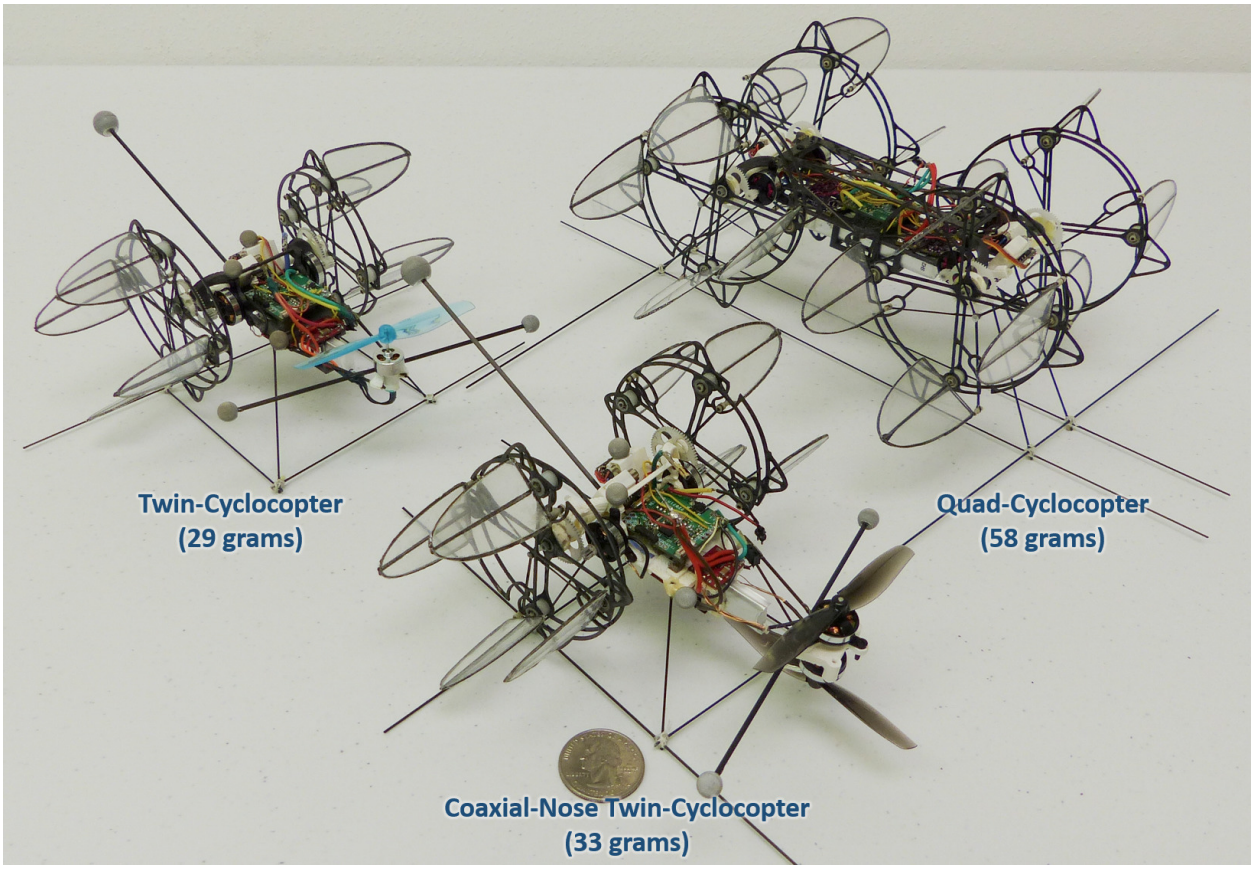

Figure 6.4: Hover-capable cyclocopters developed by the author.

6.2 Cyclorotor Development

Re-estimating vehicle weight incorporating a larger cyclorotor design and supporting hardware produced a tentative gross weight of 55 grams. Each cyclorotor then had to provide more than 13 grams, hence required thrust per cyclorotor was set to 16 grams at an operating speed of 4000 RPM, an increase of 60% from the cyclorotors used on the twin-cyclocopter. Going by the scaling laws mentioned in Chapter 1, increasing cyclorotor size by about 25% would meet this requirement. Allowing for some margin of safety, an increase of 30% was decided upon from which a 69% gain in thrust would be expected for a maximum total thrust of 68 grams. This logic established

a radius of 1.3 inches for the cyclorotors to be used on the quad. Furthermore, it was assumed that this size difference was small enough to not alter findings from Chapter 2 and therefore, the same rotor design parameters were used: 1.618 aspect ratio blades with elliptical planform, flat plate airfoils, 0.8 c/R, and $\pm 45^{\circ}$ symmetric pitching. Fabrication of the blades and linkages was accomplished using the same Teflon™ mold process, but linkage length now accounted for the 0.018-inch elongation that occurred after removal from the mold. Figure 6.5 shows a completed rotor and the scaled design. Note that the thickness of the carbon fiber frames and structural members was not changed, only the overall size was scaled.

6.3 Vehicle Design

The MAV as first constructed weighed 58 grams and is the smallest quad-cyclocopter ever built (Fig. 6.4). A weight breakdown is given in Table 6.1. Four of the 1.3-inch radius cyclorotors were mounted on an airframe made of Selective Laser Sintered (SLS) glass-filled nylon that held all of the electronics between the rotation axes. Mounting and arrangement of the rotors was similar to that on the twin-cyclocopters and mirrored about the YZ-plane to form the structure for the counter-rotating rotors. Length of the vehicle was kept as short as possible to remain compact except for a small buffer distance between the rotors. Not including landing gear, the aircraft measured $6.6" \ L \ \times \ 7.7" \ W \ \times \ 4.4" \ H$. A carbon fiber top plate and carbon fiber struts were added to resist cyclorotor torque and vibrations. More powerful motors were required to drive the larger cyclorotors, as such the Hobbyking AP-02 7000 kV motors were replaced with AP-03 7000 kV ones, but the XP-3A ESCs remained. Single stage gears transferred power at a ratio of 5.45:1, which was selected after testing a range of gear ratios. Table 6.2 shows the results of the transmission testing with the chosen ratio producing the highest thrust and efficiency. The flight controller was the same ELKA-R described in Chapter 4. Two 240 mAH LiHv battery cells underneath the chassis were connected in parallel to provide 1-cell, 3.85 V power to the system.

During flight testing the vehicle had limited endurance that prohibited any further investigation as a result of two shortcomings 1) battery voltage drop and 2) under-performing cyclorotors. Voltage drop under load from the batteries was not anticipated when sizing the cyclorotors meaning the

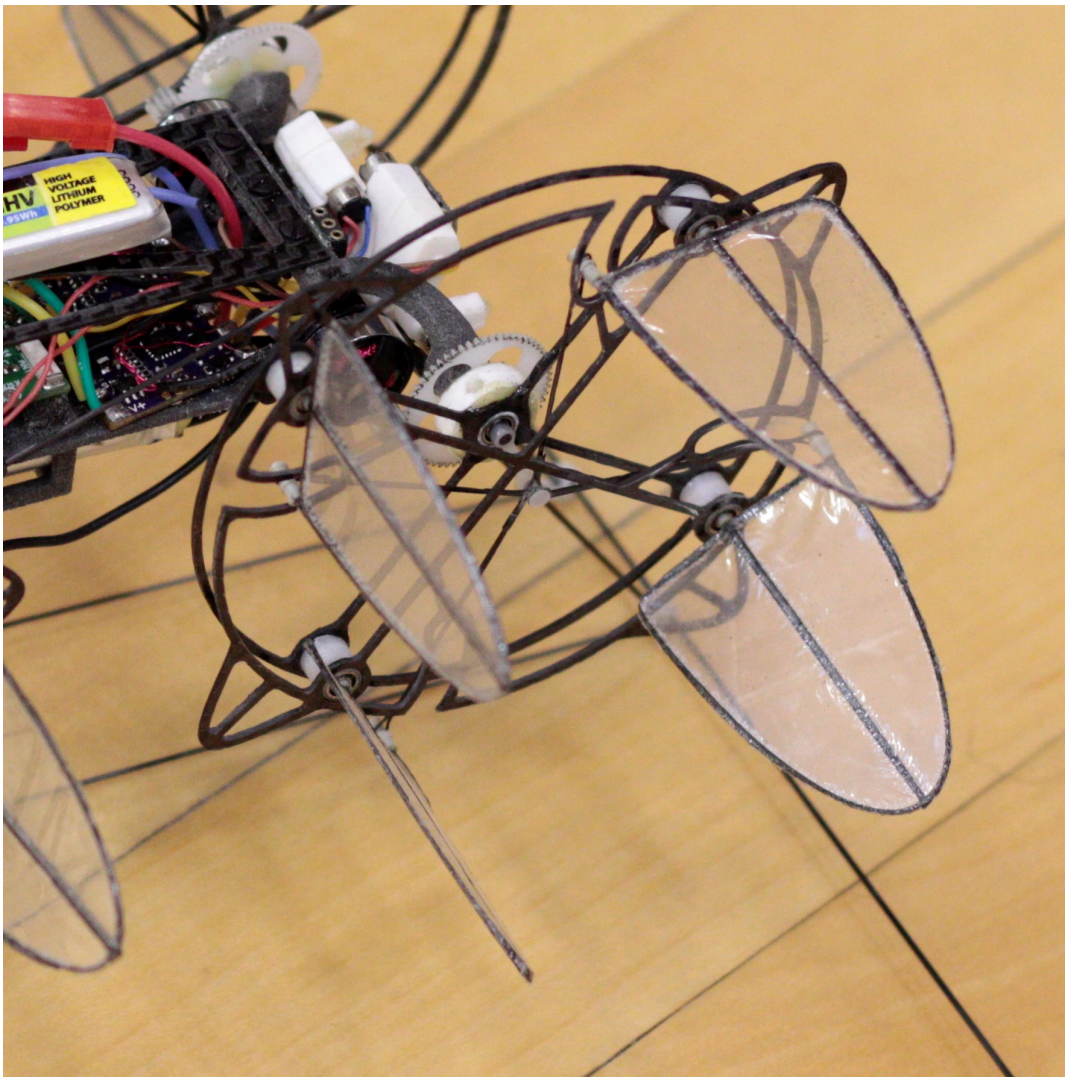

Figure 6.5: Cyclorotor with 1.3 in radius on a quad-cyclocopter.

vehicle could lift off initially, but would then slowly descend as the voltage dropped below what was required to stay aloft.

To address the under-performing rotors the electrical system was reconfigured to have the motors powered by a 2-cell battery pack while servos and flight controller were powered with a separate 1-cell battery. The two parallel 240 mAH LiPo cells were replaced by two 260 mAH LiHv batteries wired in series for the motors and a single 240 mAH LiHv cell was affixed to the top for the servos and flight controller. The XP-3A ESCs were swapped for DYS XSD7A ESCs to

Table 6.1: Component Weight Breakdown of 58-gram Quad-Cyclocopter.

Component	Weight g	Total %
Motors + Transmission	13.4	23
Digital Servos	5	9
Cyclocrotors	14.4	25
Structure + Wires	8.7	15
LiPo Batteries	12.4	21
Electronics	4.1	7
Total	58	100

Table 6.2: Gear ratio testing results for AP-03 and 1.3 in radius cyclorotor.

Pinion-Wheel Teeth	Gear Ratio g	Max RPM	Max Thrust g	Max Electrical Power W	Power Loading N/W
12-60	5	4240	16	6.2	25.4
11-60	5.45	4200	16.7	5.5	29.8
12-70	5.83	4100	15.2	5.2	28.9
10-60	6	4000	13.9	5.1	26.6
11-70	6.36	3900	14.1	4.8	28.6
9-60	6.67	3800	12.8	4.6	27.4
10-70	7	3840	12.9	4.1	30.7
9-70	7.78	3470	9.9	4.0	24.1

handle the additional current. Cumulatively, these alterations added 12 grams to vehicle mass and greatly increased the power available to the motors (Fig. 6.6). As a percentage of vehicle weight, the reconfigured quad-cyclocopter had more excess thrust than either of the previously discussed twin-cyclocopters.

6.4 Attitude Control

The magnitude and direction of thrust from each of the four cyclorotors could be controlled independently with changes to motor RPMs and servo angles, giving 8 control parameters. By combining changes in magnitude and thrust the aircraft could be commanded to roll, pitch, and yaw along with several other unique maneuvers afforded to it by the over-actuated nature. A roll

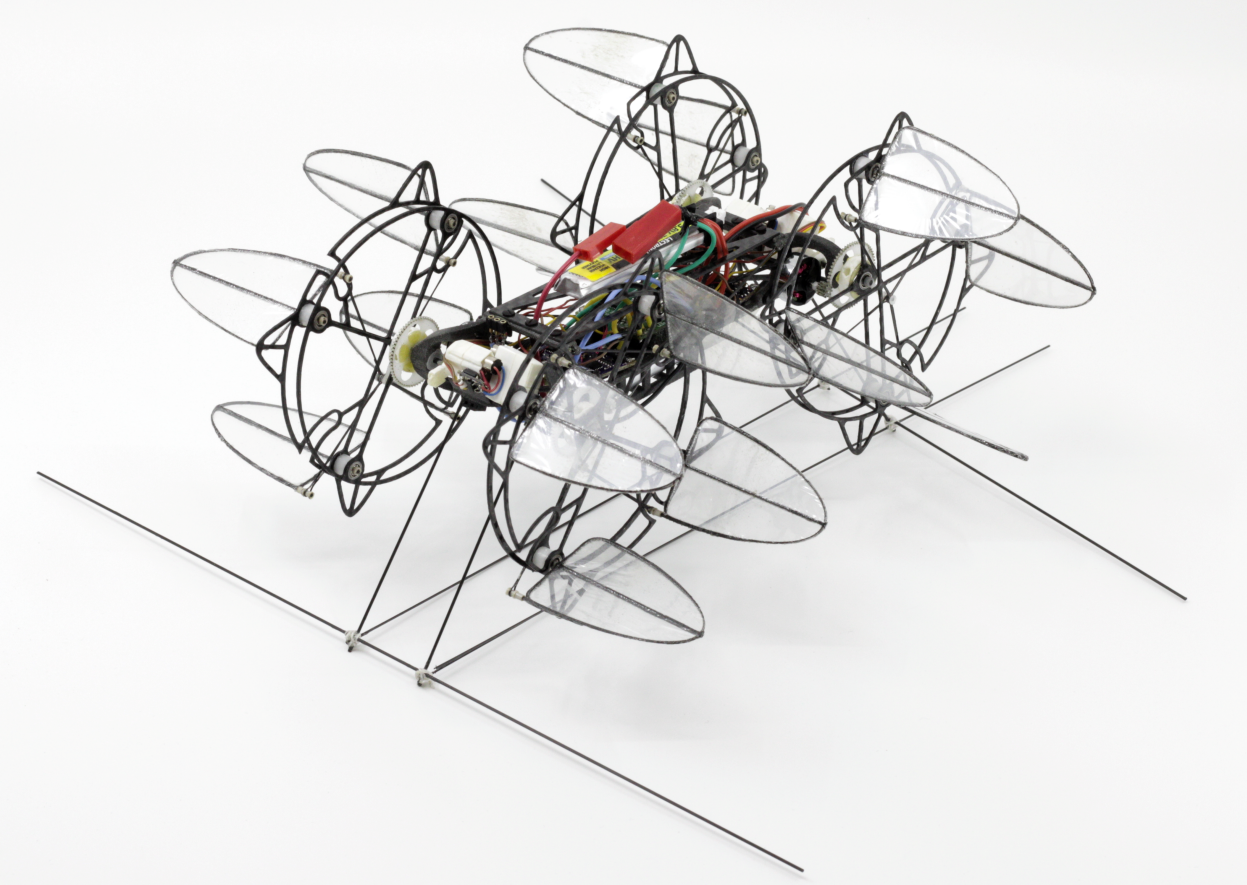

Figure 6.6: 70-gram quad-cyclocopter.

moment was generated by increasing motor RPMs on one side and reducing them on the other to create a lift differential (Fig. 6.7). Similarly, a differential between fore and aft motor RPMs would generate a pitching moment because of the change in lift and torque (Fig. 6.8). Yaw was controlled by tilting the thrust vectoring servos forward on one side and backward on the other (Fig. 6.9).

Angling all the thrust vectors in the same direction produced a pure longitudinal translation with no change in pitch attitude (Fig. 6.10). Specific to the quad-cyclocopter was the ability to perform a point hover within a range of different pitch attitudes. Figure 6.11 shows how the thrust vectors were skewed simultaneously with a change in pitch to achieve a hovering trim at a non-zero body attitude only limited by the servos' range of motion. Another possible maneuver not explored in this work is a pure lateral translation which would have required a modification of

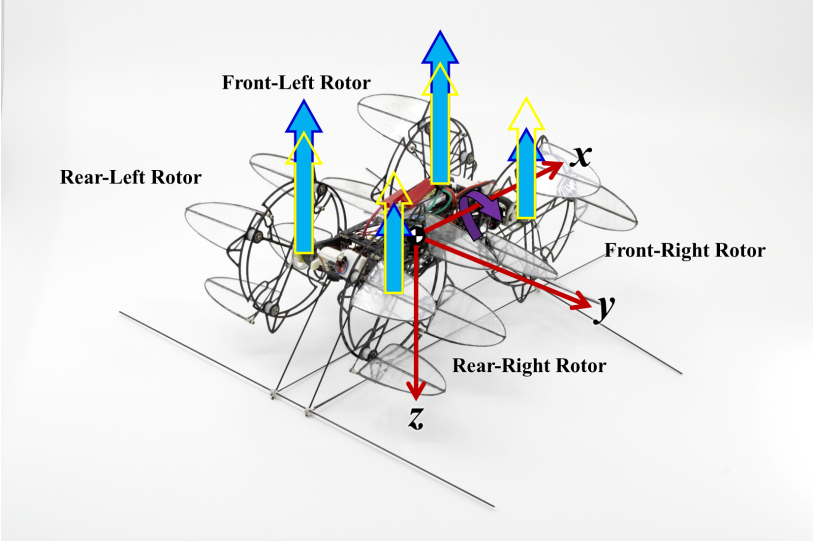

Figure 6.7: Differential RPM generating a positive rolling moment.

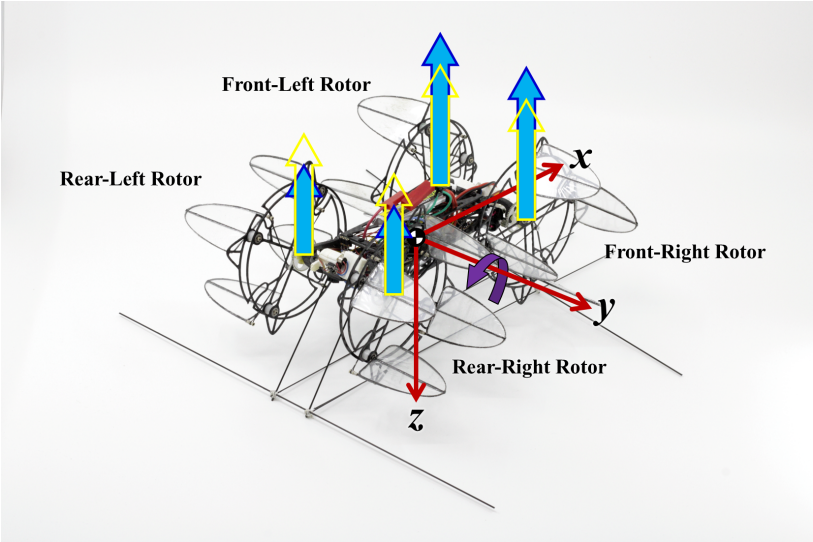

Figure 6.8: Differential RPM and torque being used to create a positive pitching moment.

the quad-cyclorotor design. If the front cyclorotors were swept backward and the rear cyclorotors swept forward (or vise versa) the servos could be used to produce a pure lateral force on the body by pointing the thrust vectors towards each other on one side of the body and away on the other (Fig. 6.12). Longitudinal forces would be canceled out and only a side force in one direction would be imparted. Maximum side force amplitude would be determined by sweep angle of the

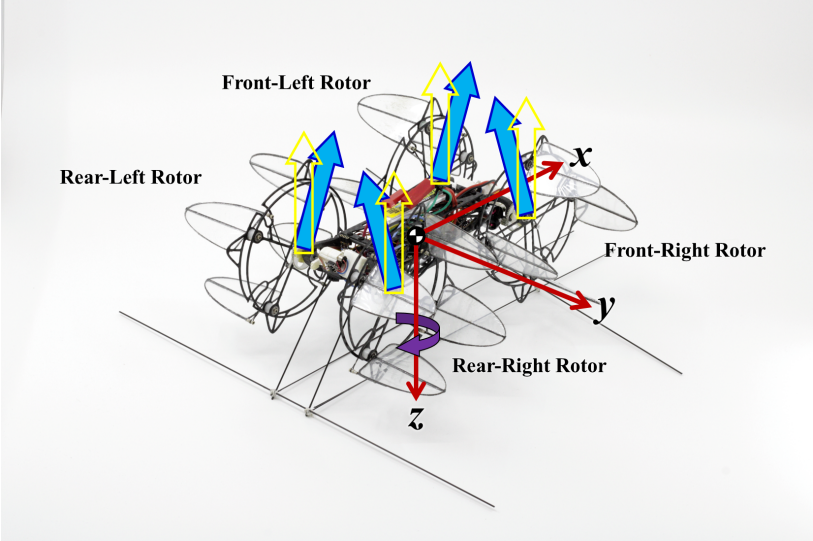

Figure 6.9: Differential thrust vectoring being used to generate a positive yawing moment.

cyclorotors at the cost of forward flight performance, whereas a 90° sweep angle would produce a "+" configuration quad-cyclocopter.

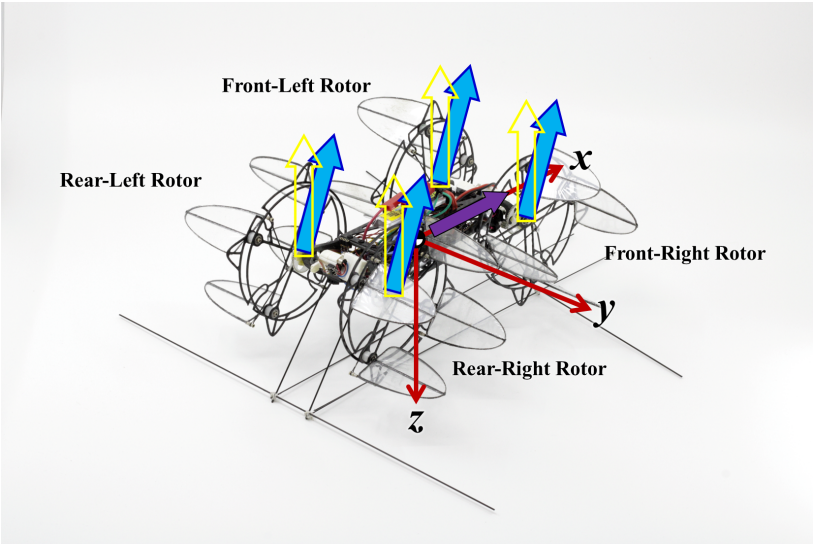

Figure 6.10: Simultaneous thrust vectoring being used to generate a longitudinal force.

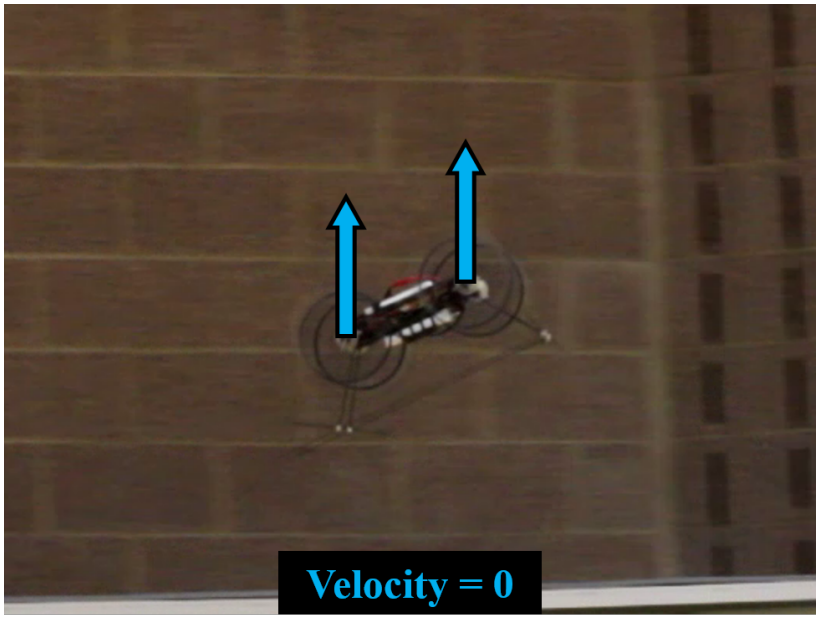

Figure 6.11: Hover in a non-zero body attitude achieved via thrust vectoring.

6.5 Flight Testing

Making the quad-cyclocopter flight-ready followed a similar process as the twins. Beginning by using the single-axis yaw stand, all of the thrust vectors were adjusted until perfectly vertical (Fig. 6.13). Afterwards hopping flights were performed with no feedback to trim out roll and pitch biases. Once vertical ascension was confirmed, the controller gains could be added to the inner rates PID loop. Onboard feedback was commanded using the same PPID loop structure described in Chapter 4, though simplified due to the absence of gyroscopic couplings and controls asymmetry eliminating the need for feed-forward gains or calibration equations. Roll and pitch attitude gains were added after the rate loop was tuned and well behaved. The transmitter pitch stick commanded either a pitch attitude or a longitudinal translation with a switch to toggle between the two modes that could be actuated mid-flight. Figure 6.14 shows the vehicle in forward flight using thrust vectoring (Fig. 6.14a) and pitching commands (Fig. 6.14b). Longitudinal translation stick inputs were fed directly to the servos with no feedback on position, longitudinal velocity, or longitudinal acceleration. A trim setting was included that allowed the pilot to set a desired pitch attitude in

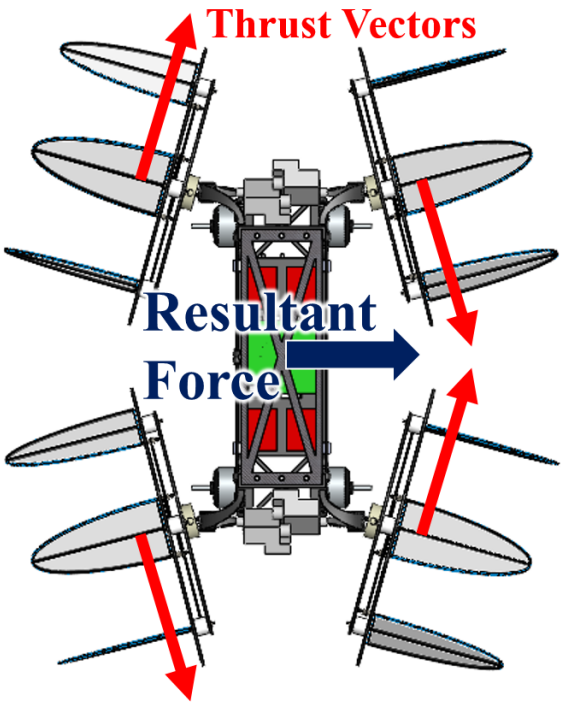

Figure 6.12: Top-down view of side force production by cyclorotors with 15° sweep angle.

hover separately from the stick inputs.

Although more mechanically complex than the twin-cyclocopters, the time and effort required to achieve controlled maneuvering flight with the quad-cyclocopter was less than the twins. Lacking the dynamical complexity caused by unbalanced angular momenta, stability and controls algorithms could be simplified in tandem with flight testing procedures. Ref. [122] shows a video of the quad-cyclocopter flying and performing maneuvers. Well-behaved controls and more consistent flights will allow for further investigation of the unique capabilities available to a quad-cyclocopter.

6.6 Concluding Remarks

In the process of studying how unbalanced angular momenta affect cyclocopter handling qualities, a quad-cyclocopter concept was developed to create a vehicle with net zero angular momen-

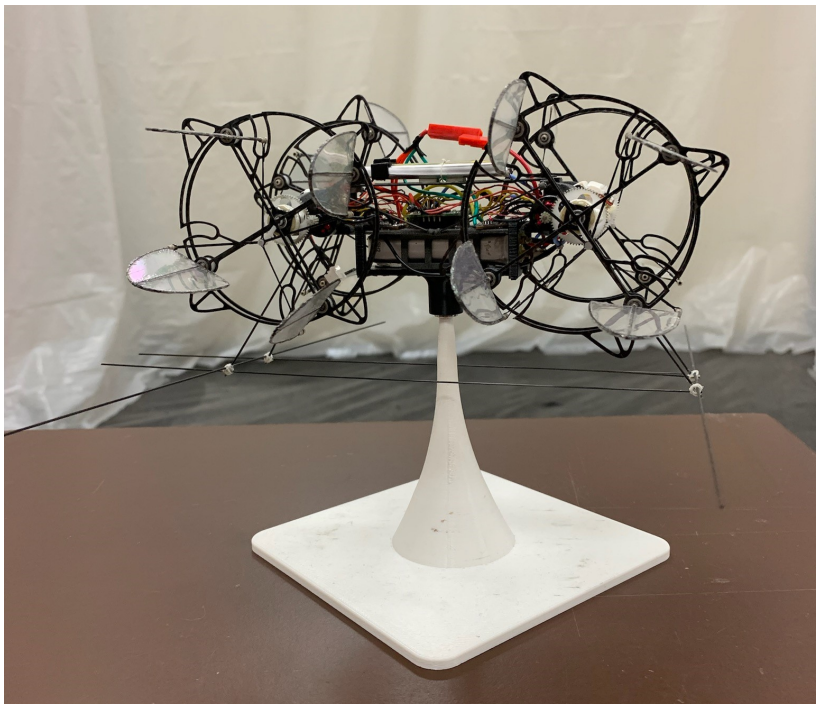

Figure 6.13: Micro quad-cyclocopter mounted on single degree of freedom yaw stand.

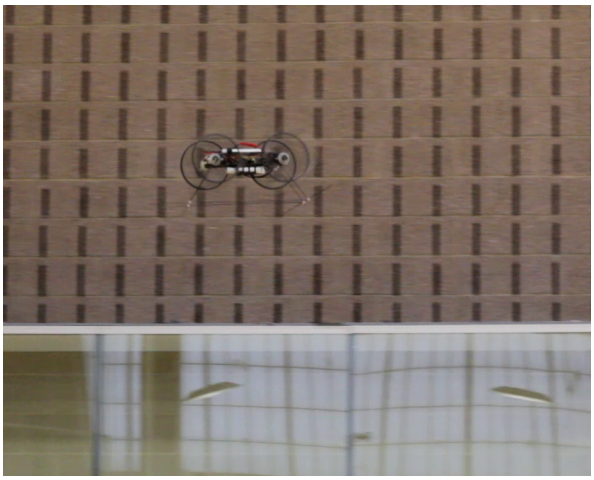

(a) Thrust vectoring being used to translate with a level attitude (motion is left to right).

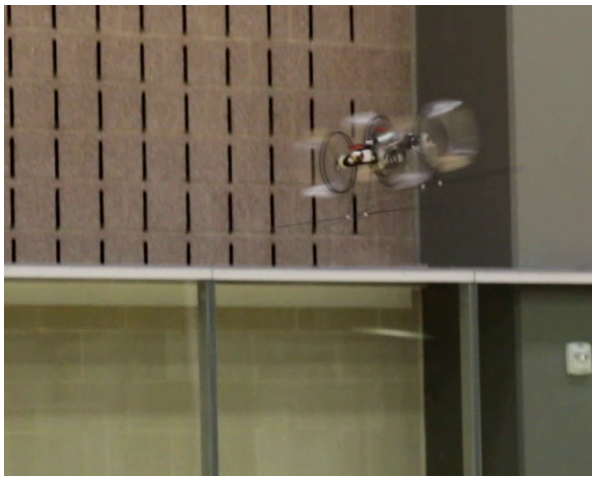

(b) Pitch attitude being used for forward flight (motion is right to left).

Figure 6.14: Micro quad-cyclocopter exhibiting two different methods for creating longitudinal motion.

tum along all axes. In order to realize a flight-capable vehicle the optimized cyclorotor had to be scaled up by 30%, however, the same design parameters were used. Four of these cyclorotors were incorporated into an “H" configuration cyclocopter that weighed 70 grams in its final iteration. Eight independent control parameters were utilized to stabilize the vehicle while performing maneuvers only possible because of the over-actuated nature they afforded. Flight testing showed that quad-cyclocopter was more well behaved and had superior flight performance over the twin-cyclocopters. Some important findings of this development process are listed below:

1. Eliminating all angular momenta allowed for the simplification of flight controller software by removing the need to compensate for gyroscopic couplings or asymmetrical controls.

2. The independent control parameters on a quad-cyclocopter can be combined in various ways to perform several unique maneuvers atypical of traditional hovering MAV. Pure longitudinal translation at a level body attitude and a point hover at multiple different pitch attitudes were demonstrated.

3. All active controls were achieved using only motors or servos without mixing the two. Not having multiple actuator types in a single control methodology meant that no allowance had to be made for differing response times or control authority. Hover attitude modulation used both motors and servos in concert was a pitch trim state adjustment, not an active control.

4. Improved handling and flight quality was observed with the quad-cyclocopter resulting from the over-actuation (eight independent control parameters), altered dynamic properties, and increased excess thrust.

7. Summary and Conclusions

Adoption of UAVs has expanded rapidly in the past decade with the advent of modern microelectronics pioneering use cases in ever more inventive ways. However, exploration of smaller and smaller aircraft has encountered the physical limitations that low Reynolds number flight imposes; specifically, the disadvantageous scaling of physical parameters and reduced efficiency of airfoils. MAV performance is hindered to such a degree that adoption of these tiny fliers is mostly relegated to toys. Research is being done on a broad range of topics such as electronic/electrical systems, controller design, and low Reynolds number aerodynamics, to overcome these shortcomings. With the pursuit of more effective UAVs came a resurgence of interest in the cyclorotor concept. Immature as a technology, cyclorotors required fundamental research before a flying vehicle incorporating them could be built. But once academic findings revealed the design principles behind cyclorotor construction several flight-capable cyclocopters were developed. Efforts at basic functionality progressed to investigations into vehicle dynamics and controls.

The research delineated in this paper studied the fundamental aeromechanics, dynamics, and control of cyclocopters through an experimental approach at a scale smaller than any prior research. Existing empirical data was scant and the limited understanding of low Reynolds number cyclorotor aerodynamics inhibited building reliable models. Therefore, producing and testing hardware generated data without the uncertainties inherent in theoretic computations. By grasping how cyclorotor performance changes at reduced scales cyclorotor-based MAVs can be tailored to encapsulate the potential benefits offered by this novel lift generation device, ultimately engendering more capability in them than traditional designs. The remainder of this chapter summarizes the process and key findings.

The project started with a cyclocopter concept that embodied the DARPA's MAV definition from 1997, described in Chapter 2. Compact and aerodynamically clean, this concept acted as a guide for the following design efforts beginning with the development of a micro-scale cyclorotor, which was the heart of the vehicle. Size and thrust requirements constrained the cyclorotor to a 1

in rotor radius and a maximum thrust of 10 grams at an operating speed of 4000 RPM ($\sim$11,000 Re). A cantilevered blade design was chosen to reduce parasitic drag from rotating structures at the blade tips. In order to optimize the remaining variables for the intended application a parametric study was conducted to investigate the design space. Cyclorotor parameters studied were blade size, number of blades, symmetric blade pitch kinematics, and blade aspect ratio. Blades with flat plate airfoils were made using a mold-layup process capable of producing consistent results. Total force perpendicular to the rotation axis and motor torque was measured for a range of each parameter up to the operating RPM. Thrust vs RPM and disk loading vs power loading plots were generated for each test and used to select the combination of parameters that could generate the required thrust in the most efficient manner. High pitch amplitudes (40°–45°) and high c/R (0.8) were found to improve rotor performance across a range of rotor solidity likely due to dynamic pitching effects and large leading edge vortex structures that delayed blade stall. Total lift per unit blade area decreased with the number of blades because of the increased inflow. The final cyclorotor configuration incorporated 4 elliptical planform blades at $\pm$45°pitch with a 1.618 aspect ratio and a 0.8 in root chord.

Having completed the optimization of a cyclorotor with a unique design, a deeper understanding of the peculiar aerodynamics was sought through flowfield measurements. Chapter 3 details particle image velocimetry experiments on a 2-bladed cyclorotor that revealed a highly complex velocity field within and around it. Data was collected on the chordwise plane perpendicular to the axis of rotation at 60% span and on the vertical spanwise plane bisecting the rotor. Evident in both was the vortex-dominated character of the flow. In the chordwise measurements, large leading edge vortices displayed asymmetry in size and strength between the top and bottom halves of rotation because of the variations in inflow, virtual camber, blade interference, and downwash effects that changed blade aerodynamic conditions at every azimuthal location. It was noted that the flow stayed attached even at very high geometric pitch angles. Curvilinear trailing wakes and a skewed rotor downwash were also observed. Spanwise measurements showed large tip and root vortices that created 3-dimensional flow along almost the entire span of the blades. Once shed,

these vortices convected downwards; those from the top blade would impinge on the lower blade while those from the bottom blade would create a contracted, undulating wake. Downwash beneath the rotor occurred almost entire inboard of the 50% spanwise location. One feature unique to the micro-cyclorotor was a small quantity of inflow being drawn into the rotor along the axis of rotation. These experiments emphasize the need for a deeper understanding of the aerodynamic mechanisms responsible for cyclorotor thrust production.

Using the optimized micro-cyclorotor, a twin-cyclocopter was constructed that had a single nose rotor, weighed 29 grams, and had no dimension greater than 6 inches making it the smallest cyclocopter ever built. Chapter 4 covers the design and development of this unconventional vehicle along with subsequent improvements. A control algorithm that used motor RPMs and servo angles to modulate cyclorotor thrust magnitude and direction together with nose rotor thrust was implemented on a custom 1.7-gram flight controller to stabilize the vehicle. While capable of sustained hovering flight, gyroscopic couplings and controls asymmetry intrinsic to the design restricted the ability to maneuver because of unbalanced angular momenta in the lateral and vertical directions. The effects of nose rotor angular momentum were apparent in flight, although in larger cyclocopters they were not explicit indicating that scaling down exacerbated the effect. The single nose rotor was replaced with a coaxial nose rotor to balance vertical angular momentum and permit further experimentation. The coaxial-nose twin-cyclocopter exhibited superior flight qualities due to decoupled dynamics and increased control authority. Improved feedback algorithms were able stabilize the vehicle and enabled the maneuvering capability necessary for the next phase of research.

Chapter 5 explains the extraction of a linear time-invariant flight dynamics model from the coaxial-nose cyclocopter using system identification techniques. Cyclocopters only recently achieved hovering flight relative to other aircraft and understanding of this nascent mode of flight means is still in its infancy. By quantifying the bare airframe dynamics of the cyclocopter, insight was gained about natural vehicle dynamics and controls effectiveness. The model can further be used to quantify maneuverability of the cyclocopter and to develop model-based control algorithms. Only

one other dynamics model has ever been derived from a flight capable cyclocopter and that was at larger scales and a substantially different design. The linear model developed for the coaxial-nose micro-cyclocopter revealed two stable lateral modes, an unstable longitudinal mode, and two neutrally stable longitudinal modes, making this the first cyclocopter to demonstrate passive roll stability. Moreover, the gyroscopic coupling between roll and yaw was quantified along with the relative control authority of the different controls techniques, including the two types of yaw control. Several other properties captured in the model intimate that cyclocopters could benefit in forward flight from a reduction in power consumption.

Finally, a quad-cyclocopter was designed and built to examine and compare how a cyclocopter would fly with no unbalanced angular momenta, discussed in Chapter 6. The coaxial nose rotor of the twin-cyclocopter balanced vertical angular momentum, however, the vehicle still experienced horizontal angular momentum from the cyclorotors. By using two pairs of counter-rotating cyclorotors a vehicle was built that had no unbalanced angular momenta. Larger cyclorotors had to be built that could produce more thrust to support the additional vehicle weight. The optimized cyclorotors were scaled up by 30% to a 1.3 in radius while retaining the same design parameters. A new control method harnessed the 8 independent actuators (4 motors and 4 servos) to stabilize and maneuver the vehicle. Additionally, over-actuation allowed the quad-cyclorotor to demonstrate pure longitudinal translation as well as hover at non-zero pitch attitudes.

7.1 Contributions to the State of the Art

This research examined fundamental aspects of cyclocopter aerodynamics using unique cyclorotor designs. Several flight worthy cyclocopters were built, one of which is the first of its kind. As a result this research made several important contributions to the field:

- Data was generated that quantified how design parameters affect cyclorotor performance at a previously unexplored MAV scale and Reynolds number regime (Re 11,000). These are the only experimental data taken on flight worthy hardware at these scales and show how different design parameters impact lift, drag, and power.

- Flowfield measurements were conducted using PIV on a cyclorotor with cantilevered blades revealing the complex aerodynamic features of a cyclorotor and how they develop over time. Flow structures particular to this design provided insight into the mechanisms of force production in a cyclorotor that helped to explain vehicle dynamics.

- The smallest cyclocopter ever was built (29 grams), and its unique flight dynamic properties were explored. Understanding gained from this vehicle was used to improve the design and control methodology of additional micro-scale cyclocopters, including a twin-cyclocopter with a coaxial-nose, which was the first cyclocopter to incorporate one.

- System identification was used to extract the only flight dynamics model of a cyclocopter at sub-100 gram scale. The inherent body dynamics and control authority of the actuators were quantified and represented in a linear state-space equation that encapsulated many characteristics of hovering cyclocopter flight.

- For the first time ever, passive stability in roll was demonstrated on a unique cyclocopter design through flight dynamics modeling and flight testing. Two stable oscillatory modes were observed in the roll degree of freedom, a high and a low frequency mode. All previous flight-capable cyclocopters required stability augmentation and active control in roll to remain airborne.

- The smallest quad-cyclocopter ever was developed and flight tested. It is one of two quad-cyclocopters to demonstrate forward flight or hover at a non-zero pitch attitude using thrust vectoring. As part of an exploration into gyroscopic effects on cyclocopter flight dynamics the quad-cyclocopter emphasized how important neutralizing or compensating for angular momentum is to flight quality.

7.2 Recommendations for Future Work

A practical, experimental approach was taken towards improving MAV performance with the application of cyclorotor technology. The endeavor produced many valuable insights into cyclo-

copter design and control by creating several of the limited number of flight-capable cyclorotor-based aircraft to date. However, in the process of elucidating fundamental aspects many more areas of potential inquiry were discovered that could aid in harnessing all of the benefits cyclorotors have to offer. Broadly, development of a cyclocopter flight dynamics model from first principles would help to explain many facets of cyclocopter flight and be useful when designing any future aircraft. To further understand cyclocopter design, analysis of hover-capable cyclocopters to quantify how changes in inertia, rotor angular momentum, CG placement, other mass properties, and the relative relationships between them affect flight dynamics could be performed. On controller design, more investigation of the unique control capabilities that cyclocopters possess would lead to better utilization of their over-actuated nature. In addition, more work needs to be conducted on cyclocopters beyond hovering flight. The exact reason for passive stability observed in the twin-cyclocopter should also be studied for aerodynamic insights and the potential to create other cyclocopters that replicate this property. As for cyclorotor design, knowing how axial inflow impacts performance could lead to the improvement of cyclorotor efficiency and could be used to augment aircraft dynamics. For example, the exterior end plate of a doubly supported cyclorotor could incorporate an airfoil that drives airflow into the rotor, possibly increasing lift. Furthermore, how angular velocity and acceleration affect instantaneous lift production of cyclorotor blades should be studied towards producing an optimized pitching kinematics. Up until now, considered kinematics have been limited by what can be generated by 4-bar, 5-bar, or cam systems, but if an optimal pitching schedule was found then a physical system to reproduce it could be designed. Likewise concerning cyclorotor design, knowing the location of time-averaged center of lift would be helpful in vehicle design and dynamic analysis. Lastly, there are many configurations of cyclocopters that have not been explored adequately which might display desirable performance.

REFERENCES

[1] McMasters, J. H. and Henderson, M. L., "Low-Speed Single-Element Airfoil Synthesis," The Science and Technology of Low Speed and Motorless Flight, NASA. Langley Res. Center The Sci. and Technol. of Low Speed and Motorless Flight, Pt. 1, January 1979.

[2] Mueller, T. J., "Aerodynamic measurements at low reynolds numbers for fixed wing micro-air vehicles," Technical report, NOTRE DAME UNIV IN DEPT OF AEROSPACE AND MECHANICAL ENGINEERING, 1999.

[3] Winslow, J., Otsuka, H., Govindarajan, B., and Chopra, I., "Basic Understanding of Airfoil Characteristics at Low Reynolds Numbers (104–105)," *Journal of Aircraft*, Vol. 55, (3), May 2017, pp. 1050–1061.
doi: 10.2514/1.c034415

[4] Benedict, M., *Fundamental Understanding of the Cycloidal-Rotor Concept for Micro Air Vehicle Applications*, phdthesis, University of Maryland, College Park, MD, December 2010.

[5] Foshag, W. F. and Boehler, G. D., "USAAVLABS Technical Report 69-13: Review and Preliminary Evaluation of Lifting Horizontal-Axis Rotating-Wing Aeronautical Systems (HARWAS)," techreport, Fort Eustis, Virginia, March 1969.

[6] Jones, G. E., "Proficient Professor," *Flying and Popular Aviation*, June 1941, pp. 39.

[7] Sachse, H., "Kirsten-Boeing Propeller," techreport 351, National Advisory Committee for Aeronautics, February 1926.

[8] "Precise and safe maneuvering," , January 2022.

[9] Pratt, F., "French Build a Paddle-Wheeler," *Popular Aviation*, May 1934, pp. 295.

[10] Wheatley, J. B. and Windler, R., "Wind-Tunnel Tests of a Cyclogiro Rotor," Technical Notes 528, NACA, May 1935.

[11] "History of the Cyclogyro," `http://rotoplan.narod.ru/history_e.htm`, June 2013.

[12] Iosilevskii, G. and Levy, Y., "Experimental and Numerical Study of Cyclogiro Aerodynamics," *AIAA Journal*, Vol. 44, (12), December 2006, pp. 2866–2870.
doi: 10.2514/1.8227

[13] Iosilevskii, G. and Levy, Y., "Aerodynamics of the Cyclogiro," 33rd AIAA Fluid Dynamics Conference and Exhibit, June 2003.
doi: 10.2514/6.2003-3473

[14] Kim, S., Yun, C., Kim, D., Yoon, Y., and Park, I., "Design and Performance Tests of Cycloidal Propulsion Systems," 44th AIAA/ASME/ASCE/AHS/ASC Structures, Structural Dynamics, and Materials Conference, April 2003.
doi: 10.2514/6.2003-1786

[15] Yun, C. Y., Park, I. K., Hwang, I. S., and Kim, S. J., "Thrust Control Mechanism of VTOL UAV Cyclocopter with Cycloidal Blades System," *Journal of Intelligent Material Systems and Structures*, Vol. 16, (11-12), December 2005, pp. 937–943.
doi: 10.1177/1045389x05057520

[16] Hwang, I. S., Hwang, C. S., Min, S. Y., Jeong, I. O., lee, C. H., and Lee, Y. H., "Design and Testing of VTOL UAV Cyclocopter with 4 Rotors," Presented at the American Helicopter Society 62nd Annual Forum, May 2006.

[17] Hwang, I. S., Min, S. Y., Lee, C. H., and Kim, S. J., "Development of a Four-Rotor Cyclocopter," *Journal of Aircraft*, Vol. 45, (6), November 2008, pp. 2151–2157.
doi: 10.2514/1.35575

[18] Min, S. Y., Lee, C. H., Seung, M. H., Kim, Y. S., Hur, C. M., and Kim, S. J., "Experimental Study of a Quadrotor Cyclocopter," *Journal of the American Helicopter Society*, Vol. 60, (3), July 2015, pp. 1–10.
doi: 10.4050/jahs.60.032010

[19] Lee, C. H., Min, S. Y., Lee, J. W., and Kim, S. J., "Design, Analysis, and Experimental Investigation of a Cyclocopter with Two Rotors," *Journal of Aircraft*, Vol. 53, (5), sep 2016, pp. 1527–1537.

doi: 10.2514/1.c032731

[20] Sirohi, J., Parsons, E., and Chopra, I., "Hover Performance of a Cycloidal Rotor for a Micro Air Vehicle," *Journal of the American Helicopter Society*, Vol. 52, (3), July 2007, pp. 263–279.

doi: 10.4050/jahs.52.263

[21] Benedict, M. and Chopra, I., "Design and development of an unconventional VTOL micro air vehicle: The Cyclocopter," Micro- and Nanotechnology Sensors, Systems, and Applications IV, edited by T. George, M. S. Islam, and A. Dutta, May 2012.

doi: 10.1117/12.919482

[22] Benedict, M., Gupta, R., and Chopra, I., "Design, Development, and Open-Loop Flight-Testing of a Twin-Rotor Cyclocopter Micro Air Vehicle," *Journal of the American Helicopter Society*, Vol. 58, (4), October 2013, pp. 1–10.

doi: 10.4050/jahs.58.042005

[23] Benedict, M., Jarugumilli, T., Lakshminarayan, V., and Chopra, I., "Effect of Flow Curvature on Forward Flight Performance of a Micro-Air-Vehicle-Scale Cycloidal-Rotor," *AIAA Journal*, Vol. 52, (6), June 2014, pp. 1159–1169.

doi: 10.2514/1.j052065

[24] Jarugumilli, T., Benedict, M., and Chopra, I., "Wind Tunnel Studies on a Micro Air Vehicle–Scale Cycloidal Rotor," *Journal of the American Helicopter Society*, Vol. 59, (2), April 2014, pp. 1–10.

doi: 10.4050/jahs.59.022008

[25] Adams, Z., Benedict, M., Hrishikeshavan, V., and Chopra, I., "Design, Development, and Flight Test of a Small-Scale Cyclogyro UAV Utilizing a Novel Cam-Based Passive Blade Pitching Mechanism," *International Journal of Micro Air Vehicles*, Vol. 5, (2), June 2013, pp. 145–162.

doi: 10.1260/1756-8293.5.2.145

[26] Benedict, M., Mullins, J., Hrishikeshavan, V., and Chopra, I., "Development of a Quad

Cycloidal-Rotor Unmanned Aerial Vehicle," *Journal of the American Helicopter Society*, Vol. 61, (2), April 2016, pp. 1–12.
doi: 10.4050/jahs.61.022005

[27] Shrestha, E., *Experimental Investigation of a MAV-Scale Cyclocopter*, Ph.D. thesis, University of Maryland, 2018.
doi: 10.13016/S6EN-WSUK

[28] Hrishikeshavan, V., Benedict, M., and Chopra, I., "Identification of Flight Dynamics of a Cylcocopter Micro Air Vehicle in Hover," *Journal of Aircraft*, Vol. 52, (1), January 2015, pp. 116–129.
doi: 10.2514/1.c032633

[29] Shrestha, E., Hrishikeshavan, V., Benedict, M., Yeo, D., and Chopra, I., "Development of Control Strategies for a Twin-Cyclocopter in Forward Flight," *Journal of the American Helicopter Society*, Vol. 61, (4), October 2016, pp. 1–9.
doi: 10.4050/jahs.61.042009

[30] Walther, C. M., Saemi, F., Benedict, M., and Lakshminarayan, V., "Symmetric Versus Asymmetric Pitching of a Cycloidal Rotor Blade at Ultra-Low Reynolds Numbers," *Journal of Aircraft*, Vol. 56, (3), May 2019, pp. 1179–1199.
doi: 10.2514/1.c034776

[31] Reed, C. M., Coleman, D. A., and Benedict, M., "Force and flowfield measurements to understand unsteady aerodynamics of cycloidal rotors in hover at ultra-low Reynolds numbers," *International Journal of Micro Air Vehicles*, Vol. 11, January 2019, pp. 175682931983367.
doi: 10.1177/1756829319833677

[32] McElreath, J. W., Benedict, M., and Tichenor, N., "Cycloidal Rotor-Blade Tip-Vortex Analysis at Low Reynolds Number," *AIAA Journal*, Vol. 58, (6), June 2020, pp. 2560–2570.
doi: 10.2514/1.j058207

[33] Halder, A. and Benedict, M., "Nonlinear Aeroelastic Coupled Trim Analysis of a Twin

Cyclocopter in Forward Flight," *AIAA Journal*, Vol. 59, (1), January 2021, pp. 305–319. doi: 10.2514/1.j059122

[34] Himmelberg, B. and Benedict, M., "Performance Measurements of Meso-Scale Cyclodial Rotors in Hover," 55th AIAA Aerospace Sciences Meeting, January 2017. doi: 10.2514/6.2017-2009

[35] Ramsey, R. and Benedict, M., "Design, Development, and Flight Testing of a 25-Kilogram Quad-Cyclocopter," Proceedings of the VFS International's 78th Annual Forum Technology Display, May 2022.

[36] 2022, S. E. A., "CycloTech GmbH," `https://www.thestormexpoasia.com/exhibitors/cyclotech-gmbh/`, Booth Number 209, December 2022.

[37] McMichael, J. M. and Francis, U. R. C. M. S., "Micro Air Vehicles Toward a New Dimension in Flight," Technical Report 13, Originally published online at http://www.darpa.mil/tto/MAV/mavauvsi.html, Aug. 7, 1997, January 2000.

[38] Spedding, G. R. and Lissaman, P. B. S., "Technical Aspects of Microscale Flight Systems," *Journal of Avian Biology*, Vol. 29, (4), December 1998, pp. 458. doi: 10.2307/3677165

[39] Epstein, A. H., "The Role of Size in the Future of Aeronautics," *The Bridge*, Vol. 34, (1), 2004, pp. 17–23.

[40] Pines, D. J. and Bohorquez, F., "Challenges Facing Future Micro-Air-Vehicle Development," *Journal of Aircraft*, Vol. 43, (2), March 2006, pp. 290–305. doi: 10.2514/1.4922

[41] Chopra, I., "Hovering Micro Air Vehicles: Challenges and Opportunities," Proceedings of American Helicopter Society Specialists' Conference, October 2007.

[42] Galinski, C. and Zbikowski, R., "Some Problems of Micro Air Vehicles Development," *Bulletin of the Polish Academy of Sciences: Technical Sciences*, Vol. 55, (1), March 2007, pp. 91–98.

[43] Selig, M. S., Donovan, J. F., and Fraser, D. B., *Airfoils at Low Speeds*, H. A. Stokely, 1504

North Horseshoe Circle, Virginia Beach, Virginia 23451, 1989.

[44] Lissaman, P. B. S., "Low-Reynolds-Number Airfoils," *Annual Review of Fluid Mechanics*, Vol. 15, (1), January 1983, pp. 223–239.
doi: 10.1146/annurev.fl.15.010183.001255

[45] Kunz, P. J., *Aerodynamics and design for ultra-low Reynolds number flight*, Ph.D. thesis, Stanford University, January 2003.

[46] Mueller, T. J. and DeLaurier, J. D., "AERODYNAMICS OF SMALL VEHICLES," *Annual Review of Fluid Mechanics*, Vol. 35, (1), January 2003, pp. 89–111.
doi: 10.1146/annurev.fluid.35.101101.161102

[47] Leishman, J. G., *Principles of Helicopter Aerodynamics*, Cambridge University Press, New York, NY, 2006, pp. 229, 280, 334–337.

[48] Ramasamy, M., Johnson, B., and Leishman, J. G., "Understanding the Aerodynamic Efficiency of a Hovering Micro-Rotor," *Journal of the American Helicopter Society*, Vol. 53, (4), 2008, pp. 412.
doi: 10.4050/jahs.53.412

[49] Abbott, I. H. and von Doenhoff, A. E., *Theory of Wing Sections*, Dover Publications, New York, 1959.

[50] O'Meara, M. M. and Mueller, T. J., "Laminar separation bubble characteristics on an airfoil at low Reynolds numbers," *AIAA Journal*, Vol. 25, (8), August 1987, pp. 1033–1041.
doi: 10.2514/3.9739

[51] Carmichael, B. H., "Low Reynolds Number Airfoil Survey," techreport NASA-CR-165803-VOL-1, National Aeronautics and Space Administration, November 1981.

[52] Mettler, B., Tischler, M., and Kanade, T., "System Identification of Small-Size Unmanned Helicopter Dynamics," Proceedings of the American Helicopter Society 55th Forum, May 1999.

[53] Burk, S. M. and Wilson, C. F., "Radio-Controlled Model Design and Testing Techniques for Stall/Spin Evaluation of General-Aviation Aircraft," SAE National Business Aircraft

Meeting, 1975.

[54] Mettler, B., *Identification Modeling and Characteristics of Miniature Rotorcraft*, Springer US, 2003.
doi: 10.1007/978-1-4757-3785-1

[55] Ivler, C. M., Rowe, E. S., Martin, J., Lopez, M. J., and Tischler, M. B., "System Identification Guidance for Multirotor Aircraft: Dynamic Scaling and Test Techniques," *Journal of the American Helicopter Society*, Vol. 66, (2), 2021, pp. 1–16.
doi: 10.4050/jahs.66.022006

[56] Zarovy, S., Costello, M., and Mehta, A., "Experimental method for studying gust effects on micro rotorcraft," *Proceedings of the Institution of Mechanical Engineers, Part G: Journal of Aerospace Engineering*, Vol. 227, (4), March 2012, pp. 703–713.
doi: 10.1177/0954410012440663

[57] Galinski, C., "Influence of MAV characteristics on their applications," *Aviation*, Vol. 9, (4), 2005, pp. 16–23.
doi: 10.1080/16487788.2005.9635913

[58] Morris, S. J. and Holden, M., "Design of Micro Air Vehicles and Flight Test Validation," Technical report, MLB Company, 1998.

[59] Grasmeyer, J. and Keennon, M., "Development of the Black Widow Micro Air Vehicle," 39th Aerospace Sciences Meeting and Exhibit, January 2001.
doi: 10.2514/6.2001-127

[60] Kellogg, J., Bovais, C., Foch, R., McFarlane, H., Sullivan, C., Dahlburg, J., Gardner, J., Ramamurti, R., Gordon, D., Hartley, R., Kamgar-Parsi, B., Pipitone, F., Spears, W., Sciambi, A., and Srull, D., "The NRL Micro Tactical Expendable (MITE) Air Vehicle," The Aeronautical Journal, April 2001.

[61] Ifju, P., Jenkins, D., Ettinger, S., Lian, Y., Shyy, W., and Waszak, M., "Flexible-wing-based micro air vehicles," 40th AIAA Aerospace Sciences Meeting & Exhibit, January 2002.
doi: 10.2514/6.2002-705

[62] Pornsin-Sirirak, T. N., Tai, Y.-C., Ho, C.-M., and Keennon, M., "Microbat: A Palm-Sized Electrically Powered Ornithopter," Proceedings of the NASA/JPL Workshop on Biomorphic Robotics, 2001.

[63] de Croon, G., de Clercq, K., Ruijsink, R., Remes, B., and de Wagter, C., "Design, Aerodynamics, and Vision-Based Control of the DelFly," *International Journal of Micro Air Vehicles*, Vol. 1, (2), June 2009, pp. 71–97.
doi: 10.1260/175682909789498288

[64] Keennon, M., Klingebiel, K., and Won, H., "Development of the Nano Hummingbird: A Tailless Flapping Wing Micro Air Vehicle," 50th AIAA Aerospace Sciences Meeting including the New Horizons Forum and Aerospace Exposition, January 2012.
doi: 10.2514/6.2012-588

[65] Ma, K. Y., Chirarattananon, P., Fuller, S. B., and Wood, R. J., "Controlled Flight of a Biologically Inspired, Insect-Scale Robot," *Science*, Vol. 340, (6132), May 2013, pp. 603–607.
doi: 10.1126/science.1231806

[66] Jafferis, N. T., Helbling, E. F., Karpelson, M., and Wood, R. J., "Untethered flight of an insect-sized flapping-wing microscale aerial vehicle," *Nature*, Vol. 570, (7762), June 2019, pp. 491–495.
doi: 10.1038/s41586-019-1322-0

[67] Nagai, H., Nakamura, K., Fujita, K., Tanaka, I., Nagasaki, S., Kinjo, Y., Kuwazono, S., and Murozono, M., "Development of Tailless Two-winged Flapping Drone with Gravity Center Position Control," *Sensors and Materials*, Vol. 33, (3), March 2021, pp. 859.
doi: 10.18494/sam.2021.3222

[68] Coleman, D. A., *FUNDAMENTAL UNDERSTANDING OF THE AEROMECHANICS, FLIGHT DYNAMICS,AND CONTROL OF HUMMINGBIRD-LIKE FLIGHT*, phdthesis, Texas A&M University, December 2021.

[69] Bohorquez, F., Samuel, P., Sirohi, J., Pines, D., Rudd, L., and Perel, R., "Design, Analysis and Hover Performance of a Rotary Wing Micro Air Vehicle," *Journal of the American*

Helicopter Society, Vol. 48, (2), 2003, pp. 80.
doi: 10.4050/jahs.48.80

[70] Fred, "Horizon Hobby Blade mCP S," https://www.helicomicro.com/2017/07/14/horizon-hobby-blade-mcp/, July 2014.

[71] Kroo, I., Prinz, F., Shantz, M., Kunz, P., Fay, G., Cheng, S., Fabian, T., and Partridge, C., "The Mesicopter: A Miniature Rotorcraft Concept Phase II Final Report," Technical report, Stanford University, November 2001.

[72] Ryseck, P., Jacobellis, G., Yeo, D., and Chopra, I., "Experimental Flight Testing of Wing Configurations for High-Speed Mini Quadrotor Biplane Tail-sitter," 9th Biennial Autonomous VTOL Technical Meeting, January 2021.

[73] Benedict, M., Jarugumilli, T., and Chopra, I., "Effect of Rotor Geometry and Blade Kinematics on Cycloidal Rotor Hover Performance," *Journal of Aircraft*, Vol. 50, (5), September 2013, pp. 1340–1352.
doi: 10.2514/1.c031461

[74] Benedict, M., Jarugumilli, T., and Chopra, I., "Experimental Optimization of MAV-Scale Cycloidal Rotor Performance," *Journal of the American Helicopter Society*, Vol. 56, (2), April 2011, pp. 22005–2200511.
doi: 10.4050/jahs.56.022005

[75] Kirsten, F. K., "Cycloidal Propulsion Applied to Aircraft," *Transactions of the American Society of Mechanical Engineers*, Vol. 50, (AER-50-12), 1928, pp. 25–47.

[76] Boirum, C. and Post, S., "Review of Historic and Modern Cyclogyro Design," 45th AIAA/ASME/SAE/ASEE Joint Propulsion Conference & Exhibit, August 2009.
doi: 10.2514/6.2009-5023

[77] Strandgren, C. B., "The Theory of the Strandgren Cyclogiro," Technical Memorandum 727, Washington, November 1933.

[78] Boschma, J. H., "Cycloidal Propulsion for UAV VTOL Applications," Technical report, November 1998.

doi: 10.21236/ada370541

[79] Gibbens, R., Boschma, J., and Sullivan, C., "Construction and testing of a new aircraft cycloidal propeller," 13th Lighter-Than-Air Systems Technology Conference, June 1999. doi: 10.2514/6.1999-3906

[80] McNabb, M. L., *Development of a Cycloidal Propulsion Computer Model and Comparison with Experiment*, mathesis, Mississippi State University, December 2001.

[81] Boschma, J., "Modern aviation applications for cycloidal propulsion," 1st AIAA, Aircraft, Technology Integration, and Operations Forum, August 2001. doi: 10.2514/6.2001-5267

[82] Gibbens, R., "Improvements in Airship Control Using Vertical Axis Propellers," AIAA's 3rd Annual Aviation Technology, Integration, and Operations (ATIO) Forum, November 2003. doi: 10.2514/6.2003-6853

[83] Yu, H., Bin, L. K., and Beng, T. W., "The Investigation of Cyclogyro Design and the Performance," 25th International Congress of the Aeronautical Sciences, 2006.

[84] Hu, Y., Lim, K., and Hu, W., "The Research on the Performance of Cyclogyro," 6th AIAA Aviation Technology, Integration and Operations Conference (ATIO), June 2006. doi: 10.2514/6.2006-7704

[85] Yun, C. Y., Park, I., Lee, H. Y., Jung, J. S., Hwang, I. S., Kim, S. J., and Jung, S. N., "A New VTOL UAV Cyclocopter with Cycloidal Blades System," Presented at the American Helicopter Society 60th Annual Forum, June 2004.

[86] Hwang, I. S., Hwang, C. S., and Kim, S. J., "Structural Design of Cyclocopter Blade System," 46th AIAA/ASME/ASCE/AHS/ASC Structures, Structural Dynamics and Materials Conference, April 2005. doi: 10.2514/6.2005-2020

[87] Hwang, I. S., Min, S. Y., Lee, C. H., Lee, Y. H., and Kim, S. J., "Structural Design and Analysis of Elliptic Cyclocopter Rotor Blades," 16th International Conference on Composite Materials, 2007.

[88] Yun, C. Y., Park, I. K., Lee, H. Y., Jung, J. S., Hwang, I. S., and Kim, S. J., "Design of a New Unmanned Aerial Vehicle Cyclocopter," *Journal of the American Helicopter Society*, Vol. 52, (1), January 2007, pp. 24–35.
doi: 10.4050/jahs.52.24

[89] Lee, C. H., Min, S. Y., Lee, J. W., and Kim, S. J., "Design and Experiment of Two-Rotored UAV Cyclocopter," 29th Congress of the International Council of the Aeronautical Sciences, 7–12, September 2014.

[90] Benedict, M., Ramasamy, M., Chopra, I., and Leishman, J. G., "Experiments on the Optimization of the MAV-Scale Cycloidal Rotor Characteristics Towards Improving Their Aerodynamic Performance," Proceedings of the International Specialists' Meeting on Unmanned Rotorcraft, 20-22, January 2009.

[91] Benedict, M., Ramasamy, M., Chopra, I., and Leishman, J. G., "Performance of a Cycloidal Rotor Concept for Micro Air Vehicle Applications," *Journal of the American Helicopter Society*, Vol. 55, (2), April 2010, pp. 22002–2200214.
doi: 10.4050/jahs.55.022002

[92] Benedict, M., Jarugumilli, T., and Chopra, I., "Experimental Performance Optimization of a MAV-Scale Cycloidal Rotor," Proceedings of the AHS Specialists' Meeting on Aeromechanics, January 2010.

[93] Jarugumilli, T., Benedict, M., and Chopra, I., "Experimental Optimization and Performance Analysis of a MAV Scale Cycloidal Rotor," 49th AIAA Aerospace Sciences Meeting including the New Horizons Forum and Aerospace Exposition, January 2011.
doi: 10.2514/6.2011-821

[94] Benedict, M., Ramasamy, M., and Chopra, I., "Improving the Aerodynamic Performance of Micro-Air-Vehicle-Scale Cycloidal Rotor: An Experimental Approach," *Journal of Aircraft*, Vol. 47, (4), July 2010, pp. 1117–1125.
doi: 10.2514/1.45791

[95] Benedict, M., Mattaboni, M., Chopra, I., and Masarati, P., "Aeroelastic Analysis of a Micro-

Air-Vehicle-Scale Cycloidal Rotor in Hover," *AIAA Journal*, Vol. 49, (11), November 2011, pp. 2430–2443.
doi: 10.2514/1.j050756

[96] Benedict, M., Jarugumilli, T., and Chopra, I., "Design and Development of a Hover-Capable Cyclocopter MAV," Proceedings of the 65th Annual National Forum of the American Helicopter Society, 27-29, May 2009.

[97] Shrestha, E., "Cyclocopter - University of Maryland," `https://www.youtube.com/watch?v=nDhlehsYiGc`, September 2015.

[98] Lind, A. H., Jarugumilli, T., Benedict, M., Lakshminarayan, V. K., Jones, A. R., and Chopra, I., "Flow field studies on a micro-air-vehicle-scale cycloidal rotor in forward flight," *Experiments in Fluids*, Vol. 55, (12), November 2014, pp. 1826.
doi: 10.1007/s00348-014-1826-1

[99] Benedict, M., Jarugumilli, T., and Chopra, I., "Effects of Asymmetric Blade-Pitching Kinematics on Forward-Flight Performance of a Micro-Air-Vehicle-Scale Cycloidal-Rotor," *Journal of Aircraft*, Vol. 53, (5), September 2016, pp. 1568–1573.
doi: 10.2514/1.c033558

[100] Benedict, M., Shrestha, E., Hrishikeshavan, V., and Chopra, I., "Development of a Micro Twin-Rotor Cyclocopter Capable of Autonomous Hover," *Journal of Aircraft*, Vol. 51, (2), March 2014, pp. 672–676.
doi: 10.2514/1.c032218

[101] Shrestha, E., Yeo, D., Benedict, M., and Chopra, I., "Development of a meso-scale cycloidal-rotor aircraft for micro air vehicle application," *International Journal of Micro Air Vehicles*, Vol. 9, (3), May 2017, pp. 218–231.
doi: 10.1177/1756829317702048

[102] Benedict, M., Lakshminarayan, V., Pino, J., and Chopra, I., "Fundamental Understanding of the Physics of a Small-Scale Vertical Axis Wind Turbine with Dynamic Blade Pitching: An Experimental and Computational Approach," 54th AIAA/ASME/ASCE/AHS/ASC Struc-

tures, Structural Dynamics, and Materials Conference, April 2013.
doi: 10.2514/6.2013-1553

[103] Benedict, M., Lakshminarayan, V., Pino, J., and Chopra, I., "Aerodynamics of a Small-Scale Vertical-Axis Wind Turbine with Dynamic Blade Pitching," *AIAA Journal*, Vol. 54, (3), March 2016, pp. 924–935.
doi: 10.2514/1.j052979

[104] Mills, A., Benedict, M., and Chopra, I., "Investigation of the Effect of Blade Kinematics and Reynolds Number on the Aerodynamic Performance of a Small-Scale Vertical Axis Wind Turbine with Dynamic Blade Pitching," 54th AIAA Aerospace Sciences Meeting, January 2016.
doi: 10.2514/6.2016-0137

[105] Halder, A. and Benedict, M., "Role of Blade Flexibility on Cycloidal Rotor Hover Performance," *Journal of Aircraft*, Vol. 55, (5), September 2018, pp. 1773–1791.
doi: 10.2514/1.c034712

[106] Halder, A., Walther, C., and Benedict, M., "Hydrodynamic modeling and experimental validation of a cycloidal propeller," *Ocean Engineering*, Vol. 154, April 2018, pp. 94–105.
doi: 10.1016/j.oceaneng.2017.12.069

[107] Walther, C., Coleman, D., Benedict, M., and Lakshminarayan, V. K., "Experimental and Computational Studies to Understand Unsteady Aerodynamics of Cycloidal Rotors in Hover at Ultra-low Reynolds Numbers," AHS International 73rd Annual Forum & Technology Display, May 2017.

[108] Runco, C. and Benedict, M., "Flowfield Measurements on a Low Aspect Ratio Cycloidal Rotor," `https://www.youtube.com/watch?v=8bidvud9ywk`, July 2017.

[109] Hrishikeshavan, V. and Chopra, I., "Refined lightweight inertial navigation system for micro air vehicle applications," *International Journal of Micro Air Vehicles*, Vol. 9, (2), June 2017, pp. 124–135.
doi: 10.1177/1756829316682534

[110] Georgy, J., Noureldin, A., Korenberg, M. J., and Bayoumi, M. M., "Modeling the Stochastic Drift of a MEMS-Based Gyroscope in Gyro/Odometer/GPS Integrated Navigation," *IEEE Transactions on Intelligent Transportation Systems*, Vol. 11, (4), December 2010, pp. 856–872.
doi: 10.1109/tits.2010.2052805

[111] Thong, Y. K., Woolfson, M. S., Crowe, J. A., Hayes-Gill, B. R., and Challis, R. E., "Dependence of inertial measurements of distance on accelerometer noise," *Measurement Science and Technology*, Vol. 13, (8), July 2002, pp. 1163–1172.
doi: 10.1088/0957-0233/13/8/301

[112] Paris, A. C. and Bonner, M., "Nonlinear Model Development from Flight-Test Data for F/A-18E Super Hornet," *Journal of Aircraft*, Vol. 41, (4), jul 2004, pp. 692–702.
doi: 10.2514/1.3167

[113] Morelli, E. A. and Klein, V., "Application of System Identification to Aircraft at NASA Langley Research Center," *Journal of Aircraft*, Vol. 42, (1), jan 2005, pp. 12–25.
doi: 10.2514/1.3648

[114] Morelli, E. A. and Klein, V., *Aircraft System Identification: Theory and Practice*, Education, American Institute of Aeronautics and Astronautics, first edition, January 2006.
doi: 10.2514/4.861505

[115] Tischler, M. B. and Remple, R. K., *Aircraft and Rotorcraft System Identification: Engineering Methods with Flight Test Examples*, AIAA Education Series, AIAA, New York, second edition, April 2006.
doi: 10.2514/4.861352

[116] Grauer, J., Conroy, J., Hubbard, J., Humbert, J., and Pines, D., "System Identification of a Miniature Helicopter," *Journal of Aircraft*, Vol. 46, (4), jul 2009, pp. 1260–1269.
doi: 10.2514/1.40561

[117] Gremillion, G. and Humbert, J., "System Identification of a Quadrotor Micro Air Vehicle," AIAA Atmospheric Flight Mechanics Conference, June 2010.

doi: 10.2514/6.2010-7644

[118] Dorobantu, A., Murch, A., Mettler, B., and Balas, G., "System Identification for Small, Low-Cost, Fixed-Wing Unmanned Aircraft," *Journal of Aircraft*, Vol. 50, (4), July 2013, pp. 1117–1130.
doi: 10.2514/1.c032065

[119] Runco, C. and Benedict, M., "System Identification of a Meso-Scale Twin-Cyclocopter in Hover," Proceedings of the VFS International's 74th Annual Forum Technology Display, May 2018.

[120] Morelli, E., "System Identification Programs for AirCraft (SIDPAC)," AIAA Atmospheric Flight Mechanics Conference and Exhibit, June 2002.
doi: 10.2514/6.2002-4704

[121] GmbH, C., "First Free Flight," `https://www.youtube.com/watch?v=I2qkhmz4z1E`, October 2021.

[122] Runco, C. and Benedict, M., "60-gram Quad Cyclocopter (Texas A&M University)," `https://www.youtube.com/watch?v=eL4gXdwA8vg`, October 2021.